Title
Molecular Gas and Star Formation in Nearby Galaxies

Author
Utomo, Dyas

Publication Date
2017

Peer reviewed|Thesis/dissertation

MOLECULAR GAS AND STAR FORMATION IN NEARBY GALAXIES

By

Dyas Utomo

A dissertation submitted in partial satisfaction of the

requirements for the degree of

Doctor of Philosophy

in

Astrophysics

in the

Graduate Division

of the

University of California, Berkeley

Committee in charge:

Professor Leo Blitz, Chair
Professor Christopher McKee
Professor Chung-Pei Ma
Professor Adrian Lee

Summer 2017

MOLECULAR GAS AND STAR FORMATION IN NEARBY GALAXIES

Abstract

MOLECULAR GAS AND STAR FORMATION IN NEARBY GALAXIES

by

Dyas Utomo

Doctor of Philosophy in Astrophysics

University of California, Berkeley

Professor Leo Blitz, Chair

In the local Universe, stars form within molecular clouds. Therefore, the properties of molecular clouds may determine the star formation rate. Conversely, star formation also gives feedback to the clouds where the stars reside. In this dissertation, I present the interplay between the molecular gas and star formation, through three parts below.

First, I identify and characterize the properties of molecular clouds in NGC4526, resulting in the first catalog of molecular clouds in an early-type galaxy. As a population, the molecular clouds in NGC4526 are gravitationally bound and have a steeper mass distribution than that in the Milky Way. These molecular clouds are also more luminous, denser, and have a higher velocity dispersion than their counterparts in the Milky Way. These different properties may be due to a more intense interstellar radiation field than in the Galactic disk and a weaker external pressure than in the Galactic center.

Second, I combine the mm-wave interferometric data from CARMA and the optical Integral Field Unit data from CALIFA to study the molecular depletion time on kilo-parsec scales of nearby galaxies. In particular, the molecular depletion time between the galactic centers and disks is compared. I find that some galactic centers have shorter depletion time than that in the disks, which means that those centers form stars more efficiently per unit molecular gas mass. This places the galactic centers as an intermediate regime between galactic disks and starburst galaxies. The central drop of depletion time is also correlated with a central increase in the stellar mass surface density, suggesting that a shorter depletion time is associated with the molecular gas compression by the stellar gravitational potential.

Third, the feedback from star formation to maintain turbulence in the interstellar matter of M33 is investigated. I show that supernovae have enough energy to maintain atomic gas turbulence inside $\sim$ 4 kpc radius and within molecular clouds, assuming a constant value of turbulent dissipation time of 9.8 Myrs. In the outer parts, the energy from the differential rotation of galaxy is large enough to maintain atomic gas turbulence through the magneto-rotational instability (MRI). I conclude that the sum of supernovae and MRI energy maintains turbulence at all radii where H I is detected in M33.

Contents

List of Figures

List of Tables

Chapter 1

Introduction

1.1 Motivation

Since the dawn of human history, mankind always wondered of the twinkling objects they saw in the sky that we call stars. But only about a century ago, we started to understand their origin and formation processes. The advancement of astronomical instruments that are sensitive to radio and infrared wavelengths opened a new view of the cosmos, previously unseen through optical instruments: we can directly observe the interstellar matter (as the fuel of star formation) and the stellar nursery, deeply embedded inside the optically opaque interstellar matter.

In a broad picture, the diffuse, atomic hydrogen gas in a galaxy condenses to form a colder, denser gas, perhaps as a result of some gravitational instabilities. With help from dust, this gas can shield itself from the interstellar radiation field, so that the dominant constituent is molecular (H_2 and CO). This molecular gas is stabilized against the gravitational contraction through turbulence and magnetic support. However, in some clumps of dense gas, proto-stars are born and eventually become zero age main-sequence stars. The most massive stars then provide feedback to their natal clouds in the forms of ionized photons, winds, and outflow, which give rise to the formation of H II regions. Within a few 10^7 years, these stars become supernovae with enough energy to disrupt the natal clouds, halt the star formation locally, but may induce the star formation in the neighborhood shocked regions (Elmegreen & Lada 1977). This process is repeated in cycles throughout the life of a galaxy, until the gas is exhausted.

This dissertation adds a small chunk into our understanding on the formation of stars out of their natal clouds and their feedback in generating turbulence to the surrounding gas. It is based on multi-wavelength observational data (proprietary and archival), as opposed to theory and simulations. Specifically, it focuses on the three topics below.

1. *The properties of molecular clouds in an early-type galaxy.* While surveys of molecular clouds have been done in the Milky Way and other nearby galaxies, those surveys targeted star forming galaxies (spirals and dwarfs). Here, I extend those surveys to the

early-type galaxy, NGC4526, to investigate whether the properties of molecular clouds in the early-type galaxies are similar or different than those in the late-type galaxies.

2. *The star formation efficiency on kilo-parsec scales.* The rate of star formation depends on the amount of molecular gas and the efficiency of transforming that gas into stars per unit gas mass. While the current consensus favors a constant efficiency (in the order of $\sim 1\%$ per free-fall time), recent result showed that there is an enhancement of this efficiency in the galactic center (Leroy et al. 2013). Here, I revisit their study using a new and more complete dataset as a part of the largest interferometric CO survey of nearby galaxies, called the Extragalactic Database for Galaxy Evolution (EDGE; Bolatto et al. 2017).

3. *What is the energy source of interstellar turbulence?* While the stellar feedback has enough energy to drive turbulence in the inner disk of galaxies, the gas remains turbulent in the outer part where the star formation is negligible. Here, I propose the magneto-rotational instability as a viable source of turbulence in the outer part of a galaxy. The high resolution data of M33 (Figure 1.1) also enables me to show that the stellar feedback has enough energy to maintain turbulence in the molecular clouds.

Nearby galaxies are chosen to be the avenue of this dissertation because of practical and philosophical reasons. Nearby galaxies are well resolved (on $\lesssim$ kpc scale) by ground-based and space telescopes. This enables astronomers to study the ISM in different environments than in the Milky Way, without having to deal with the complexities of micro-processes (on pc scales). Nearby galaxies are also close enough, so that we do not have to spend too much telescope time for one galaxy. This allows astronomers to conduct (a statistically significant) galaxy survey on a reasonable time scale ($\lesssim$ Ph.D. time-scale). Finally, in relation to galaxy evolution itself, nearby galaxies are the final product of galaxy evolution throughout the Hubble time, and hence, serve as a benchmark for observations of high-redshift galaxies and as a constraint for any theories of galaxy evolution and star formation.

1.1.1 Dissertation Outline

This dissertation builds on three projects during my graduate school: (1) the molecular clouds in NGC4526, (2) the EDGE CO-survey as a follow-up to the optical IFU survey, and (3) the turbulence in M33. Each project is organized as a single chapter (from chapter 2 to 4) that has its own introduction, contents, summary, and appendices as in a published paper format. For the convenience of readers, I add the first chapter as a general introduction to what comes next. This introduction is less rigorous than a textbook explanation and less comprehensive than a review paper, pointing only to information that is directly related to the contents of dissertation. I also add the last chapter, as a concluding remark to highlight the important points of my work and how it is connected to the broad topics of molecular gas and star formation in nearby galaxies. Finally, I insert a section in the last chapter to give a teaser about the research opportunities that await me right after graduation.

Figure 1.1: This image of the Triangulum Galaxy (M33) was created by combining optical data (through B, V, I and Hα filters) from the National Science Foundation's 0.9-meter telescope on Kitt Peak in Arizona with radio data (21-cm, shown as blue-violet) from the Very Large Array and the Westerbork Synthesis Radio Telescope. The optical data show the stars as well as reddish star-forming regions that are filled with hot ionized hydrogen gas (H II). The radio data reveal the cool atomic hydrogen gas (H I) within the galaxy, which extend farther than the stellar disk. The image is one square degree in field of view, roughly five times the angular size of the Moon. Image credit: T. A. Rector (NRAO/AUI/NSF and NOAO/AURA/NSF) and M. Hanna (NOAO/AURA/NSF).

1.2 Galaxy Populations in the Local Universe

Based on their morphologies, galaxy populations can be divided into ellipticals (that have roundish, spheroidal shape) and disk-like spirals (with a spheroidal or elongated shape bulge in the center). There is an intermediate shape between them, which is called lenticulars (it has a disk-like shape, but no spiral arms and lack of star formation). Hubble (1926) further made finer classifications based on the ellipticities (from E0 to E7 for elliptical galaxies) and the tightness of spiral arms, in addition to the prominence of the bulge (from Sa to Sd for spiral galaxies). The lenticular is designated as S0 galaxy. This classification is widely accepted as the Hubble sequence due to false impression that this sequence (from E0 to Sd) marked the evolutionary sequence of galaxies. Furthermore, some spirals galaxies have elongated structure in their center, which is called bar.

Beyond those classifications, there exist low mass, dwarf galaxies with irregular shape or galaxies undergo merger that disrupt their morphologies to be irregular (designated as Irr), and the brightest galaxy in a galaxy cluster (Dubinski 1998) that exhibits an extended diffuse envelope surrounding its nucleus, which is thought to be the result of galaxy mergers (designated as cD). As a general term, cD, E and S0-types galaxies are called the early-types, while the spirals and Irr-types galaxies are called the late-types. There is a tendency that the early-types are located in a denser environment (galaxy clusters) and the late-types are located in the field or galaxy groups. Our Galaxy, the Milky Way, is a barred spiral galaxy (Blitz & Spergel 1991) located in the Local Group. This Local Group consists of three spiral galaxies (the Milky Way, M31, and M33, Figure 1.1) and many dwarf galaxies (van den Bergh 2000; Mateo 1998).

Besides morphologies, the distinctive features of galaxy population are their absolute magnitude (a measure of how luminous is an object in a given filter, e.g. M_V for absolute magnitude in the visual band) and their color (defined as the difference between the amount of light at given filters, e.g. $g-r$ for green and red filters). M_V also correlates strongly with stellar mass. Based on large spectroscopic surveys (e.g., SDSS; York et al. 2000), galaxy populations appear to be bimodal in M_V versus $g-r$ diagram as the blue cloud and the red sequence (Figure 1.2; Schawinski et al. 2014). Galaxies in the blue cloud are star forming spirals, dwarfs, and irregulars, therefore, they have bluer color (i.e. smaller value of $g-r$). On the other hand, the red sequence consists of E, S0, and (dust obscured) Sa-types galaxies, with minor addition from dwarf and giant ellipticals. They are more massive, older, and redder due to lack of star formation. For a review, see Blanton & Moustakas (2009).

1.3 Molecular Gas and its Role in Galaxy Evolution

In general, the interstellar medium consists of three phases: cold and warm (neutral or ionized) medium (Field 1965), and hot ionized medium (McKee & Ostriker 1977). Stars form in the dense ($n \sim 100$ cm^{-3}) and cold ($T \sim 10$ K) interstellar region within a galaxy. In this condition, the gas is well shielded ($A_V > 1$ mag) from the stellar radiation field

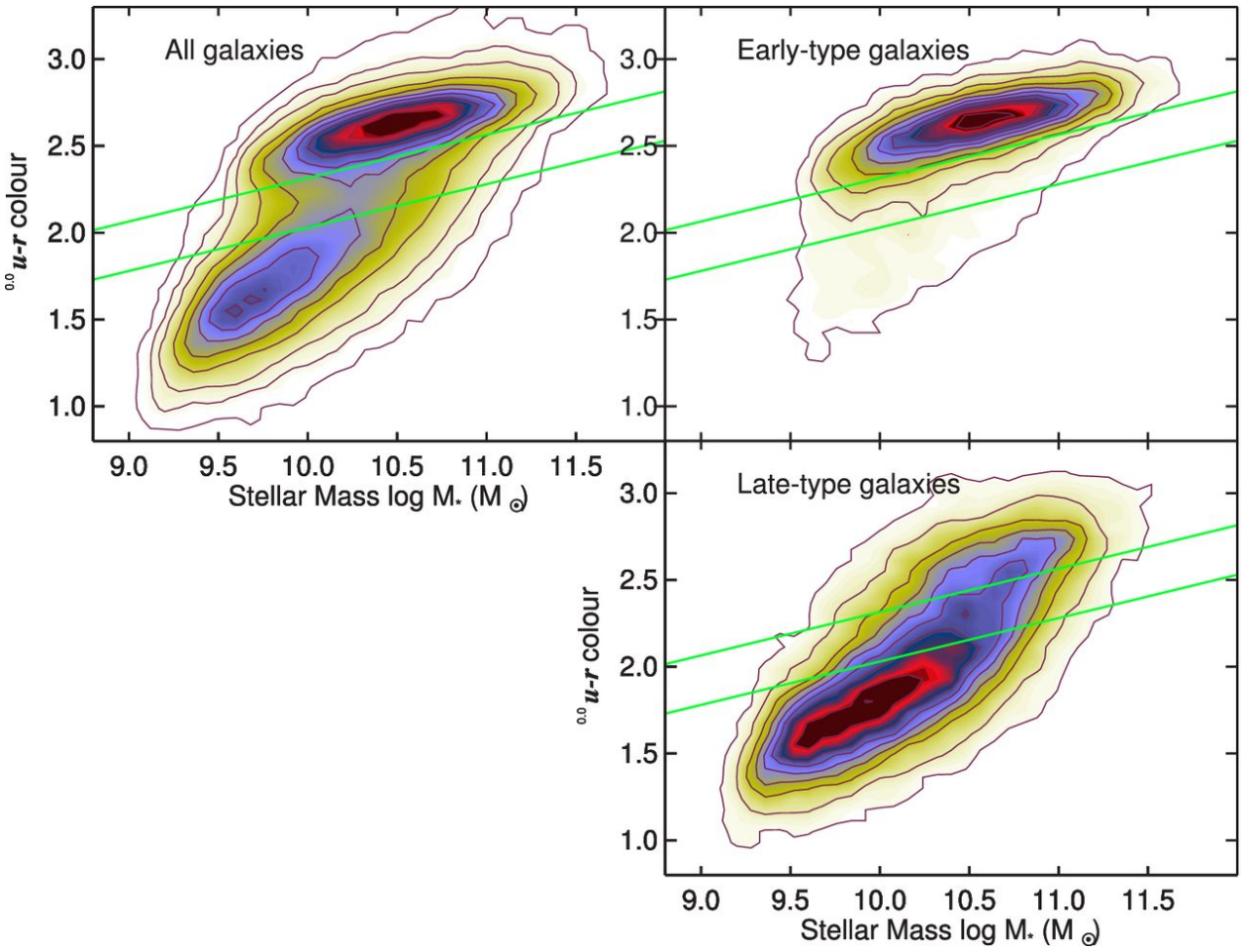

Figure 1.2: Left panel: the bimodality in galaxy populations: red sequence and blue clouds (data from SDSS, GALEX, and Galaxy Zoo). The green line marks the "green valley" as a transitional zone between red sequence and blue cloud. Left panel: the contour plot of early-type galaxies and late-type galaxies. This shows that a small fraction of early-type galaxies is in the blue cloud, while some fractions of late-type galaxies is in the red sequence. Image credit: Schawinski et al. (2014).

through dust extinction and gas self-shielding. In this environment, the primary form of hydrogen is molecular (H_2) which is called the molecular clouds. For Solar metallicity and low to moderate radiation fields, the gas is almost fully molecular at gas surface density of $\sim 10\ M_\odot\ \mathrm{pc}^{-2}$ (Wong & Blitz 2002; Bigiel et al. 2008; Krumholz et al. 2009). Except for the first stars in the early Universe, the present day stars are form within the core of molecular clouds.

1.3.1 CO as a Surrogate for H_2

H_2 is the most abundant molecule in the Universe. H_2 forms primarily on the surface of dust grains (Gould & Salpeter 1963; Hollenbach & Salpeter 1971) and dissociated by UV photons with energy above the Lyman band. In the Milky Way, the mass of H_2 ($\sim 1\times10^9 M_\odot$) represents $\sim 10\%$ the interstellar medium mass (Heyer & Dame 2015). However, detecting radiation from H_2 in radio wavelength is not practical because its dipole moment is zero (due to its symmetric geometrical shape). Even though H_2 has signatures in UV (Carruthers 1970) and IR (Gould & Harwit 1963; Leung 1976; Gautier 1978), it is not practical for observations because of the opacity of the Earth's atmosphere and those lines do not trace cold, dense molecular gas. For example, the two lowest ortho and para transitions of H_2 are only excited in gas with temperature $\gtrsim 100$ K (Bolatto et al. 2013).

Therefore, carbon-monoxide (CO; first detected by Wilson et al. 1970) is used as a surrogate for H_2 because it is a fairly abundant molecule ($N_{\rm CO}/N_{\rm H_2} \lesssim 10^{-4}$), roughly co-exist with H_2, and have a fairly strong emission ($J = 1-0$) at 115 GHz where the Earth's atmosphere is transparent. This lowest rotational transition ($J = 1-0$) lies only $5-22$ K above the ground state and at a critical density of $\sim 2\times10^3$ cm^{-3}, enabling CO to probe the cold, dense region. The abundance of CO at higher excitation state (e.g. $J = 2-1$) depends on the temperature and volume density of the gas. The median value of the intensity ratio $R = I(J=2-1)/I(J=1-0)$ in the Milky Way is 0.64 ± 0.05 (Heyer & Dame 2015).

For most cases, CO emission is measured to be optically thick. To overcome this limitation, we measured the molecular column density using other tracers (such as optically thin ^{13}CO, dust emission, and gamma rays) and CO emission at the same location. Then, the CO emission and H_2 column density are connected through a conversion factor. In this way, we calibrated the CO emission as a tracer of molecular gas column density. For example, this calibration yields a conversion factor of $X_{\rm CO} \approx 2\times10^{20}$ cm^{-2} (K km s^{-1})$^{-1}$ in the Milky Way. Note that in radio astronomy, the units K km s^{-1} are often used as the units for luminosity. Actually, $X_{\rm CO}$ depends on the local environment (for example, $X_{\rm CO}$ is higher in low metallicity environment and lower in starburst galaxies), and hence, the actual value of $X_{\rm CO}$ is one of the most debatable when considering the H_2 mass. For a review of CO-to-H_2 conversion factor see Bolatto et al. (2013).

Note that CO and H_2 are not always co-located. At the very low gas column density or low metallicity, there is not enough shielding to protect CO from dissociation, even though hydrogen is molecular. This gas is called the "dark" molecular gas because it is deficient CO and the use of Galactic $X_{\rm CO}$ underestimates the true H_2 mass (van Dishoeck & Black 1988; Blitz et al. 1990; Sternberg & Dalgarno 1995; Wolfire et al. 2010). Nevertheless, the use of IR light or gamma rays can overcome this limitation. In the Milky Way, these dark gas may account for $30-50\%$ of the total molecular gas (Grenier et al. 2005; Wolfire et al. 2010). Furthermore, at very high volume density ($\gtrsim 10^4$ cm^{-3}) and low temperature ($\lesssim 25$ K), CO begins to freeze-out onto grain surfaces, causing CO abundance to decrease (Heyer & Dame 2015). Thus, CO is safely co-exist with H_2 at column density around 1 to 3×10^{21} cm^{-2} (Visser et al. 2009).

1.3.2 Molecular Gas in Nearby Galaxies

As the fuel of star formation, the formation, destruction, and the efficiency of molecular gas to form stars (i.e. the star formation rate per unit gas mass, or called the star formation efficiency, SFE) are important factors that drive galaxy evolution. The existence of red sequence population with lack or negligible star formation suggests that those galaxies are either lack of molecular gas or the gas is stable against gravitational contraction, or both. In galaxy-by-galaxy measurements, Saintonge et al. (2016) showed that the SFE declines by ~ 0.2 dex and the molecular gas fraction ($f_{\rm H_2} = M_{\rm H_2}/M_*$) declines by ~ 0.5 dex for galaxies with masses from 10^{10} to 10^{11} $M_\odot$. This means lack of the molecular gas is the main reason of galaxies that undergo quenching. Interestingly, the atomic gas fraction ($f_{\rm HI} = M_{\rm HI}/M_*$) also declines at the same rate as $f_{\rm H_2}$, which means the conversion of atomic to molecular gas is not the bottleneck that inhibit star formation in quiescent galaxies.

Since ellipticals tend to be more massive than spirals, the difference of the molecular gas fraction is also apparent in morphological basis. The recent result from the EDGE survey (Bolatto et al. 2017) showed that the ellipticals has an order-of-magnitude lower molecular gas fraction ($f_{\rm H_2} \sim 0.6\%$) than the spirals ($f_{\rm H_2} \sim 5\%$). The detection rate of molecular gas in the early type galaxies is around $22 - 32\%$ (Combes et al. 2007; Sage et al. 2007; Young et al. 2011). Interestingly, the molecular gas in early-type galaxies show varieties of morphologies: disk, ring, bar, and spiral arm (Young 2002; Alatalo et al. 2013). This molecular gas has higher specific angular momentum than the stars, counter rotating, or kinematically misaligned, which suggests their external origin (Young et al. 2008; Davis et al. 2011).

H_2 gas can be diffuse or coagulated in higher density region as clouds. The diffuse gas can be considered to be all material with total hydrogen column density less than a few 10^{21} cm^{-2} (Hennebelle & Falgarone 2012). This diffuse molecular gas may contribute to $\sim 20\% - 50\%$ of the total CO emission in a galaxy and has a scale height of ~ 0.2 to 1 kpc (Garcia-Burillo et al. 1992; Wilson & Walker 1994; Rosolowsky & Blitz 2005; Goldsmith et al. 2008; Pety et al. 2013). The small scale measurement, especially conducted by radio interferometer, is less sensitive to the diffuse emission, and hence, most of the CO emission is originated from molecular clouds or associations. In the Milky Way, most of the H_2 mass resides in the molecular clouds. This dissertation assumes all CO emission comes from molecular clouds.

1.3.3 The Properties of Molecular Clouds

There is no clear boundary or absolute definition of molecular clouds. A molecular cloud is often seen as a contiguous volume of detected pixels in the position-position-velocity data cube, providing the resolution of observation is smaller than the size of molecular clouds. For practical purposes, the boundary of molecular clouds are determined by the sensitivity of the observation, e.g. whereever we can reach 2σ sensitivity, or set by an absolute intensity value, e.g. brightness temperature of 1 K. The molecular clouds are also hierarchical, it can consist of multiple denser regions within it, so that one big clouds may be decomposed

into multiple clouds (e.g., Blitz & Thaddeus 1980; Blitz & Stark 1986). This hierarchy can be traced, for example, by using the dendogram method of Rosolowsky et al. (2008). The current state of art algorithms to identify and decompose molecular clouds are CPROPS (Rosolowsky & Leroy 2006) and SCIMES (Colombo et al. 2015). Earlier surveys (e.g., Dame et al. 1986; Myers et al. 1986; Solomon et al. 1987; Scoville et al. 1987) used different method to identify and measure the properties of molecular clouds. Therefore, we should be wary of these systematic effects due to different methodologies (which is not discussed in this dissertation, but see Heyer et al. 2001; Brunt et al. 2003; Rathborne et al. 2009).

The typical size of giant molecular clouds is $\sim$ 50 pc, with temperature of $\sim$ 15 K, volume density of few hundreds cm^{-3}, and masses of $\sim 10^5 - 10^6 M_\odot$ (e.g., Blitz 1993). Molecular clouds are dynamic structures (can be formed and dispersed) with a lifetime of $\sim$ 20 Myrs (Blitz & Shu 1980; Fukui & Kawamura 2010; Meidt et al. 2015), faster than the Galactic orbital time ($\sim$ 200 Myr). Except in the Galactic center and the low mass clouds, the molecular clouds are gravitationally bound (with virial parameter $\alpha \sim 1$), where the gravitational force is balanced by the kinetic force, dominated by the supersonic turbulent motion of the gas. The molecular clouds in Galactic center are pressure bound, where they are held by the ambient pressure of interstellar medium, rather than their self-gravity (Oka et al. 2001). At some degree, the magnetic field can contribute to counter the gravitational force (e.g., Mouschovias & Spitzer 1976).

In the Milky Way, the surface density of GMCs varies as a function of Galactocentric distance (see Figure 8 in Heyer & Dame 2015): 1800 $M_\odot$ pc^{-2} in the Galactic center (Oka et al. 2001), 200 $M_\odot$ pc^{-2} in the molecular ring ($r \approx 3$ to 7 kpc; Solomon et al. 1987), and 30 $M_\odot$ pc^{-2} in the outer Galaxy ($r \approx 10$ to 20 kpc; Heyer et al. 2001) for a Galactic $X_{\rm CO}$. This variation can be explained partly due to the variation of $X_{\rm CO}$ in the Milky Way. Alternative measurements using ^{13}CO emission confirmed this difference in GMC surface density: 140 $M_\odot$ pc^{-2} in the molecular ring (Roman-Duval et al. 2010), and 40 $M_\odot$ pc^{-2} in the outer Galaxy (Brand & Wouterloot 1994), meaning the variation of surface density cannot be explained by $X_{\rm CO}$ alone. Furthermore, the variation of GMC surface density in extragalaxies is also observed between galaxies (see Section 2.5.2 in this dissertation) and within a galaxy (M51; Colombo et al. 2014). Thus, this variation may depends on the local environment of the ISM.

The mass distribution of GMC is not universal from galaxy to galaxy. Usually, it is described through a functional form that includes the upper limit cutoff (Williams & McKee 1997) as

$$\frac{dN}{dlnM} = N_{\rm cu} \left(\frac{M_u}{M} \right)^{-(\alpha_M - 1)}, \text{ for } M < M_u, \tag{1.1}$$

where M_u is the upper limit mass and $N_{\rm cu}$ is the number of clouds near the upper limit mass. The integral of Equation (1.1) is given in Equation (2.6). The best-fit values for the Milky Way are $\alpha_M - 1 = 0.7$, $N_{\rm cu} = 10$, and $M_u = 6 \times 10^6 M_\odot$ (Williams & McKee 1997). In extragalaxies, Rosolowsky (2005) calculated $\alpha_M - 1 = 2.9$ in M33 (with no evidence of mass cut-off) and 1.7 in LMC. Within M51, $\alpha_M - 1$ varies between 1.3 and 2.5 from region

to region (Colombo et al. 2014). As in other GMC properties, the variation of GMC mass distribution may also be determined by the local environment of the ISM.

1.3.4 The Formation and Destruction of Molecular Clouds

The molecular clouds are formed in the high density region, where there is enough shielding to protect H_2 from dissociation. Following arguments by Blitz & Shu (1980), McKee & Ostriker (2007) and references therein, this high density region can be formed in two ways: (1) "bottom-up" scenario (coagulation theory), where the inelastic collisions of H I clouds increase the size, mass, and density until sufficient conditions needed for GMC formation are achieved, and (2) "top-down" scenario, where the large-scale instabilities in diffuse ISM, such as Parker (1958) and Jeans (1902) instabilities, cause the diffuse gas to contract under its self-gravity to form denser gas. The time-scale for "bottom-up" scenario is $\sim$ 100 Myrs (Scoville & Hersh 1979), which is longer than the estimated GMC lifetime ($\sim$ 20 Myr). The "top-down" scenario has faster time scale by a factor of $2-5$, therefore, this scenario is preferred. Nevertheless, during its formation, a braking mechanism (Mouschovias & Paleologou 1979) must occurs to slow down the angular momentum of GMCs (Rosolowsky et al. 2003; Imara & Blitz 2011).

Ironically, the most possible reason of the GMCs destruction is done by the massive stars (O and B associations) that born within the GMCs itself (Figure 1.3). These stars emit intense radiation that ionizes and evaporates molecular clouds through the expansion of H II regions, and even, disrupts the clouds through the momentum injection from stellar winds and supernovae. Blitz & Shu (1980) argued that the O and B associations only need $\sim 0.1\%$ of their energy to evaporate GMCs. Given the age of O and B stars, the co-existence of molecular clouds and O and B stars means that GMCs can only survive in about 10 Myrs *after* the formation of O and B stars. How about the GMC age *before* the formation of O and B stars? Based on the clumpiness of molecular complexes, Blitz & Shu (1980) argued that a maximum collision time of $\sim$ 10 Myrs is needed, above which the molecular complexes would be featureless because of the coalescence between their clumps. In total, they predicted the age of GMCs is about 20 Myrs.

Besides the stellar feedback, another possible mechanism for GMC destruction is galactic shear. By measuring the relative number of GMCs in the inter-arm regions of M51, Meidt et al. (2015) concluded that the GMC lifetime in the inner disk of M51 is $20-30$ Myr. The galactic shear is the primary limit of the GMC lifetime in the inner disk, while the stellar feedback dominates in the outer part. They also predicted that GMCs in massive galaxies and in the center of galaxies tend to be short lived because the shear is strong. If this lifetime is shorter than the GMC free-fall time, then the clouds would be destroyed before star formations can occur. This mechanism may be the reason for star formation suppression in massive galaxies.

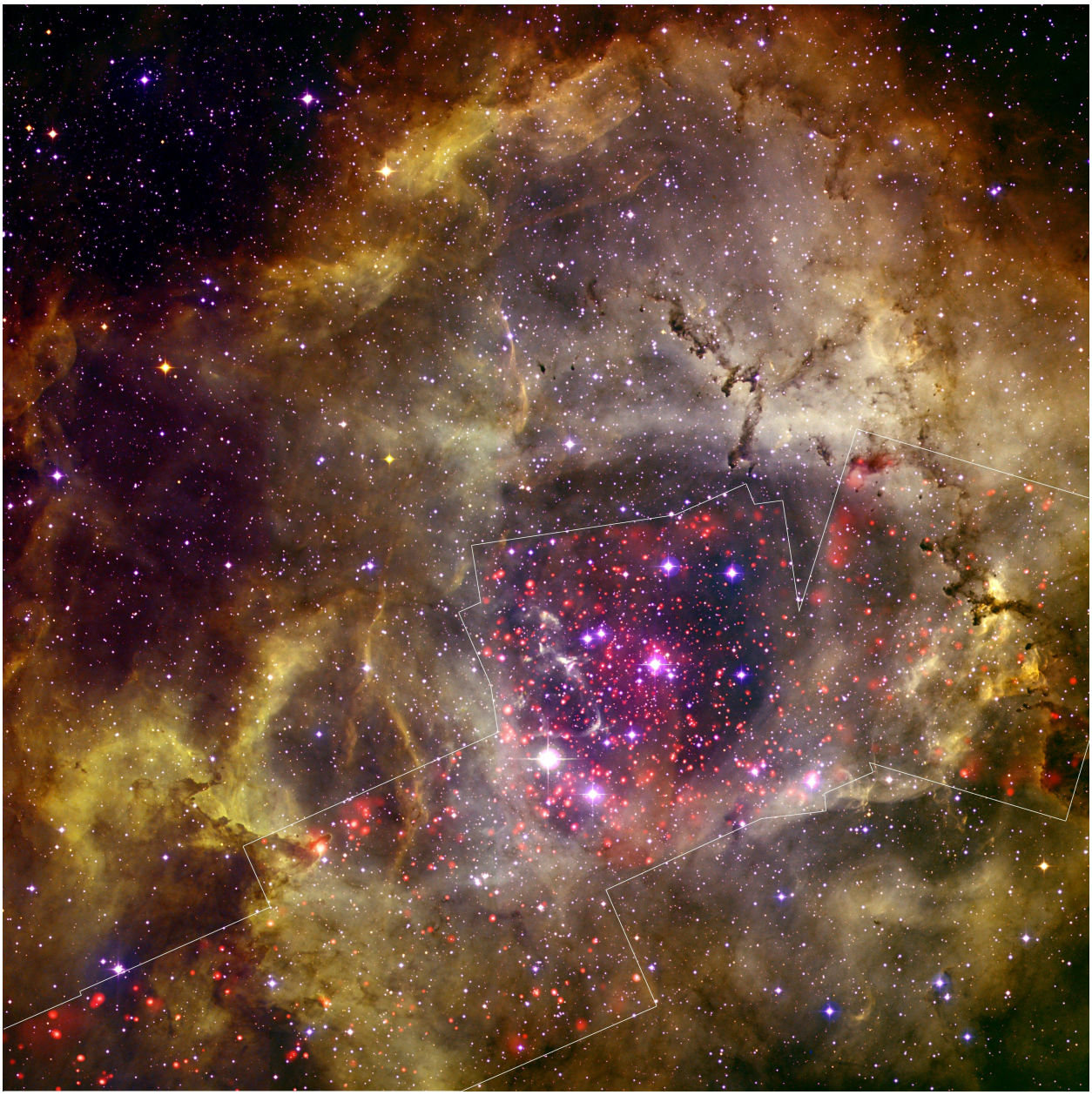

Figure 1.3: The composite image of the Rosette star forming region, located about 5,000 light years from Earth. Data from the Chandra X-ray Observatory are colored red and outlined by a white line. The X-rays reveal hundreds of young stars clustered in the center of the image and additional fainter clusters on either side. Optical data from the Digitized Sky Survey and the Kitt Peak National Observatory (purple, orange, green and blue) show large areas of gas and dust, including giant pillars that remain behind after intense radiation from massive stars has eroded the more diffuse gas. Image credit: X-ray (NASA/CXC/SAO, Wang et al. 2009) and optical (DSS & NOAO/AURA/NSF/KPNO 0.9-m/T. Rector et al)

1.4 Star Formation Rates in kilo-parsec Scale

For most telescopes, the individual stars in nearby galaxies are unresolved. Even with the Hubble Space Telescope (HST), mapping individual stars in nearby galaxies is time consuming. Therefore, the following tracers of star formation rates (SFR) have been used.

- The ultraviolet (UV) photons emitted by young, massive (spectral types O and B) stars.
- Those UV photons that excite the surrounding atomic hydrogen, and eventually emit Hα radiation (assuming case B recombination). Other recombination lines of atomic hydrogen can be used as SFR tracers, but Hα is more popular due to its higher intensity and less extinction.
- Those UV photons that heat the surrounding dust and reradiated as infrared (IR) light.
- The radio continuum emission originated from synchrotron process in the supernovae remnant (e.g., Murphy et al. 2011).
- Modeling of the stellar population synthesis that takes into account many parameters (e.g. dust extinction, star formation history, and metallicity) as free parameters (e.g., Conroy 2013).

UV and Hα suffer from interstellar extinction and absorption, therefore, they are used in linear combination with IR light (often called as "hybrid" tracers). Note that the Hα photons trace the most recent star formation ($\sim$ 2 Myrs) than that of the UV photons ($\sim$ 14 Myrs). Hence, the side effect is Hα tracer is more sensitive to stochasticity and variation of the Initial Mass Function (IMF), while UV light is also sensitive to the intermediate age of stellar population (a few tens of Myr; Leroy et al. 2012). On the other hand, IR light at 24μm wavelength (rather than the total IR light) is often used as the SFR tracer (including in this dissertation). Extrapolating the total IR light from 24μm light seems worrisome but still reasonable (Dale & Helou 2002). The drawbacks of 24 μm as a tracer of SFR are (1) this is the band of Polycyclic Aromatic Hydrocarbon (PAH) emission, therefore, the emission in this band depends on the dust size distribution and the mixture of radiation field that illuminates the dust (Draine & Li 2007), and (2) heating by older stellar population (not related to SFR) contributes to the emission in 24 μm band and becomes problematic for $\Sigma_{\rm SFR} \lesssim 10^{-3}\ M_\odot\ {\rm yr}^{-1}\ {\rm kpc}^{-2}$ (Calzetti et al. 2007; Leroy et al. 2012; Utomo et al. 2014).

In order to infer SFR using those tracers, calibrations are needed. Roughly speaking, the calibration provides us with the conversion factor to estimate SFR from the measured radiation. From many SFR calibrations, I only mentioned few of them that are used in this dissertation. For example, Calzetti et al. (2007) proposed calibrations in the forms of ${\rm SFR}\ [M_\odot\ {\rm yr}^{-1}] = 5.3 \times 10^{-42}\ L_{H\alpha,{\rm corr}}\ [{\rm erg\ s}^{-1}]$ for the dust-corrected Hα emission and ${\rm SFR}\ [M_\odot\ {\rm yr}^{-1}] = 5.3 \times 10^{-42}\ (L_{H\alpha,{\rm obs}} + 0.031 L_{24\mu{\rm m}})\ [{\rm erg\ s}^{-1}]$ for the hybrid Hα + 24μm tracer.

The constants are determined from the stellar population synthesis with 100 Myrs of star formation duration, Calzetti (2001) extinction curve, and an IMF similar to Kroupa (2001) IMF.

The study of star formation in kpc scale offers an advantage: it simplifies the physics of interstellar medium by taking an average over spatial and temporal dimensions. At small ($\sim$ pc) scale, star formation is a stochastic process and evolves rapidly ($\sim$ 10 Myr), i.e. it depends on the evolution of GMCs. While at kpc scale, we cover multiple GMCs at different evolutionary stages, so that on average, our measurement is less sensitive to temporal variation. In addition, the peaks of CO and Hα are not co-located at scale $\lesssim$ 500 pc (Schruba et al. 2010; Kruijssen & Longmore 2014), which introduce a large scatter in the molecular gas versus star formation rate relation (Schmidt 1959; Kennicutt 1998a). Only at the $\sim$ kpc scale, the amount of molecular gas is linearly correlated to the star formation rate, leading to an approximately constant star formation efficiency (Bigiel et al. 2008; Leroy et al. 2008, 2013).

1.5 Turbulent Interstellar Medium

Turbulent flow represents a chaotic fluid motion, as opposed to an ordered, laminar motion. A fluid motion starts to be turbulent when the Reynolds number is $Re \gtrsim 10^3$. The Reynolds number is defined as the ratio between the inertial force and the viscous force within a fluid ($Re = \rho v L/\mu$). Here, ρ and v are the density and velocity of the fluid, L is the characteristic scale length, and μ is the dynamic viscosity of the fluid ($\mu = \rho v_{\rm th}\lambda$, where $v_{\rm th}$ is the thermal speed and λ is the particle's mean-free-path). At lower Re, any perturbation leads to chaotic motions is damped by the viscosity, and vice versa.

The condition for turbulence can also be approximated as $(v/v_{\rm th})(L/\lambda) \gg 1$ (von Weizsäcker 1951). In astrophysical scales, the gas is supersonic ($v > v_{\rm th}$) and the scale under consideration (e.g. $L \sim$ the size of molecular clouds $\sim$ 50 pc $\sim 10^{20}$ cm) is much larger than the particle's mean-free-path ($\lambda \sim (n\sigma)^{-1} \sim 10^{16}$ cm, for gas density $n \sim 1$ cm^{-3} and the collisional cross section of neutral atom $\sigma \sim 10^{-16}$ cm^2). Therefore, based on this order-of-magnitude estimate, the interstellar medium is expected to be turbulent.

Despite its nature as a chaotic (unpredictable) phenomenon, turbulent motion can be described in a statistical sense. In a turbulent motion, the kinetic energy of the fluid is distributed among various scales, through cascades of energy from the largest (driving) scale to the dissipative scale (roughly the particle's mean-free-path), where the energy is converted to heat through the molecular viscosity. Through these energy cascades, Kolmogorov (1941) predicted that the velocity difference at two points Δv, separated by distance l (where l is between the driving and dissipative scales), is described as a power law: $(\Delta v)^p \propto l^{p/3}$. This prediction has been confirmed by various laboratory experiments, albeit with its spatio-temporal variation that is called intermittency (Sreenivasan & Antonia 1997; Anselmet et al. 2001).

Perhaps, the first evidence of turbulent molecular gas is reported by Larson (1981), when

he showed that the velocity dispersion of GMCs (first order structure function, $p = 1$) and the size of GMCs are correlated through a power law with an exponent of 0.38, which is close enough to Kolmogorov (1941) prediction of one-third. Later, this exponent value was revised by Solomon et al. (1987) to be 0.5 which is more consistent with compressible turbulence. Approximately the same exponent was also found by Heyer & Brunt (2004) using ^{12}CO data and by Roman-Duval et al. (2011) using ^{13}CO data. For $p = 2$, Miesch & Bally (1994) found an exponent of 0.43 using ^{13}CO data. The work by Hily-Blant et al. (2008) made further step by identifying the signature of turbulent intermittency in the Polaris field. These and other evidences (see reviews by Elmegreen & Scalo 2004; McKee & Ostriker 2007, and references therein) point towards the turbulent interstellar medium.

Along with the magnetic field, turbulence represents the main contributor to the ISM pressure to be in equilibrium with the galactic gravitation potential, and also, the main support of molecular clouds against their self-gravity. Turbulence dissipation is therefore a key process that leads to the formation of molecular clouds and stars (Hennebelle & Falgarone 2012, and references therein). Krumholz & McKee (2005) successfully derived the Kennicutt-Schmidt law from first principles: the gas is isothermal and supersonically turbulent, so that their density distribution is log-normal, and stars form in over-dense regions where gravitational energy exceeds turbulent energy. The consistency between their prediction and previous observation means turbulence regulates the star formation rate. Without turbulence, the gas would contract and form stars in one free-fall time (~ 1 Myr), which is much faster than what was observed (~ 2 Gyr).

It is not clear what is the scale of turbulence dissipation in ISM. This dissipation can occur in an intermittent way, where its signature has been observed at a scale of ~ 600 AU (Falgarone et al. 2009) or larger (Hily-Blant et al. 2008). Nevertheless, turbulence has to be maintained because the dissipation time-scale (estimated as the crossing time of turbulent velocity dispersion ~ 10 Myr) is much shorter than the Hubble time (~ 14 Gyr). Mac Low & Klessen (2004) gave a review of possible driving mechanisms of turbulence: magneto-rotational instability (MRI), gravitational instability, proto-stellar outflows, stellar winds, ionizing radiation, and supernovae. In this dissertation (see Chapter 4), I consider the two most important energy sources (MRI and supernovae) in driving turbulence in M33.

1.6 Multiwavelength Observations

This dissertation builds on several multiwavelength observations, from UV to radio. In this section, I highlight some key points of those observations.

1.6.1 Optical Integral Field Unit

The Integral Field Unit (IFU, sometimes is also called the Integral Field Spectrograph) is an instrument to capture the image of an object (resembles the function of a camera) and the spectrum of that object at one or multiple positions, *simultaneously*. IFU is the

next generation of the single-fiber (SDSS-type) survey. The output of IFU is a data cube, consists of two-dimensional spatial information and one-dimensional spectral of an object. If the field-of-view of an IFU is wide enough to cover the whole object, IFU observation is efficient because there is no need to shift the observation from one position to another position within an object (a small shift, called dithering, may be needed to fully sample the object). IFU observations of a galaxy allow us to (1) extract the stellar spectra to derive the stellar populations, (2) measure the strength of ionization lines to get information about star formation rates (e.g. through Hα) and the physical condition of ionized gas, and (3) determine the resolved stellar and ionized gas kinematics from the redshift of stellar absorption lines and ionization lines, which allows us to determine the enclosed dynamical mass of a galaxy.

There are many IFU surveys that have been done: e.g., SAURON (Bacon et al. 2001), SINFONI (Förster Schreiber et al. 2009), Atlas-3D (Cappellari et al. 2011), SAMI (Croom et al. 2012), MASSIVE (Ma et al. 2014), and MaNGa (Bundy et al. 2015). In this dissertation, I make use of the data products from CALIFA survey (Sánchez et al. 2012), which targeted a diameter selected sample of ~ 600 galaxies in the local Universe ($0.005 < z < 0.03$). CALIFA covered optical wavelength from 3700 to 7000 Å, with a field-of-view of 1.3 arcmin. This survey captured the properties and kinematics of stars and ionized gas in a representative sample of the local galaxy population. The final data cubes have surface brightness depth (3σ sensitivity) of ~ 23 mag arcsec^{-2}, where $\sim 70\%$ of the field-of-view is above this 3σ limit, and velocity resolution from ~ 85 to 150 km s^{-1}. Compared to other IFU surveys, CALIFA has better angular resolution than MaNGa, and wider field-of-view than Atlas-3D.

1.6.2 Radio Interferometry

Typical radio wavelength that is observed by astronomer is a factor of 10^4 to 10^5 times longer than optical wavelength. If we neglect the atmospheric effect, this means we need a radio telescope (single dish) of at least 100 km in diameter to match the resolution of the Keck 10-m telescope, which is impractical. Hence, the interferometry technique is utilized, where multiple single dish telescopes are combined, spread over a certain area, to act as a single telescope. In this way, we can achieve higher angular resolution by filling some "spots" within the area with dishes, rather that covering all of the area with one gigantic dish. To give a brief description of how radio interferometer works, here I follow a lecture by R. Perley during the NRAO summer school at Socorro, New Mexico in 2014.[1]

The simplest case of radio interferometer consists of only two elements. In this case, two antennas (separated by distance $\mathbf{b}$, called the baseline) receive signals from the same source at direction $\mathbf{s}$. Due to different geometrical distance, travelled by the signal from the source to each antennas, the signal that is received by one of the antenna is delayed by $\tau_g = \mathbf{b}\cdot\mathbf{s}/c$, where c is the speed of light. Then, signals from both antennas are multiplied by each other and averaged inside a correlator, resulting in the correlator response as $R_c = P$

[1] https://science.nrao.edu/science/meetings/2014/14th-synthesis-imaging-workshop/archive/SISS14Intro.pdf

$\cos(\omega\tau_g)$, where P is the power and ω is the angular frequency of the signals. This cosine function represents fringes of radio interferometry. In other words, radio interferometer scans the source (assuming it is a resolved source) in these fringes pattern. However, the cosine function only represents the "even" part of the source distribution. Therefore, a (90°) phase shifter is added to the correlator to cover the "odd" part as $R_s = P\,\sin(\omega\tau_g)$.

The output of radio interferometry is called visibility, defined as $V_\nu = R_c - iR_s = I_\nu\, e^{-i\omega\tau_g}$, where i is the imaginary number and I_ν is the source intensity at frequency ν. If the source is resolved, the visibility is integrated for all solid angle Ω as

$$V_\nu = \int I_\nu\, e^{-i\omega\tau_g}\, d\Omega. \tag{1.2}$$

Finally, we can recover the source intensity I_ν from the measured visibility V_ν by using the Fourier transform.

There are variations of the bandpass response as a function of frequency and variations of instrumental gain as a function of time. These variations are need to be calibrated by observing bright objects (such as quasars) across bandpass frequency and observing time. Furthermore, the absolute value of source intensity is also need to be calibrated by observing objects with know flux (such as planets). In practice, the radio data reduction for the CARMA telescopes can be done using the `MIRIAD` package (Sault et al. 1995). The final data product of radio interferometer is in the form of three dimensional data cube with two axes refer to positions and one axis refers to frequency or velocity.

Chapter 2

The Molecular Clouds in Early-type Galaxy: NGC4526

I present a high spatial resolution (≈ 20 pc) of ^{12}CO$(2-1)$ observations of the lenticular galaxy NGC4526. I identify 103 resolved Giant Molecular Clouds (GMCs) and measure their properties: size R, velocity dispersion σ_v, and luminosity L. This is the first GMC catalog of an early-type galaxy. I find that the GMC population in NGC4526 is gravitationally bound, with a virial parameter $\alpha \sim 1$. The mass distribution, $dN/dM \propto M^{-2.39\pm0.03}$, is steeper than that for GMCs in the inner Milky Way, but comparable to that found in some late-type galaxies. Interestingly, there is no size-linewidth correlation for the NGC4526 clouds, in contradiction to the expectation from Larson's relation. In general, the GMCs in NGC4526 are more luminous, denser, and have a higher velocity dispersion than equal size GMCs in the Milky Way and other galaxies in the Local Group. This may be due to higher interstellar radiation field than in the Milky Way disk and weaker external pressure than in the Galactic center. In addition, a kinematic measurement of cloud rotation shows that the rotation is driven by galactic shear. For the vast majority of the clouds, the rotational energy is less than the turbulent and gravitational energy, while the four innermost clouds are unbound and will likely be torn apart by the strong shear at the galactic center. By including the archival data of other galaxies, I show that the surface density Σ of GMCs is not approximately constant as previously believed, but varies by ~ 3 orders of magnitude. I also show that the size and velocity dispersion of GMC population across galaxies are related to the surface density, as expected from gravitational and pressure equilibrium, i.e. $\sigma_v R^{-1/2} \propto \Sigma^{1/2}$.

2.1 Introduction

Giant molecular clouds (GMCs) are the sites of star formation in galaxies. The existing correlation between molecular gas surface density and star formation rate (Wong & Blitz 2002; Bigiel et al. 2008; Leroy et al. 2013) implies that the formation and evolution of GMCs are essential to understand the build-up of stellar masses in galaxies. However, up-to-date

studies of extragalactic GMC populations are limited to Local Group galaxies; LMC (Fukui et al. 2008; Wong et al. 2011), SMC (Mizuno et al. 2001), M31 (Rosolowsky 2007), M33 (Engargiola et al. 2003; Rosolowsky et al. 2007; Gratier et al. 2012), and IC10 (Leroy et al. 2006), the nearby spirals; M64 (Rosolowsky & Blitz 2005) and M51 (Colombo et al. 2014), and the nearby starburst; M82 (Keto et al. 2005) and NGC253 (Leroy et al. 2014), due to the limited angular resolution and sensitivity of radio telescopes. Galaxies in the Local Group are mostly dwarfs with few spirals. Therefore, an additional study of GMCs in the early-type galaxies, such as NGC4526, is needed to provide a comprehensive analysis of GMC properties across different galaxy environments.

There are four resolved GMC properties that can be directly measured: size, linewidth, luminosity, and metallicity. The relationships between these properties were first studied by Larson (1981), who suggested the importance of turbulence in the stability of GMCs against self-gravity. These relations were then refined by Solomon et al. (1987, hereafter S87) for GMCs in the Milky Way disk. Basically, GMC properties in the Milky Way can be described by three Larson's 'laws': (1) GMCs are gravitationally bound objects, (2) the size and velocity dispersion of GMCs follows a $\sigma_v \propto R^{0.5}$ relation, and by implication of (1) and (2): (3) the surface density of GMCs is approximately constant ($\Sigma_{\rm GMC} \approx 170\ M_\odot\ {\rm pc}^{-2}$, S87). Interestingly, these relations were also observed, albeit with scatter, for extragalactic GMCs in Local Group galaxies (Blitz et al. 2007; Bolatto et al. 2008; Fukui & Kawamura 2010). At face value, this suggested that GMC properties are universal.

However, further studies revealed that GMC properties deviate from Larson's relations. Heyer et al. (2001) found that low mass GMCs ($M \leq 10^3 M_\odot$) in the outer part of the Milky Way are not gravitationally bound. Their luminous masses, inferred from the CO-to-H_2 conversion factor, are smaller than their virial masses. The required external pressure to bind these clouds is $P_{\rm ext}/k \sim 1 \times 10^4$ K cm^{-3}. Furthermore, when re-examining S87 clouds using more sensitive instruments, Heyer et al. (2009) found that the surface density of GMCs in the Milky Way disk varies from $\sim$ 10 to 200 $M_\odot$ pc^{-2}, and they deviate from gravitational equilibrium. Field et al. (2011) suggested that these clouds may be in pressure virial equilibrium, where the clouds' mass and radius are described by a Bonnor-Ebert sphere with various external pressures (Bonnor 1956; Ebert 1955). In addition, several authors (e.g. Kegel 1989; Ballesteros-Paredes & Mac Low 2002) argued that the observed constancy of surface density might be affected by observational biases.

If this is really the case, then what are the factors that determine the different properties of GMCs? These parameters may be external (environmental) effects, such as hydrostatic pressure (Elmegreen 1993; Blitz & Rosolowsky 2004; Meidt et al. 2013), interstellar radiation field strength (McKee 1989), and shear from galaxy rotation (Koda et al. 2009; Miyamoto et al. 2014), or internal, such as feedback of the star formation that is embedded inside GMCs (Blitz & Shu 1980; McKee 1989). To answer this question, we need a complete sample of GMCs across different environments: from bulge to spiral-arm and inter-arm regions, from late-type to early-type galaxies, and from low to high metallicity galaxies.

In this respect, I analyze the GMC properties in the bulge of NGC4526, an S0-type galaxy in the Virgo cluster. NGC4526 is selected because all of the CO in the galaxy has

been observed at a linear resolution of ≈ 20 pc, sufficient to resolve Milky Way sized GMCs. The galaxy has prominent central dust lanes with mass $\sim 10^7 M_\odot$ (Ciesla et al. 2014) and supersolar metallicity ($\log(Z/Z_\odot) \approx 0.2$; Davis et al. 2013a), but lack of star formation (SFR $\approx 0.03\ M_\odot\ \mathrm{yr}^{-1}$; Amblard et al. 2014) and devoid of atomic gas ($M_{\rm HI} < 1.9 \times 10^7 M_\odot$; Lucero & Young 2013). The HI deficiency in this galaxy may be caused by ram pressure or evaporation by hot gas (as the galaxy resides in the Virgo cluster), or by abrupt conversion of HI into molecular gas due to high pressure (Elmegreen 1993). There is no indication of recent tidal interaction (Young et al. 2008), suggesting that this mechanism is not the primary cause of HI deficiency in NGC4526.

In fact, the molecular gas in NGC4526 is confined within the central ~ 1 kpc region (the top panel of Figure 2.1; Davis et al. 2013b). The central regions of galaxies, such as in the Milky Way, tend to have high interstellar pressures ($\sim 5 \times 10^6$ K cm^{-3}; Spergel & Blitz 1992), strong magnetic fields (~ 1 mG; Yusef-Zadeh & Morris 1987), and lower than expected star formation rate (Longmore et al. 2013). These properties offer a unique environment for GMCs in NGC4526, significantly different than those studied in other nearby galaxies.

This chapter is organized as follows. In Section 2.2, I describe the data and methodology to identify GMCs in NGC4526. The properties and kinematics of the GMCs are reported in Sections 2.3 and 2.4, respectively, and catalogued in Table 2.2. I discuss the pressure balance of GMCs, the Larson's 'laws', and the environmental effects to the GMC properties in Section 2.5. Lastly, I summarize the results in Section 2.6.

2.2 Data and Methodology

2.2.1 Data Descriptions

NGC4526 was observed in the ^{12}CO$(2-1)$ line (230 GHz or 1.3 mm) using the Combined Array for Research in Millimeter-wave Astronomy (CARMA) in A, B, and C configurations (Bock et al. 2006). The data were taken as part of the mm-Wave Interferometric Survey of Dark Object Masses project (WISDOM; Onishi et al. 2017; Davis et al. 2017). Results for the innermost CO were reported by Davis et al. (2013b, the top panel of Figure 2.1), who showed that the kinematics of the central CO imply the presence of a $4.5 \times 10^8 M_\odot$ supermassive black hole.

The beam width of the observations is 0.278×0.173 arcsec^2 and the spectral resolution (after Hanning smoothing) is 10 km s^{-1}. This beam width covers 5.56×3.46 pixels and corresponds to a projected physical size of $\approx 22 \times 14$ pc^2 at the adopted distance of 16.4 Mpc (Tonry et al. 2001). These high resolution data able to resolve individual GMCs and measure their properties, since the typical Milky Way's GMC sizes are ~ 50 pc (e.g. Blitz 1993).

The noise in data is not uniform, with higher noise appearing at the corners of the data cube. The overall pixel-by-pixel root-mean-square (rms) noise $\sigma_{\rm rms}$ distribution is a positively-skewed Gaussian with minimum, average, and maximum values of 0.33, 0.71, and

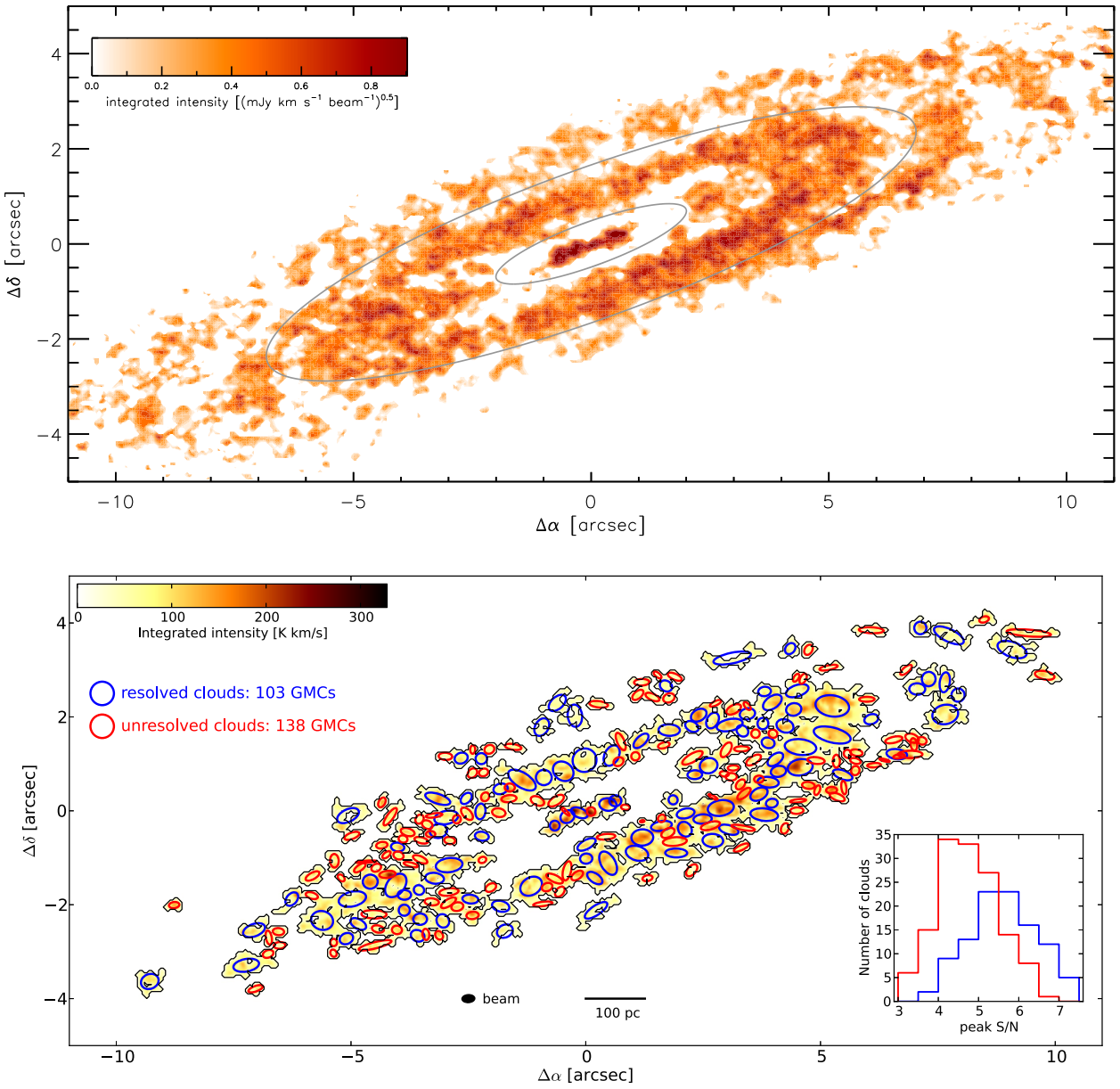

Figure 2.1: Top: The integrated intensity map of NGC4526. The map is created by applying a Gaussian fit to each spectrum in the data cube. Any Gaussian that has peak less than $2.5\sigma_{\rm rms}$ are excluded. The ellipses divide the CO emission into three zones: inner region, molecular ring, and outer region. Bottom: Identified GMCs in NGC4526 are overploted on the masked integrated intensity map. The mask covers regions with connected emission above $2\sigma_{\rm rms}$ and having at least one pixel with $3\sigma_{\rm rms}$. The beam size and the projected physical size are indicated. The blue and red circles mark the location of the resolved and unresolved clouds, respectively. The distribution of the peak S/N of clouds is shown as an inset in the bottom right corner.

1.33 K, respectively.

2.2.2 Methodology

GMC candidates in NGC4526 are identified using the modified CLUMPFIND algorithm (Williams et al. 1994), implemented in the CPROPS program (Rosolowsky & Leroy 2006, hereafter RL06). The main goal of this program is to identify all real clouds and minimize false detections due to noise fluctuations. Descriptions of the CPROPS program, together with our chosen values of the input parameters of the program, are given in Sections 2.7 and 2.8.

As a result of the CPROPS analysis, 241 GMCs are identified in NGC4526, of which 103 of them are resolved clouds. I assume all GMCs are real since the probability of false detections is very small (see Section 2.9). In the bottom panel of Figure 2.1, I show the integrated CO emission of connected regions that have brightness temperatures $T_{\rm b} > 2\sigma_{\rm rms}$ and have at least one pixel with $T_{\rm b} \geq 3\sigma_{\rm rms}$. Locations of the resolved and unresolved clouds are marked as blue and red ellipses, respectively. The peak S/N distribution of identified GMCs is shown as an inset. The mean peak S/N of resolved and unresolved clouds is 5.6 and 4.7, respectively.

Most GMCs are located in the molecular ring, a few hundred parsecs from the galactic center (Figure 2.1). This molecular ring is the largest contiguous CO emission in our data. In addition, there are a few clouds located in the central region. The outer region of the molecular gas exhibits a spiral-arm structure, possibly with an outer pseudo-ring, which fragments into smaller structures consisting of one or multiple GMCs. Except for one cloud that is described below, all identified GMCs are within 900 pc of the galactic center, i.e. inside the bulge of NGC4526. Note that our primary beam covers all of the CO emission in the galaxy, so our GMC catalog is complete.

There is one unresolved cloud which is located on the edge of the data cube (not shown in Figure 2.1), out of the plane of the CO emission. I overplotted the location of this cloud with the HST archival image of the galaxy. Although this cloud is likely to be real (Section 2.9), its distance is uncertain, i.e. it may be located outside the galaxy. Therefore, this cloud is excluded from the following analysis but it is still in the catalog (as cloud no.80, see Section 2.10). Inclusion of this cloud does not alter the conclusions of our analysis.

2.3 Cloud Properties

2.3.1 Definition of GMC Properties

Cloud properties, such as position, size, velocity dispersion, luminosity, and mass, are catalogued in Section 2.10. Here, I briefly describe the method used to measure the cloud properties. Full explanations of the method are given in RL06.

The cloud size, R, is measured using the *deconvolved* second-moment:

$$R = \eta \sqrt{(\sigma^2_{\rm maj}[0\ {\rm K}] - \sigma^2_{\rm beam})^{1/2} (\sigma^2_{\rm min}[0\ {\rm K}] - \sigma^2_{\rm beam})^{1/2}}, \tag{2.1}$$

where η is a factor that depends on the density distribution of spherically symmetric clouds. A uniform sphere has $\eta = \sqrt{5}$, while an isothermal sphere has $\eta = 3$. Here, I adopt $\eta = 1.91$, a value from S87, to make it consistent with previous studies. The major, $\sigma_{\rm maj}$, and minor, $\sigma_{\rm min}$, spatial dispersions are the spatial second moments, weighted by the intensity, along the major and minor axis of the clouds, respectively. Both $\sigma_{\rm maj}$ and $\sigma_{\rm min}$ are extrapolated to zero intensity (0 K) to avoid bias due to the limited sensitivity of the instrument. Deconvolution is applied, by the inclusion of the beam-width ($\sigma_{\rm beam}$) terms in Equation (2.1), to avoid bias due to the finite beam resolution (RL06). Since the beam is not circular, I take $\sigma_{\rm beam}$ as the geometrical mean of the major and minor axes of the beam. The uncertainty, δR, is determined using bootstrap resampling.

In order to measure the clouds' velocity dispersions, I attempt Gaussian fitting to the composite spectrum of each cloud through the following steps. First, I calculate the offset of the mean velocity at all lines of sight within the cloud (x_i, y_i), with respect to the mean velocity at the center of the cloud (x_0, y_0). This offset is caused by large scale motions, such as the cloud's rotation or shear due to galactic rotation. Then, I shift each line of sight velocity spectrum to match the mean velocity of the central position of the cloud. Except for the innermost clouds, this shift removes any velocity dispersions due to large scale motions, and leaves only turbulence and thermal broadening as sources of velocity dispersions. To make a composite spectrum, I take the average velocity profile from each line of sight. Finally, I fit the composite spectrum with a Gaussian. The standard deviation of the Gaussian fit is taken as the velocity dispersion (σ_v) of the cloud. I take the uncertainty ($\delta\sigma_v$) from the bootstrap resampling.

RL06 showed that measurements of velocity dispersion suffer bias towards higher values due to finite spectral resolution of the instruments. Therefore, I take the deconvolved value ($\sigma_{v,{\rm dc}}$) to remove this bias using the same prescription as in RL06:

$$\sigma_{v,{\rm dc}} = \left(\sigma_v^2 - \frac{\delta v^2}{2\pi} \right)^{1/2}, \tag{2.2}$$

where δv is the spectral resolution, and $\delta v\ (2\pi)^{-0.5}$ is the standard deviation of a Gaussian that has an integrated area equal to a spectral channel with width δv. For brevity, I refer to $\sigma_{v,{\rm dc}}$ as σ_v. Note that the deconvolved values of σ_v and R are always smaller than their measured values (Equation 2.1 and 2.2). Thus, any clouds that are barely resolved would have the deconvolved value smaller than the resolution of observations.

The cloud luminosity is the integrated CO flux over the position-position-velocity volume occupied by the cloud (RL06):

$$L_{\rm CO(2-1)} = \left(\frac{\pi}{180 \times 3600} \right)^2 D^2 \sum_i T_{{\rm b},i}\ \delta x\ \delta y\ \delta v, \tag{2.3}$$

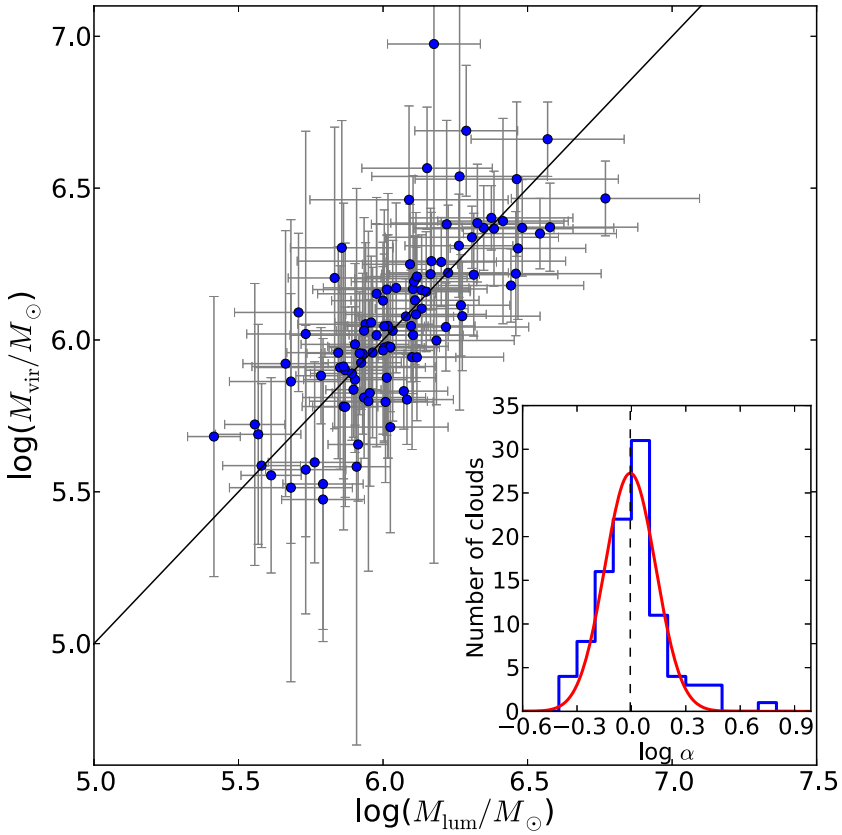

Figure 2.2: Correlation between virial and luminous masses of GMCs. The solid line is the one-to-one relationship. The distribution of log α with a log-normal fit is shown as an inset. The mean of the log-normal fit is $\alpha \approx 0.99$ with a standard deviation of 0.14 dex. Thus, the GMC population in NGC4526 is in gravitational equilibrium.

where $T_{\mathrm{b},i}$ is the brightness temperature of the i-th pixel in K, δx and δy are the pixel sizes in arcsec, D is the distance to NGC4526 in pc, and $L_{\rm CO}$ is the cloud luminosity in K km s^{-1} pc^2. The luminosity is extrapolated to 0 K intensity as described in RL06. The uncertainty, δL, is determined using a bootstrap resampling method. There is an additional $\sim 20\%$ (absolute, but systematic) flux calibration uncertainty that we do not include in the analysis.

The luminosity is then converted to mass using the Milky Way's CO$(1-0)$-to-H$_2$ conversion factor $X_{\rm CO} = 2 \times 10^{20}$ cm^{-2} (K km s^{-1})$^{-1}$, which is assumed to be constant throughout the galaxy. This is a reasonable assumption since $X_{\rm CO}$ does not vary significantly due to metallicity in the supersolar metallicity regime (Bolatto et al. 2013, and references therein). The ratio of ^{12}CO$(1-0)$ to ^{12}CO$(2-1)$ intensity in NGC4526 is 1.15 (Crocker et al. 2012). This $X_{\rm CO}$-derived mass is referred as as the luminous mass: $M_{\rm lum}/M_\odot = (4.4 \times 1.15)\ (L_{\rm CO(2-1)}/\mathrm{K\ km\ s^{-1} pc^2})$, which takes into account the mass contribution by helium. The factor of 4.4 comes from our adopted $X_{\rm CO}$ value.

Each cloud's distance is calculated from the center of NGC4526 using the assumption that they are located in the plane of the galaxy with axis ratio of 0.216 and position angle of 290.2°. The position angle is measured from the north, counter-clockwise to the receding part of the kinematical major axis of the galaxy. The axis ratio and position angle are calculated using part of the multi-Gaussian expansion (MGE) fit of Cappellari (2002).

2.3.2 Gravitational Equilibrium of Clouds

The mass of a gravitationally bound cloud is given by (Bertoldi & McKee 1992, hereafter BM92)

$$M_{\rm vir} = \frac{5\sigma_v^2 R}{G} \approx 1048\ M_\odot \left(\frac{\sigma_v}{\rm km\ s^{-1}}\right)^2 \left(\frac{R}{\rm pc}\right), \tag{2.4}$$

where σ_v is the 1-D velocity dispersion of the CO line. I refer to this mass as the virial mass. If the luminous mass is equal, or comparable, to the virial mass, then the cloud is in gravitational equilibrium, where the kinetic energy balances its self-gravity. If the luminous mass is smaller than the virial mass, then, in addition to gravity, the clouds must be held together by the external pressure of the ambient medium, $P_{\rm ext}$, to reach dynamical equilibrium. Such clouds are pressure-bound clouds.

Here, the virial parameter is defined as the ratio between twice the kinetic energy and the gravitational energy,

$$\alpha \equiv \frac{5\sigma_v^2 R}{G M_{\rm lum}} = \frac{M_{\rm vir}}{M_{\rm lum}}. \tag{2.5}$$

According to BM92, clouds with $\alpha \approx 1.13$ are gravitationally-bound and clouds with $\alpha \gg 1$ are pressure-bound. In Figure 2.2, the luminous masses are plotted against the virial masses of the resolved clouds, together with the distribution of log α as an inset. A log-normal fit to the distribution yields a mean $\alpha = 0.99 \pm 0.02$ and a standard deviation of 0.14 dex. Roughly 99% of the resolved clouds have $0.3 \leq \alpha \leq 3$, and 89% of the resolved clouds have $0.5 \leq \alpha \leq 2$. Therefore, the GMC population in NGC4526 is in a state of gravitational equilibrium.

In Equation (2.4), we assume that all clouds are spherically symmetric and have a uniform density distribution. If the clouds were isothermal spheres, then the virial mass would be 60% lower than what is calculated here. Moreover, the uncertainty in $X_{\rm CO}$ also affects the luminous mass measurements. From observations of local galaxies, the typical uncertainty in $X_{\rm CO}$ is about 0.3 dex (Bolatto et al. 2013, and references therein). Taken all together, this introduces an uncertainty of ~ 0.5 dex in the worst case.

Variations of the input parameters of the CPROPS program do not affect the result that the cloud population is gravitationally-bound. However, we have to keep in mind that we do not yet take into account the magnetic pressure and rotation of the clouds. The effect of rotation is discussed in §4.3. Furthermore, I find no correlation between the mass of a GMC and its distance from the galactic center, possibly because all GMCs are distributed in a small region (within a radius of 900 pc) inside the bulge of the galaxy, so environmental

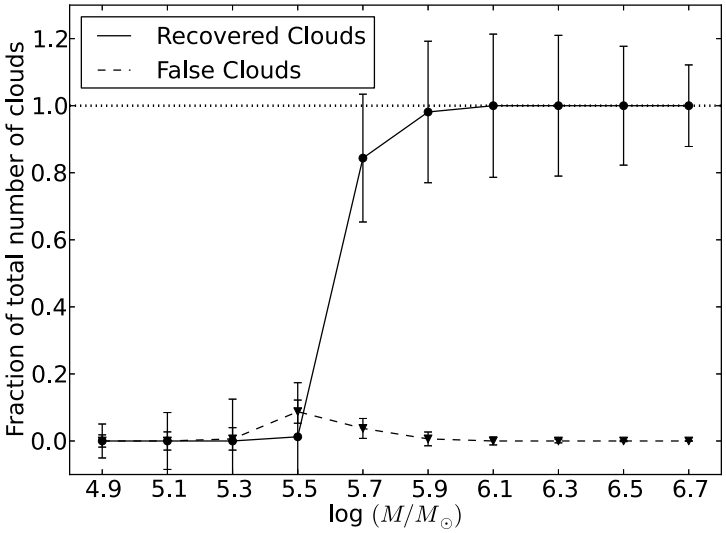

Figure 2.3: Fraction of the recovered clouds as a function of cloud mass, from the simulation described in the text. Simulated clouds with $M \geq 5 \times 10^5 M_\odot$ are well recovered by the program (solid line), contaminated by only a small fraction of false clouds (dashed line). The fraction of false clouds is negligible for low mass regime because these clouds are too small and faint, and hence undetected by the CPROPS program. Therefore, I adopt $\log(M/M_\odot) = 5.7$ as the completeness level of our observations.

variations from GMC to GMC, such as ambient pressure and the interstellar radiation field, are small.

2.3.3 Cloud Mass Distribution

The luminous mass is used to determine the mass function because it is well-defined even for unresolved clouds. Since the GMC population in NGC4526 is in gravitational equilibrium ($M_{\rm lum} \approx M_{\rm vir}$), we should not expect variation of the mass function between the two mass measurements. The mass function is determined using three different methods: equal bin-width, equal bin-size, and the cumulative distribution function. All measurements are taken from the most massive clouds in our sample ($M_{\rm lum} \approx 5.9 \times 10^6 M_\odot$) down to the completeness level of the observations.

To determine the completeness level of our observations, we create simulated Gaussian clouds. Their properties are related through known scaling relationships: $\sigma_v \propto R^{0.5}$ and $M \propto R^2$ (e.g. S87). To mimic the observed data, we add the typical noise of our observations into the simulated data cubes. In total we consider 1600 mock clouds with $\log(M/M_\odot)$ ranging from 4.9 to 6.7, with an increment of 0.2, and feed these mock clouds into the CPROPS program. A cloud is defined as recovered if its location in the data cube is within one beamwidth of its input location. Otherwise, this cloud is defined as false detection. The

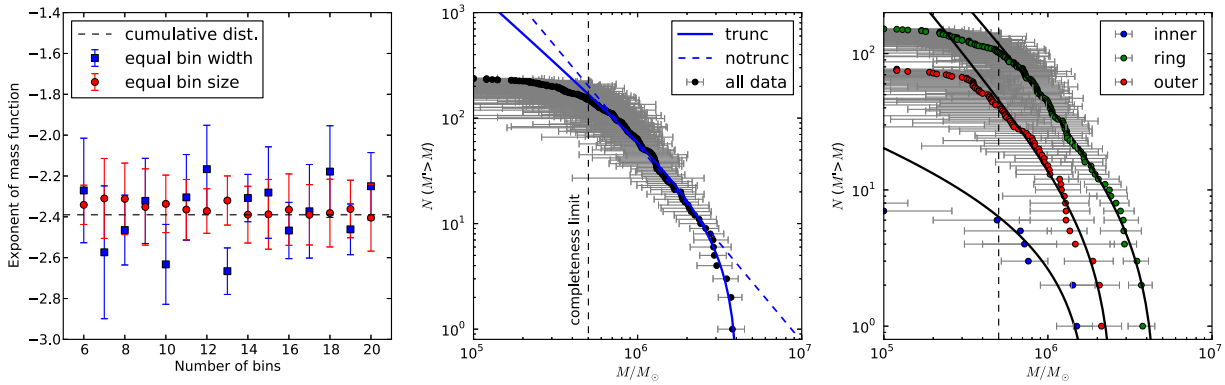

Figure 2.4: Left: The best fit slope of the mass function against the number of bins. The equal bin-width method (blue squares) has large scatter due to the choice of the number of bins, while the equal bin-size method (red circles) is in agreement with the cumulative distribution mass function (dashed line). Middle: Fits to the cumulative mass function with and without truncation. The data favor the truncated (solid blue curve) over the non-truncated (dashed blue curve) mass function. Right: Cumulative mass distribution of the inner region (blue), molecular ring (green), and outer region (red), with the overlaid truncated fits.

false detection rate is effectively zero for the least massive clouds because these false clouds, if they are exist, are too small to be recovered. I find that clouds with $\log(M/M_\odot) \geq 5.9$ are well recovered by the program, while more than 80% of clouds with $\log(M/M_\odot) \approx 5.7$ are recovered (Figure 2.3). Therefore, I adopt the completeness level as $\log(M/M_\odot) = 5.7$.

Equal bin-width

In the equal bin-width method, the masses are grouped into bins of equal width in log-space. Then, each histogram is fitted with a straight line, weighted by the uncertainty of dN/dM, from the highest mass bin down to the completeness level. The slope of the best fit line, x, is the exponent of the mass function $dN/dM \propto M^x$.

The uncertainty on the number of clouds in each bin is calculated as follows. First, the uncertainties of the masses δM are calculated through a bootstrap resampling method (RL06). Then, I use δM to calculate the uncertainty in $\mathrm{d}N/\mathrm{d}M$ using Monte Carlo simulations. In these simulations, I resample the masses of the cloud, given a log-normal probability function with a mean M and a standard deviation δM. The resampled masses are grouped into the same mass bins as the data, so that each simulation gives a new mass distribution. I repeat these steps 10,000 times, and take the uncertainty in $\mathrm{d}N/\mathrm{d}M$ as the standard deviation of these 10,000 simulations.

To check the robustness of our results, the number of bins is varied from 6 to 20. I find that x changes from -2.67 to -2.16 (left panel of Figure 2.4). The uncertainty of the slope

Table 2.1: The best-fit parameters of the cumulative mass distributions

Region	Distance [pc]	x	$M_0[10^6 M_\odot]$	N_0
All	$0 < d \leq 900$	-2.39 ± 0.03	4.12 ± 0.08	9.40 ± 0.70
Inner	$0 < d \leq 170$	-1.40 ± 1.19	1.88 ± 0.23	9.13 ± 33.21
Ring	$170 < d \leq 580$	-2.38 ± 0.03	4.66 ± 0.11	5.66 ± 0.47
Outer	$580 < d \leq 900$	-2.46 ± 0.12	2.56 ± 0.12	4.67 ± 1.12

is taken from the covariance matrix of the fit. From these variations of x, I conclude that the equal bin-width method has large scatters due to the choice of the number of bins.

Equal bin-size

D'Agostino & Stephens (1986) and Maíz Apellániz & Úbeda (2005) found that variable bin-widths with equally divided numbers of data points per bin can minimize the binning uncertainty, and hence, is more robust. This is because no bin has a much smaller number of data points than the others, in contrast to the equal bin-width method. For these data, the actual number of data points in a bin is not exactly the same; it can differ from that in other bins by one data point, due to non integer numbers after division. To check the robustness of the result, I vary the number of bins as in the equal bin-width method, and fit the resulting histogram with a straight line. The results are indeed more robust than the equal bin-width method, with a maximum slope of -2.31 and a minimum slope of -2.41 (left panel of Figure 2.4).

Cumulative distribution

In addition, I also calculate the mass function using the (truncated) cumulative distribution function (e.g. Williams & McKee 1997; Rosolowsky 2005),

$$N(M' > M) = N_0 \left[\left(\frac{M}{M_0} \right)^{x+1} - 1 \right], \tag{2.6}$$

and the simple (non-truncated) power-law distribution function,

$$N(M' > M) = \left(\frac{M}{M_0} \right)^{x+1}, \tag{2.7}$$

where M_0 is the cut-off mass of the distribution and N_0 is the number of clouds with $M > 2^{1/(x+1)} M_0$, i.e. the cut-off point of the distribution. The truncated mass distribution takes into account that the mass distribution of a population lacks clouds more massive than M_0. The cumulative distribution function is robust against the number of bins since we do not bin the data into a histogram.

I fit the cumulative distributions of masses using the orthogonal distance regression method in Scipy. The fit is made for all data above the completeness level. I find $x =$

-2.39 ± 0.03 and $M_0 = (4.12 \pm 0.08) \times 10^6 M_\odot$, in agreement with the equal bin-size method. The data are inconsistent with simple (non-truncated) power-law mass distributions (middle panel of Figure 2.4). As a result, the GMC mass distribution in NGC4526 is steeper than in the inner MW ($x = -1.5$; Rosolowsky 2005), but comparable to the GMC mass distribution in the outer MW ($x = -2.1$; Rosolowsky 2005) and central M33 ($x = -2.0$; Rosolowsky 2007).

All three methods of measurements suggest that $x < -2$. In this case, most of the mass resides in the low mass clouds. Furthermore, the total mass diverges for integration down to an infinitely small mass. Hence, there must be a lower limit to the cloud masses or a change in the slope, i.e. $x > -2$ for lower mass clouds below our completeness level, so that the total mass remains finite.

I further divide the galaxy into three distinct regions: inner ($0 < d \leq 170$ pc), molecular ring ($170 < d \leq 580$ pc), and outer ($580 < d \leq 900$ pc) region (concentric ellipses in Figure 2.1), and measure their mass distributions. The molecular ring and the outer region have a similar mass distributions with an exponent of $x \approx -2.4$, while the inner region is much flatter ($x \approx -1.4$), albeit with a large uncertainty due to the small number of clouds in the inner region. The best-fit parameters are compiled in Table 2.1. A radial dependence of the mass function was also discovered in M33 (Gratier et al. 2012) and M51 (Colombo et al. 2014).

I calculate the total mass of detected GMCs (including the non-resolved clouds) to be $M_{\rm GMC} = (2.0 \pm 0.1) \times 10^8 M_\odot$. The total H_2 mass is $M(H_2) = (3.8 \pm 1.1) \times 10^8 M_\odot$ (Young et al. 2008)[1], so the fraction of molecular mass that residing in GMCs is $M_{\rm GMC}/M(H_2) \approx 0.53$. This value is formally a lower limit, since there are GMCs with masses below the completeness level of our observations that are undetected. The rest of the molecular gas may be in the form of diffuse gas which is undetected by interferometric observations.

2.3.4 Larson's Relations

Larson (1981) found that the velocity dispersion of GMCs is correlated with their size through a power-law relation with exponent of ≈ 0.38. This correlation is similar to that expected if turbulence governs the velocity dispersion within clouds as described by the Kolmogorov law. In subsequent work, S87 refined the exponent to be 0.5 ± 0.05 for GMCs in the Milky Way's inner disk.

Larson's relations in the Milky Way consist of two independent equations (e.g. S87, Bolatto et al. 2008):

$$\sigma_v \approx 0.72 \left(\frac{R}{\rm pc}\right)^{0.5} \ {\rm km\ s^{-1}} \tag{2.8}$$

and either

$$L_{\rm CO} \approx 25 \left(\frac{R}{\rm pc}\right)^{2.5} \ {\rm K\ km\ s^{-1}\ pc^2} \tag{2.9}$$

[1] We recalculate the total H_2 mass using $X_{\rm CO}$ as in this paper.

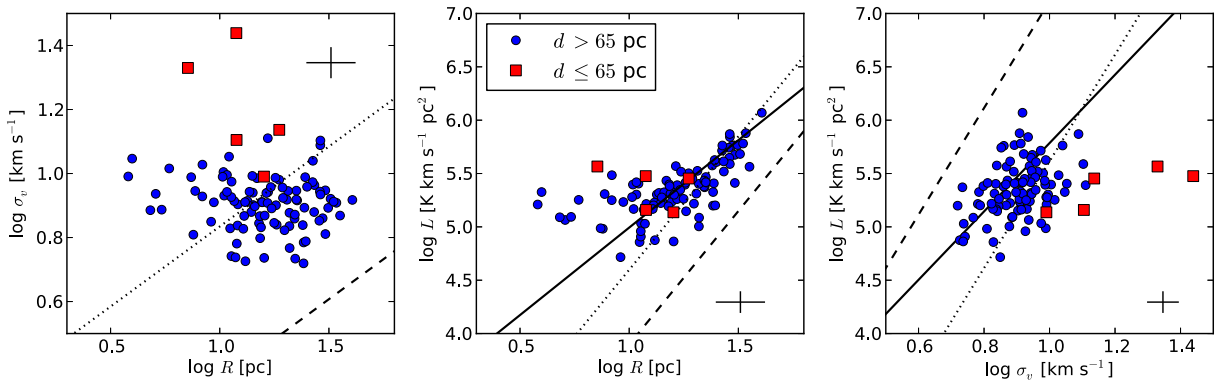

Figure 2.5: The GMCs properties (radius, velocity dispersion, and luminosity) are plotted relative to one another. The color codes are for inner GMCs (distance $\leq$ 65 pc; red squares) and outer GMCs (distance $>$ 65 pc; blue dots). The fits of all data points (including the inner clouds) are shown as solid lines. The typical uncertainty is shown as a cross sign in the corner of each panel. For clarity, I do not plot the uncertainties of individual data. However, I fit the data points by including the non-uniform error bar of the individual data point, not only the typical uncertainty. The dashed lines are Larson's relations for the Milky Way disk (S87), and the dotted lines are Larson's relations with different normalization factors: 3, 0.03, and 5 from left to right panel, respectively. It shows that GMCs in NGC4526 are more turbulent and more luminous than equal-size clouds in the Milky Way disk. There is no size-linewidth relation, in contradiction to the expectation from Larson's relation (left panel).

or

$$L_{\rm CO} \approx 130 \left(\frac{\sigma_v}{\rm km\ s^{-1}} \right)^5 \ {\rm K\ km\ s^{-1}\ pc^2}. \tag{2.10}$$

Since the linewidth, ΔV, is just $\Delta V = \sigma_v \sqrt{8 \ln 2}$, I refer to Equation (2.8) as the size-linewidth relation. For extragalactic clouds in the Local Group, Bolatto et al. (2008) found $\sigma_v \propto R^{0.6}$, $L_{\rm CO} \propto R^{2.54}$, and $L_{\rm CO} \propto \sigma_v^{3.35}$, which is close to the Milky Way relations.

Interestingly, there is no size-linewidth correlation for NGC4526 (left panel of Figure 2.5), which is parameterized by very weak Pearson and Spearman correlation coefficients ($r_{\rm ps} = -0.18$ and $r_{\rm sp} = -0.14$). This result is in line with GMCs in M33 (Gratier et al. 2012) and M51 (Colombo et al. 2014), where no clear trend was observed ($r_{\rm sp} = 0.12$ and 0.16 for M33 and M51, respectively). The NGC4526 data are located above the Milky Way's relation, which means that for a given size, GMCs in the bulge of NGC4526 have a higher velocity dispersion than those in Milky Way disk GMCs by a factor of ~ 3. This could be due to an environmental effect, since Shetty et al. (2012) and Colombo et al. (2014) found evidence that GMCs in the central regions of the Milky Way and M51 have a higher velocity dispersion than those in the disks. I discuss this environmental effect in Section 2.5.4.

The cloud luminosity is also plotted against the velocity dispersion and size in the middle and right panels of Figure 2.5. The results of the error-weighted fit are

$$L_{\rm CO} = 2258.5^{+1033.0}_{-708.8} \left(\frac{R}{\rm pc}\right)^{1.6\pm0.1} \ {\rm K\ km\ s^{-1}\ pc^2} \tag{2.11}$$

and

$$L_{\rm CO} = 381.3^{+635.8}_{-238.4} \left(\frac{\sigma_v}{\rm km\ s^{-1}}\right)^{3.2\pm0.5} \ {\rm K\ km\ s^{-1}\ pc^2}, \tag{2.12}$$

which is shallower than the exponents in the Milky Way relations (Equations 2.9 and 2.10). The correlation coefficients are moderate for the luminosity-size relation ($r_{\rm ps} = 0.63$ and $r_{\rm sp} = 0.67$), and weak for the luminosity-velocity dispersion relation ($r_{\rm ps} = 0.33$ and $r_{\rm sp} = 0.36$).

The quoted results above take into account all resolved clouds. In Figure 2.5, the inner clouds with distance ≤ 65 pc from the galactic center tend to have higher velocity dispersion, which may be due to contamination by the galactic shear (see Section 2.4 for detailed discussion of cloud kinematics). The conclusions for the size-linewidth and size-luminosity relation are not affected if these inner clouds are excluded. However, the slope of linewidth-luminosity relation becomes steeper by excluding those inner clouds ($L_{\rm CO} \propto \sigma_v^{3.8\pm0.6}$).

In the middle panel of Figure 2.5, the clouds in NGC4526 lie below the Milky Way luminosity-velocity dispersion relation. Thus, for a given velocity dispersion, the clouds are less luminous than GMCs in the disk of the Milky Way. Because CO luminosity is a tracer of the amount of molecular gas, the clouds in NGC4526 are more turbulent per unit mass than those in the Milky Way. Also, from the right panel of Figure 2.5, clouds in NGC4526 are ~ 5 times more luminous than equal size clouds in the Milky Way, which means they have a higher surface density. This result is in agreement with GMCs in M51 (Colombo et al. 2014), where GMCs in the central region are brighter than those in the inter-arms region. Again, this could be due to environmental effects which are discussed in Section 2.5.4.

Finally, there is no bias that affects the results due to the choice of input parameters of the CPROPS program. Even though the properties of individual clouds vary by changing the input parameters, the overall distributions are similar (see Section 2.11 for details).

2.4 Cloud Kinematics

2.4.1 The Velocity Gradient of Molecular Clouds

Previous studies (e.g. Imara et al. 2011; Rosolowsky et al. 2003; Phillips 1999; Kane & Clemens 1997; Goodman et al. 1993) have found velocity gradients across atomic and molecular clouds and clumps, which are interpreted as the rotation of GMCs. Moreover, most of the GMC rotation exhibits solid body rotation. Here, I perform analyses on the resolved clouds to gain insight into the origin of their kinematics and the role of rotation in the dynamical stability of GMCs.

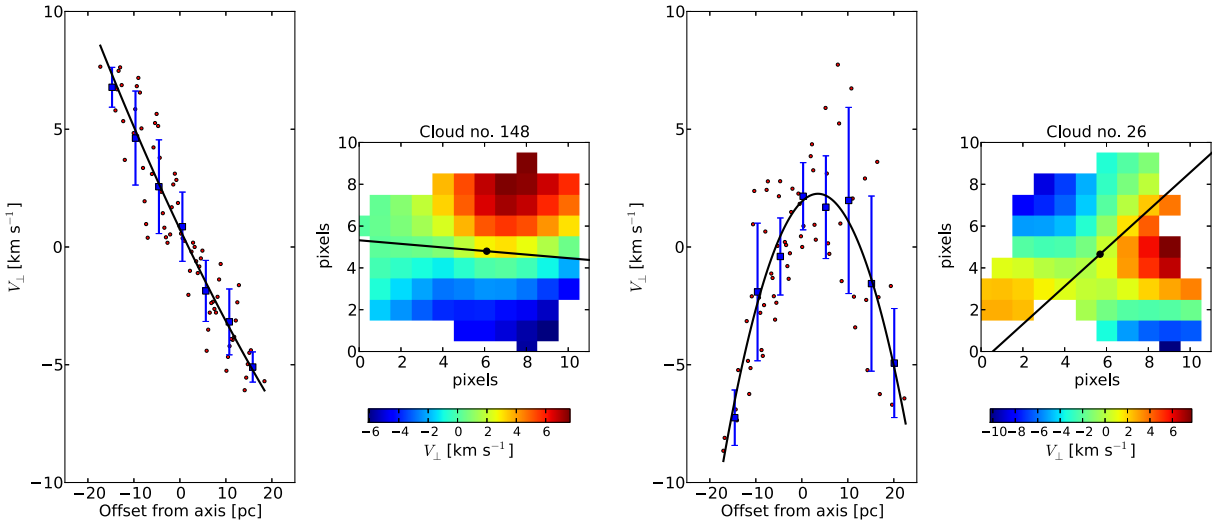

Figure 2.6: Examples of plane fitting to find the rotation signature of GMCs. The right panels are GMC first-moment maps with the rotation axis (black line) overplotted. On the left panels, the mean velocity of each pixel is plotted against its perpendicular distance from the rotation axis. The black line is the fit and blue dots are the mean of the velocity in bins of perpendicular distance from the rotation axis (i.e. $v_\perp$ vs d). The cloud in the top panels shows the signature of solid body rotation with $\chi^2_{\nu,\mathrm{line}} \approx 0.18$, while the cloud in the bottom panels shows bow-shock motions and is well fitted by a parabolic curve with $\chi^2_{\nu,\mathrm{para}} \approx 0.68$.

In order to quantify any rotation signature, I do the following steps. First, the velocity field (first-moment map) of the cloud is smoothed with a Gaussian kernel, where the dispersion of the Gaussian kernel is half the telescope beamwidth. The aim of this smoothing is to 'average' the velocity field at the cost of losing independence among the neighboring pixels (left panels of Figure 2.6). Then, I fit the first-moment map of individual clouds with a plane (e.g. Goodman et al. 1993; Rosolowsky et al. 2003; Imara et al. 2011):

$$v_{\mathrm{los}} = v_0 + a(x - x_0) + b(y - y_0), \tag{2.13}$$

where (x_0, y_0) is the cloud's central pixel coordinate, and

$$a = \frac{\partial v}{\partial x} \quad \text{and} \quad b = \frac{\partial v}{\partial y} \tag{2.14}$$

are the velocity gradients along the x and y axes. v_0, a, and b are free parameters to be determined from the fit.

The angle from the positive x-axis to the receding part of kinematical major axis of the cloud is $\tan^{-1}(b/a)$, and hence, the angle to the cloud rotation axis (i.e. the angular momentum vector) is $\theta = \tan^{-1}(b/a) + 90^\circ$ (i.e., right hand rule).

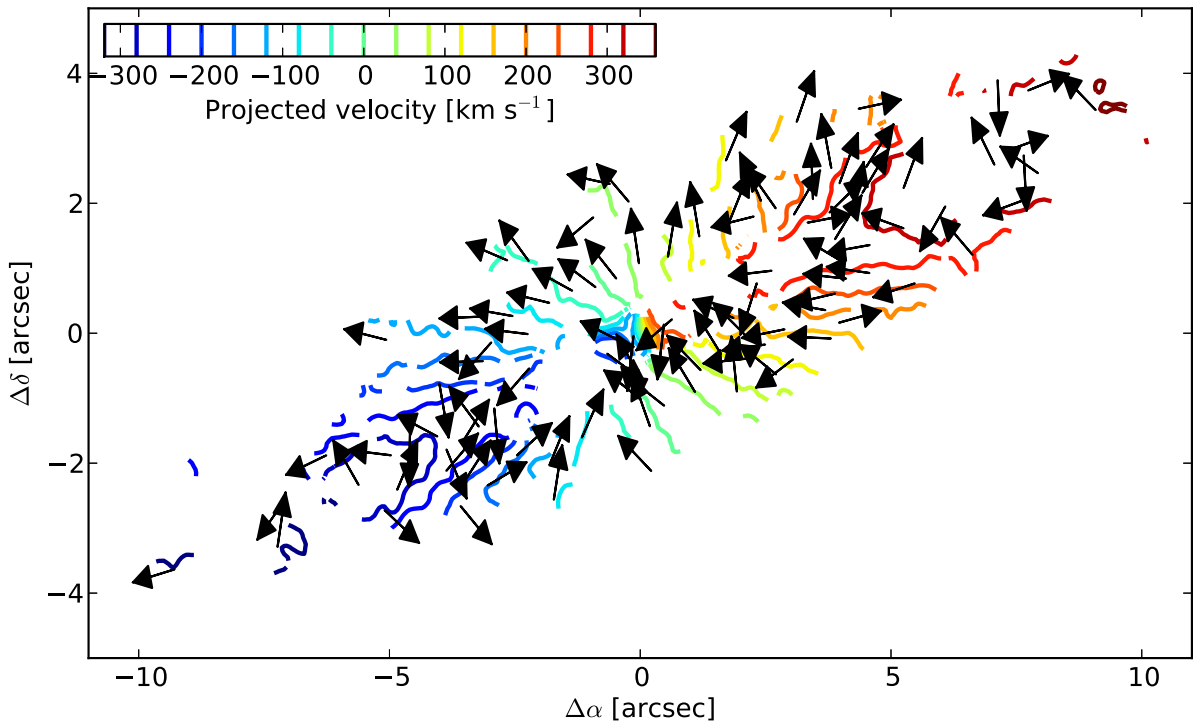

Figure 2.7: The angular momentum vectors of GMCs (black arrows), overplotted with the isovelocity contours of NGC4526 (color coded by their projected velocities) convolved with a Gaussian kernel. There is a strong tendency for the vectors to be tangential to the isovelocity contours, as expected if the measured velocity gradients of GMCs are just the projection of the galaxy rotation. Correlations between the angular momentum of the clouds and isovelocity contours of the galaxy are shown in Figure 2.8.

The angular speed of the cloud is given by

$$\Omega \cos(\psi) = \sqrt{\left(\frac{\partial v}{\partial x}\right)^2 + \left(\frac{\partial v}{\partial y}\right)^2}, \tag{2.15}$$

where ψ is the angle from the cloud rotation axis to the sky plane. Since ψ can not be measured directly, I drop the $\cos(\psi)$ term from Equation (2.15). Thus, the true angular speed is underestimated by a factor of $\cos(\psi)$, i.e. $\Omega_{\rm projected} = \Omega_{\rm true}\ \cos(\psi)$.

The next step is to check whether the clouds show solid-body or differential rotation. I plot the mean velocity of each pixel within a cloud against its perpendicular distance from the cloud rotation axis, i.e. $v_\perp$ vs. d in Figure 2.6, and then the data are fitted with a straight line. Solid body rotators should show a clear linear behavior on this plot, where the constant slope is the angular speed, i.e. $v_\perp = \Omega\ d$. On the other hand, the slope of Keplerian

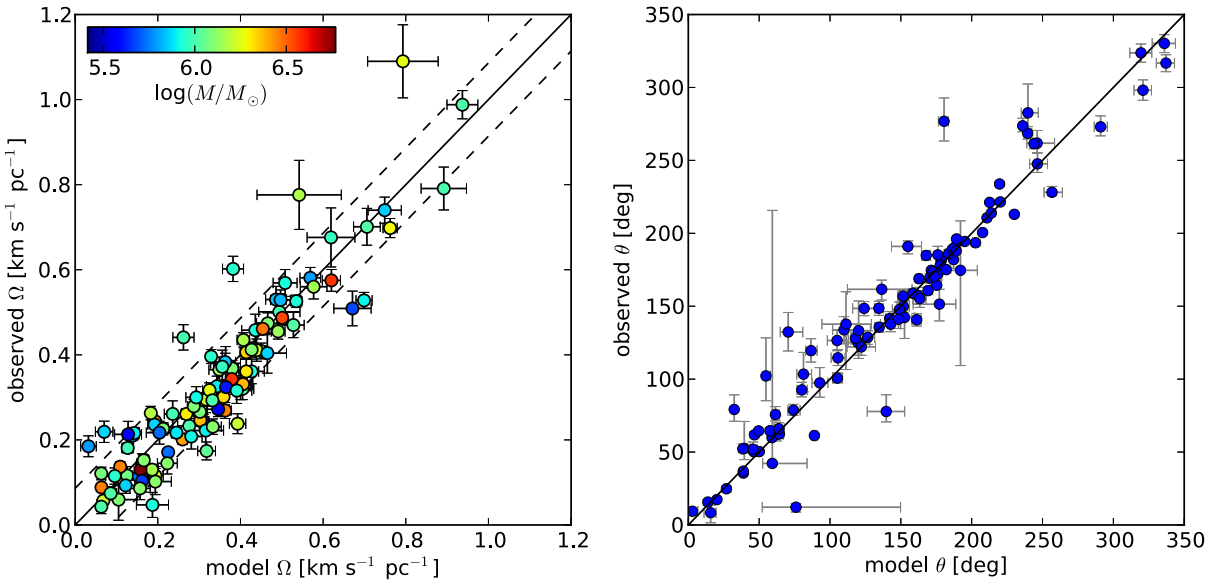

Figure 2.8: Correlations between the model and observed angular speed Ω (left panel) and the angle of rotation axis θ (right panel). The observed Ω and θ are calculated from the best fit of the velocity field of the cloud (e.g., Goodman et al. 1993). The model Ω and θ are purely based on the galaxy rotation and created using the KinMS package of Davis et al. (2013c) as described in the text. The error bars are derived from the covariance matrix of the best fit. The excellent one-to-one correlations (solid line) indicate that the velocity gradients that we measure are actually just a projection of the galaxy rotation. The dashed lines on the left panel are the standard deviation from Monte Carlo simulations that gives the upper limit of the angular speed of the cloud.

rotators varies with distance from the center, i.e. the slope gets shallower outside (resembles an S-shape; $v_\perp \propto d^{-0.5}$), while bow-shock motions tend to have a parabolic shape (Kane & Clemens 1997).

Finally, I divide the clouds into two groups: clouds that show solid-body rotation (SB) and clouds that show deviations from solid-body rotation (NSB). This division is based on the reduced χ^2 value from the binned $v_\perp$ (blue squares in Figure 2.6) to the straight line fit. I classify clouds with $\chi^2_{\nu,\mathrm{line}} \leq 1.5$ as SB and the rest as NSB. For NSB, I also fit $v_\perp(d)$ with a parabolic curve and calculate its $\chi^2_{\nu,\mathrm{para}}$. Eye inspections confirm that this classification is reasonable. As a result, 46 of 103 resolved clouds are classified as SB, while the rest are NSB. Examples of SB and NSB clouds are shown in Figure 2.6.

2.4.2 The Origin of Velocity Gradients

A purely rotating galaxy with an inclination angle i has a line of sight velocity component of $V_{\rm los} = V_{\rm sys} + V(R)\cos(\phi)\sin(i)$ at (R, ϕ), where $V_{\rm sys}$ is the systemic velocity of the galaxy, $V(R)$ is the circular velocity at radius R from the galactic center, and ϕ is the angle from the kinematic major axis of the galaxy. In the simplest case, for a region with a flat rotation curve, i.e. $V(R) =$ constant, the observed iso-velocity contours of the galaxy are given by contours of equal ϕ. Therefore, velocity gradients exist along any path that perpendicularly crosses those iso-velocity contours. The last statement is true for any rotation curve, not just for a flat rotation curve.

On the other hand, I also find velocity gradient in any small patches of the data that occupy the GMC regions. This velocity gradient can be due to a projection of the galaxy rotation, and therefore, can mimic the cloud rotation. In Figure 2.7, I show the angular momentum vectors of GMCs, overplotted with the iso-velocity contours of NGC4526. The tendency of the angular momentum vectors of the clouds to be tangential to the iso-velocity contours of the galaxy suggests that the velocity gradients of the clouds are actually just a projection of the galaxy rotation.

In order to quantify this finding, I create a gas dynamical model using the KinMS (Kinematic Molecular Simulation) package of Davis et al. (2013c). This model is basically a purely rotating disk based on a rotation curve of the galaxy, i.e. this is what the galaxy looks like if its dynamic is just a rotation. The rotation curve is calculated from the multi-Gaussian expansion (MGE) of Cappellari (2002) to the I-band images of HST and MDM 1.3-m telescope, and includes the presence of a supermassive black hole at the center (Davis et al. 2013b). This MGE fit gives the mass distribution of the galaxy, and hence the galaxy rotation curve, parameterized by the stellar mass-to-light ratio and the galaxy inclination. The model is inclined so that it matches the inclination of the observed galaxy ($i \approx 79°$). Any deviations of the data from the model can be caused by small scale turbulence, inflow or outflow gas motion, and the cloud rotation.

Then, I measure the angular momentum of the model at the location of the observed clouds by using the same method as described in Section 2.4.1. We find a strong one-to-one correlation for both angular speed and rotation angle between the model and the data, albeit with small scatter (Figure 2.8). The correlation holds true for both SB and NSB groups. This reinforces the previous suspicion that the velocity gradients of the clouds are just a consequence of the underlying velocity field due to galaxy rotation, i.e. the gas within clouds moves following the galaxy rotation. Therefore, Ω that is calculated using the plane-fitting method (Equation 2.15) is not the intrinsic angular speed of the clouds.

In this case, the gas within the cloud must rotate due to galactic shear. The amount of shear is given by the Oort constant A (Fleck & Clark 1981):

$$\Omega_{\rm shear} = \left|\frac{\Delta v}{\Delta r}\right| = |2A| = \left|\frac{V_0}{R_0} - \left(\frac{dV}{dR}\right)_0\right|, \tag{2.16}$$

where the subscripts 0 denote the evaluation at the location of the GMCs, and $V(R)$ is the rotation curve of the galaxy. Hereafter, *I take this shear as the angular speed of the cloud*, not

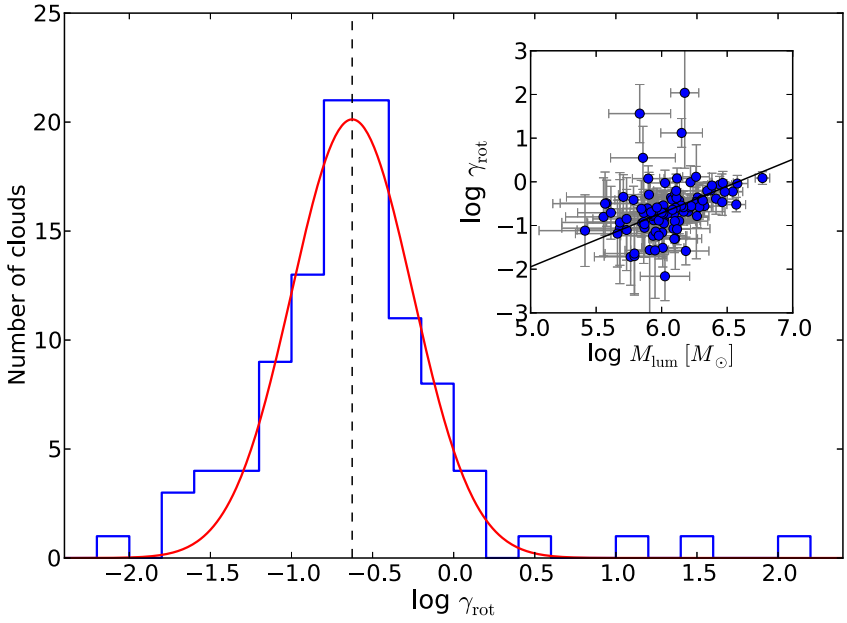

Figure 2.9: The distribution of $\gamma_{\rm rot}$, defined as the ratio between rotational and turbulent energy. The dashed line is the mean of the log-normal fit (red). For the majority of the clouds, the rotational energy due to galactic shear is smaller than the turbulent energy. From the correlation between $\gamma_{\rm rot}$ and luminous mass (shown as an inset), I infer that the relative importance of rotation over turbulence is increasing for more massive clouds.

Ω from Equation (2.15). Furthermore, the angle of the rotation axis θ from the plane-fitting is not physically meaningful anymore, because if the cloud rotation is due to galactic shear then their rotation axes tend to be parallel to the galaxy rotation axis.

The intrinsic scatter in Figure 2.8 may be due to the intrinsic angular momentum of the cloud, $\Omega_{\rm cloud}$, where the origin is something other than galactic shear. From 1,000 Monte Carlo simulations, I determine the upper limit of the cloud's angular speed to be $\Omega_{\rm cloud} < 8.6 \times 10^{-2}$ km s^{-1} pc^{-1} (dashed line in Figure 2.8), which is comparable to the angular speed of GMCs and HI cloud in M33 (Rosolowsky et al. 2003; Imara et al. 2011). This upper limit is generally smaller than the galactic shear at the cloud's location, i.e. $\Omega_{\rm cloud} < \Omega_{\rm shear}$, so that $\Omega \approx \Omega_{\rm shear}$.

Based on our analysis, any measurements of the velocity gradient of an extragalactic cloud must be performed carefully, to avoid bias due to the projection of the galaxy rotation. The only exception is if the galaxy is nearly face-on ($i \approx 0°$), as the line of sight velocity due to galaxy rotation is negligible.

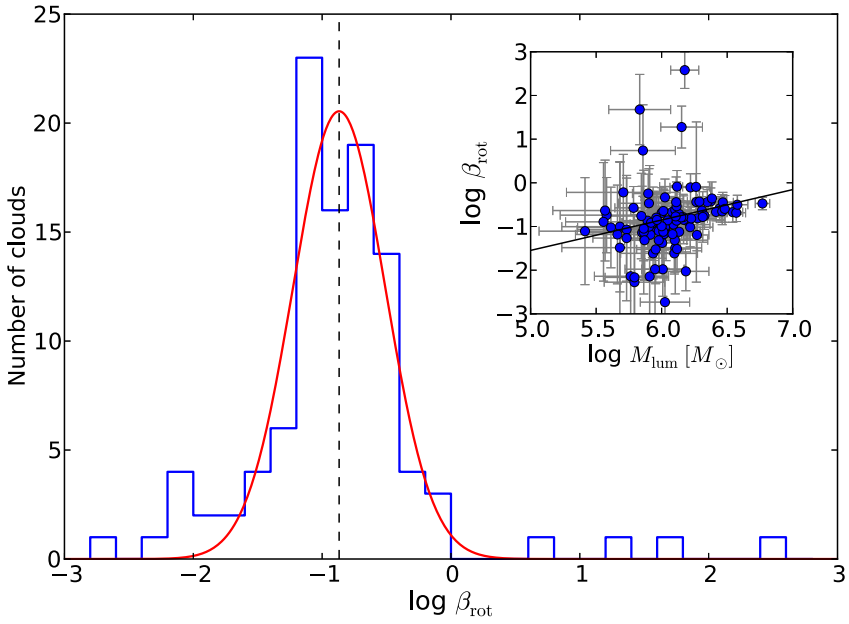

Figure 2.10: Same as Figure 2.9, but for $\beta_{\rm rot}$, which is defined as the ratio between rotational and gravitational energy. Most of the clouds are not in rotational equilibrium, i.e. $\beta_{\rm rot} < 1$. The four clouds in the tail of the distribution are the innermost clouds that suffer strong shear. From the correlation between $\beta_{\rm rot}$ and luminous mass (shown as an inset), I infer that the relative importance of rotation over gravity is increasing for more massive clouds.

2.4.3 Stability of Rotating Clouds

In Section 2.3.2, the clouds were supported by turbulence only. In the presence of rotation (due to shear), the rotational energy also contributes to the clouds' stability against gravitational collapse. Here, the parameter $\gamma_{\rm rot}$ is defined as the ratio of rotational over turbulent energy:

$$\gamma_{\rm rot} = \frac{p\Omega^2 R^2}{3\sigma_v^2}, \tag{2.17}$$

where $p = 2/5$, the value for a uniform sphere (Goodman et al. 1993).

In Figure 2.9, I show the histogram of the $\gamma_{\rm rot}$ values of the clouds. A log-normal fit to the distribution yields a mean $\gamma_{\rm rot} \approx 0.24$ with a standard deviation of 0.37 dex. Roughly 92% of the resolved clouds have $\gamma_{\rm rot} < 1$. This means that the rotational energy is smaller than the turbulent energy for the vast majority of the clouds. There is also a correlation with mass as $\gamma_{\rm rot} \propto M_{\rm lum}^{1.23\pm0.16}$, so that the relative importance of rotation over turbulence is increasing for more massive clouds.

It is also useful to define the ratio between rotational kinetic energy and self-gravitational

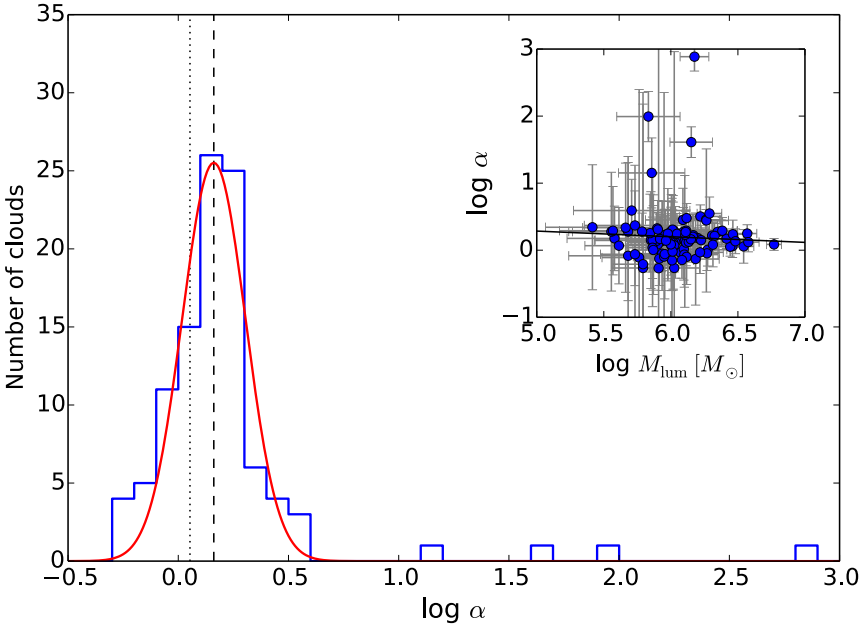

Figure 2.11: Same as Figure 2.9, but for the virial parameter α. The dashed line is the mean Gaussian fit, and the dotted line is $\alpha = 1.13$. The four clouds in the tail of the distribution are the innermost clouds that undergo a strong shear. Except for those four clouds, the cloud population is in gravitational equilibrium, i.e. the mean $\alpha \approx 1.45$ (dashed line). The inset shows no correlation between the virial parameter and the luminous mass.

energy:

$$\beta_{\rm rot} = \frac{1}{2}\frac{p}{q}\frac{\Omega^2 R^3}{GM}, \tag{2.18}$$

where $p/q = 2/3$, the value for a uniform sphere (Goodman et al. 1993). Clouds with $\beta_{\rm rot} \approx 1$ are rotationally-stable against gravitational collapse. About 96% percent of the resolved clouds have $\beta < 1$. A log-normal fit to the distribution yields a mean $\beta_{\rm rot} \approx 0.14$ with a standard deviation of 0.36 dex (Figure 2.10). This means that the rotational energy is smaller than the gravitational energy for the vast majority of the clouds. Furthermore, there is a correlation with mass as $\beta_{\rm rot} \propto M_{\rm lum}^{0.70\pm0.21}$, so that the relative importance of rotation over gravity is increasing for more massive clouds.

Finally, the virial parameter α, which includes turbulence, gravity, and rotation, can be expressed as

$$\alpha = 2\ \beta_{\rm rot}\left(1 + \frac{1}{\gamma_{\rm rot}}\right). \tag{2.19}$$

Non-magnetic, rotating clouds with $\alpha \approx 1.13$ are in virial-equilibrium (BM92), while clouds with $\alpha \gg 1$ are either pressure-confined clouds, or still gravitationally bound but with an underestimated CO-to-H_2 conversion factor.

The distribution of α values is shown in Figure 2.11, where it can be approximated by a log-normal distribution with a tail at the high end. The log-normal mean is $\alpha \approx 1.45$ with a standard deviation of 0.14 dex. This suggests that the GMC population in NGC4526 is gravitationally-bound, even after the inclusion of rotational energy. If non-gravitational equilibrium is defined as having $\alpha > 5 \approx 0.7$ dex (i.e. the tail of the distribution), then only $\approx 4\%$ of resolved clouds are not gravitationally-bound. As shown in the inset in Figure 2.11, by excluding those four clouds, α has no correlation with mass, because the best-fit relation is $\alpha \propto M_{\rm lum}^{-0.08\pm0.05}$.

Further investigation reveals that the four gravitationally-unbound clouds (with $\log \alpha > 0.7$) are the clouds closest to the center of the galaxy, at a distance of ≈ 10, 34, 42, and 54 pc. These clouds suffer strong shear ($|\Delta v/\Delta r| \sim 10$ km s^{-1} pc^{-1}) due to the presence of a supermassive black hole (SMBH) at the center of NGC4526, with $M_{\rm BH} \approx 4.5 \times 10^8 M_\odot$ and radius of influence of ≈ 45 pc (Davis et al. 2013b). This SMBH makes the circular velocity curve of the galaxy increase abruptly towards the galactic center (Figure 2.12), and hence yields a large Oort A constant.

2.5 Discussion

2.5.1 Pressure Balance

In general, the dynamical equilibrium state of a cloud can be written as

$$P_{\rm int} + P_B = P_G + P_{\rm ext}, \tag{2.20}$$

where $P_{\rm int} \approx P_{\rm turb}\ (1 + \gamma_{\rm rot})$ is the internal pressure of the cloud, including the correction factor $(1 + \gamma_{\rm rot})$, due to the contribution of rotation. $P_{\rm turb} = \bar{\rho}\sigma_v^2$ is the kinetic pressure due to turbulence, $P_{\rm ext}$ is the external pressure of the ambient medium, and $P_B = B^2/8\pi$ is the magnetic pressure. Here, I assume that the thermal pressure is much smaller than the pressure due to turbulent motion, and it is neglected. P_G is the internal gas pressure that is required to support the cloud against gravity in the absence of any other forces (BM92):

$$\frac{P_G}{k} = 1.3\ \bar{\phi_G} \left(\frac{M}{M_\odot}\right)^2 \left(\frac{R}{\rm pc}\right)^{-4}\ {\rm K\ cm^{-3}}, \tag{2.21}$$

where $\bar{\phi_G}$ is a dimensionless factor that measures the ratio between the gravitational pressure of ellipsoidal and spherical clouds, and depends only on the cloud's axis ratio: $\sigma_{\rm maj}/\sigma_{\rm min}$ for prolate clouds and $\sigma_{\rm min}/\sigma_{\rm maj}$ for oblate clouds. Here, I assume all clouds are prolate. The value of $< \phi_G >$ for oblate clouds is within the uncertainty of that for prolate clouds.

For non-magnetic, rotating, gravitationally-bound clouds: $P_{\rm int} \approx P_G$. In Figure 2.12, I plot $\log(P_{\rm int}/P_G)$ versus the distance of clouds from the galactic center. Except for the four innermost clouds, $\log(P_{\rm int}/P_G)$ has a mean value of ≈ -0.03 and standard deviation of ≈ 0.18 dex, consistent with a gravitationally bound state. The error bars of individual data points are not included to calculate those values.

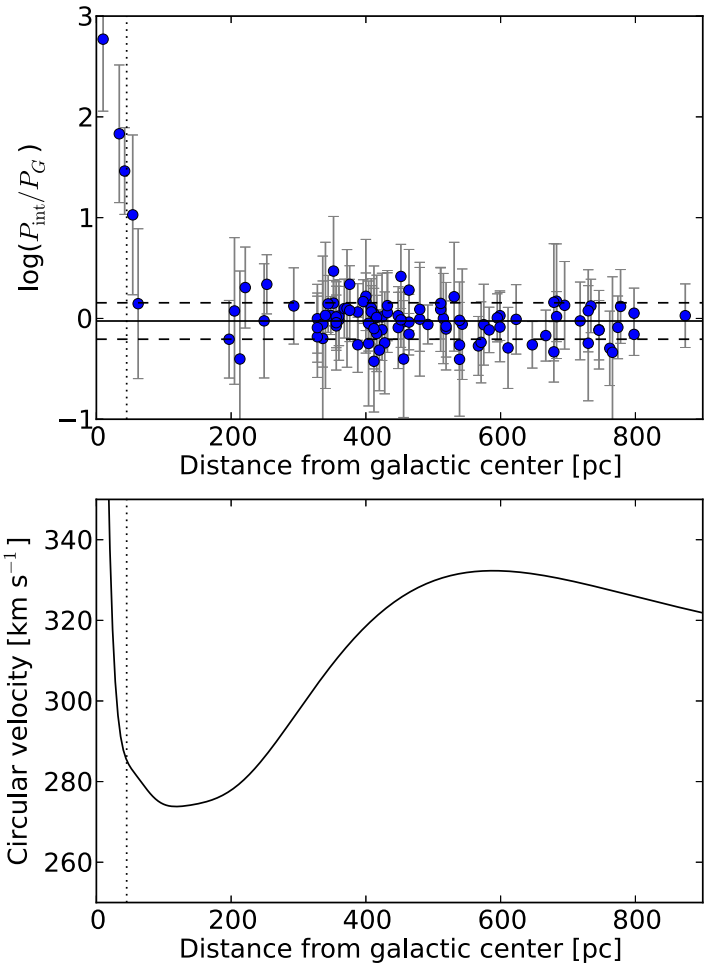

Figure 2.12: Top: the ratio of internal and gravitational pressure as a function of distance from the galactic center. Except for the four innermost clouds, the data points are consistent with gravitationally-bound clouds. The 1σ scatters are indicated with dashed lines. The SMBH radius of influence ($\approx$ 45 pc) are indicated as vertical dotted lines. Bottom: the galaxy circular velocity curve. The sharp increase near the center is due to the presence of a supermassive black hole (Davis et al. 2013b).

As mentioned in Section 2.4.3, there are four central clouds that experience strong galactic shear. By using Equation (2.20) and an assumption of zero magnetic pressure, the external pressure that is required to bind the clouds against galactic shear is $P_{\rm ext} \sim 10^9$ K cm^{-3}, which is extremely high and unrealistic. These may be unbound clouds. If nothing balances the shear, then these clouds will be ripped apart by strong shear within a timescale of $\sim 2\pi/|\Delta v/\Delta r| \sim 1$ Myr. This timescale is smaller than the expected lifetimes of GMCs ($\approx$ 30 Myr; Blitz & Shu 1980) based on the clumpiness nature of GMCs and destruction

processes from massive star formation inside GMC complexes. Another evidence of the role of shear in the destruction of GMCs is found in the M51 disk, where Miyamoto et al. (2014) reported that the locations of giant molecular associations are anti-correlated with the shear strength.

2.5.2 Does a Size-linewidth Relation Really Exist?

Clouds in NGC4526 do not show a size-linewidth relation (see Figure 2.5), in contrast to the previous arguments that supported the Larson's 'law' (e.g. in the Milky Way disk; S87, and Local Group galaxies; Bolatto et al. 2008). Most of the Local Group members are late-type galaxies, while our clouds reside in the bulge of a S0-type galaxy. Does this discrepancy suggest that GMC properties in the early-type galaxies are intrinsically different? Here, I argue that the size-linewidth relation may not exist in all galaxy morphologies, because the cloud's size and linewidth within a single galaxy only have weak to modest correlation coefficients.

Recent studies of GMCs in spirals, such as M33 (Gratier et al. 2012) and M51 (Colombo et al. 2014), also found no clear size-linewidth relation, with a Spearman correlation coefficient $r_{\rm sp}$ of 0.12 and 0.16, respectively. A modest correlation ($r_{\rm sp} = 0.51$) was found by Heyer et al. (2009), who re-examined S87 clouds in the Milky Way disk using more sensitive instruments. Furthermore, clouds in the LMC also show a weak correlation ($r_{\rm sp} = 0.37$; Hughes et al. 2013; Wong et al. 2011). These evidence suggest that the size-linewidth relation may not exist in all galaxy morphologies.

If the argument for a size-linewidth relation is not conclusive for GMCs *within* a single galaxy, then how about a compilation of GMC data from various galaxies (e.g. Bolatto et al. 2008)? In this case, one must pay attention to different data sets that have different physical resolutions and sensitivities. Coarse resolution and low S/N observations can only measure average properties within a larger area, without the ability to decompose the CO structure into multiple smaller clouds, while finer resolution observations tend to over-decompose CO emission into smaller scale structures. This means that the identified GMCs in different data sets are likely to probe different scales of CO emission. This bias, which is due to the ability to decompose structure in GMCs, is separate from the bias of measured properties due to finite resolution and sensitivity, which has been minimized by the CPROPS program. Hence, plotting those data in a size-linewidth diagram leads us to compare different structure of GMCs. For example, Bolatto et al. (2008) compare composite extragalactic GMCs that have been observed with a range of resolution from $\sim$ 6 pc (about the size of a clump) to $\sim$ 117 pc (about the size of a giant molecular association). Therefore, any scatter in the size vs. linewidth diagram is overcome by the large range of GMC size, which gives rise to a slope. Even in this case, however, the correlation coefficient is still moderate ($r_{\rm sp} = 0.57$).

A self-consistent study of the size-linewidth relation, then, requires a common physical resolution and sensitivity across the extragalactic GMC data sets. Any similarity or discrepancy among the extragalactic GMCs measured in this way would then be genuine. In a recent work, Hughes et al. (2013) showed that a size-linewidth relation is apparent when

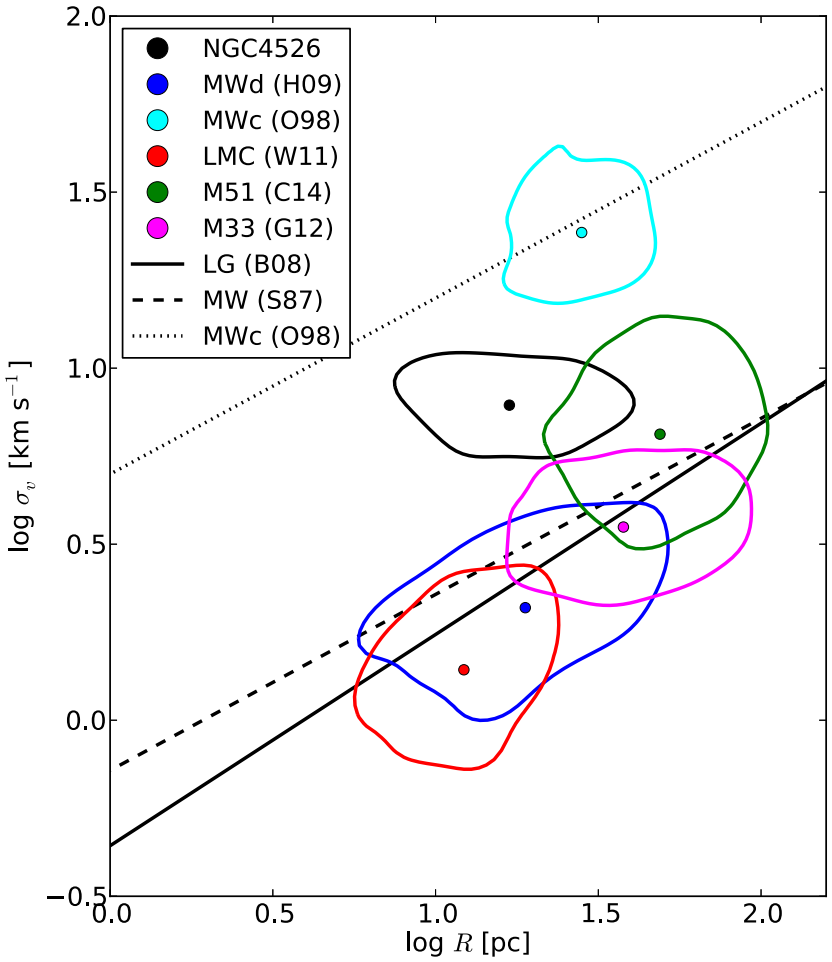

Figure 2.13: Plots of size vs. velocity dispersion for extragalactic GMC populations. The contours enclose 68% of the distribution of data points of a given galaxy: NGC4526 (black; this paper), Milky Way disk (blue; Heyer et al. 2009), Milky Way center (cyan; Oka et al. 1998), Large Magellanic Cloud (red; Wong et al. 2011), M51 (green; Colombo et al. 2014), and M33 (magenta; Gratier et al. 2012). The centers of a Gaussian fit to each distribution are shown as filled circles. The dashed line is the Milky Way disk relationship (S87), the dotted line is the Milky Way center relationship (Oka et al. 1998), and the solid line is the Local Group relationship (Bolatto et al. 2008).

M51, M33, and LMC data were analyzed at their original (different) resolutions and sensitivities (as in Bolatto et al. 2008), but no compelling evidence was found when the data were degraded to a single ('matched') common resolution and sensitivity. From the 'matched' data, they inferred that GMCs in M51 are in general larger, brighter, and have higher velocity dispersions than equivalent structures in M33 and the LMC, which can be interpreted as a genuine variation of GMC properties.

In this respect, we can compare NGC4526 and LMC data (Wong et al. 2011), since they have comparable physical resolutions and sensitivities ($\sim$ 20 pc and $\sigma_{\rm rms} \approx 0.7$ K for NGC4526, and $\sim$ 11 pc and $\sigma_{\rm rms} \approx 0.3$ K for LMC). I find that GMCs in NGC4526 tend to have higher velocity dispersions than equal size clouds in the LMC (Figure 2.13). With respect to the Milky Way disk, clouds in NGC4526 lie above the Milky Way disk size-linewidth relation (S87) by a factor of ~ 3 (Figure 2.13) and above the Milky Way size-luminosity relation by a factor of ~ 5 (Figure 2.5), which implies that clouds in NGC4526 are brighter and more turbulent than similarly-sized clouds in the Milky Way. In contrast, NGC4526 clouds are less turbulent than the Galactic center clouds by a factor of ~ 0.4 dex (Figure 2.13). This genuine variation of GMC properties may be influenced by a different environment between galaxies (Hughes et al. 2013) and is discussed in Section 2.5.4.

2.5.3 Variations of GMC Surface Density

If the standard size-linewidth relation ($\sigma_v \propto R^{1/2}$) is valid for GMCs, then as a consequence the mass of gravitationally bound clouds is $M_{\rm vir} \propto R^2$ (Equation 2.4), and hence the mass surface density $\Sigma = M_{\rm vir}/\pi R^2 =$ constant. However, Heyer et al. (2009), who revisited the GMCs of S87 using more sensitive and better sampled data, found that the surface density is actually not constant, and the coefficient of the size-linewidth relation ($C_0 = \sigma_v R^{-1/2}$) correlates with the surface density as $C_0 \propto \Sigma^{1/2}$. This relation is expected from gravitational equilibrium (Equation 2.4), and does not depend on whether the clouds follow the size-linewidth relation or not. The same relation ($C_0 \propto \Sigma^{1/2}$) also holds for pressure-confined, self-gravitating isothermal sphere (which I refer as "pressure equilibrium" for brevity), but with $\Sigma = \Sigma_{\rm c} \propto P_{\rm ext}^{1/2}$ (Field et al. 2011), where $\Sigma_{\rm c}$ is the critical surface density of a Bonnor-Ebert sphere (Bonnor 1956; Ebert 1955). The difference between the two is that pressure equilibrium has a higher normalization than the gravitational equilibrium. The Heyer et al. (2009) data favor pressure equilibrium rather than gravitational equilibrium (Field et al. 2011).

In Figure 2.14, I compile extragalactic GMC dataset. The contours enclose 68% of the distribution of data points of each galaxy. This compilation of extragalactic GMC data shows that the surface density is not constant, but varies from $\sim$ 10 to 3000 $M_\odot$ pc^{-2}. GMCs in the Milky Way disk, LMC, and M33 have lower surface densities than GMCs in M51 and NGC4526. The median surface density of the NGC4526 clouds is $\Sigma_{\rm med} \approx 1.2 \times 10^3$ $M_\odot$ pc^{-2}, which is ~ 7 times greater than in the Milky Way disk clouds (170 $M_\odot$ pc^{-2}; S87). However, NGC4526 clouds have similar surface density as the Galactic center clouds. This high surface density may be a common feature for clouds in the galaxy bulge.

In Figure 2.14, we also see that there is a correlation between $\sigma_v R^{-1/2}$ and surface density, as expected from gravitational (and pressure) equilibrium. The Milky Way disk, LMC, M51, and NGC4526 clouds roughly follow $\sigma_v R^{-1/2} \propto \Sigma^{1/2}$, but the Galactic center and M33 clouds have higher normalizations, i.e. they lie above the gravitational equilibrium relation (dotted line). As Field et al. (2011) suggested, Milky Way disk clouds are likely to be in pressure-equilibrium (dashed line) rather than gravitational equilibrium, and hence

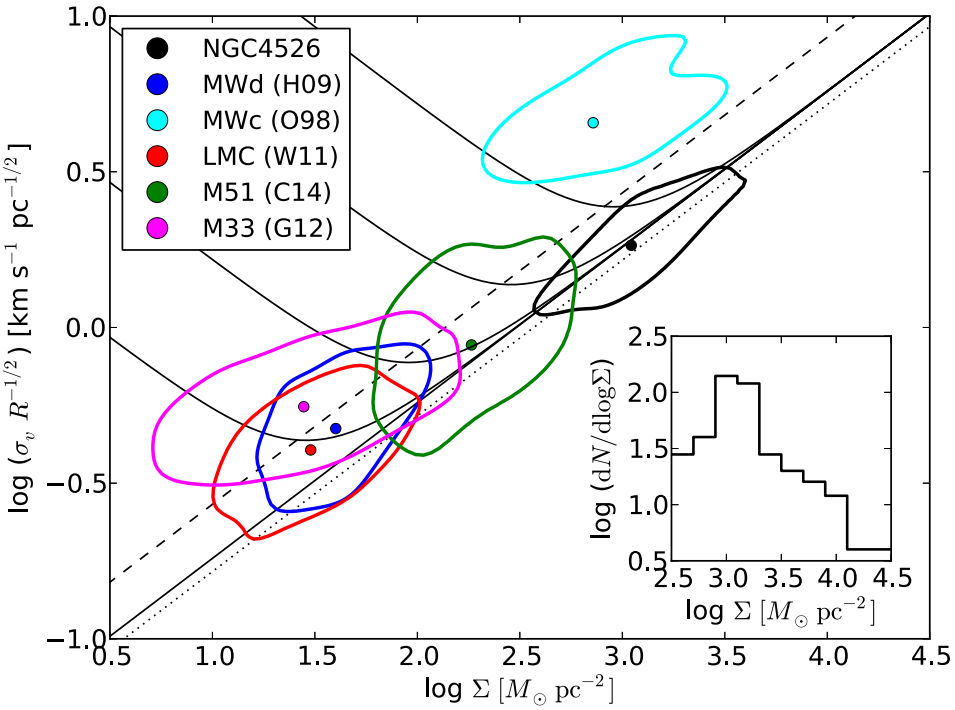

Figure 2.14: The correlation between $\sigma_v R^{-1/2}$ and surface density for extragalactic GMC populations (color coded as in Figure 2.13). The contours enclose 68% of the distribution of data points of a given galaxy. The solid 'V'-curves are the pressure equilibrium condition of an isothermal sphere for various external pressures ($P_{\rm ext}/k = 10^7, 10^6, 10^5, 10^4$, and 0 K cm^{-3}, respectively, from top to bottom; Field et al. 2011). The dashed line is the locus of critical surface density for a Bonnor-Ebert sphere. The dotted line is the gravitational equilibrium of a constant density sphere. This plot shows that the surface density of GMCs is not constant as previously believed. *Inset:* the surface density function of the clouds in NGC4526.

have a higher normalization factor. With the exception of Galactic center clouds, it is interesting to note the trend that GMCs with lower surface densities tend to be in pressure equilibrium. The Galactic center clouds are unique because they are pressure-bound clouds with $M_{\rm vir} \sim 10\ M_{\rm lum}$ and they reside in the high external pressure environment (Oka et al. 1998; Miyazaki & Tsuboi 2000).

Based on this finding (Figure 2.14), I argue against the current mainstream view regarding the constancy of cloud surface density. Indeed, theoretical studies (e.g. Kegel 1989; Ballesteros-Paredes & Mac Low 2002) found that limited observational sensitivities can give biased results, so that previous measurements of the surface density of GMCs appear constant. Moreover, size, velocity dispersion, and surface density are correlated with each other as expected from gravitational equilibrium (or pressure equilibrium as in the Milky Way, LMC, and M33).

Here, I propose a modified version of the Larson's relations. (1) The clouds are in either gravitational or pressure equilibrium; the relative contribution of gravity and external pressure to cloud stability needs further study on a cloud-by-cloud basis. (2) The coefficient of the size-linewidth relation depends on the cloud surface density as $C_0 \propto \Sigma^{1/2}$. This relation also holds true in the pressure equilibrium case, where surface density depends on the external pressure of the ambient medium ($\Sigma \propto P_{\rm ext}^{1/2}$; Field et al. 2011). (3) The cloud surface densities are not all the same, but may depend on the environment, such as the external pressure (Chieze 1987; Elmegreen 1993), interstellar radiation field strength (McKee 1989), and interstellar gas flow and turbulence (Vázquez-Semadeni et al. 2007), which need further investigation. These environmental dependencies could explain variations of GMC properties across different galaxies (Hughes et al. 2010; Rosolowsky & Blitz 2005).

2.5.4 Environmental Effects

GMCs in NGC4526 are denser and more turbulent than those in the Galactic disk, but have similar surface density and are less turbulent than those in the Galactic center (Figures 2.13 and 2.14). These differences may be caused by different environment, such as the interstellar radiation field strength (ISRF) and the external ambient pressure ($P_{\rm ext}$), between NGC4526 and the Milky Way. Here, the ISRF and $P_{\rm ext}$ are inferred based on the global properties of the galaxy and discuss their possible roles to explain the differences between GMCs in NGC4526 and the Milky Way.

A Comparison with GMCs in the Milky Way disk

Ciesla et al. (2014) have used the Herschel photometric data to derive the dust spectral energy distribution of 322 nearby galaxies, including NGC4526. They fit the data with the dust emission model of Draine & Li (2007). In this model, a large fraction of dust is located in the diffuse interstellar medium, exposed to a single ISRF with intensity $U = U_{\rm min}$. I define U as the intensity normalized to the Milky Way value, i.e. ISRF $= U \times {\rm ISRF_{MW}}$, where ${\rm ISRF_{MW}}$ is the ISRF of the Milky Way (Mathis et al. 1983). In addition, there is a small fraction (γ) of dust located in regions where the ISRF is more intense (e.g. photodissociation regions), with ISRF ranging from $U_{\rm min}$ to $U_{\rm max}$ and described by a power law $U^{-\alpha}$. Draine & Li (2007) found $U_{\rm max} = 10^6$ and $\alpha = 2$ are the best fit to the SINGS sample (Kennicutt et al. 2003). The free parameters of the model are then reduced to $U_{\rm min}$ and γ.[2] Ciesla et al. (2014) found the best fit parameters of $U_{\rm min} = 3.92 \pm 0.32$ and $\gamma = (0.19 \pm 0.09)\%$ for NGC4526.

Then, the mean ISRF ($\bar{U}$) in NGC4526, weighted by the dust mass, can be calculated by using Equation (2.17) of Draine & Li (2007):

$$\bar{U} = (1-\gamma)\, U_{\rm min} + \frac{\gamma\, \ln(U_{\rm max}/U_{\rm min})}{U_{\rm min}^{-1} - U_{\rm max}^{-1}} \approx 4.0. \tag{2.22}$$

[2]There is a third parameter of the model, namely the fraction of dust mass contributed by Polycyclic Aromatic Hydrocarbons (PAHs), but we do not need it to calculate the mean ISRF.

Thus, the ISRF in NGC4526 is ~ 4 times higher than in the Milky Way.

This higher ISRF means a higher photoionization rate to the molecular gas, so that the CO emission emerges from a deeper layer within the cold gas, i.e. at higher extinction (A_V) than in the typical Milky Way disk. This higher extinction translates into higher gas surface density via (McKee 1989)

$$\Sigma_{\rm H_2} = 22.3 \ \frac{A_V}{\delta_{\rm gr}} \ M_\odot \ {\rm pc}^{-2}, \tag{2.23}$$

where $\delta_{\rm gr}$ is the ratio of the extinction per hydrogen nucleus in the cloud to the standard value given by Spitzer (1978). Generally, $\delta_{\rm gr} = 1$ in the Milky Way. The value of $\delta_{\rm gr}$ in NGC4526 is unknown, but we can assume that $\delta_{\rm gr}$ is proportional to the metallicity as $\delta_{\rm gr} \sim Z/Z_\odot$ (Bolatto et al. 2008). By using Equation (2.23) and $\log(Z/Z_\odot) \approx 0.2$ (Davis et al. 2013a), I can estimate the value of A_V that is required to reproduce the observed surface density of GMCs in NGC4526. A cloud's surface density in NGC4526 is ~ 7 times higher than those values in the Milky Way disk (Figure 2.14), so that A_V in NGC4526 is estimated to be 11 times higher than that in the Milky Way disk.

Furthermore, McKee (1989) predicts that the velocity dispersion of GMCs is proportional to the square-root of A_V and the cloud size as $\sigma_v \propto (A_V/\delta_{\rm gr})^{1/2} \ R^{1/2}$. This relation arises naturally from the gravitational equilibrium state and by using A_V as a proxy of surface density as in Equation (2.23). By using the estimated value of A_V above, the theory predicts that the velocity dispersion in NGC4526 clouds is about 2.6 times higher than the velocity dispersion of equal-size clouds in the Milky Way disk. This prediction is in agreement with our measurements, which show the velocity dispersion of equal-size clouds in NGC4526 is higher than those in the Milky Way disk by a factor of ~ 3 (Figure 2.5 and 2.13). Thus, I speculate that the surface density and velocity dispersion in NGC4526 clouds are higher because those clouds have higher extinction than clouds in the Milky Way disk.

A Comparison with GMCs in the Galactic center

Clouds in NGC4526 have similar surface density and a smaller velocity dispersion than equal size clouds in the Galactic center (Oka et al. 1998) by a factor of ~ 0.4 dex (Figure 2.13 and 2.14). This may be due to the fact that Oka et al. (1998) clouds and Miyazaki & Tsuboi (2000) clumps are in pressure equilibrium, rather than in gravitational equilibrium as in NGC4526 clouds. From Equation (2.20), by neglecting the magnetic pressure term, this means the internal pressure of pressure-bound clouds needs to balance against gravity and external pressure, while gravitationally bound clouds need to balance against gravity only. Therefore, for a given cloud mass and radius, the velocity dispersion of pressure-bound clouds is higher than the velocity dispersion of gravitationally bound clouds in order to maintain a dynamical equilibrium state.

I do the following calculations to support this argument. By neglecting the magnetic field, gravitationally bound clouds have $\sigma^2_{v,\rm vir} = P_G \ \rho^{-1}$, while pressure-bound clouds have $\sigma^2_{v,\rm pres} = (P_G + P_{\rm ext}) \ \rho^{-1}$, where $\rho \propto \Sigma \ R^{-1}$ and $P_G \propto \Sigma^2$ (BM92). For equal-size clouds with

similar density, the ratio between the two is

$$\frac{\sigma_{v,\mathrm{pres}}}{\sigma_{v,\mathrm{vir}}} = \left(1 + \frac{P_{\mathrm{ext}}}{P_G}\right)^{1/2}. \tag{2.24}$$

For spherical clouds, like those in NGC4526, with mass $\sim 10^6 M_\odot$ and radius ~ 20 pc, P_G is $\sim 8 \times 10^6$ K cm^{-3}. The external pressure P_{ext} in the Galactic center is rather uncertain. For P_{ext}/k between $\sim 5\times10^6$ K cm^{-3} (Spergel & Blitz 1992) and $\sim 1\times10^8$ K cm^{-3} (Miyazaki & Tsuboi 2000), the Galactic center clouds are expected to have a higher velocity dispersion by a factor of 1.3 to 3.7 (c.f. Equation 2.24). This range is also in agreement with our measurement (~ 0.4 dex ≈ 2.5; Figure 2.13).

If this is true, then why are the clouds in NGC4526 bulge in gravitational equilibrium but clouds in the Galactic center pressure bound? To get insight into this question, I estimate the global ambient hydrostatic pressure P_h in NGC4526 as a proxy of the external pressure (Elmegreen 1989):

$$P_{\mathrm{h}} = \frac{\pi G}{2}\Sigma_g \left(\Sigma_g + \frac{\sigma_g}{\sigma_*}\,\Sigma_*\right), \tag{2.25}$$

where $\Sigma_g \equiv \Sigma_{\mathrm{HI}}$ is the ambient gas surface density, Σ_* is the stellar surface density, σ_g is the ambient gas velocity dispersion, and σ_* is the stellar velocity dispersion.

I use ATLAS-3D (Cappellari et al. 2011) results to get the stellar properties of NGC4526: $\sigma_* \approx 233.3$ km/s (at the central 1 kpc), $L \approx 3.13\times10^{10} L_{\odot,\mathrm{r}}$ (Cappellari et al. 2013a), stellar $M/L_{\mathrm{r}} \approx 5.6\ M_\odot/L_{\odot,\mathrm{r}}$ (Cappellari et al. 2013b), and $R_e \approx 74.1" \approx 5.9$ kpc (Krajnović et al. 2013). The quoted luminosity value is global, so the enclosed luminosity at R_e is simply half the quoted value, i.e. $L(R_e) \approx 1.57 \times 10^{10}\ L_\odot$. Thus, the stellar surface density can be estimated as $\Sigma_* \approx M(R_e)/\pi R_e^2 \approx 804\ M_\odot$ pc^{-2}.

H I is undetected in NGC4526 with an upper limit of $M_{\mathrm{HI}} < 1.9 \times 10^7\ M_\odot$ (Lucero & Young 2013). The physical resolution of their observations is 5.4×4.2 kpc^2. This gives an upper limit of the gas surface density as $\Sigma_g < 0.27\ M_\odot$ pc^{-2}. The value of σ_g is unknown, so I assume $\sigma_g = 10$ km s^{-1} (Blitz & Rosolowsky 2006).

Taken all together, we estimate the external pressure to be $P_h/k < 1.5 \times 10^6$ K cm^{-3}. Thus, unlike the Galactic center clouds, where $P_{\mathrm{ext}} \sim P_G$, NGC4526 clouds have $P_{\mathrm{ext}} < P_G$. This may cause the Galactic center clouds to be pressure bound, while clouds in NGC4526 to be gravitationally bound (since the external pressure is small with respect to the gravity). This small external pressure is presumably due to lack of H I in NGC4526, which may be caused by ram pressure or hot gas evaporation as the galaxy resides in the Virgo cluster.

2.6 Summary

I identify 241 GMCs based on ^{12}CO(2−1) observation at ≈ 20 pc resolution in the galaxy NGC4526 using the CPROPS program (RL06), where 103 of them are spatially resolved. As a population, the clouds are in gravitational equilibrium. A log-normal fit to the population yields a mean virial parameter $\alpha \approx 0.99$ with a standard deviation of ~ 0.14 dex.

The cloud mass distribution follows $\mathrm{d}N/\mathrm{d}M \propto M^{-2.39\pm0.03}$, steeper than that in the inner Milky Way but comparable to previous measurements in several nearby galaxies. Since the exponent is less than -2, the total molecular mass is dominated by the contribution of low mass clouds. The data favor a truncated-distribution with truncation mass of $4.12 \times 10^6 M_\odot$.

In general, clouds in NGC4526 are more luminous and more turbulent than equal-size clouds in the Milky Way disk by a factor of ~ 5 and ~ 3, respectively. Moreover, the surface density of GMCs in NGC4526 is ~ 7 times higher than those in the Milky Way disk. These differences may be due to higher ISRF and cloud extinction (A_V) in NGC4526, so that the CO emission emerges from a deeper layer in the cold gas, and hence, a higher gas density region.

On the other hand, NGC4526 clouds are less turbulent than the Galactic center clouds. This may be caused by different equilibrium state of GMCs: Galactic center clouds are pressure-bound, while clouds in NGC4526 are gravitationally bound. The velocity dispersion of the pressure-bound clouds needs to balance both gravity and the external pressure, while gravitationally bound clouds just need to balance gravity only. Indeed, our estimation shows that the external pressure in NGC4526 is smaller than the gravity, so that the external pressure is less important in the dynamical state of NGC4526 clouds. This situation is different in the Galactic center, where the external pressure is comparable or higher than the cloud self-gravity.

There is no size-linewidth correlation in NGC4526 in contrast to what is expected from Larson's relation. This finding is robust against the choice of the input parameters of the CPROPS program or different measurement methods (Section 2.11). This implies that the surface density of GMCs is not constant, but follows the relation $\sigma_v R^{-1/2} \propto \Sigma^{1/2}$ as expected from gravitational equilibrium.

In the kinematic analysis, I find that the velocity gradient of individual clouds are just a consequence of galactic rotation. In this case, if the clouds are rotating, then the rotation follows the galactic shear, which is the Oort A constant at the location of the cloud. I calculate Ω_{shear} and find that 92% of resolved clouds have a turbulent energy exceeding the rotational energy, and 96% of resolved clouds have a gravitational energy exceeding the rotational energy. This means that the rotational energy is a minor contribution to the clouds' dynamical stability.

Even with the inclusion of rotational energy, the cloud population is still in gravitational equilibrium. The distribution of the virial parameter can be approximated by a log-normal distribution with a tail at the high-end. The mean of the distribution is $\alpha \approx 1.26$ with a standard deviation of ~ 0.15 dex. There are only 4 clouds with $\alpha \gtrsim 3.5$. These clouds are the innermost clouds and undergo extreme galactic shear. These unbound clouds should be ripped apart in a timescale of less than ~ 1 Myr.

2.7 Appendix A. Cloud Identification Algorithm

I use the modified CLUMPFIND algorithm (Williams et al. 1994), implemented in the CPROPS program (Rosolowsky & Leroy 2006, hereafter RL06) to identify GMCs in NGC4526. Below are descriptions of the code, together with our chosen values of input parameters.

First, the program identifies connected regions of significant emission as *islands*. An island is defined as CO emission that has at least one pixel higher than $3\sigma_{\rm rms}$ (the threshold parameter of the program) and extends to all connected pixels with emission higher than $2\sigma_{\rm rms}$ (the edge parameter of the program). An island consists of one or more clouds after the decomposition process. I set the minimum volume of islands to be 1 beamwidth^2 $\times$ 1 velocity channel. I choose these values to include any possible small island in our data, since our resolution is somewhat comparable to the typical size of Milky Way GMCs.

The decomposition of each island begins by looking for local maxima. Local maxima are identified by looking for pixels that are greater than or equal to all neighbors in a 1 beamwidth^2 $\times$ 1 velocity channel volume. The choice of these values is to separate an island into potentially smaller clouds.

For each local maximum, working from the local maximum that has the lowest emission to the highest, the algorithm identifies pixels associated *exclusively* with each local maximum by contouring the data cube in three dimensions. If the emission of a local maximum is less than $n\sigma_{\rm rms}$ above the *merge level* with neighboring local maxima, or there are fewer than $m\times$beamwidth pixels associated with the local maxima, then the local maximum is removed from consideration. The merge level is the contour level that encloses two neighboring local maxima. The purpose of this decimation process is to remove spurious peaks of noise, i.e. false clouds. Higher values of n and m gives a smaller probability of false clouds, at the cost of losing small genuine clouds. We adopt $m = 0.5$ to account for small clouds and determine the best value of n from simulations (described in Section 2.8).

Then, the program decides whether two neighboring clouds are a merged cloud or distinct clouds. The algorithm compares the values of emission moments for the separated and combined clouds. If the flux F and moment σ of an individual cloud differ by more than a fraction of the flux and the moment of the merged cloud ($\delta F/F$ and $\delta\sigma/\sigma$), then the local maxima are categorized as distinct. The values of $\delta F/F$ and $\delta\sigma/\sigma$ are chosen from the simulations (Section 2.8).

At the end of the process, the program calculates the properties of the clouds (described in Section 2.3.1) and records them into a catalog (Section 2.10).

2.8 Appendix B. Decomposition Parameters

In order to choose the best decomposition parameters ($n, \delta F/F$, and $\delta\sigma/\sigma$) that are suitable for the data, I create two simulated clouds with a 3D-Gaussian shape in a single data cube, and add the typical noise of our observations. The dispersions of the Gaussian

are $\sigma_{\rm x} = \sigma_{\rm y} = 1$ beam width and $\sigma_v = 1$ velocity channel, so that they are resolved by the antenna beam and spectral channels. I vary the separation (center-to-center) of those gaussians in units of R, which is defined as $R = 2\sigma_{\rm x}$. Two Gaussians are almost fully resolved if they are separated by a distance larger than $2R$. I also vary the peak S/N of the Gaussians from $3\sigma_{\rm rms}$ to $6\sigma_{\rm rms}$, to take into account any possible dependence of our simulations on S/N. I run 10 simulations for each choice of separation distance and peak S/N, so that the results are statistically robust.

I feed the simulated data cubes into the CPROPS program and vary the three input parameters that drive the decomposition of the clouds (n, $\delta F/F$, and $\delta\sigma/\sigma$) from 0 to 3 with an increment of 0.5. The program then identifies the number of clouds in a given data cube. For various decomposition parameters and peak S/N, I plot the average number of clouds identified by the program against the separation distance in Figure 2.15. The program successfully resolves two clouds for a separation distance larger than $2R$. However, for blended Gaussians (separated by a distance shorter than $2R$), the values of $n = \delta F/F = \delta\sigma/\sigma = 1$ best recover the correct number of clouds at all S/N. Therefore, we adopt these values as the decomposition parameters for our data. In Section 2.11, I further show that the results of our studies are not sensitive to the choice of decomposition parameters.

2.9 Appendix C. Probability Analysis of Real Detections

In order to check the probability that the identified clouds are real, I do a probability analysis similar to that given in Engargiola et al. (2003). If we have n-adjacent channels with the same brightness temperature $T_{\rm b} = k\sigma_{\rm rms}$, then the probability of this being a false detection is $P_n(k) = [0.5 \times {\rm erfc}(k/\sqrt{2})]^n$, where erfc is the Gaussian complementary error function. The probability of real detection is $P_{\rm real} = 1 - N_{\rm trial}P_n(k)$ for $N_{\rm trial}P_n(k) \ll 1$. Here, $N_{\rm trial} = N/n$, where $N \approx 2.37 \times 10^7$ is the number of pixels in our data cube. If the pixels are not independent due to beam convolution and spectral smoothing, then the inferred $P_{\rm real}$ is smaller than the true $P_{\rm real}$. I set the edge parameter of the CPROPS program to be $2\sigma_{\rm rms}$, so that all pixels in a cloud must have $T_b \geq 2\sigma_{\rm rms}$. Hence, the probability that a cloud occupying n-adjacent channels is a real detection is $P_{\rm real} > 1 - N_{\rm trial}P_n(2\sigma_{\rm rms})$. In this case, $P_{\rm real} > 0.97$ for $n = 5$. The smallest identified cloud has total number of pixels $n = 13$. This suggests that it is unlikely that we detect false clouds, so we assume all identified GMCs are real structures.

2.10 Appendix D. Cloud Properties in NGC4526

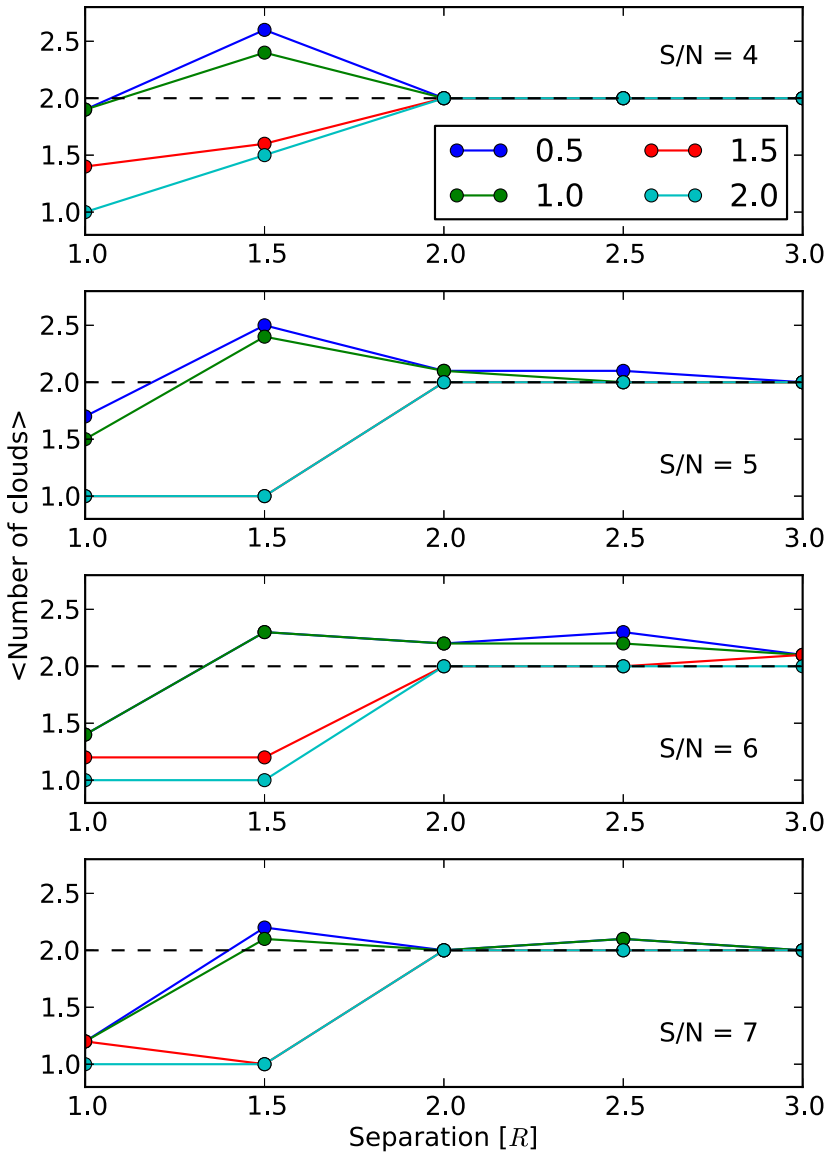

Figure 2.15: The average number of recovered clouds as a function of the separation (center-to-center) between two clouds. The separation distance is in units of $R = 2\sigma_{\rm x}$, where $\sigma_{\rm x}$ is the dispersion of the Gaussian clouds. Different panels show different peak S/N of the simulated clouds. In each panel, different values of the decomposition parameters (n, $\delta F/F$, and $\delta\sigma/\sigma$) are shown in different colors. The correct number of clouds is indicated by the dashed lines. The program recovers approximately two clouds for separations of at least $2R$. Unity input parameters approach the correct number of clouds even for blended clouds.

Table 2.2: Cloud Properties in NGC4526.

ID	RA(2000) [h:m:s]	Dec(2000) [° :′:″]	$V_{\rm LSR}$[a]	R[b] [pc]	δR[b] [pc]	σ_v[a]	$\delta\sigma_v$[a]	L[c]	δL[c]	$M_{\rm lum}$[d]	$\delta M_{\rm lum}$[d]	S/N	$T_{b,\rm max}$ [K]	$\Omega_{\rm shear}$[e]	d[f] [pc]
1	12:34:3.5	7:41:54.7	276.0	24.00	7.65	6.90	0.48	3.76	1.24	1.88	0.62	5.0	7.7	0.52	667
2	12:34:3.5	7:41:54.9	283.4	...	...	6.14	1.30	0.67	0.60	0.33	0.30	4.1	6.3	0.55	619
3	12:34:3.4	7:41:55.1	286.7	...	...	6.37	1.21	0.27	0.19	0.14	0.09	3.4	4.7	0.57	587
4	12:34:3.6	7:41:54.3	279.6	22.16	5.54	5.42	0.55	2.35	0.70	1.18	0.35	6.6	10.4	0.44	798
5	12:34:3.5	7:41:55.2	286.7	...	...	5.64	1.55	0.71	0.68	0.35	0.34	4.6	6.7	0.57	583
6	12:34:3.4	7:41:55.4	293.2	...	...	9.74	2.35	1.13	0.60	0.57	0.30	5.2	6.7	0.58	563
7	12:34:3.5	7:41:55.4	298.3	22.01	5.52	7.23	0.96	2.39	0.76	1.20	0.38	5.7	8.1	0.56	599
8	12:34:3.4	7:41:55.1	298.5	...	...	6.28	1.67	0.67	0.99	0.33	0.50	3.6	5.1	0.58	559
9	12:34:3.4	7:41:55.6	297.2	29.60	6.81	7.25	0.63	5.75	1.35	2.88	0.68	6.2	9.0	0.61	492
10	12:34:3.3	7:41:55.5	311.0	12.11	9.12	8.01	1.41	1.42	1.35	0.71	0.68	4.4	6.4	0.61	480
11	12:34:3.3	7:41:55.7	314.9	...	...	6.27	0.55	1.05	0.68	0.53	0.34	5.1	7.1	0.62	440
12	12:34:3.3	7:41:56.1	309.0	28.58	5.57	7.12	0.33	5.52	1.16	2.77	0.58	7.3	10.2	0.63	424
13	12:34:3.3	7:41:56.4	323.3	31.38	5.24	7.81	0.86	5.84	1.08	2.93	0.54	7.3	10.3	0.66	348
14	12:34:3.3	7:41:55.2	323.5	13.38	8.55	8.21	4.00	2.01	0.87	1.01	0.44	5.1	7.4	0.59	543
15	12:34:3.3	7:41:56.4	333.7	18.72	5.54	9.56	2.32	3.18	0.87	1.59	0.44	6.6	8.9	0.64	388
16	12:34:3.2	7:41:56.5	344.0	16.65	7.01	8.75	2.44	2.00	0.83	1.00	0.41	5.8	7.8	0.76	293
17	12:34:3.2	7:41:56.8	328.9	...	...	7.64	1.41	0.29	0.21	0.14	0.11	4.1	5.8	0.70	320
18	12:34:3.4	7:41:56.1	335.7	...	...	7.39	3.21	0.80	0.91	0.40	0.46	4.4	6.0	0.60	499
19	12:34:3.3	7:41:56.2	330.3	10.48	7.41	8.53	1.50	1.47	0.64	0.74	0.32	5.5	7.9	0.66	360
20	12:34:3.2	7:41:56.3	337.5	7.57	11.12	6.44	1.74	0.96	0.97	0.48	0.49	3.9	5.9	0.68	336
21	12:34:3.3	7:41:56.5	342.7	...	...	6.97	1.17	0.44	0.58	0.22	0.29	4.2	5.7	0.62	460
22	12:34:3.4	7:41:54.9	352.1	...	...	6.83	2.66	0.40	0.62	0.20	0.31	3.5	4.8	0.56	607
23	12:34:3.3	7:41:55.4	337.7	...	...	6.99	1.59	0.94	0.95	0.47	0.48	4.1	5.8	0.60	503
24	12:34:3.2	7:41:56.8	342.7	27.14	5.62	9.20	1.74	3.30	1.20	1.66	0.60	6.3	8.3	0.92	253
25	12:34:3.1	7:41:56.9	357.4	...	...	9.35	3.95	1.68	1.36	0.84	0.68	3.7	5.1	1.20	209
26	12:34:3.3	7:41:55.8	348.6	11.03	8.67	11.29	2.22	2.54	1.17	1.27	0.59	5.8	7.5	0.63	424
27	12:34:3.3	7:41:56.6	360.3	...	...	7.04	2.61	1.25	0.56	0.62	0.28	5.7	8.0	0.66	360
28	12:34:3.3	7:41:56.7	363.0	...	...	4.63	0.96	0.56	0.49	0.28	0.24	4.6	6.2	0.64	396
29	12:34:3.2	7:41:56.9	359.7	...	...	6.70	0.94	1.04	0.71	0.52	0.36	5.7	7.8	0.73	304
30	12:34:3.3	7:41:55.4	377.4	...	...	9.27	1.86	1.66	0.85	0.83	0.43	5.1	7.1	0.59	519
31	12:34:3.2	7:41:56.0	374.0	...	...	7.31	1.52	0.98	0.57	0.49	0.29	5.3	6.9	0.64	392
32	12:34:3.2	7:41:56.2	371.9	...	...	6.60	1.49	0.98	0.52	0.49	0.26	5.3	6.5	0.66	348

Continued on Next Page

ID	RA(2000) [h:m:s]	Dec(2000) [° ′ ″]	$V_{\rm LSR}$[a]	R[b] [pc]	δR[b] [pc]	σ_v[a]	$\delta\sigma_v$[a]	L[c]	δL[c]	$M_{\rm lum}$[d]	$\delta M_{\rm lum}$[d]	S/N	$T_{b,\rm max}$ [K]	$\Omega_{\rm shear}$[e]	d[f] [pc]
33	12:34:3.3	7:41:56.7	368.6	...	...	9.87	1.65	1.46	0.78	0.73	0.39	5.7	7.2	0.63	436
34	12:34:3.3	7:41:57.0	376.4	...	...	5.89	1.97	0.49	0.34	0.25	0.17	5.0	6.5	0.64	404
35	12:34:3.3	7:41:57.0	386.6	...	...	7.40	3.93	0.67	0.75	0.34	0.38	4.8	6.2	0.65	368
36	12:34:3.2	7:41:55.6	400.0	14.17	7.71	8.71	1.98	1.74	1.07	0.87	0.54	4.7	6.0	0.61	480
37	12:34:3.2	7:41:56.0	400.0	...	...	6.96	0.62	1.39	0.70	0.70	0.35	4.9	6.3	0.64	408
38	12:34:3.3	7:41:56.9	404.7	...	...	6.04	0.59	0.27	0.35	0.13	0.18	3.0	3.7	0.62	440
39	12:34:3.3	7:41:57.2	404.8	5.09	3.84	8.64	4.37	1.16	0.74	0.58	0.37	5.1	6.7	0.64	404
40	12:34:3.2	7:41:55.3	411.9	14.23	10.60	7.97	0.79	2.07	0.96	1.04	0.48	4.7	6.6	0.57	575
41	12:34:3.2	7:41:57.3	416.2	...	...	9.15	3.55	0.71	0.59	0.36	0.30	4.2	5.4	0.82	277
42	12:34:3.2	7:41:57.5	408.4	...	...	5.60	0.96	0.35	0.45	0.17	0.22	4.3	5.8	0.66	360
43	12:34:3.3	7:41:57.2	422.6	...	...	8.34	1.77	1.14	0.63	0.57	0.31	5.3	7.0	0.62	456
44	12:34:3.2	7:41:56.1	438.3	3.97	2.32	11.13	4.84	2.12	0.92	1.06	0.46	5.0	6.1	0.63	412
45	12:34:3.3	7:41:57.3	428.0	...	...	5.37	1.45	0.60	0.44	0.30	0.22	5.0	6.6	0.63	420
46	12:34:3.2	7:41:57.3	423.9	...	...	7.09	1.37	0.66	0.52	0.33	0.26	4.7	5.7	0.66	360
47	12:34:3.2	7:41:55.3	433.5	...	...	6.93	1.47	0.46	0.57	0.23	0.29	4.0	5.3	0.57	579
48	12:34:3.1	7:41:56.3	446.1	...	...	7.98	0.67	0.86	0.61	0.43	0.31	4.6	6.2	0.65	364
49	12:34:3.2	7:41:57.5	438.9	20.86	12.06	7.54	1.05	1.01	1.02	0.51	0.51	4.0	5.7	0.66	352
50	12:34:3.2	7:41:55.3	437.0	...	...	10.45	2.06	0.69	0.55	0.34	0.28	4.5	6.1	0.56	603
51	12:34:3.2	7:41:55.6	438.3	15.56	9.04	8.15	2.90	2.15	0.89	1.08	0.45	5.1	6.7	0.60	515
52	12:34:3.2	7:41:55.9	442.2	...	...	7.34	1.62	1.44	1.15	0.72	0.58	4.3	5.8	0.62	444
53	12:34:3.3	7:41:57.5	440.2	...	...	8.27	2.93	1.27	0.64	0.64	0.32	4.8	6.3	0.62	440
54	12:34:3.2	7:41:57.9	455.8	...	...	6.33	1.05	0.36	0.25	0.18	0.12	5.0	6.1	0.62	448
55	12:34:3.2	7:41:57.7	464.0	...	...	7.43	2.37	1.15	1.04	0.58	0.52	4.0	5.8	0.63	420
56	12:34:3.2	7:41:57.8	474.1	...	...	5.25	0.78	0.34	0.32	0.17	0.16	3.8	5.4	0.61	472
57	12:34:3.2	7:41:57.8	476.2	24.20	7.91	5.24	0.58	1.58	0.44	0.79	0.22	7.0	8.7	0.64	400
58	12:34:3.2	7:41:55.7	472.9	...	...	10.15	1.91	1.72	0.74	0.86	0.37	5.4	6.5	0.59	523
59	12:34:3.2	7:41:57.9	488.1	...	...	7.20	0.98	1.28	0.44	0.64	0.22	5.6	7.4	0.66	356
60	12:34:3.2	7:41:57.8	498.4	...	...	7.58	2.44	0.72	0.71	0.36	0.36	4.2	5.2	0.66	356
61	12:34:3.1	7:41:57.9	498.2	13.06	6.82	8.14	1.46	1.69	0.65	0.85	0.33	6.1	7.8	0.69	328
62	12:34:3.2	7:41:58.2	501.4	16.35	4.45	8.69	1.53	3.71	0.78	1.86	0.39	6.3	8.4	0.59	539
63	12:34:3.1	7:41:57.9	504.9	...	...	8.43	3.32	1.41	0.81	0.71	0.40	4.6	6.1	0.88	261
64	12:34:3.1	7:41:58.2	522.1	...	...	8.34	2.78	1.62	1.04	0.81	0.52	4.3	6.2	0.64	404
65	12:34:3.2	7:41:58.2	516.4	4.81	4.63	7.68	2.81	1.23	0.66	0.62	0.33	4.9	6.2	0.62	456
66	12:34:3.1	7:41:58.2	548.1	...	...	7.15	2.14	1.15	0.76	0.58	0.38	5.3	6.8	1.13	217

Continued on Next Page

ID	RA(2000) [h:m:s]	Dec(2000) [° ′ ″]	$V_{\rm LSR}$[a]	R[b] [pc]	δR[b] [pc]	σ_v[a]	$\delta\sigma_v$[a]	L[c]	δL[c]	$M_{\rm lum}$[d]	$\delta M_{\rm lum}$[d]	S/N	$T_{b,\rm max}$ [K]	$\Omega_{\rm shear}$[e]	d[f] [pc]
67	12:34:3.1	7:41:58.2	535.8	...	...	9.10	3.12	1.29	0.90	0.65	0.45	4.7	6.6	0.70	320
68	12:34:3.1	7:41:58.4	547.7	13.11	7.85	5.32	0.62	0.75	0.62	0.38	0.31	5.5	7.5	0.63	412
69	12:34:3.0	7:41:58.2	567.1	...	...	6.12	0.60	0.98	0.58	0.49	0.29	5.1	7.0	1.69	161
70	12:34:3.1	7:41:58.4	567.1	...	...	8.23	3.55	1.08	0.99	0.54	0.49	4.8	6.2	0.64	392
71	12:34:3.1	7:41:58.6	568.7	30.45	6.64	8.86	0.78	4.73	1.29	2.37	0.65	6.9	9.2	0.64	408
72	12:34:3.1	7:41:58.7	589.2	20.85	8.53	6.85	0.70	2.53	1.02	1.27	0.51	5.3	6.8	0.66	360
73	12:34:3.0	7:41:58.8	617.6	28.75	5.81	8.78	1.47	4.44	1.12	2.23	0.56	6.7	8.5	0.66	352
74	12:34:3.0	7:41:59.0	652.1	35.57	7.76	7.39	0.40	3.66	0.85	1.83	0.43	6.2	7.6	0.65	376
75	12:34:3.0	7:41:59.1	678.3	24.23	7.49	6.09	1.00	2.12	0.54	1.06	0.27	6.1	7.4	0.67	344
76	12:34:3.0	7:41:59.4	699.7	...	...	7.99	2.38	1.39	0.50	0.70	0.25	5.7	6.9	0.63	428
77	12:34:3.0	7:41:59.0	702.8	...	...	8.86	2.71	1.13	0.56	0.57	0.28	4.9	5.9	0.79	285
78	12:34:3.5	7:41:54.2	296.4	...	...	8.41	2.25	1.10	1.47	0.55	0.74	3.7	5.6	0.47	754
79	12:34:3.4	7:41:56.1	346.0	13.69	10.37	8.77	0.88	2.08	0.63	1.04	0.32	5.9	7.7	0.59	539
80	12:34:3.1	7:41:44.3	345.5	...	...	7.09	4.23	0.84	1.03	0.42	0.52	4.1	7.4	...	...
81	12:34:3.0	7:41:57.8	389.1	15.94	9.44	9.78	2.32	1.37	0.74	0.68	0.37	5.1	6.3	10.19	34
82	12:34:3.0	7:41:57.9	484.1	11.91	3.70	27.46	14.38	2.99	0.74	1.50	0.37	5.7	6.1	66.09	10
83	12:34:3.0	7:41:57.6	392.4	7.15	10.14	21.37	4.32	3.68	1.40	1.84	0.70	5.6	7.2	4.81	62
84	12:34:3.0	7:41:57.9	436.5	...	...	6.56	1.84	0.17	0.09	0.09	0.05	3.3	3.8	4.81	62
85	12:34:3.3	7:41:55.1	384.7	...	...	8.00	0.52	1.67	1.31	0.83	0.66	4.3	5.8	0.56	591
86	12:34:3.6	7:41:55.9	359.0	...	...	7.10	0.87	0.96	0.52	0.48	0.26	6.2	9.4	0.43	826
87	12:34:3.4	7:41:56.6	370.8	...	...	8.82	2.25	2.30	1.04	1.15	0.52	4.6	6.3	0.59	539
88	12:34:3.4	7:41:56.9	391.8	...	...	8.42	3.17	1.44	0.66	0.72	0.33	5.2	7.1	0.59	531
89	12:34:3.1	7:41:57.4	407.0	7.40	8.05	9.74	3.26	0.97	0.99	0.48	0.49	4.1	5.1	1.23	205
90	12:34:3.3	7:41:57.4	442.5	...	...	6.88	1.14	0.76	0.57	0.38	0.29	5.2	6.6	0.56	591
91	12:34:3.3	7:41:57.8	468.4	22.44	7.70	8.84	0.95	2.93	2.14	1.47	1.07	4.4	5.8	0.49	718
92	12:34:3.3	7:41:57.8	468.7	...	...	7.08	0.54	1.31	0.67	0.65	0.33	5.3	6.9	0.57	579
93	12:34:3.1	7:41:55.9	496.9	15.65	9.28	8.13	1.88	1.72	0.93	0.86	0.47	4.6	5.7	0.60	511
94	12:34:3.1	7:41:56.3	518.7	28.93	4.80	8.60	4.43	6.95	1.21	3.49	0.61	6.3	8.1	0.63	428
95	12:34:3.1	7:41:56.0	548.1	...	...	5.43	0.73	0.63	0.49	0.32	0.25	4.9	5.9	0.57	583
96	12:34:3.0	7:41:56.5	549.6	...	...	6.03	0.60	1.04	0.51	0.52	0.26	6.4	8.2	0.63	424
97	12:34:3.0	7:41:56.2	556.5	...	...	6.03	0.84	0.35	0.35	0.18	0.17	3.9	4.9	0.59	531
98	12:34:3.1	7:41:56.3	558.3	...	...	5.68	1.08	0.86	0.50	0.43	0.25	5.6	7.0	0.61	468
99	12:34:3.0	7:41:56.7	565.6	...	...	8.60	4.28	1.83	0.99	0.92	0.49	5.5	6.8	0.64	396
100	12:34:3.0	7:41:56.6	574.9	...	...	7.91	1.12	1.07	0.55	0.54	0.28	6.2	8.3	0.62	456

Continued on Next Page

ID	RA(2000) [h:m:s]	Dec(2000) [° ′:″]	$V_{\rm LSR}$[a]	R[b] [pc]	δR[b] [pc]	σ_v[a]	$\delta\sigma_v$[a]	L[c]	δL[c]	$M_{\rm lum}$[d]	$\delta M_{\rm lum}$[d]	S/N	$T_{b,\rm max}$ [K]	$\Omega_{\rm shear}$[e]	d[f] [pc]
101	12:34:3.0	7:41:56.5	592.2	10.40	3.50	10.11	1.75	2.49	1.02	1.25	0.51	6.0	7.3	0.59	519
102	12:34:3.0	7:41:56.9	599.4	10.79	6.53	9.90	3.39	2.01	0.63	1.01	0.32	5.4	6.8	0.66	356
103	12:34:3.0	7:41:57.2	605.8	10.31	5.76	9.77	4.31	1.90	1.37	0.95	0.69	4.2	5.1	0.94	249
104	12:34:3.0	7:41:56.8	613.0	26.63	3.83	9.40	1.87	5.18	1.04	2.60	0.52	6.7	8.5	0.62	448
105	12:34:2.9	7:41:57.0	642.6	25.11	5.50	9.09	2.51	4.05	1.37	2.03	0.69	6.0	7.6	0.62	456
106	12:34:3.0	7:41:57.4	654.7	...	...	6.55	1.08	0.44	0.40	0.22	0.20	4.7	5.6	0.96	245
107	12:34:2.9	7:41:57.4	673.8	26.71	5.72	10.96	2.79	5.79	1.61	2.90	0.81	6.6	8.6	0.66	356
108	12:34:2.9	7:41:57.3	683.5	...	...	6.56	1.34	1.74	0.77	0.87	0.38	6.5	7.6	0.61	484
109	12:34:2.9	7:41:57.1	673.4	8.33	2.62	10.66	2.05	3.05	1.24	1.53	0.62	5.2	6.4	0.57	567
110	12:34:2.8	7:41:57.3	705.3	22.08	5.45	7.44	1.12	2.72	0.73	1.36	0.37	6.0	7.4	0.56	595
111	12:34:2.9	7:41:57.5	711.4	...	...	7.59	0.91	1.14	0.50	0.57	0.25	5.9	7.3	0.64	404
112	12:34:2.9	7:41:57.6	717.5	18.00	6.26	9.70	3.46	2.48	0.76	1.24	0.38	6.0	7.4	0.63	432
113	12:34:2.8	7:41:57.6	717.4	...	...	8.30	3.24	1.44	0.76	0.72	0.38	5.2	6.5	0.61	488
114	12:34:2.8	7:41:57.5	729.4	9.40	3.84	8.13	2.19	1.71	0.98	0.86	0.49	4.9	6.3	0.57	571
115	12:34:2.9	7:41:57.6	721.6	13.95	4.78	7.58	2.94	1.67	0.65	0.84	0.32	5.1	6.7	0.68	336
116	12:34:2.9	7:41:57.7	731.1	...	...	7.25	3.98	0.50	0.97	0.25	0.49	3.5	4.4	0.96	245
117	12:34:2.7	7:41:57.6	737.9	...	...	9.56	2.18	0.59	0.43	0.30	0.21	4.7	5.6	0.48	738
118	12:34:2.8	7:41:57.8	743.2	11.97	5.05	6.04	2.11	1.64	0.48	0.82	0.24	6.9	8.2	0.63	420
119	12:34:2.7	7:41:57.9	755.7	24.62	5.32	9.74	0.96	4.23	1.38	2.12	0.69	5.4	6.8	0.57	583
120	12:34:2.8	7:41:57.6	749.7	...	...	6.44	1.06	1.11	0.68	0.55	0.34	4.9	6.0	0.56	603
121	12:34:2.9	7:41:57.8	757.6	...	...	10.86	3.25	0.56	0.63	0.28	0.31	4.3	5.2	0.79	285
122	12:34:2.9	7:41:57.9	757.3	12.94	5.20	7.37	2.13	1.59	0.82	0.80	0.41	5.8	7.0	0.69	328
123	12:34:2.8	7:41:58.2	756.2	...	...	7.14	1.85	0.21	0.33	0.10	0.17	3.3	4.0	0.70	320
124	12:34:2.8	7:41:58.0	770.7	28.88	4.07	12.26	1.55	7.41	1.21	3.71	0.61	6.5	8.0	0.64	408
125	12:34:2.7	7:41:58.2	785.6	...	...	7.83	0.76	1.31	0.82	0.66	0.41	4.5	6.1	0.56	607
126	12:34:2.7	7:41:58.1	774.9	5.42	5.87	7.71	1.60	1.24	0.63	0.62	0.32	5.5	7.1	0.59	539
127	12:34:2.6	7:41:58.2	782.1	...	...	6.50	1.43	0.90	0.91	0.45	0.46	4.0	5.3	0.50	710
128	12:34:2.8	7:42:00.0	799.8	16.60	7.01	12.89	2.88	2.46	1.57	1.23	0.79	5.1	6.4	0.62	464
129	12:34:2.7	7:41:58.4	803.9	...	...	8.69	2.65	0.70	0.47	0.35	0.24	5.3	6.4	0.56	607
130	12:34:2.6	7:41:58.4	803.3	...	...	7.81	3.07	0.92	0.72	0.46	0.36	4.3	5.6	0.52	679
131	12:34:2.8	7:42: 0.2	803.6	...	...	4.90	1.08	0.25	0.23	0.12	0.11	4.4	5.8	0.60	515
132	12:34:2.8	7:41:58.3	810.8	18.09	6.67	7.96	2.62	2.59	1.12	1.30	0.56	5.3	6.6	0.62	448
133	12:34:2.8	7:41:58.3	812.2	...	...	10.30	2.52	1.97	0.59	0.99	0.30	6.6	8.4	0.64	400
134	12:34:2.8	7:41:59.7	799.4	11.33	9.72	9.43	1.69	1.08	0.94	0.54	0.47	4.5	5.8	0.64	400

Continued on Next Page

ID	RA(2000) [h:m:s]	Dec(2000) [° ′ ″]	$V_{\rm LSR}$[a]	R[b] [pc]	δR[b] [pc]	σ_v[a]	$\delta\sigma_v$[a]	L[c]	δL[c]	$M_{\rm lum}$[d]	$\delta M_{\rm lum}$[d]	S/N	$T_{b,\rm max}$ [K]	$\Omega_{\rm shear}$[e]	d[f] [pc]
135	12:34:2.7	7:41:58.4	816.1	...	...	12.39	4.63	1.89	0.64	0.95	0.32	5.6	7.6	0.53	655
136	12:34:2.7	7:41:58.5	828.6	...	...	10.37	1.98	1.10	0.52	0.55	0.26	5.7	7.0	0.58	555
137	12:34:2.8	7:41:59.9	831.1	16.56	7.45	8.09	1.68	1.82	0.59	0.91	0.29	7.1	8.5	0.64	408
138	12:34:2.8	7:42: 0.1	835.0	...	...	9.00	2.63	1.47	0.56	0.74	0.28	6.3	7.7	0.62	456
139	12:34:2.8	7:41:58.5	834.4	...	...	8.29	2.71	0.66	0.38	0.33	0.19	5.7	6.5	0.67	344
140	12:34:2.7	7:41:58.6	842.4	17.28	5.50	7.78	2.63	3.29	1.32	1.65	0.66	5.1	6.5	0.63	416
141	12:34:2.6	7:41:58.8	845.7	...	...	11.55	5.14	1.04	0.75	0.52	0.38	4.5	5.8	0.55	627
142	12:34:2.8	7:41:59.8	850.0	22.62	9.21	8.24	0.38	2.60	0.97	1.30	0.49	5.5	7.0	0.65	368
143	12:34:2.6	7:41:58.7	851.1	7.72	3.50	8.82	3.03	2.03	0.76	1.02	0.38	5.7	7.8	0.55	611
144	12:34:2.7	7:41:58.9	871.0	28.91	6.62	12.68	3.94	3.88	0.82	1.94	0.41	6.9	8.5	0.62	452
145	12:34:2.8	7:42: 0.0	863.8	15.13	7.22	6.99	2.34	1.56	0.66	0.78	0.33	5.3	6.9	0.63	416
146	12:34:2.7	7:42: 0.5	866.1	9.13	8.19	7.07	0.81	0.52	0.42	0.26	0.21	4.3	5.2	0.59	531
147	12:34:2.8	7:41:58.6	871.9	...	...	7.31	1.67	0.66	0.55	0.33	0.27	4.0	5.2	0.65	376
148	12:34:2.7	7:41:58.8	870.3	14.80	4.46	9.67	1.90	2.71	0.78	1.36	0.39	6.3	8.1	0.64	404
149	12:34:2.8	7:42: 0.2	867.2	...	...	8.71	2.66	0.44	0.60	0.22	0.30	3.6	5.1	0.62	460
150	12:34:2.7	7:42: 0.8	871.1	...	...	6.67	2.46	0.41	0.44	0.21	0.22	4.5	5.4	0.57	583
151	12:34:2.6	7:41:59.0	875.8	...	...	3.79	0.44	0.25	0.28	0.12	0.14	4.0	5.2	0.57	587
152	12:34:2.7	7:41:59.0	881.8	...	...	4.73	1.29	0.99	0.48	0.50	0.24	5.1	6.8	0.61	472
153	12:34:2.6	7:41:59.2	879.2	...	...	8.35	1.44	0.44	0.60	0.22	0.30	3.7	4.7	0.58	555
154	12:34:2.7	7:42: 0.8	891.3	...	...	5.41	2.36	0.45	0.47	0.22	0.23	4.8	6.2	0.57	571
155	12:34:2.6	7:41:59.0	886.5	...	...	6.17	1.11	0.50	0.52	0.25	0.26	4.2	5.9	0.59	531
156	12:34:2.7	7:42: 0.3	888.9	20.54	4.93	8.82	1.80	3.35	0.95	1.68	0.48	6.0	7.7	0.62	464
157	12:34:2.8	7:41:59.0	894.6	...	...	7.56	1.82	0.90	0.52	0.45	0.26	5.2	5.9	0.72	308
158	12:34:2.8	7:41:59.7	895.4	11.65	12.02	8.20	3.36	1.45	1.46	0.73	0.73	4.3	5.2	0.67	340
159	12:34:2.7	7:41:59.8	894.5	11.16	11.39	6.74	1.41	0.72	0.49	0.36	0.24	4.8	6.0	0.65	372
160	12:34:2.7	7:42: 0.5	901.1	20.31	6.84	8.28	1.51	2.05	1.18	1.03	0.59	4.8	6.4	0.60	511
161	12:34:2.7	7:41:59.0	899.7	14.47	5.63	7.90	1.29	2.11	0.75	1.06	0.37	5.9	7.5	0.66	356
162	12:34:2.6	7:41:59.2	913.7	...	...	6.01	1.08	0.60	0.85	0.30	0.43	3.4	4.6	0.59	535
163	12:34:2.7	7:41:59.3	911.3	32.19	8.85	8.34	0.65	4.82	1.26	2.42	0.63	6.8	8.6	0.64	396
164	12:34:2.7	7:41:59.4	908.7	12.07	6.58	6.88	0.89	1.46	0.66	0.73	0.33	5.7	7.4	0.69	328
165	12:34:2.7	7:41:59.8	914.9	19.38	7.56	9.04	2.19	2.91	0.78	1.46	0.39	6.2	7.7	0.65	376
166	12:34:2.7	7:42: 0.1	915.2	17.13	5.09	9.07	2.33	2.22	1.15	1.11	0.58	5.5	7.2	0.63	432
167	12:34:2.7	7:41:59.6	921.5	...	...	6.62	0.84	0.57	0.40	0.28	0.20	5.0	6.4	0.66	348
168	12:34:2.8	7:41:59.6	916.7	...	...	5.80	1.28	0.69	0.44	0.34	0.22	5.6	7.0	0.68	332

Continued on Next Page

ID	RA(2000) [h:m:s]	Dec(2000) [° :′:″]	$V_{\rm LSR}$[a]	R[b] [pc]	δR[b] [pc]	σ_v[a]	$\delta\sigma_v$[a]	L[c]	δL[c]	$M_{\rm lum}$[d]	$\delta M_{\rm lum}$[d]	S/N	$T_{b,\rm max}$ [K]	$\Omega_{\rm shear}$[e]	d[f] [pc]
169	12:34:2.7	7:41:59.6	926.0	34.21	5.34	8.10	1.94	7.55	1.40	3.78	0.70	7.4	9.9	0.62	452
170	12:34:2.6	7:41:59.9	942.1	11.31	7.66	5.52	0.88	0.81	0.49	0.41	0.24	4.7	6.3	0.59	519
171	12:34:2.6	7:42: 0.2	935.2	40.49	4.13	8.27	1.17	11.74	1.50	5.88	0.75	7.5	10.0	0.62	464
172	12:34:2.6	7:42: 0.3	949.6	...	...	7.86	0.78	0.95	0.45	0.48	0.23	5.9	7.7	0.60	515
173	12:34:3.3	7:41:58.1	491.8	...	...	8.44	2.06	1.11	0.63	0.56	0.31	5.4	7.5	0.51	691
174	12:34:3.1	7:41:55.4	517.5	18.22	13.15	6.92	0.70	1.40	0.83	0.70	0.41	4.8	6.4	0.51	695
175	12:34:3.2	7:41:58.8	543.8	...	...	7.19	2.58	0.64	0.69	0.32	0.34	4.0	5.4	0.56	607
176	12:34:3.1	7:41:58.8	551.0	...	...	6.16	1.33	0.46	0.55	0.23	0.28	4.1	5.5	0.57	575
177	12:34:3.2	7:41:59.1	558.7	12.82	8.86	6.72	1.45	1.47	0.52	0.74	0.26	5.6	7.5	0.47	746
178	12:34:3.1	7:41:59.1	561.3	11.30	9.40	8.44	2.68	0.91	0.67	0.46	0.34	4.3	5.4	0.52	683
179	12:34:3.2	7:41:59.1	572.5	...	...	6.48	1.06	0.24	0.16	0.12	0.08	3.5	4.3	0.44	806
180	12:34:3.1	7:41:59.3	585.0	...	...	6.55	1.30	0.75	0.54	0.38	0.27	4.9	6.2	0.49	722
181	12:34:3.2	7:41:59.3	579.8	...	...	8.60	1.64	0.39	0.63	0.19	0.32	4.4	5.3	0.46	770
182	12:34:3.0	7:41:55.8	583.1	15.26	8.12	7.36	0.34	2.50	1.45	1.26	0.73	4.6	5.9	0.47	762
183	12:34:3.1	7:41:59.3	596.2	...	...	6.64	0.68	0.72	0.44	0.36	0.22	5.3	6.6	0.52	671
184	12:34:3.1	7:41:59.7	622.2	20.90	7.48	5.85	0.57	1.22	0.41	0.61	0.20	6.7	8.5	0.48	734
185	12:34:2.9	7:41:56.5	629.4	...	...	7.89	1.88	0.71	0.90	0.36	0.45	3.6	4.6	0.52	667
186	12:34:2.8	7:41:56.7	644.8	...	...	8.11	1.11	1.01	0.59	0.51	0.30	5.4	6.8	0.48	738
187	12:34:3.0	7:42: 0.2	647.3	19.80	8.51	6.65	0.53	1.65	0.83	0.83	0.42	5.2	6.4	0.41	874
188	12:34:3.0	7:42:00.0	651.0	24.78	14.45	6.14	0.40	1.59	0.85	0.80	0.43	5.2	6.3	0.48	730
189	12:34:3.0	7:42: 0.2	668.3	...	...	8.92	1.81	0.88	0.52	0.44	0.26	5.2	6.2	0.47	754
190	12:34:3.0	7:41:57.9	712.0	...	...	27.31	2.41	1.51	0.48	0.76	0.24	5.9	6.1	19.65	22
191	12:34:2.8	7:41:57.2	699.4	...	...	9.09	1.70	1.05	0.71	0.53	0.35	4.6	5.5	0.48	730
192	12:34:2.9	7:42: 0.7	695.8	...	...	8.29	2.82	1.17	0.71	0.59	0.36	5.0	6.3	0.44	810
193	12:34:2.9	7:42: 0.4	708.5	...	...	7.87	1.18	0.70	0.67	0.35	0.34	4.6	5.6	0.48	730
194	12:34:2.9	7:42: 0.4	714.7	...	...	5.80	0.98	0.79	0.30	0.39	0.15	6.5	7.6	0.52	679
195	12:34:2.9	7:42: 0.6	725.9	11.81	12.80	5.47	0.66	1.07	0.63	0.54	0.32	4.6	5.8	0.48	730
196	12:34:2.9	7:42: 0.8	713.9	...	...	6.09	1.28	0.49	0.58	0.24	0.29	4.1	5.4	0.43	830
197	12:34:2.9	7:42: 0.4	733.0	...	...	6.62	1.15	1.16	0.94	0.58	0.47	4.6	6.0	0.54	639
198	12:34:2.9	7:42: 0.8	736.9	...	...	6.07	1.12	0.70	0.49	0.35	0.25	4.4	5.3	0.46	778
199	12:34:2.9	7:41:59.1	724.5	...	...	7.30	2.03	0.75	0.42	0.37	0.21	6.1	7.5	0.78	289
200	12:34:2.9	7:41:59.4	729.9	10.79	4.11	8.76	1.58	2.62	0.61	1.31	0.31	6.9	9.0	0.64	388
201	12:34:2.9	7:41:59.7	765.2	19.48	5.53	8.39	3.20	2.82	0.69	1.41	0.35	6.2	7.9	0.63	412
202	12:34:2.8	7:42: 1.2	775.6	24.42	7.13	7.82	0.30	2.56	0.99	1.28	0.50	5.1	6.4	0.44	798

Continued on Next Page

ID	RA(2000) [h:m:s]	Dec(2000) [° :′:″]	$V_{\rm LSR}$[a]	R[b] [pc]	δR[b] [pc]	σ_v[a]	$\delta\sigma_v$[a]	L[c]	δL[c]	$M_{\rm lum}$[d]	$\delta M_{\rm lum}$[d]	S/N	$T_{b,\rm max}$ [K]	$\Omega_{\rm shear}$[e]	d[f] [pc]
203	12:34:2.9	7:41:59.3	762.9	...	...	8.30	2.06	1.40	0.88	0.70	0.44	4.8	6.2	0.71	316
204	12:34:2.7	7:41:58.0	784.3	...	...	7.02	1.95	0.88	0.40	0.44	0.20	5.1	6.3	0.53	663
205	12:34:2.9	7:41:58.2	800.7	3.81	7.43	9.79	1.45	1.62	0.54	0.81	0.27	6.0	7.0	1.17	213
206	12:34:2.7	7:42: 1.4	788.7	...	...	5.36	2.14	0.80	0.44	0.40	0.22	4.9	6.8	0.48	734
207	12:34:3.0	7:41:58.1	842.5	18.73	6.50	13.69	2.56	2.84	1.05	1.42	0.52	6.2	7.0	7.28	42
208	12:34:2.9	7:41:58.0	884.5	...	...	5.56	0.72	0.20	0.32	0.10	0.16	3.5	4.8	2.62	105
209	12:34:3.0	7:41:58.2	881.1	11.94	9.34	12.73	4.74	1.44	0.82	0.72	0.41	5.6	6.3	5.50	54
210	12:34:2.7	7:42: 1.4	820.1	8.32	10.36	8.48	4.38	1.78	0.94	0.89	0.47	5.1	6.5	0.46	766
211	12:34:2.6	7:41:58.9	858.2	...	...	9.75	2.83	0.90	0.77	0.45	0.39	4.5	5.4	0.53	659
212	12:34:2.8	7:41:58.7	864.0	...	...	6.62	1.52	0.55	0.83	0.28	0.42	4.1	4.9	0.78	289
213	12:34:2.8	7:41:58.7	888.1	5.87	3.52	10.37	2.64	1.79	0.59	0.90	0.30	5.6	6.7	1.30	197
214	12:34:2.8	7:41:58.7	889.1	...	...	6.27	3.09	0.48	0.36	0.24	0.18	4.5	5.6	0.86	265
215	12:34:2.8	7:41:58.9	897.1	...	...	8.42	1.13	0.53	0.46	0.27	0.23	4.5	5.3	0.83	273
216	12:34:2.8	7:41:59.1	887.1	...	...	7.63	1.70	1.96	0.74	0.98	0.37	6.0	7.1	1.08	225
217	12:34:2.8	7:41:58.9	903.5	22.42	5.85	8.29	2.69	2.62	0.79	1.31	0.40	6.2	7.6	1.11	221
218	12:34:2.8	7:41:59.2	902.6	...	...	6.78	1.30	1.34	0.95	0.67	0.47	5.1	6.7	0.85	269
219	12:34:2.8	7:41:59.3	909.2	...	...	7.47	1.20	0.55	0.61	0.28	0.30	4.5	5.7	0.79	285
220	12:34:2.5	7:41:59.2	855.4	...	...	7.49	1.01	1.75	0.97	0.88	0.49	5.2	6.9	0.49	718
221	12:34:2.5	7:41:59.4	867.6	...	...	7.89	2.13	0.70	0.49	0.35	0.25	4.9	6.2	0.51	698
222	12:34:2.5	7:41:59.4	875.8	...	...	9.80	2.99	1.03	0.65	0.52	0.33	4.9	6.5	0.51	691
223	12:34:2.6	7:41:59.2	886.5	15.45	5.42	6.79	1.20	2.05	0.79	1.03	0.39	6.3	8.6	0.52	679
224	12:34:2.6	7:41:59.0	904.9	...	...	4.90	0.57	0.23	0.34	0.12	0.17	4.0	5.3	0.52	667
225	12:34:2.6	7:41:59.1	910.8	...	...	5.93	1.21	0.50	0.50	0.25	0.25	4.3	5.3	0.51	695
226	12:34:2.6	7:41:59.5	905.2	...	...	6.84	2.70	1.61	1.17	0.81	0.58	3.9	5.3	0.55	615
227	12:34:2.5	7:41:59.5	909.5	...	...	6.28	0.91	0.95	1.00	0.48	0.50	4.7	6.2	0.53	663
228	12:34:2.6	7:42: 1.8	875.2	...	...	8.58	3.49	1.20	0.89	0.60	0.45	5.0	6.4	0.45	790
229	12:34:2.7	7:42: 1.0	883.4	...	...	7.58	1.27	0.86	0.68	0.43	0.34	4.6	5.7	0.55	615
230	12:34:2.5	7:42: 1.8	910.8	14.10	7.89	9.83	1.75	1.89	0.93	0.95	0.47	5.4	7.5	0.46	778
231	12:34:2.5	7:42: 0.0	929.8	33.24	7.35	8.17	1.68	6.04	1.46	3.03	0.73	5.9	8.2	0.52	683
232	12:34:2.5	7:42: 0.4	947.9	15.98	13.31	5.45	0.71	0.73	0.69	0.37	0.34	4.1	5.7	0.52	679
233	12:34:2.5	7:42: 0.5	951.6	16.06	8.85	7.39	0.86	2.00	0.83	1.00	0.41	5.3	7.4	0.56	599
234	12:34:2.5	7:42: 0.7	948.7	15.31	4.96	6.28	0.81	2.41	0.73	1.21	0.37	6.2	8.8	0.54	647
235	12:34:2.5	7:42: 0.8	953.3	17.75	8.09	7.01	1.39	1.83	0.76	0.92	0.38	5.3	7.8	0.55	623
236	12:34:2.4	7:42: 2.0	929.9	...	...	7.86	2.27	1.25	1.34	0.62	0.67	4.0	6.0	0.44	814

Continued on Next Page

ID	RA(2000) [h:m:s]	Dec(2000) [° ′ ″]	$V_{\rm LSR}$[a]	R[b] [pc]	δR[b] [pc]	σ_v[a]	$\delta\sigma_v$[a]	L[c]	δL[c]	$M_{\rm lum}$[d]	$\delta M_{\rm lum}$[d]	S/N	$T_{b,\rm max}$ [K]	$\Omega_{\rm shear}$[e]	d[f] [pc]
237	12:34:2.5	7:42: 1.7	928.8	27.06	11.64	7.58	0.69	4.11	1.34	2.06	0.67	4.8	7.0	0.47	746
238	12:34:2.3	7:42: 0.8	946.9	...	...	7.90	0.81	1.51	0.79	0.76	0.40	5.3	8.0	0.42	846
239	12:34:2.5	7:42: 1.0	949.2	...	...	6.42	0.63	0.51	0.67	0.26	0.33	4.0	5.3	0.55	615
240	12:34:2.4	7:42: 1.4	957.5	30.47	12.89	6.47	0.33	2.58	1.02	1.29	0.51	5.5	8.1	0.46	774
241	12:34:2.4	7:42: 1.7	958.3	...	...	7.40	0.49	2.58	1.24	1.29	0.62	4.5	6.9	0.43	818

[1] Units are km s^{-1}.
[2] The size of unresolved clouds is less than the linear size of the beam, denoted as $R = \ldots$.
[3] Units are 10^5 K km s^{-1} pc^2.
[4] Units are $10^6 M_\odot$.
[5] Units are km s^{-1} pc^{-1}.
[6] Distance from the center of NGC4526, assuming clouds are in the plane of the galaxy with axis ratio of 0.216 and position angle of 20.2°.

2.11 Appendix E. Checking Bias Against the Choice of Input Parameters

I evaluate how the results are affected by the choice of input parameters of the CPROPS program (as described in Section 2.8) and the methods to measure the cloud properties (as described in Section 2.3). I rerun the program and recalculate the cloud properties (radius, velocity dispersion, and luminosity) using various decomposition parameters ($n, \delta F/F$, and $\delta\sigma/\sigma$), edge and threshold parameters for islands, and methods of measurement (by excluding deconvolution, excluding extrapolation, and excluding both deconvolution and extrapolation).

The decomposition parameters are varied from 1 to 3 with unity increment (first column of Figure 2.16), the edge parameter varies from $2\sigma_{rms}$ to $3\sigma_{\rm rms}$, and the threshold parameter varies from $3\sigma_{\rm rms}$ to $4\sigma_{\rm rms}$ (second column of Figure 2.16). Different methods of measurements are given in the third column of Figure 2.16. Each row in Figure 2.16 shows the plots between various cloud properties, i.e. size vs. linewidth in the first row, linewidth vs. luminosity in the second row, and size vs. luminosity in the third row. Larson's relations for the Milky Way are shown as the solid lines. For comparison, the dashed lines are Larson's relations with different normalization factors: 3, 0.05, and 5 for R vs. σ_v, σ_v vs. L, and R vs. L, respectively. To check how strong the correlation between various cloud properties are, we tabulate the Spearman correlation coefficients $r_{\rm sp}$ in Table 2.3.

For each plot, we build an estimate of the probability density function (PDF) based on the data scatter in two-dimension, using the kernel-density-estimate method in Scipy. The contours in Figure 2.16 enclose to the 68% confidence level of the PDFs. We also fit the PDFs with a 2D-Gaussian and show the Gaussian centers as filled circles in Figure 2.16. The center and dispersion of the Gaussians are tabulated in Table 2.4. For clarity, we do not show the data points. In addition, we check whether the PDFs in a given panel of Figure 2.16 are sampled from the same parent distribution or not. This is tested with the two-dimensional Kolmogorov-Smirnov (KS) probability value (Table 2.5). The higher the probability the more likely the PDFs are drawn from the same parent distribution.

For the first column in Figure 2.16, we see that higher decomposition parameters (e.g. $n = \delta F/F = \delta\sigma/\sigma = 3$, green contours) yield larger scatters than lower decomposition parameters (red and blue contours). The number of clouds for higher decomposition parameters is less than for lower decomposition parameters, so this larger scatter is not due to a larger number of data points. The larger scatter is probably due to the tendency of the program to combine small, neighboring clouds into bigger, merged clouds in the molecular ring island, while leaving the outer small islands as small clouds (Figure 2.1). This tendency can be seen in Figure 2.16, as the PDFs of higher decomposition parameters extend to larger radii and higher luminosities. The Gaussian centers of higher decomposition parameter also have larger radii and higher luminosities than those of lower decomposition parameters. In any case, none of those distributions shows a size-linewidth relation ($-0.14 \leq r_{\rm sp} \leq 0.09$), and they have different normalization factors than Larson's relations.

For the second column in Figure 2.16, the parameters (edge, threshold) = $(2\sigma_{\rm rms}, 3\sigma_{\rm rms})$ almost have the same PDF as (edge, threshold) = $(2\sigma_{\rm rms}, 4\sigma_{\rm rms})$. The KS-test yields a probability value of ~ 1. This is because we only lose a few clouds with peak S/N $< 4\sigma_{\rm rms}$. However, for parameters (edge, threshold) = $(3\sigma_{\rm rms}, 4\sigma_{\rm rms})$, we lose many clouds because the islands only extend to connected pixels with $T_b > 3\sigma_{\rm rms}$ (i.e. the islands get smaller), and hence the spread of the PDF decreases due to a smaller number of data points. None of the distributions shows a size-linewidth relation, and they have different normalization factors than Larson's relations.

For the third column in Figure 2.16, there is no distribution that yields the size-linewidth relation found in the Milky Way. In the linewidth vs luminosity plot, the non-deconvolved distributions (red and green contours) yield larger velocity dispersions, as expected from Equation (2.2) by excluding the $\delta v^2/2\pi$ term, and the extrapolated distribution (red contour) yields higher luminosities. All distributions in the linewidth vs. luminosity plot lie below Larson's relation. In the size vs luminosity plot, the non-deconvolved distribution (red contour) yields a larger size, as expected from Equation (2.1) by excluding the $\sigma^2_{\rm beam}$ terms. All distributions in the size vs. luminosity plot lie above Larson's relation.

Overall, I conclude that there is no significant effect on our general results due to the choice of input parameters and measurement methods. In particular, the absence of a size-linewidth relation and the different normalization factors of Larson's relations are still remain.

Acknowledgments

I thank collaborators in this work: Leo Blitz, Timothy Davis, Erik Rosolowsky, Martin Bureau, Michelle Cappellari, and Marc Sarzi. I also thank Christopher McKee, Richard Plambeck, Tom Hartquist, Eve Ostriker, and Adam Leroy for valuable discussions. This work was partially supported by a grant from the National Science Foundation. Support for CARMA construction was derived from the states of California, Illinois, and Maryland, the James S. McDonnell Foundation, the Gordon and Betty Moore Foundation, the Kenneth T. and Eileen L. Norris Foundation, the University of Chicago, the Associates of the California Institute of Technology, and the National Science Foundation. Ongoing CARMA development and operations are supported by the National Science Foundation under a cooperative agreement, and by the CARMA partner universities. This research has made use of the NASA/IPAC Extragalactic Database (NED) which is operated by the Jet Propulsion Laboratory, California Institute of Technology, under contract with the National Aeronautics and Space Administration.

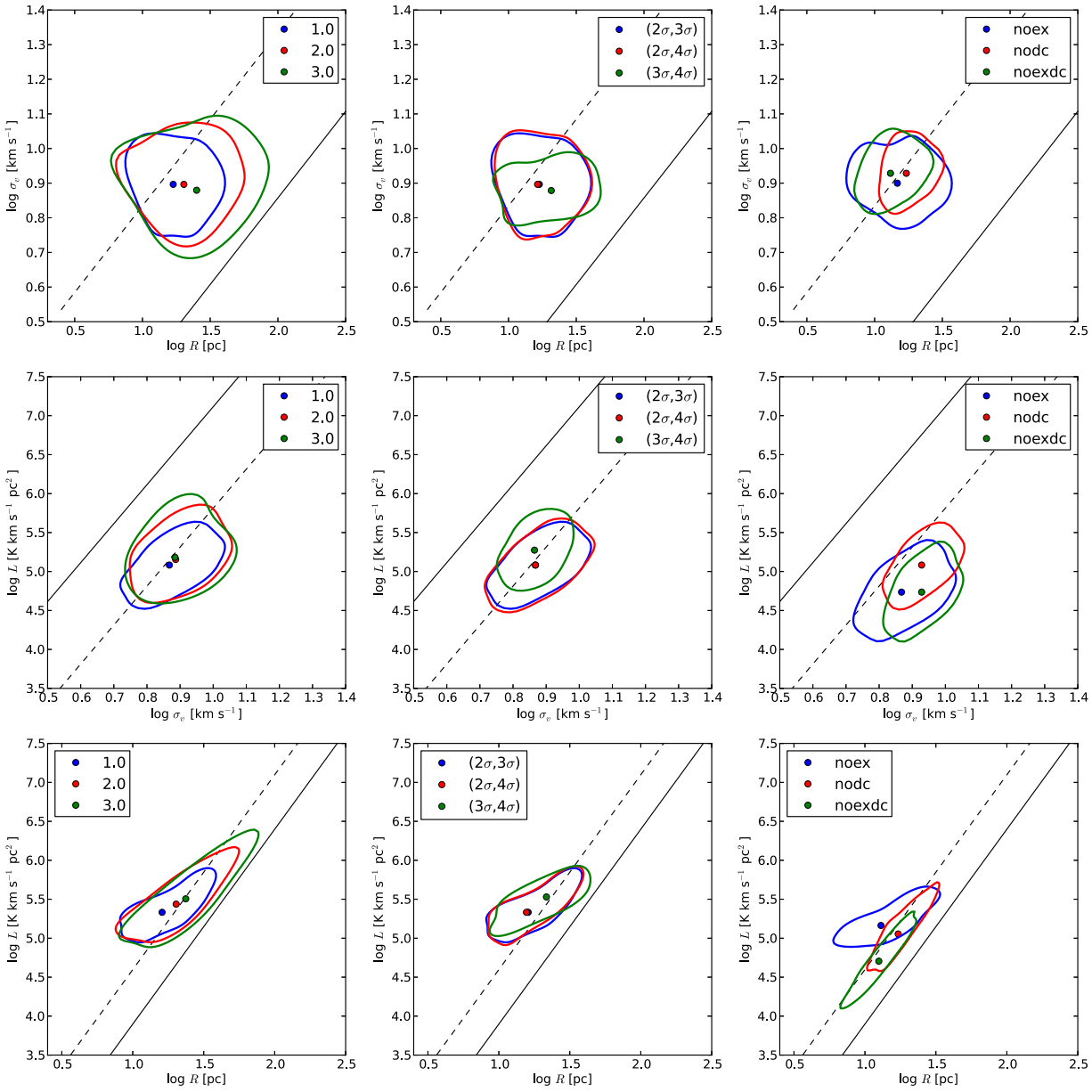

Figure 2.16: The plots of GMC properties (radius, velocity dispersion, and luminosity) for various decomposition parameters (left), islands parameters (middle), and methods of measurement (right). The black lines are Larson's relations and the dashed lines are Larson's relations with higher or lower normalization factors. There is no obvious bias due to the choice of input parameters of the program.

Table 2.3: Spearman Correlation Coefficients for Various Input Parameters and Measurement Methods

Parameters	R vs. σ_v	σ_v vs. L	R vs. L
$n = \delta F/F = \delta\sigma/\sigma = 1$	-0.14	0.51	0.67
$n = \delta F/F = \delta\sigma/\sigma = 2$	0.04	0.45	0.81
$n = \delta F/F = \delta\sigma/\sigma = 3$	0.09	0.37	0.87
(edge,threshold) $= (2\sigma, 3\sigma)$	-0.14	0.51	0.67
(edge,threshold) $= (2\sigma, 4\sigma)$	-0.09	0.53	0.69
(edge,threshold) $= (3\sigma, 4\sigma)$	0.06	0.40	0.68
no extrapolation	-0.12	0.48	0.68
no deconvolution	0.21	0.51	0.83
no extrapolation & no deconvolution	0.28	0.48	0.94

Table 2.4: Gaussian Fit Coefficients of the Distributions in Figure 2.16

Parameters	Gaussian center			Gaussian dispersion		
	R vs. σ_v	σ_v vs. L	R vs. L	R vs. σ_v	σ_v vs. L	R vs. L
$n = \delta F/F = \delta\sigma/\sigma = 1$	(34.39, 14.14)	(16.98, 8.04)	(31.05, 13.04)	(24.11, 8.47)	(6.86, 8.67)	(16.72, 9.27)
$n = \delta F/F = \delta\sigma/\sigma = 2$	(11.97, 14.88)	(16.12, 1.40)	(14.85, 3.86)	(11.62, 10.62)	(8.73, 5.97)	(7.02, 5.91)
$n = \delta F/F = \delta\sigma/\sigma = 3$	(12.50, 13.95)	(13.93, 1.25)	(16.61, 4.74)	(14.46, 12.73)	(10.29, 7.94)	(7.75, 7.26)
(edge,thres) $= (2\sigma, 3\sigma)$	(34.39, 14.14)	(16.98, 8.04)	(31.05, 13.04)	(24.11, 8.47)	(6.86, 8.67)	(16.72, 9.27)
(edge,thres) $= (2\sigma, 4\sigma)$	(33.49, 14.42)	(16.83, 7.74)	(30.00, 13.09)	(24.95, 8.94)	(7.17, 9.11)	(15.70, 9.51)
(edge,thres) $= (3\sigma, 4\sigma)$	(51.39, 27.88)	(38.92, 11.43)	(52.06, 31.64)	(32.53, 14.59)	(9.08, 21.79)	(25.97, 16.04)
no extrapolation	(28.00, 34.30)	(17.00, 5.54)	(25.50, 12.18)	(35.47, 17.38)	(6.86, 7.71)	(22.53, 12.72)
no deconvolution	(32.10, 15.19)	(14.96, 7.99)	(30.12, 7.65)	(14.26, 6.91)	(6.54, 8.68)	(9.50, 6.04)
no extrap & no decon	(24.78, 15.22)	(14.99, 5.50)	(23.20, 5.70)	(14.90, 6.88)	(6.55, 7.71)	(8.77, 4.66)

Table 2.5: Two-Dimensional Kolmogorov-Smirnov Test

R vs. σ_v										
Parameters	1	2	3	Parameters	$(2\sigma, 3\sigma)$	$(2\sigma, 4\sigma)$	$(3\sigma, 4\sigma)$	Parameters	noex	nodc	noexdc
1	1.00	-	-	$(2\sigma, 3\sigma)$	1.00	-	-	noex	1.00	-	-
2	0.11	1.00	-	$(2\sigma, 4\sigma)$	1.00	1.00	-	nodc	0.00	1.00	-
3	0.01	0.72	1.00	$(3\sigma, 4\sigma)$	0.05	0.04	1.00	noexdc	0.08	0.00	1.00
σ_v vs. L										
Parameters	1	2	3	Parameters	$(2\sigma, 3\sigma)$	$(2\sigma, 4\sigma)$	$(3\sigma, 4\sigma)$	Parameters	noex	nodc	noexdc
1	1.00	-	-	$(2\sigma, 3\sigma)$	1.00	-	-	noex	1.00	-	-
2	0.13	1.00	-	$(2\sigma, 4\sigma)$	1.00	1.00	-	nodc	0.00	1.00	-
3	0.15	0.74	1.00	$(3\sigma, 4\sigma)$	0.005	0.004	1.00	noexdc	0.00	0.00	1.00
R vs. L										
Parameters	1	2	3	Parameters	$(2\sigma, 3\sigma)$	$(2\sigma, 4\sigma)$	$(3\sigma, 4\sigma)$	Parameters	noex	nodc	noexdc
1	1.00	-	-	$(2\sigma, 3\sigma)$	1.00	-	-	noex	1.00	-	-
2	0.07	1.00	-	$(2\sigma, 4\sigma)$	1.00	1.00	-	nodc	0.00	1.00	-
3	0.01	0.74	1.00	$(3\sigma, 4\sigma)$	0.02	0.02	1.00	noexdc	0.00	0.00	1.00

Chapter 3

The Molecular Gas Depletion Time in Nearby Galaxies

I present results from the EDGE survey, a spatially resolved CO(1–0) follow-up to CALIFA, an optical Integral Field Unit (IFU) survey of local galaxies. By combining the data products of EDGE and CALIFA, I study the variation of molecular gas depletion time ($\tau_{\rm dep}$) on kiloparsec scales in 52 galaxies. I divide each galaxy into two parts: the center, defined as the region within 0.1 R_{25}, and the disk, defined as the region between 0.1 and 0.7 R_{25}. I find that 13 galaxies show a shorter $\tau_{\rm dep}$ ($\sim$ 1 Gyr) in the center relative to the disk ($\tau_{\rm dep} \sim 2.4$ Gyrs), which means the central region in those galaxies is more efficient at forming stars per unit molecular gas mass. This finding implies that the centers with shorter $\tau_{\rm dep}$ resemble the intermediate regime between galactic disks and starburst galaxies. Furthermore, the central drop in $\tau_{\rm dep}$ is correlated with a central increase in the stellar surface density, suggesting that a shorter $\tau_{\rm dep}$ is associated with molecular gas compression by the stellar gravitational potential. I argue that varying the CO-to-H_2 conversion factor only exaggerates the central drop of $\tau_{\rm dep}$.

3.1 Introduction

Galactic stellar masses grow through a combination of mergers and the formation of stars from their gas reservoir over cosmic time. Therefore, the star formation rate (SFR) is an important element in driving galaxy evolution (e.g., Kennicutt 1998a; McKee & Ostriker 2007; Kennicutt & Evans 2012). In general, star formation involves two processes: (1) the conversion of diffuse, atomic gas into molecular gas in well-shielded regions of high density, and (2) the dynamical collapse of self-gravitating regions within the molecular component to form stars. In galactic regions with low volume density and low surface density of the gas, local gas compression by spiral arms or self-gravity may be needed for molecules to form, whereas in galactic regions of high mean gas volume and surface density, most of the gas may be molecular (e.g., in M51; Schinnerer et al. 2013). In this chapter, I focus on the

second part of the star formation processes, specifically, we study how the relation between molecular gas and SFR changes between the galactic centers and the disks.

In a simple-minded picture, stars form from the gas that contracts under its self-gravity. Naively, one would expect that the relevant time-scale of this process is the free-fall time ($\tau_{\rm ff}$) of the total gas (atomic and molecular), which is inversely proportional to the square-root of gas volume density ($\rho_{\rm gas}^{-0.5}$). The implication of this simple scenario is that SFR relates to the amount of gas as $\rho_{\rm SFR} \propto \rho_{\rm gas}/\tau_{\rm ff} \propto \rho_{\rm gas}^{1.5}$.[1] In general, the relation between SFR and total gas density is called the Kennicutt-Schmidt (KS) relation, after the seminal papers by Schmidt (1959) and Kennicutt (1998b).[2]

Observations in the local universe show that stars form in molecular clouds, so we expect that SFR correlates better with the amount of molecular gas, rather than the total amount of atomic plus molecular gas (e.g., Wong & Blitz 2002; Bigiel et al. 2008). Even though the molecular phase may itself not be necessary to form stars (Glover & Clark 2012), molecular gas that forms under the high-density conditions are also favorable to gravitational collapse, thus giving rise to a strong KS relation (Krumholz et al. 2011). For convenience, in this chapter, I refer to the relationship between SFR and molecular gas surface densities as the KS relation.

Resolved studies of nearby galaxies found that the correlation between SFR and molecular gas surface densities is approximately linear in galaxy disks, with $\Sigma_{\rm SFR} \propto \Sigma_{\rm mol}$ on kiloparsec (kpc) scales for surface densities $\Sigma_{\rm H2} \gtrsim 3\ M_\odot\ {\rm pc}^{-2}$ over a wide range of local environments (e.g., Bigiel et al. 2008; Leroy et al. 2008). Furthermore, in nearby galaxies, the near-linear molecular KS relation extends to the low metallicity regime ($Z/Z_\odot \approx 0.2$; Bolatto et al. 2011; Jameson et al. 2016) and to the outer part of galaxies, where the gas surface density is low and atomic dominated (Schruba et al. 2011). A possible reason for this widespread relationship is that the properties of molecular clouds are similar from one galaxy and region to another (Bolatto et al. 2008), so that GMCs convert the molecular gas into stars at the same rate (cf. Hughes et al. 2010, 2013; Colombo et al. 2014).

For most of the gas in normal galaxies, the linearity of KS relation implies the molecular gas depletion time, defined as $\tau_{\rm dep} \equiv \Sigma_{\rm mol}/\Sigma_{\rm SFR}$, is approximately constant, with a typical value of ~ 2.2 Gyrs in nearby galaxies (e.g., Bigiel et al. 2008; Leroy et al. 2008; Rahman et al. 2012; Leroy et al. 2013). Loosely, we can interpret $\tau_{\rm dep}$ as the time scale to convert all molecular gas reservoir in a galaxy (or a given region within a galaxy) into stars at the current SFR. The fact that $\tau_{\rm dep}$ is less than the Hubble time implies that galaxies need to replenish their molecular gas reservoir, for e.g., through conversion from atomic gas and accretion from the intergalactic medium or from their satellite galaxies (e.g., Genzel et al. 2010; Bauermeister et al. 2010; Lilly et al. 2013). However, the direct observational signature of this accretion is still challenging.

[1] The other time scales that are often used in literature are the orbital time Ω^{-1} (e.g., Elmegreen 1997; Silk 1997), where Ω is the angular speed of the disk, and the vertical time H/σ (Ostriker et al. 2010; Ostriker & Shetty 2011), where H and σ are the thickness and velocity dispersion of the gas.

[2] Actually, Schmidt (1959) proposed $\Sigma_{\rm SFR} \propto \Sigma_{\rm gas}^2$ and Kennicutt (1998b) found $\Sigma_{\rm SFR} \propto \Sigma_{\rm gas}^{1.4}$, where Σ is the surface density.

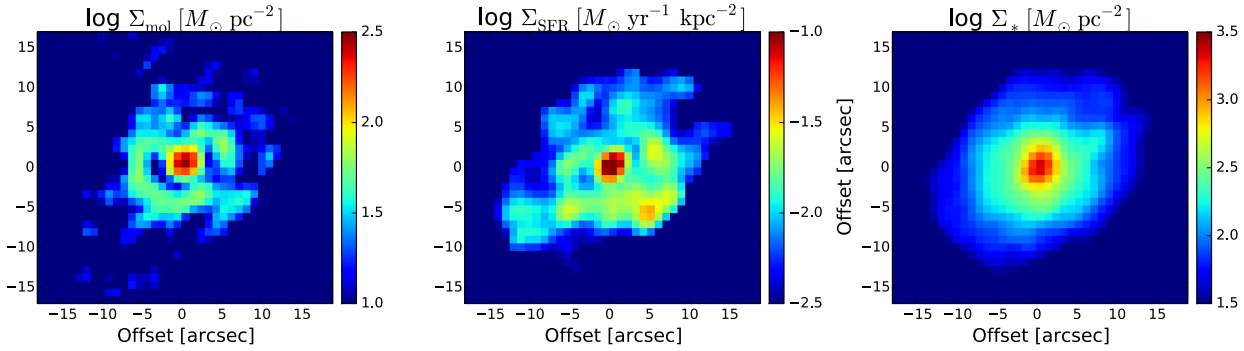

Figure 3.1: From left to right: the maps of molecular gas, SFR, and stellar mass surface density of NGC 2253.

Despite the current consensus of the linearity of KS relation in many situations, there are, at least, three regimes where this linearity break down: (1) in the ULIRGs and starburst galaxies, i.e. galaxies above the star forming main-sequence (e.g., Daddi et al. 2010; Genzel et al. 2010, 2015), (2) at resolution finer than $\sim$ 500 pc (e.g., Schruba et al. 2010; Kruijssen & Longmore 2014), and (3) in the galactic centers (e.g., Jogee et al. 2005; Leroy et al. 2013). The steeper-than-linear molecular KS relation in regions of very high molecular surface density has been interpreted as a result of higher molecular gas pressure (Ostriker & Shetty 2011) and density (Krumholz et al. 2012). Higher pressure requires a higher star formation rate per unit molecular mass to offset enhanced turbulent dissipation and cooling, and higher density is associated with shorter dynamical times, which control gravitational contraction.

In this chapter, I study the variations of $\tau_{\rm dep}$ between galactic centers and disks by combining the CO data from the EDGE survey (Bolatto et al. 2017) and the optical IFU data from the CALIFA survey (Sánchez et al. 2012), with a goal to quantify and understand the cause of those variations and its implications in galaxy evolution. This chapter is organized as follows. Overviews of the EDGE and CALIFA data products and the sample selection are described in Sections 3.2 and 3.3, respectively. Then, in Section 3.4, I compare $\tau_{\rm dep}$ in the centers relative to those in the disk. Specifically, I investigate whether the difference of $\tau_{\rm dep}$ between the centers and the disks is driven by the star formation rate or molecular gas surface density. In Section 3.5, I discuss the effect of the CO-to-H_2 conversion factor, and the connection between $\tau_{\rm dep}$, oxygen abundance, and the size of stellar and molecular gas disk. Lastly, I summarize the findings in Section 3.6.

3.2 Data Descriptions

3.2.1 The EDGE Survey

The EDGE survey observed 126 galaxies in the CO(1–0) and ^{13}CO(1–0) lines using the CARMA observatory (Bock et al. 2006) in the D and E arrays from 2014 October until 2015 May. The EDGE sample was selected from the CALIFA Second Data Release (García-Benito et al. 2015) based on their fluxes in the WISE 22μm band (Wright et al. 2010), i.e. bright infrared galaxies were preferred to increase the chance of CO detection. All targets were observed in a 7-point hexagonal mosaic with pointings separated by 27″ (half the primary beam width of the 10 m telescopes of CARMA). This yielded a half-power field-of-view (FOV) with radius about 50″.

As described in Bolatto et al. (2017), the EDGE sample was observed in CARMA's "snapshot" mode. In this mode, a list of targets was built, ordered by priority based on their WISE 22μ fluxes. Then, the system automatically selected the highest priority target that was visible by CARMA at that moment. Observations were conducted on that target until it falls below the elevation threshold or until the integration time has been completed. Bright ($>$ 8 Jy) quasars, usually 3C273 or OJ 287 (J0854+201) were observed as passband calibrators, while Mars and Uranus were used as flux calibrators. If those planets were not visible, the compact HII region, MWC349 (with an adopted flux of 1.2 Jy), or the quasar, 3C273, (with an adopted flux of $8 - 12$ Jy) was used for flux calibration.

As a practical convenience, the sample was divided into three groups based on their optical redshift ($1500 - 4000$ km s^{-1}, $4000 - 6500$ km s^{-1}, and $6500 - 9000$ km s^{-1}). The advantage of this division is only three fixed tuning and correlator setups were needed (i.e. one for each group, rather than one for each galaxy). During a typical 4-hour observational slot, only sources in one redshift group were observed, along with passband and flux calibrators. The CARMA correlator was configured with five 250-MHz windows covering the ^{12}CO line (with 3.4 km s^{-1} resolution and a 3000 km s^{-1} velocity range), and three 500-MHz windows covering the ^{13}CO line (with 14.3 km s^{-1} resolution and a 3800 km s^{-1} velocity range).

The visibility data were calibrated in `MIRIAD` (Sault et al. 1995) using an automated pipeline based on scripts developed for the STING galaxy survey (Rahman et al. 2011, 2012; Wong et al. 2013). The antenna gains of CARMA are approximately known, so that the data are processed with a default calibration. The distribution of the derived flux calibration factors is Gaussian, with a standard deviation of $\sigma = 0.10$. This provides a measure of the systematic uncertainty in the flux calibration scale to be $\pm 10\%$. In cases where a nuclear continuum source was detected (ARP220, NGC1167, NGC2639, NGC6146), a first-order spectral baseline was subtracted from the visibility spectra before imaging.

The typical time invested per galaxy between the two CARMA configurations was 4.3 hours. The beam size for each galaxy varies with a typical value of 4″.5, which corresponds to a median physical scale of about 1.5 kpc. This physical resolution is slightly larger than previous CO surveys, such as BIMA SONG ($\sim$ 360 pc; Helfer et al. 2003), HERACLES ($\sim$ 500 pc; Leroy et al. 2009), and STING ($160 - 1250$ pc; Rahman et al. 2012), because

our sample covers farther median distance than those surveys. The velocity resolution is 10 km s^{-1} with a typical velocity range of 860 km s^{-1}. This velocity range generally covers CO emission out to the flat part of the rotation curve.

Data cubes which provide an estimate of $1\sigma_{\rm rms}$ noise level at each pixel were also generated during the data reduction processes. The RMS noise is typically ~ 11.6 mJy beam^{-1} measured in 10 km s^{-1} channels, although it can be as small as 4 and as large as 18.5 mJy beam^{-1} depending on the weather conditions during the observations and the actual integration time. This RMS in flux density yields a distribution of Rayleigh-Jeans brightness temperature sensitivities centered on 53 mK, with most values between 40 and 65 mK, depending on the synthesized beam.

The H_2 column density associated with 1σ sensitivity of 53 mK is $N(H_2) \sim 1 \times 10^{20}$ cm^{-2} in 10 km s^{-1} channel (assuming a Galactic conversion factor of $X_{\rm CO} = 2 \times 10^{20}$ cm^{-2} (K km s^{-1})$^{-1}$; Bolatto et al. 2013, and references therein). This corresponds to $A_V \sim 0.1$ mag for a Galactic dust-to-gas ratio (Bohlin et al. 1978), and to a molecular gas surface density (including He) of $\Sigma_{\rm mol}$= $2.3 M_\odot$ pc^{-2} . Given the distribution of distances, this translates into a typical 4σ mass sensitivity of $3.5 \times 10^7 M_\odot$ for a 30 km s^{-1} line in a beam (which is a representative linewidth for our typical spatial resolution), although there is a wide distribution for this parameter, with cubes as sensitive as $6 \times 10^6 M_\odot$ for the nearest galaxies. Therefore, EDGE is sensitive to objects on the mass scale of Giant Molecular Associations (GMAs, Vogel et al. 1988). The median integrated molecular gas for the detected EDGE galaxies is $2.3 \times 10^9 M_\odot$.

In order to separate signal from noise, masks are created through the following steps using `IDL` (code available at `https://github.com/tonywong94/idl_mommaps`; Wong et al. 2013). First, the data to 9″ resolution are smoothed using a Gaussian kernel. The aim of this smoothing is to reach a higher signal to noise ratio (SNR). Then, the contiguous regions are searched, starting from pixels that have SNR ≥ 3.5 extending down to regions that have SNR $= 2$. The aim of these contiguous regions is to exclude pixels that by chance have high flux due to noise, but only localized into one to few pixels (e.g., Rosolowsky & Leroy 2006). An additional padding of 2 pixels surrounding the $2\sigma_{\rm rms}$ contours are added into the mask to capture low level emission. Finally, these masks are applied to the data cubes in their original resolutions (4″.5 and 10 km/s). These contiguous regions, including the padding, are defined as masked regions.

The masked data cubes are integrated along the velocity axis to get the CO surface brightness maps (zeroth moment maps). Similarly, the uncertainties of the maps are derived by integrating the estimated noise along the velocity axis within the masked cubes. In the analyses, these uncertainty maps are used as $1\sigma_{\rm rms}$ noise level. Note that not all masked CO surface brightness maps are higher than $2\sigma_{\rm rms}$ level, therefore, the emissions below $2\sigma_{\rm rms}$ level are treated as non-detections, even though these emissions are located within the mask.

The CO surface brightness and its uncertainty maps are converted into the molecular gas surface density ($\Sigma_{\rm mol}$) maps by using a constant CO-to-H_2 conversion factor ($\alpha_{\rm CO}$) of 4.4 $M_\odot$ pc^{-2} (K km s^{-1} pc^2)$^{-1}$, including the mass contribution from Helium. In general, $\alpha_{\rm CO}$ can vary as a function of metallicity and stellar surface density (Bolatto et al. 2013). In this

study, I assume a Galactic value of $\alpha_{\rm CO}$, and then, I consider how the variations in $\alpha_{\rm CO}$ affect the results. Note that the surface density measurement has been corrected (deprojected) for inclination (i) by using a correction factor of $\cos(i)$. An example map of $\Sigma_{\rm mol}$ is shown as the first column of Figure 3.1.

3.2.2 The CALIFA Survey

CALIFA is an optical Integral Field Unit (IFU) survey of $\sim$ 600 local galaxies in a redshift range of $0.005 \lesssim z \lesssim 0.03$ using the 3.5-m telescope at the Calar-Alto observatory (Sánchez et al. 2012). In IFU surveys, we get spatial and spectral information of an object, simultaneously. The CALIFA samples are selected from the SDSS DR7 database (Abazajian et al. 2009) based on their diameter in $r-$band ($45'' < D_{25} < 80''$), so that they fit well within the IFU field-of-view of $1'.3$, or equivalently ~ 2.5 effective radius (Walcher et al. 2014), but statistically still represents the population of $z \sim 0$ galaxies in the color-magnitude diagram. The spatial resolution of CALIFA is $\sim 2''.5$ (equivalents to ~ 1 kpc) and the spectral range of CALIFA covers 3700 to 7000 Å, so that it captures the stellar absorption lines and the nebular emission lines.

I do the following additional processes to create homogeneous datasets to combine EDGE and CALIFA results. (1) Regrid the CALIFA data by using `MIRIAD` task `regrid`, so that it has the same spatial coordinate as in the EDGE data with a common pixel size of $2'' \times 2''$ (approximately, there are four pixels per synthesized beam area). In this process, we also degrade the resolution of CALIFA images to match the resolution of EDGE images by using `MIRIAD` task `convol`. The total flux is conserved during those processes. (2) Blanking the CALIFA data that are contaminated by foreground stars and neighboring galaxies. (3) Separating signals from noise by blanking any pixels that have SNR < 2, where the median-absolute-deviation of the CALIFA image is used as an estimate of the noise. As in the EDGE dataset, all surface density that is derived from the CALIFA dataset has been corrected by $\cos(i)$ to take into account the deprojection due to inclination.

The physical resolution from galaxy-to-galaxy varies between ~ 0.5 to 2 kpc. However, I do not expect that these variations affect our results because Schruba et al. (2010) and Kruijssen & Longmore (2014) concluded that the locations of CO and Hα peak are co-spatial on scales larger than ~ 0.5 kpc, i.e. we only capture the time-average of the star formation process, not its time evolution. In addition, degrading all samples to a resolution of 2 kpc is not suitable for studying the variation of $\tau_{\rm dep}$ in the central part of galaxies ($r < 2$ kpc) versus the galaxy disks. Conversely, only a small fraction of galaxy sample has resolution of ~ 0.5 kpc, which will minimize the statistical significance of this study.

The Star Formation Rate Surface Density

The post-processing of CALIFA data (`Pipe3D` version 2.2 from Sánchez et al. 2016) provided the intensity maps of emission lines, such as Hα and Hβ. To derive the maps of SFR surface density ($\Sigma_{\rm SFR}$), first, I calculate the nebular extinction at Hα ($A_{\rm H\alpha}$), by utilizing

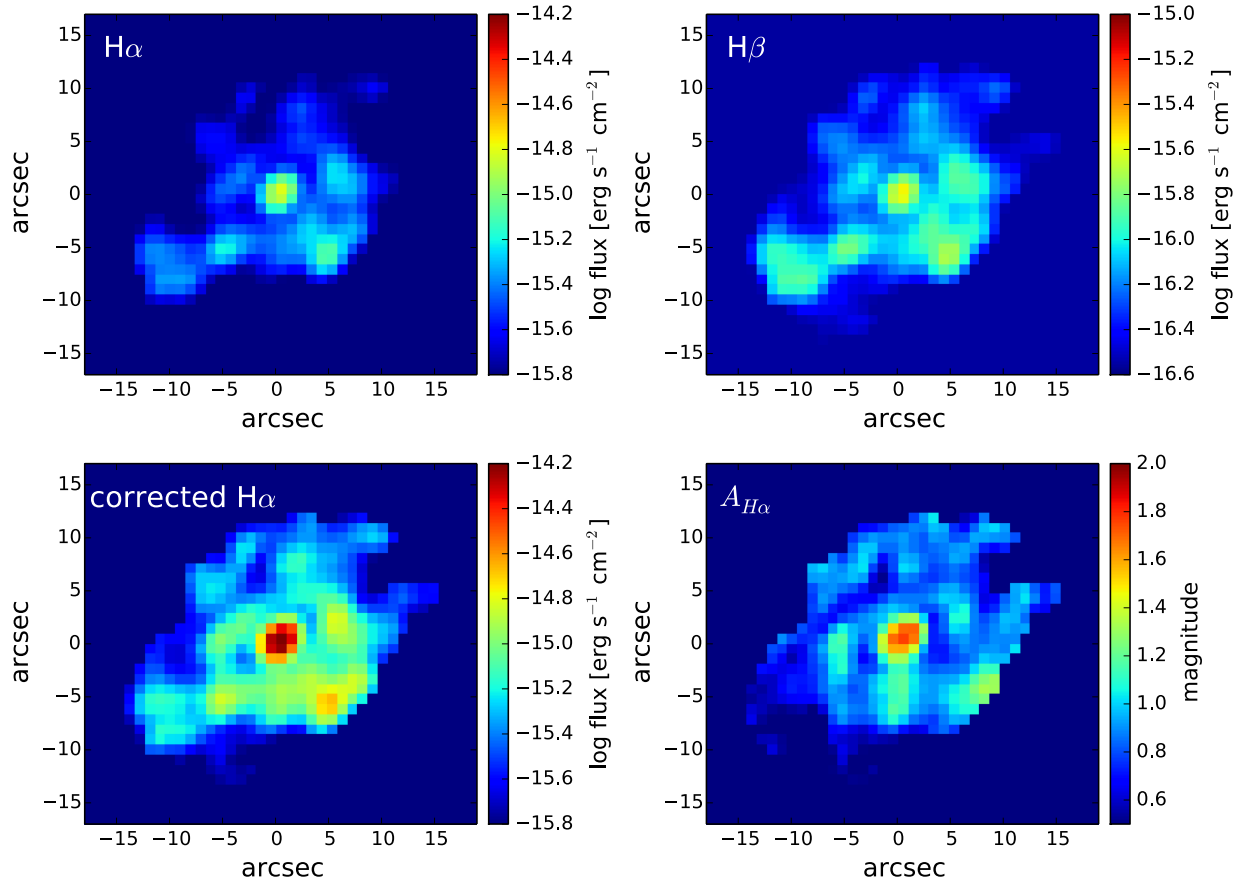

Figure 3.2: An application of the Balmer decrement method to NGC 2253. Top left: Hα fluxes. Top right: Hβ fluxes. Bottom right: Dust extinction at Hα ($A_{H\alpha}$). Bottom left: Extinction corrected Hα fluxes.

the ratio of Hα and Hβ fluxes (Balmer decrement method; e.g., Domínguez et al. 2013) and compare it with its intrinsic value (zero extinction) of 2.86 (for case B recombination at temperature of 10^4 K and electron density of 100 cm^{-3}; Osterbrock 1989). I also use a Galactic extinction curve (Cardelli et al. 1989) with $R_V = 3.1$. The result would be similar if Calzetti et al. (2000) extinction curve with $R_V = 4.1$ is used, because $A_{\mathrm{H}\alpha,\mathrm{Calzetti}}/A_{\mathrm{H}\alpha,\mathrm{Cardelli}} = 1.03$ (Catalán-Torrecilla et al. 2015). The resulting pixel-by-pixel mean value of $A_{\mathrm{H}\alpha}$ is ~ 1 magnitude.

Then, I apply this $A_{\mathrm{H}\alpha}$ to Hα maps to get the *dust-corrected* (or extinction-free) Hα maps. An example of this Balmer decrement method is shown in Figure 3.2. Finally, I convert the dust-corrected Hα maps to the SFR surface density maps following the prescriptions in Calzetti et al. (2007), based on a stellar population model with 100 Myr of constant SFR, solar metallicity, and an IMF that has a slope of -1.3 within $0.1 < M_*/M_\odot < 0.5$ and a

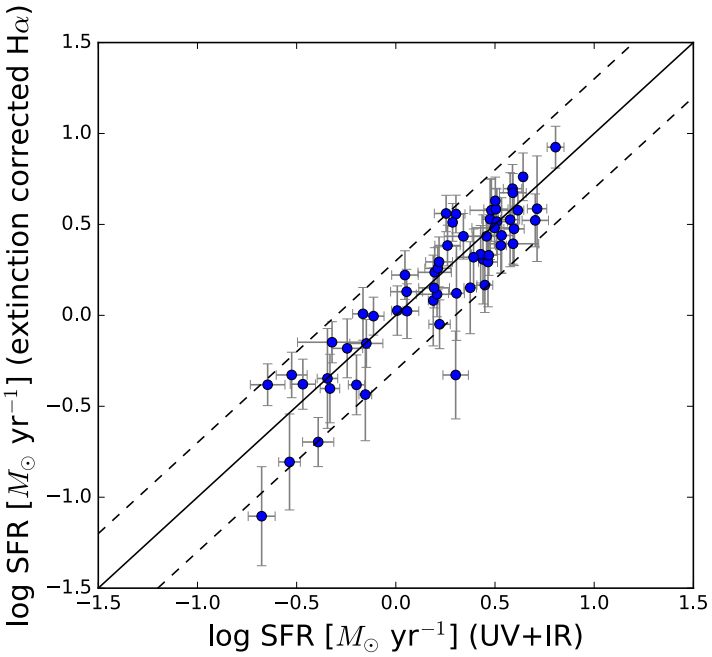

Figure 3.3: A comparison of SFR measurements from extinction-corrected Hα (this paper) and UV+IR from Catalán-Torrecilla et al. (2015). We apply aperture correction for our SFR measurement as suggested by Catalán-Torrecilla et al. (2015). The solid line is the one-to-one relationship, while the dashed line is 0.3 dex away from the solid line. The uncertainties of SFR measurement in this paper is calculated using the error propagation from the uncertainties in Hα and Hβ measurements. A 20% uncertainty due to SFR calibration (Calzetti et al. 2007) has been included.

slope of -2.3 within $0.5 < M_*/M_\odot < 120$. The IMF for this SFR prescription is similar to a Kroupa (2001) IMF, which is a factor of 1.59 smaller than those derived from a Salpeter (1955) IMF with a mass range of $0.1 - 100\ M_\odot$ (Madau & Dickinson 2014). An example of the $\Sigma_{\rm SFR}$ maps is shown as the second column of Figure 3.1.

As a check, I compare the SFR of *extinction-corrected* Hα emission that we derived above with the SFR derived from the ultraviolet (UV) emission plus total-infrared (TIR) emission from Catalán-Torrecilla et al. (2015). The UV emission traces the unobscured SFR, while the TIR emission compensates for the obscured SFR that is reradiated by dust. I do galaxy-by-galaxy comparison by integrating our resolved SFR because the IR data is unresolved. Since the Hα emission is more extended than the FoV of CALIFA survey, an aperture correction of 1.4 is applied as suggested by Catalán-Torrecilla et al. (2015). In Figure 3.3, I show that both measurements are in agreement to better than a factor of ~ 2.

The Gas-phase Metallicities

The gas-phase metallicities (oxygen abundance) are derived by using emission line ratios of OIII[5007Å]/Hβ and NII[6583Å]/Hα (i.e. the O3N2 method; Alloin et al. 1979; Pettini & Pagel 2004). I use the following prescription from Marino et al. (2013)

$$12 + \log(\mathrm{O/H}) = 8.533 - 0.214 \log\left(\frac{\mathrm{OIII}}{\mathrm{H}\beta}\frac{\mathrm{H}\alpha}{\mathrm{NII}}\right). \tag{3.1}$$

The coefficient of this method has been calibrated by using the electron temperature based on the measurements of 603 HII regions extracted from the literature and 3423 additional HII complexes from the CALIFA survey. The resolved metallicities in our sample range from 8.3 to 8.6, which is slightly below the Solar metallicity of 8.7 (Allende Prieto et al. 2001; Asplund et al. 2009).

The Stellar Ages and Mass Surface Densities

We take the luminosity-weighted, stellar population ages and the dust-corrected, stellar mass surface densities (Σ_*) from the data products of `Pipe3D` version 2.2 (Sánchez et al. 2016). Briefly, the data products are derived from the best fit of stellar spectrum from a combination of the GRANADA (Martins et al. 2005) and MILES libraries (Sánchez-Blázquez et al. 2006; Vazdekis et al. 2010; Falcón-Barroso et al. 2011), that cover 39 grids of stellar ages (from 1 Myr to 13 Gyrs) and 4 grids of stellar metallicities ($Z/Z_\odot = 0.2, 0.4, 1$ and 1.5). We convert the Σ_* maps from a Salpeter (1955) IMF to a Kroupa (2001) IMF by divide it with a factor of 1.6 (Madau & Dickinson 2014).

3.2.3 Sample Selections

I select 52 galaxies from 126 EDGE-CALIFA samples based on the following three criteria. (1) They are not dominated by AGN/LINER. (2) They have sufficient SFR and CO detections that cover both the center of a galaxy and its disk. (3) The inclination (i) is less than 75°. The inclinations are taken from the following, ordered by priority: (1) the best fit of CO rotation curve, whenever it is possible (Levy et al. in preparation), (2) from the shape of the outer isophote, or (3) from the HyperLEDA catalog (Makarov et al. 2014). A list of the galaxy sample is tabulated in Table 3.1 in Section 3.6.

I exclude AGN and LINER emission regions based on N[II]/Hα and O[III]/Hβ line ratios (i.e. the BPT diagram; Baldwin et al. 1981; Kewley & Dopita 2002; Kauffmann et al. 2003). Any data points above the demarcation line of Kewley & Dopita (2002) are blanked. Note that the LINER emission regions are not only concentrated in the center, but also in the disk, possibly due to photo-ionization from AGB stars (Singh et al. 2013; Belfiore et al. 2016). As a rule-of-thumb, a galaxy is removed from the sample if all pixels in the center (i.e. within 0.1 R_{25}) are AGN/LINER-like emission. Based on the criteria above, 31 galaxies are removed from the sample. I also blanked any regions that have Hα equivalent width less

than 6 Å, because $\sim$ 80% of stars in those regions are older than $\sim$ 500 Myrs, and hence, are not associated to star forming regions (Sánchez et al. 2014).

I further remove 17 galaxies that do not have sufficient CO or SFR detection in their center or disk, because measurement of $\tau_{\rm dep}$ is severely contaminated by non-detection. If a galaxy has less than 2 detected pixels in the center or in the disk, then that galaxy is removed from the sample. Lastly, 26 galaxies with $i \gtrsim 75^{\circ}$ (the ratio of minor to major axis is less than 0.25) are removed because high inclination galaxies yield few sampling points along the minor axis, resulting in a deprojected beam elongated parallel to the minor axis in the plane of the galaxy, and large uncertainty in the estimation of dust extinction.

The final sample has stellar masses (M_*) from 4×10^9 to 2×10^{11} $M_{\odot}$, molecular gas masses ($M_{\rm mol}$) from 8×10^7 to 1×10^{10} $M_{\odot}$, and gas-phase metallicities (12+log[O/H]) from 8.4 to 8.6. This sample consists of 49 spirals (Hubble type from Sa to Sd) and 3 early-types, within which there are 24 barred galaxies (Méndez-Abreu et al. 2017) and 7 interacting galaxies (Barrera-Ballesteros et al. 2015). The ranges in the stellar and molecular gas masses are comparable to the unresolved survey of COLDGASS (Saintonge et al. 2011a,b). In addition, the sample has a comparable number of galaxies and covers farther distance (d) in the local volume ($26 \lesssim d \lesssim 169$ Mpc) than previous resolved surveys, such as BIMA SONG (44 galaxies; $2 \lesssim d \lesssim 26$ Mpc; Helfer et al. 2003), HERACLES (48 galaxies; $3 \lesssim d \lesssim 15$ Mpc; Leroy et al. 2013; Schruba et al. 2012), and CARMA STING (14 galaxies; $5 \lesssim d \lesssim 43$ Mpc; Rahman et al. 2012). Thus, this sample bridges the gap between nearby and higher redshift galaxies.

3.3 Results

In Figure 3.4, I show the KS relation for molecular gas. The data points are from pixel measurements (detected both in SFR and CO) in 52 galaxies. The median values of $\Sigma_{\rm SFR}$ for a given bin of $\Sigma_{\rm mol}$ are marked as black dots, while the constant values of $\tau_{\rm dep} = 1$, 2, and 4 Gyrs are indicated. There is a tendency for high $\Sigma_{\rm mol}$ regions (top right in Figure 3.4) to have shorter $\tau_{\rm dep}$ than low $\Sigma_{\rm mol}$ regions. Since galactic centers have higher $\Sigma_{\rm mol}$ than those in the disks, this indicates that the centers have shorter $\tau_{\rm dep}$ than those in the disks.

In order to study the variation of $\tau_{\rm dep}$ between galactic centers and disks, we first need to separate the center of a galaxy from its disk. To do so, I define the center as a region at distance $r \leq 0.1\ R_{25}$ from the galactic nucleus, and the disk as a region between 0.1 R_{25} and 0.7 R_{25}. I define $\tau_{\rm center}$ as the median of $\tau_{\rm dep}$ over all detected pixels in the center, and the same for $\tau_{\rm disk}$ in the disk. If the median of $\tau_{\rm dep}$ in a galaxy is used ($\tau_{\rm median}$), this means both the center and the disk are included. If the number of detected pixels in the disks is much larger than those in the centers, then the values of $\tau_{\rm median}$ is similar to $\tau_{\rm disk}$. I adopt $r = 0.7\ R_{25}$ as the outermost radius because CO in this sample is almost never detected beyond that radius.

The radial distance to the galactic nucleus is calculated using the assumption that the molecular gas lies in the galactic mid-plane, without a warp, isophotal twist, or misalignment.

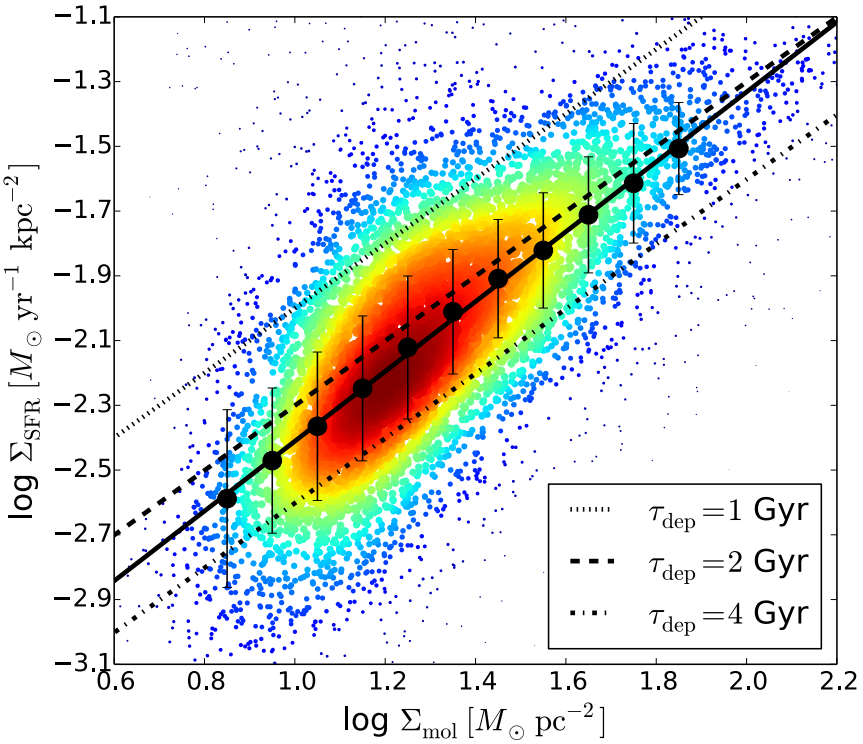

Figure 3.4: The relationship between $\Sigma_{\rm mol}$ and $\Sigma_{\rm SFR}$ for our sample of 52 galaxies selected from the EDGE survey. The data point plots these values for a $2'' \times 2''$ pixel, with color and point size are coded by the density of data points. The black dots are the median value of $\Sigma_{\rm SFR}$ within bins of $\Sigma_{\rm mol}$. A linear fit to the black dots is given by the solid black line. This linear fit has a slope of 1.08 ± 0.01 and an intercept point of -3.49 ± 0.02. The dotted, dashed, and dash-dotted lines correspond to $\tau_{\rm dep}$ = 1, 2, and 4 Gyrs, respectively.

Since each galaxy has different physical size in kpc, the radius is normalized with respect to R_{25}, i.e. the radius where the surface brightness is 25 mag/arcsec^2 in the $B-$band. The values of R_{25} are taken from the HyperLEDA catalog. The conversion between R_{25} and the stellar scale length (l_*) is $R_{25} = (4.6 \pm 0.8)\ l_*$ (Leroy et al. 2008). Unless otherwise stated, in this study, I focus on pixels detected in both CO ($\Sigma_{\rm mol} \gtrsim 10\ M_\odot$ pc^{-2}) and Hα.

3.3.1 Variations of the Molecular Gas Depletion Time

Since CO emission is patchy, not all regions within a galaxy are detected in both CO and Hα. To investigate $\tau_{\rm dep}$ as a function of radius, I stack the pixels from all galaxies in the sample. In Figure 3.5, $\tau_{\rm dep}$ for each pixel detected in both CO and Hα is plotted as a function of radius (r/R_{25}). The median value of $\tau_{\rm dep}$ (for $\Sigma_{\rm mol}$ between ~ 10 and $\sim 100\ M_\odot$ pc^{-2}) is 2.4 Gyrs with ~ 0.5 dex scatter. This value is in line with previous measurements in

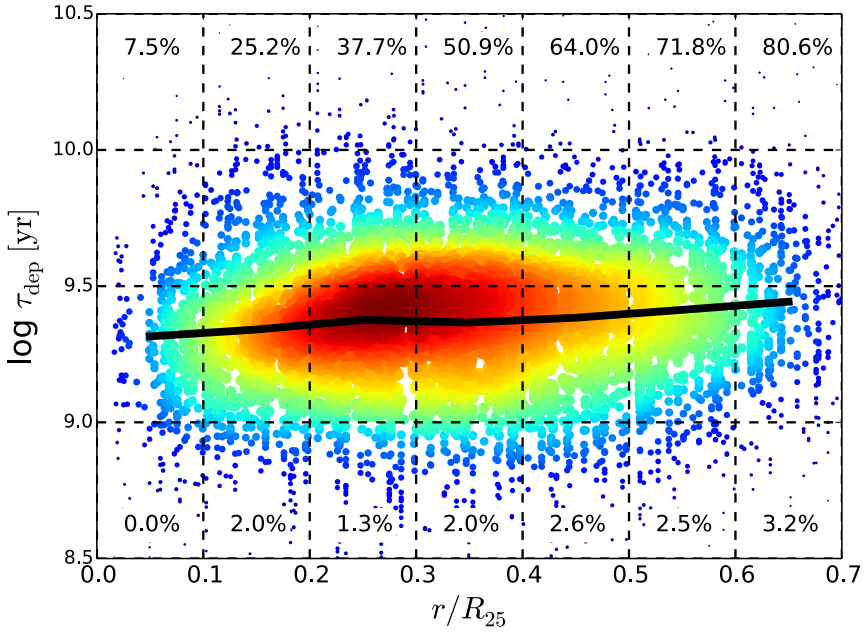

Figure 3.5: The depletion time as a function of radius, stacked over all detected regions in all galaxy in the sample. The data points are $2'' \times 2''$ pixel measurements. The colors and sizes of points represent the global density of the data points and the solid line is the median value of $\tau_{\rm dep}$ in a radial bin. On the top and bottom of the figure, I label the fractions of non-detection pixels that correspond to upper and lower limits in $\tau_{\rm dep}$, respectively. Upper limits in $\tau_{\rm dep}$ are pixels with known SFR but CO is not detected, and vice versa for lower limits. The Hα measurements are more sensitive than the CO maps, therefore, the fractions of upper limits are higher than the fractions of lower limits at any radius.

nearby galaxies (e.g., Rahman et al. 2012; Bigiel et al. 2011; Leroy et al. 2013). Interestingly, Figure 3.5 shows that the centers have shorter $\tau_{\rm dep}$ than those in the disks, due to the dip of $\tau_{\rm center}$ in some galaxies in the sample. As a consequence, the dip of $\tau_{\rm dep}$ becomes more prominent when I separate those galaxies from the rest of the sample (see Section 3.3.2).

In Figure 3.6, we see that $\tau_{\rm center}$ is an order of magnitude shorter than $\tau_{\rm disk}$ in some galaxies, and an order of magnitude higher than $\tau_{\rm disk}$ in other galaxies. Then, I investigate whether the variations of $\tau_{\rm center}$, relative to $\tau_{\rm disk}$, are correlated with the global properties of galaxies, namely the stellar masses (M_*), the molecular gas masses ($M_{\rm mol}$), the Hubble types, the gas-phase metallicities, and the age of stellar populations. RC3 de Vaucouleurs et al. (1991) indices from the HyperLEDA database (Makarov et al. 2014) are adopted as morphological types. For the oxygen abundance and the age of stellar population, I use their median value within 1 ± 0.2 effective radius (R_e), because Sánchez et al. (2016) suggested that the value at R_e is a good representation in a galaxy.

There are no correlations between $\log(\tau_{\rm center}/\tau_{\rm disk})$ and morphology, gas-phase metallic-

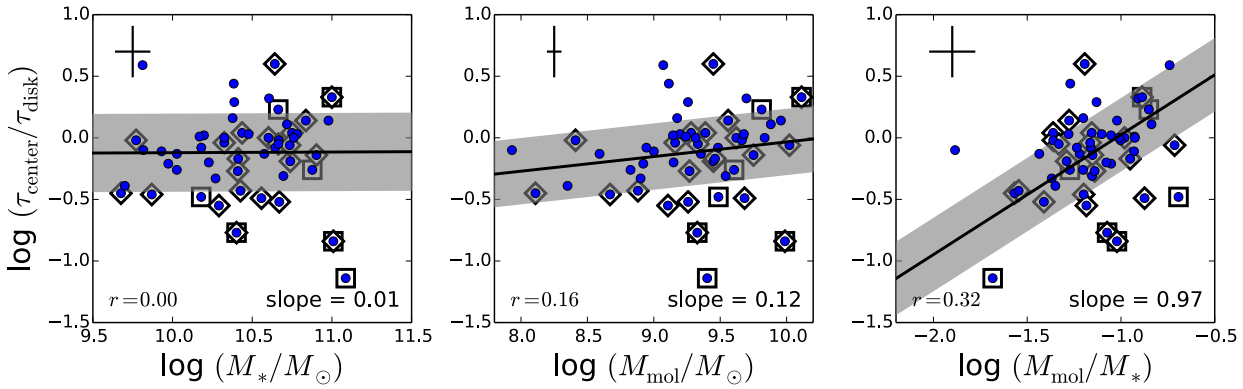

Figure 3.6: The ratio of $\tau_{\rm dep}$ in a galactic center to that in its disk for each galaxy is plotted as a function of various global parameters: stellar masses (left panel), molecular gas masses (middle panel), molecular-to-stellar mass ratio (right panel). The diamonds mark the barred galaxies, while the squares mark the interacting galaxies. The black lines are the linear best-fit using Orthogonal Distance Regression method in `Scipy` package, which takes into account the errors in both axes, and the gray regions cover 68% of the nearest data points to the best-fit lines. The slope of the best-fit line and the Pearson correlation coefficient are indicated. The crosses represent the typical error bars of the data points.

ity, or age of stellar populations at R_e, probably because the sample has limited range in morphology (94% of our samples are spirals) and gas phase metallicity (only $\sim$ 0.2 dex of variations). Furthermore, the age of stellar populations at R_e reflects the value in the disks, where $\tau_{\rm disk}$ does not vary as much as $\tau_{\rm center}$. If the stellar age is measured in the center, however, galaxies with low values of $\log(\tau_{\rm center}/\tau_{\rm disk})$ have younger ages for their stellar populations (see Section 3.4.4).

Furthermore, $\log(\tau_{\rm center}/\tau_{\rm disk})$ is correlated with $M_{\rm mol}/M_*$, but there is no significant correlation with $M_{\rm mol}$, and no correlation with M_* (Figure 3.6). Galaxies with shorter $\tau_{\rm center}$ than $\tau_{\rm disk}$ have lower fraction of molecular gas to stellar mass. The physical reason for this correlation is unknown. Sandstrom et al. (2013) found that the CO-to-H_2 conversion factor ($\alpha_{\rm CO}$) is lower in galactic centers. If we apply this variation to our sample, it makes the difference between $\tau_{\rm center}$ and $\tau_{\rm disk}$ is even larger.

It should be noted that three galaxies with the lowest values of $\log(\tau_{\rm center}/\tau_{\rm disk})$ are interacting galaxies (marked as black squares in Figure 3.6). In addition, barred galaxies (identified from the photometric fit of Méndez-Abreu et al. 2017, or from HyperLEDA catalog) tend to have lower values of $\log(\tau_{\rm center}/\tau_{\rm disk})$ than unbarred galaxies (marked as black diamonds in Figure 3.6). The mean values of $\log(\tau_{\rm center}/\tau_{\rm disk})$ for interacting and barred galaxies are -0.42 ± 0.51 and -0.22 ± 0.28, while the corresponding value for unbarred galaxies is -0.03 ± 0.35. This indicates that the perturbed systems can enhance the star formation efficiency in the center.

3.3.2 Separations of Galaxies into Three Groups of $\tau_{\rm dep}$

To see clear variations of $\tau_{\rm center}$ with respect to $\tau_{\rm disk}$, I separate galaxies into three groups based on their $\log(\tau_{\rm center}/\tau_{\rm median})$ values. The three groups of $\tau_{\rm dep}$ are the following.

1. Galaxies with falling $\tau_{\rm center}$, defined as those with $\log(\tau_{\rm center}/\tau_{\rm median}) < -0.26$ dex, which represent 25.0% of the galaxy sample.

2. Galaxies with rising $\tau_{\rm center}$, defined as those with $\log(\tau_{\rm center}/\tau_{\rm median}) > 0.26$ dex, which represent 9.6% of the galaxy sample.

3. The rest of them (65.4% of the sample) have $\log(\tau_{\rm center}/\tau_{\rm median})$ within ± 0.26 dex, which we defined as flat $\tau_{\rm dep}$.

I list the values of $\tau_{\rm dep}$ in the centers, disks, and whole galaxy (median) in Table 3.1, where the notation "drop", "rise", and "flat" are used for these three groups. In this respect, I expand the previous finding by Leroy et al. (2013) to include the galactic centers that have similar, and even, longer $\tau_{\rm center}$ compared to $\tau_{\rm median}$. The results of this $\tau_{\rm dep}$ segregation are shown in the top row of Figure 3.7.

I use 0.26 dex as a separator between the three different groups of $\tau_{\rm dep}$ because this value is the standard deviation of the resolved $\tau_{\rm dep}$ within 0.7 R_{25}. This value also coincides with that was observed in the HERACLES sample, which shows a dip of $\tau_{\rm center}$ by about 0.2 dex relative to $\tau_{\rm median}$ (for a constant CO-to-H_2 conversion factor; Leroy et al. 2013). However, keep in mind that the variation of $\tau_{\rm center}$ is continuous, i.e. there is no clear separation or clustering between those three groups (see Figure 3.6). The classification of galaxies into three groups is just an approach to see a difference between $\tau_{\rm center}$ and $\tau_{\rm median}$ in some galaxies.

In the bottom row of Figure 3.7, I show each of the three groups on an absolute scale of $\tau_{\rm dep}$ (in years). It can be seen that the galactic centers in the drop $\tau_{\rm center}$ group form stars more efficiently than those in the flat $\tau_{\rm dep}$ group, i.e. their locations in the KS diagram lie above the disks, and vice versa for the rise $\tau_{\rm center}$ group. The value of $\tau_{\rm center}$ in the drop $\tau_{\rm dep}$ group (≈ 1 Gyr) is not only lower relative to $\tau_{\rm median}$, but also in the absolute value, because $\tau_{\rm median} \approx 2.4$ Gyr. Therefore, those galactic centers resemble an intermediate regime between the disks and starbursts.

I check whether the difference in physical resolution of each galaxy can introduce a systematic bias that affects the results. The physical resolution, defined as the angular resolution (interferometric beam) multiplied by distance to the galaxy, varies among the sample, from 0.5 to 2.8 kpc (Table 3.1). However, the best-fit relation between $\log(\tau_{\rm center}/\tau_{\rm disk})$ and physical resolution is almost flat (slope ≈ 0.11) with a negligible correlation coefficient (≈ 0.15), which is unlikely to affect the conclusion.

3.3.3 The Local Properties

Is the variation of $\tau_{\rm dep}$ between the centers and the disks correlated with $\Sigma_{\rm SFR}$, $\Sigma_{\rm mol}$, or both? In Figure 3.8, I show that there is an anti-correlation between $\log(\tau_{\rm center}/\tau_{\rm disk})$ and

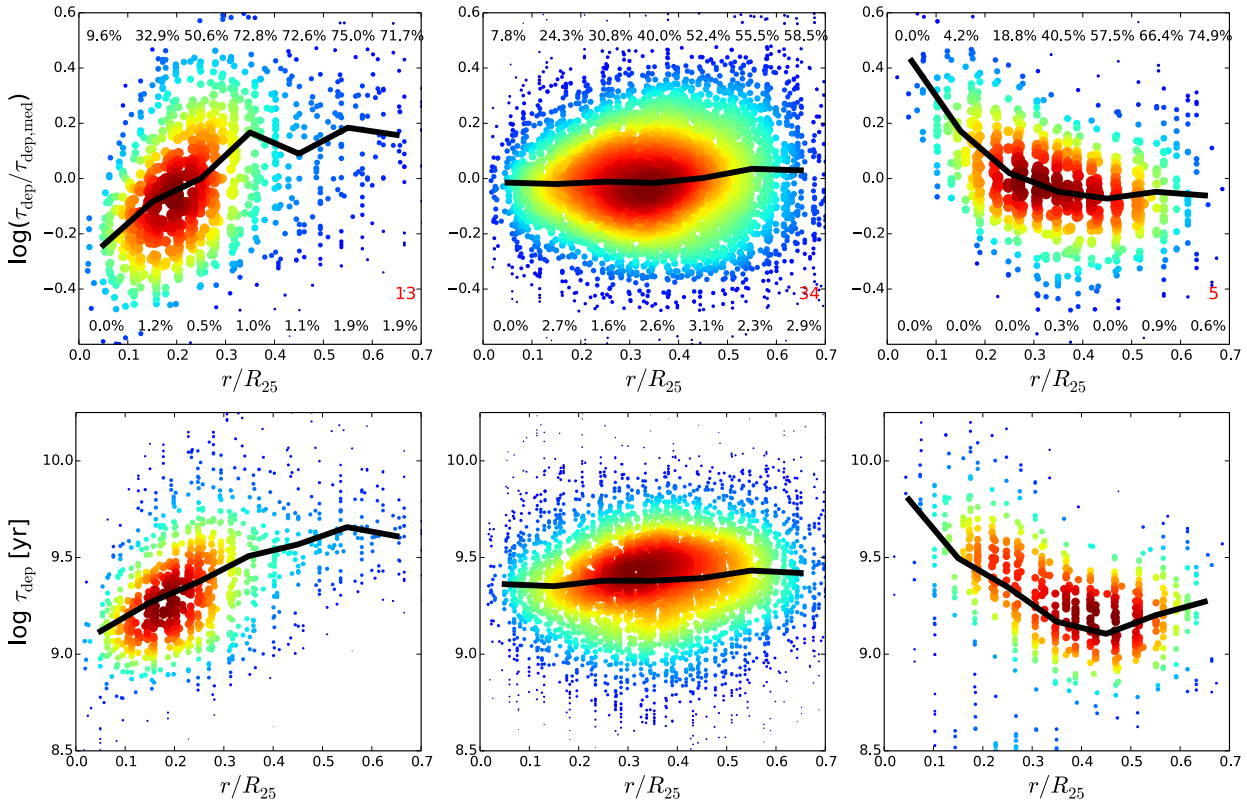

Figure 3.7: Classifications of $\tau_{\rm dep}$ over detected pixels: galaxies that show a drop of $\tau_{\rm dep}$ in the center (left), similar $\tau_{\rm dep}$ to the disk (middle), and longer $\tau_{\rm dep}$ in the center (right), in relative (top row) and absolute (bottom row) scales. The colors and sizes represent the density of data points. The median profiles for each groups are shown as black curves. The percentages on the top and bottom of top row are the fraction of non-detection, and the number of galaxies in each groups are stated in the bottom right corner of each top panels. This result extends the finding by Leroy et al. (2013), where I show more complex behaviors: galactic centers can have shorter, similar, or longer $\tau_{\rm dep}$ with respect to the disk.

$\log(\Sigma_{\rm SFR}^{\rm center}/\Sigma_{\rm SFR}^{\rm disk})$, but no correlation between $\log(\tau_{\rm center}/\tau_{\rm disk})$ and $\log(\Sigma_{\rm mol}^{\rm center}/\Sigma_{\rm mol}^{\rm disk})$. This means the drop of $\tau_{\rm center}$ is due to higher $\Sigma_{\rm SFR}$, not lower $\Sigma_{\rm mol}$ in the center. In other words, the centers can have any values of $\Sigma_{\rm mol}$, but those with higher $\Sigma_{\rm SFR}$ are associated with the drops of $\tau_{\rm center}$. However, we should be cautious because the range of $\Sigma_{\rm mol}$ variations ($\sim$ 1 dex) is smaller than the range of $\Sigma_{\rm SFR}$ variations ($\sim$ 2 dex).

Why do some centers have higher $\Sigma_{\rm SFR}$, irrespective of the $\Sigma_{\rm mol}$ value? In thermal and dynamical equilibrium, the weight of the ISM in the vertical gravitational field of stars and gas is balanced by the pressure created by momentum and energy from stellar feedback (Ostriker et al. 2010; Ostriker & Shetty 2011; Kim et al. 2011, 2013). Therefore, a relation

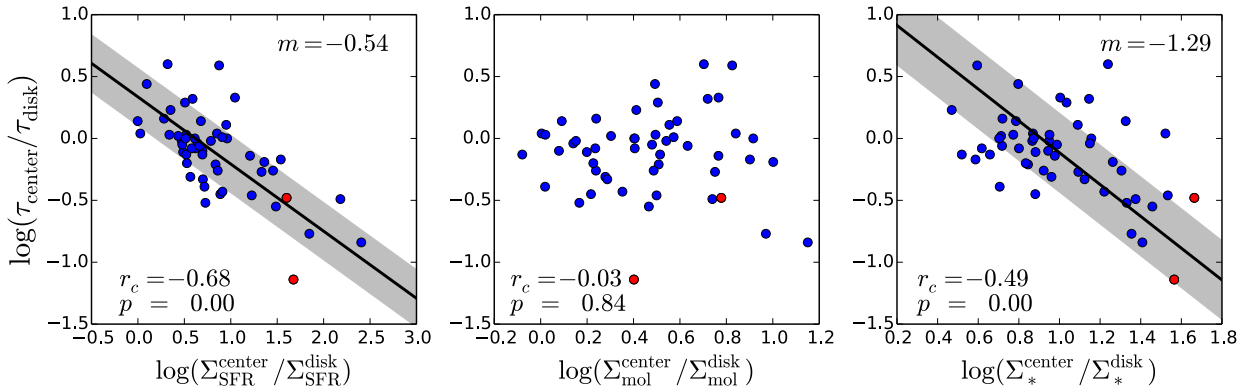

Figure 3.8: $\tau_{\rm center}$ relative to $\tau_{\rm disk}$ are plotted against Σ_*, $\Sigma_{\rm mol}$, and $\Sigma_{\rm SFR}$, averaged over detected regions in the center (left panel), the disk (middle panel), and the ratio between the two (right panel). The black lines are the linear fit with equal weight using the Orthogonal Distance Regression in `Scipy`, and the gray regions cover 68% of data points from the linear fit. The typical uncertainties of the data points are 4 $M_\odot$ pc^{-2} for Σ_* and $\Sigma_{\rm mol}$, and 10^{-4} $M_\odot$ yr^{-1} kpc^{-2} for $\Sigma_{\rm SFR}$. The slope of the correlation (m), the correlation coefficient (r_c), and the p-value (p) are indicated at the corner of each panels. I do not fit the middle panel because of low r_c and high p values, indicative of no correlation between $\log(\tau_{\rm center}/\tau_{\rm disk})$ and $\Sigma_{\rm mol}$.

between $\Sigma_{\rm SFR}$ (which sets the thermal, turbulent, and magnetic pressure via feedback) and Σ_* (which sets the ISM weight) is expected. Interestingly, in the right panels of Figure 3.8, we see that $\log(\tau_{\rm center}/\tau_{\rm disk})$ correlates with the ratio of the mean values of Σ_* between the center and the disk. Galaxies with higher ratio of central Σ_* relative to those in the disks, have a drop of $\tau_{\rm center}$. Since Σ_* is one of the determining factors for hydrostatic pressure (Elmegreen 1989; Blitz & Rosolowsky 2004, 2006; Ostriker et al. 2010), this means the drops of $\tau_{\rm center}$ are associated with high ISM pressure. Indeed, previous observations showed that the galactic center is a high pressure region (Spergel & Blitz 1992; Oka et al. 2001; Rosolowsky & Blitz 2005). This result suggests the star formation efficiency depends on the local environment within a galaxy.

3.4 Discussion

3.4.1 The CO-to-H_2 Conversion Factor

How is the variation of $\tau_{\rm center}$ affected by the change in the CO-to-H_2 conversion factor ($\alpha_{\rm CO}$)? In general, there are two scenarios where $\alpha_{\rm CO}$ varies (Bolatto et al. 2013). First, the dependence of $\alpha_{\rm CO}$ on gas metallicity – a lower gas metallicity needs a higher H_2 column density to shield the gas until it reaches sufficient extinction for CO to exist (e.g., Leroy et al. 2007, 2011). However, the variation of metallicity from center to disk within a galaxy

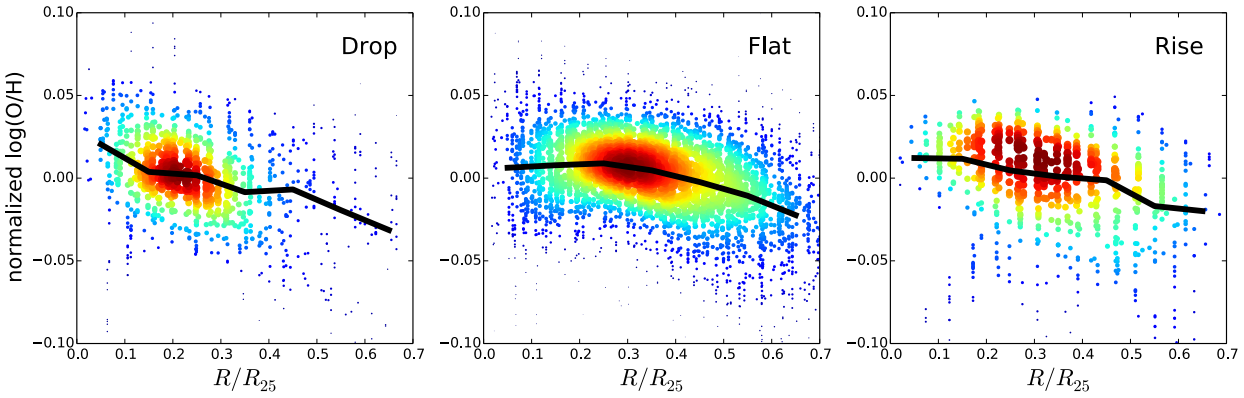

Figure 3.9: Plots of the gas-phase metallicities (12+log[O/H]), relative to their median value in a galaxy, as a function of radius for the three groups: drop of $\tau_{\rm center}$ (left), flat $\tau_{\rm dep}$ (middle), and rise of $\tau_{\rm center}$ (right). The median values are shown as the solid black curves and the colors represent the density of data points. The galaxies that show drops of $\tau_{\rm center}$ have steeper gradient of metallicity than the other two groups.

is very small ($\sim$ 0.1 dex; Figure 3.9), so that metallicity is unlikely to induce a significant variation in $\alpha_{\rm CO}$. Furthermore, in the group that shows a drop of $\tau_{\rm center}$, metallicities slightly rise towards the center, which means $\alpha_{\rm CO}$ is slightly lower in the center than in the disk. If we take this effect into account, it would only exaggerate the drop in $\tau_{\rm center}$.

The second source of $\alpha_{\rm CO}$ variations is the CO emission from diffuse gas that is bound by the gravitational potential of stars and gas. The velocity dispersion of this diffuse gas ($\sigma_{\rm CO,diff}$) reflects the additional stellar gravitational potential (Bolatto et al. 2013). This effect increases the CO luminosity ($L_{\rm CO}$) per unit molecular gas mass because $L_{\rm CO}$ is proportional to the brightness temperature (T_B) and $\sigma_{\rm CO,diff}$ (assuming CO is optically thick throughout the medium). Bolatto et al. (2013) and Sandstrom et al. (2013) suggested that the variation of $\alpha_{\rm CO}$ is related to the total surface density due to stars and gas as $\alpha_{\rm CO} \propto \Sigma_{\rm total}^{-\gamma}$, where $\gamma \approx 0.5$ for $\Sigma_{\rm total} > 100\ M_\odot\ {\rm pc}^{-2}$. Applying this prescription for $\alpha_{\rm CO}$ would exaggerate the drop in $\tau_{\rm center}$ and resulting in more galaxies in the group of $\tau_{\rm center}$ drops.

3.4.2 Metallicity Gradients

It is interesting that the metallicity in the drop $\tau_{\rm center}$ group rises toward the centers, while the metallicity profiles in the other two groups are flatten toward the centers (Figure 3.9). In the CALIFA sample, Sánchez-Menguiano et al. (2016) found the variation of metallicity gradients for different stellar masses: the metallicity gradient in higher mass galaxies is flattening in the center, while the metallicity gradient in lower mass galaxies is rising toward the center. Since the drop of $\tau_{\rm dep}$ is more prominent in the lowest mass bin (Figure 3.10), the variation of metallicity gradients in Figure 3.9 is possibly driven by their correlation with

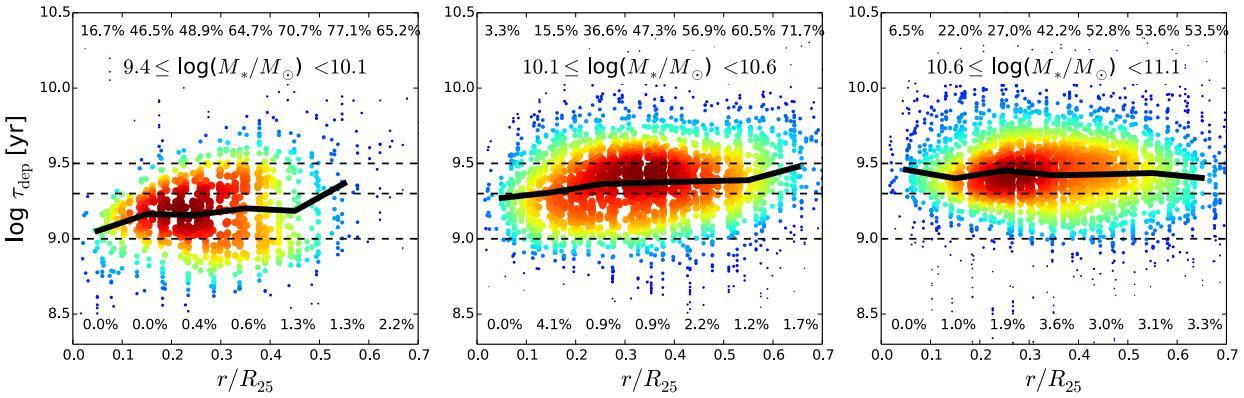

Figure 3.10: The molecular gas depletion time as a function of radius, separated in three mass bins: $9.6 \leq \log(M_*/M_\odot) < 10.3$ (left panel), $10.3 \leq \log(M_*/M_\odot) < 10.8$ (middle panel), and $10.8 \leq \log(M_*/M_\odot) < 11.3$ (right panel). The colors represent the density of data points. The percentages are the fraction of upper and lower limits at a given radial bin. The solid black lines are the median value of τ_{dep} at a given radial bin, while the dashed lines are the constant τ_{dep} values of 1, 2, and 3 Gyrs. This figure shows that the drop of τ_{dep} in the centers is more prominent in the lowest mass bin.

stellar masses. However, it remains unknown why the metallicity gradient depends on the stellar masses.

An alternative interpretation of steeper metallicity gradient is an enhancement of SFR per unit gas mass in the center (i.e. a low value of τ_{center}) leads to more metal enrichment than in the disk. Unlike stellar metallicity, gas-phase metallicity is more sensitive to the recent star formation, and hence, reflects the current value of τ_{center}. However, the center is not a closed-box system because of inflowing gas from the disk and outflowing gas driven by the stellar feedback. Furthermore, the gas-phase metallicity is also determined by the star formation history, not only the current star formation. Therefore, the rising gradient of metallicity in the short τ_{center} group is not clearly understood.

3.4.3 The Size of Molecular Disk

In Figure 3.7, we see that the distribution of data points in the short τ_{center} group is more concentrated toward the center, compared to those in the flat τ_{dep} group. This gives a clue that the size of molecular disk in the short τ_{center} group may be smaller (more compact). In order to quantify the compactness of the molecular gas and stellar distribution, I calculate the half-mass radius of molecular gas (R_{50}^{mol}) and stars (R_{50}^{*}) from the cumulative distribution of Σ_{mol} and Σ_* as a function of radius.

In Figure 3.11, we plot $\log(\tau_{center}/\tau_{disk})$ against R_{50}^{mol} and R_{50}^{*}. It turns out that galaxies in the drop τ_{center} group have smaller R_{50}^{mol} and R_{50}^{*} than those in the other groups. Furthermore,

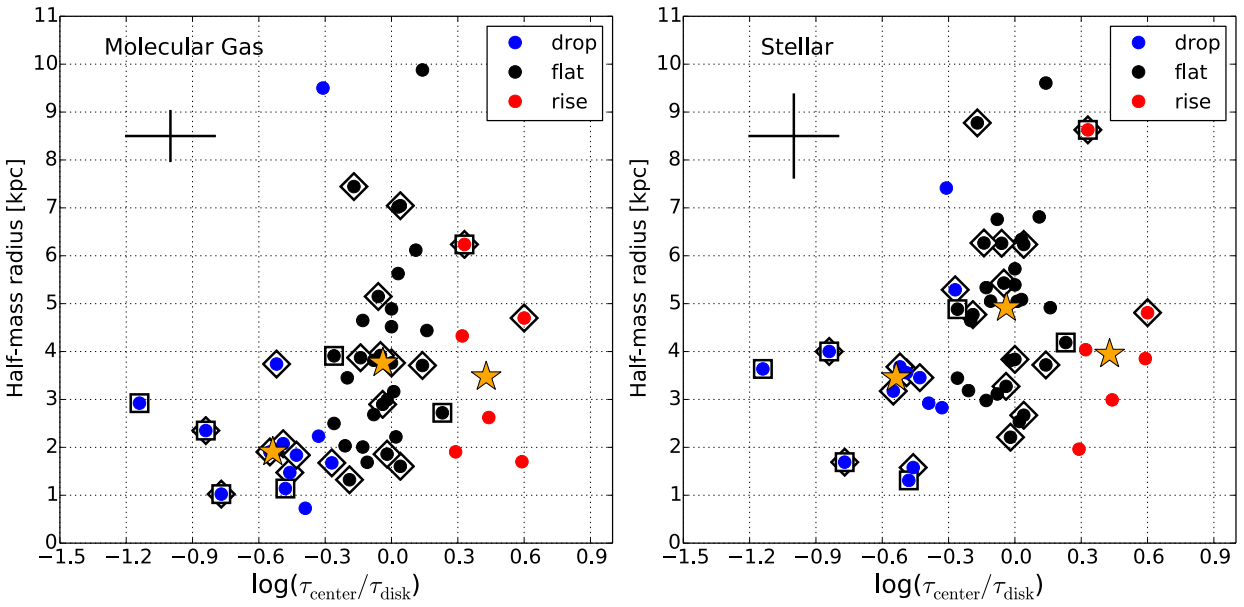

Figure 3.11: The half-mass radius of molecular gas (left panel) and stars (right panel) for three groups: central drop (blue dots), flat (black dots), and central rise (red dots) of $\tau_{\rm dep}$. The mean values for each three groups are marked as orange stars symbols. The typical errors are shown as crosses. The diamond symbols marked the barred galaxies, while the square symbols marked the interacting galaxies. This shows that the molecular gas distribution in the drop $\tau_{\rm center}$ group and in the disturbed (barred or interacting) galaxies is more compact than those in the other groups.

the disturbed (barred and interacting) galaxies tend to have smaller $R_{50}^{\rm mol}$ than unbarred, isolated galaxies. Quantitatively, about 75% of galaxies in the drop $\tau_{\rm center}$ group are disturbed system, compared to only 44% and 40% for the flat $\tau_{\rm dep}$ and the rise $\tau_{\rm center}$ group, respectively. The mean values of $\log(\tau_{\rm center}/\tau_{\rm disk})$ for the disturbed and isolated galaxies are -0.22 ± 0.38 and 0.00 ± 0.23, respectively, while the mean values of $R_{50}^{\rm mol}$ for the disturbed and isolated galaxies are 3.21 ± 1.77 kpc and 3.87 ± 2.28 kpc, respectively. This suggests that the driver of physical size of the stellar and molecular gas distribution (e.g. bar and interactions) is linked to the cause of $\tau_{\rm dep}$ variation in the centers. I suspect that the bar drives the gas inward toward the center (or in the case of interacting galaxies, the gas loses its angular momentum). This radial gas compression increases the pressure, and resulting in a higher star formation efficiency in the galactic center.

3.4.4 A Burst of Star Formation

There may be a central starburst activity on scales below our resolution, as indicated by the stellar population ages. At least there are two tracers of the stellar population ages: the UV-to-Hα ratio (e.g., Leroy et al. 2012; Weisz et al. 2012) and the age derived from the stellar

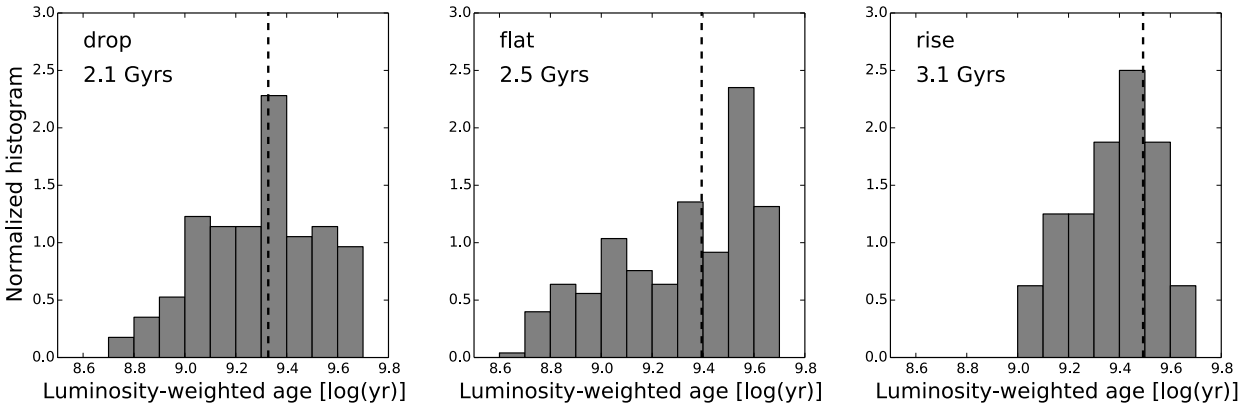

Figure 3.12: The histogram of luminosity-weighted stellar population ages (from CALIFA; Sánchez et al. 2016) in the center of galaxies ($r \leq 0.1\ R_{25}$) that show a drop of $\tau_{\rm center}$(left panel), flat $\tau_{\rm dep}$ (middle panel), and a rise of $\tau_{\rm center}$ (right panel). The dashed lines mark the median ages, with their values are noted in top left corner of each panels. The stellar populations in the centers of drop $\tau_{\rm center}$ group tend to be younger than the other two groups, consistent with the idea of a bursting period of star formation.

population synthesis (which is available in the IFU data products of Sánchez et al. 2016). Since I do not have the resolved UV maps in hand, I can only rely on the second tracer. In Figure 3.12, I show the histogram of the luminosity-weighted ages of stellar populations in the centers ($r < 0.1\ R_{25}$) for each $\tau_{\rm dep}$ groups. It turns out that the centers in the drop $\tau_{\rm center}$ group (left panel) tend to have younger ages of stellar populations ($\approx 2.1 \pm 1.1$ Gyrs) than the other two groups ($\approx 2.5 \pm 1.6$ and $\approx 3.1 \pm 1.6$ Gyrs; middle and right panels). This strengthens our suspicion that the centers of the short $\tau_{\rm center}$ group currently undergo a burst of star formation. However, further high resolution data are needed to confirm it.

3.5 Summary

I present results from the EDGE survey, a spatially resolved CO follow-up to an IFU survey of local galaxies (CALIFA). I combine the CO and optical IFU data to study the variation of $\tau_{\rm dep}$ between the centers and the disks in 52 local galaxies. The findings of this study are the following.

1. Galactic centers can have shorter, longer, or similar $\tau_{\rm dep}$ compared to the disks (Figure 3.7), extending the previous result by Leroy et al. (2013). The short $\tau_{\rm center}$ group (representing 25% of the samples with $\tau_{\rm center} \sim 1$ Gyr) resembles the intermediate regime between the disks ($\tau_{\rm disk} \sim 2.4$ Gyrs) and starbursts ($\tau_{\rm dep} \sim 0.2$ Gyrs). Applying the decrease in CO-to-H_2 conversion factor inferred from the increase in metallicity

and stellar surface density towards the galactic center would increase the estimated drop in $\tau_{\rm center}$.

2. The drop of $\tau_{\rm center}$ is caused by higher central $\Sigma_{\rm SFR}$ than those in the disk, not lower $\Sigma_{\rm mol}$ (Figure 3.8), and vice versa. Furthermore, galaxies with higher stellar density contrast in the center (i.e. higher $\Sigma_*^{\rm center}/\Sigma_*^{\rm disk}$) tend to have shorter $\tau_{\rm center}/\tau_{\rm disk}$. Since the dynamical equilibrium pressure depends on Σ_* (Blitz & Rosolowsky 2004, 2006; Ostriker et al. 2010), this suggests that the central drop in $\tau_{\rm dep}$ is driven by high pressure. This is expected for the star formation self-regulated model, in which the star formation rate locally adjusts so that feedback from massive stars offsets turbulent energy dissipation and cooling. A high feedback rate (short $\tau_{\rm dep}$) is required to maintain the high pressure in regions where the vertical gravity from stars and gas is very strong (Ostriker et al. 2010; Ostriker & Shetty 2011; Kim et al. 2011, 2013).

3. The gradient of oxygen abundance rise towards the center for galaxies in the short $\tau_{\rm center}$ group, while the gradient is flat in the other groups (Figure 3.9). This could be either the stellar mass effect, where the gradient of oxygen abundance is flat in massive galaxies (as found by Sánchez-Menguiano et al. 2016), or the oxygen abundance is sensitive to the current star formation efficiency. However, the narrow range of the oxygen abundance variation in the sample ($\sim$ 0.2 dex) becomes the limitation of the analysis.

4. There are two signatures for dynamical effects that drive the variation of $\tau_{\rm center}$ versus $\tau_{\rm disk}$. First, the barred and interacting galaxies tend to have lower values of $\log(\tau_{\rm center}/\tau_{\rm disk})$ than the unbarred, isolated galaxies (Figure 3.6). Second, the size of molecular gas disk is smaller in the drop $\tau_{\rm center}$ group than in the other groups (Figure 3.11). I suspect that the bar drives the gas inward toward the center (or in the case of interacting galaxies, the gas loses its angular momentum). This radial gas compression increases the pressure, resulting in higher star formation efficiency in the galactic center (Krumholz & Kruijssen 2015).

In conclusion, these findings imply that the formation of stars from the molecular gas depends on the local environment within a galaxy (such as Σ_*) and the galaxy dynamics induced by bar or interactions. In the future, I am interested to measure the dense gas (as traced by HCN lines) to investigate whether the short $\tau_{\rm center}$ is also due to a higher fraction of the dense gas in the center. In addition, measuring the shear rate and the inflow speed in barred galaxies will give a better evidence of the importance of galactic dynamics in driving $\tau_{\rm dep}$. Finally, expanding our sample towards early-type and low mass galaxies using ALMA is a natural approach to expand our statistical sample in the three groups of $\tau_{\rm dep}$.

3.6 Appendix A. List of Galaxy Sample

Table 3.1: The list of galaxy properties in the sample.

No.	Galaxies	M_*[a] $\log(M_\odot)$	$M_{\rm mol}$[b] $\log(M_\odot)$	R_{25}[c] kpc	Beam[d] kpc	Dist.[e] Mpc	Inc.[f] deg.	P.A.[f] deg.	$\tau_{\rm center}$ log(yr)	$\tau_{\rm disk}$ log(yr)	$\tau_{\rm med}$ log(yr)	Group	Bar[g]	Inter.[h]
1	IC1151	9.82	7.93	10.01	0.67	30.80	68.0	208.9	8.94	9.04	8.99	flat	N	N
2	IC1199	10.58	9.35	11.83	1.52	68.25	64.5	337.3	9.45	9.58	9.56	flat	N	N
3	IC1683	10.56	9.68	13.34	1.47	69.73	44.8	20.6	9.15	9.64	9.64	drop	Y	N
4	NGC0477	10.70	9.54	19.29	1.86	85.42	60.0	150.0	9.37	9.68	9.66	drop	N	N
5	NGC0496	10.64	9.48	11.34	1.82	87.47	57.0	38.5	9.15	9.23	9.22	flat	N	N
6	NGC0551	10.75	9.39	16.10	1.54	74.50	64.2	320.0	9.62	9.58	9.61	flat	Y	N
7	NGC2253	10.60	9.62	10.61	1.20	51.16	47.4	300.0	9.37	9.37	9.37	flat	Y	N
8	NGC2347	10.84	9.56	15.25	1.49	63.75	50.2	189.1	9.48	9.34	9.38	flat	Y	N
9	NGC2730	9.93	9.00	11.52	1.26	54.78	27.7	260.8	9.13	9.24	9.23	flat	N	N
10	NGC2906	10.38	9.11	7.44	0.94	37.73	55.7	265.0	9.78	9.34	9.40	rise	N	N
11	NGC3381	9.68	8.11	6.87	0.50	23.40	30.8	43.1	8.86	9.31	9.30	drop	Y	N
12	NGC3811	10.44	9.28	13.05	0.96	44.25	42.5	359.0	9.32	9.28	9.31	flat	Y	N
13	NGC3815	10.32	9.16	11.22	1.14	53.59	59.9	67.8	9.43	9.47	9.45	flat	Y	N
14	NGC3994	10.39	9.26	5.53	1.02	44.75	59.5	188.1	9.07	8.78	8.81	flat	N	N
15	NGC4047	10.67	9.66	10.95	1.06	49.06	42.1	105.0	9.41	9.43	9.41	flat	N	N
16	NGC4470	10.03	8.59	6.23	0.78	33.43	47.5	359.5	8.74	8.87	8.85	flat	N	N
17	NGC4644	10.48	9.20	15.77	1.60	71.65	72.9	57.0	9.59	9.56	9.57	flat	N	N
18	NGC4711	10.38	9.18	10.31	1.32	58.83	58.3	215.0	9.60	9.44	9.45	flat	N	N
19	NGC4961	9.77	8.41	5.93	0.78	36.58	46.6	90.0	9.21	9.23	9.22	flat	Y	N
20	NGC5000	10.74	9.45	15.04	1.62	80.80	20.0	1.3	9.40	9.59	9.53	flat	Y	N
21	NGC5016	10.27	8.90	8.45	0.83	36.90	39.9	57.4	9.10	9.43	9.40	drop	N	N
22	NGC5056	10.64	9.45	19.14	1.96	81.14	61.4	178.0	9.03	8.43	8.51	rise	Y	N
23	NGC5480	9.97	8.92	6.57	0.52	26.96	41.5	178.0	8.99	9.20	9.20	flat	N	N
24	NGC5520	9.87	8.67	6.25	0.55	26.73	59.1	245.1	8.99	9.45	9.30	drop	Y	N
25	NGC5633	10.20	9.14	5.29	0.71	33.38	41.9	16.9	9.25	9.23	9.24	flat	N	N
26	NGC5657	10.29	9.11	14.34	1.20	56.33	68.3	344.0	9.00	9.55	9.52	drop	Y	N
27	NGC5732	10.03	8.82	9.66	1.25	54.00	58.4	43.2	9.16	9.42	9.41	flat	N	N
28	NGC5784	11.09	9.40	17.12	1.67	79.42	45.0	252.0	9.26	10.40	9.95	drop	N	Y
29	NGC5930	10.40	9.33	10.01	0.83	37.23	45.0	155.0	9.27	10.04	9.71	drop	Y	Y
30	NGC5934	10.66	9.81	7.35	1.76	82.71	55.0	5.0	10.00	9.77	9.79	flat	N	Y
31	NGC5947	10.67	9.26	14.61	1.92	86.07	32.2	206.6	9.09	9.61	9.59	drop	Y	N
32	NGC5953	10.18	9.49	6.09	0.61	28.43	26.1	43.3	9.12	9.60	9.47	drop	N	Y

Continued on Next Page

No.	Galaxies	M_*[a] log($M_\odot$)	$M_{\rm mol}$[b]	R_{25}[c] kpc	Beam[d] kpc	Dist.[e] Mpc	Inc.[f] deg.	P.A.[f] deg.	$\tau_{\rm center}$ log(yr)	$\tau_{\rm disk}$ log(yr)	$\tau_{\rm med}$ log(yr)	Group	Bar[g]	Inter.[h]
33	NGC5980	10.61	9.70	14.10	1.27	59.36	66.2	15.0	9.47	9.15	9.19	rise	N	N
34	NGC6004	10.66	9.33	15.19	1.22	55.21	37.3	277.3	9.61	9.66	9.63	flat	Y	N
35	NGC6060	10.78	9.68	17.41	1.28	63.24	64.3	102.0	9.39	9.36	9.38	flat	N	N
36	NGC6155	10.18	8.94	6.68	0.77	34.60	44.7	130.0	9.02	9.10	9.08	flat	N	N
37	NGC6186	10.41	9.46	9.68	0.92	42.38	71.2	69.8	9.32	9.49	9.46	flat	Y	N
38	NGC6301	10.98	9.96	31.24	2.63	121.36	52.8	288.5	9.75	9.61	9.65	flat	N	N
39	NGC7738	11.01	9.99	16.87	1.90	97.82	65.6	244.7	9.17	10.01	9.74	drop	Y	Y
40	NGC7819	10.41	9.27	14.99	1.43	71.62	54.0	280.3	9.28	9.55	9.54	flat	Y	N
41	UGC03253	10.43	8.88	11.88	1.57	59.46	58.3	267.7	8.88	9.31	9.29	drop	Y	N
42	UGC04132	10.74	10.02	13.51	1.70	75.35	72.0	212.6	9.35	9.41	9.41	flat	Y	N
43	UGC04461	10.17	9.24	14.51	1.59	72.27	70.1	215.8	9.36	9.35	9.36	flat	N	N
44	UGC05108	10.90	9.75	18.84	2.81	118.41	66.1	133.1	9.47	9.61	9.53	flat	Y	N
45	UGC07012	9.70	8.35	6.96	0.92	44.28	60.5	182.1	8.75	9.14	9.13	drop	N	N
46	UGC08107	11.00	10.11	40.43	2.75	121.62	71.4	233.2	9.92	9.59	9.60	rise	Y	Y
47	UGC09067	10.76	9.83	13.54	2.75	114.50	62.4	14.6	9.46	9.46	9.46	flat	N	N
48	UGC09476	10.23	9.15	10.19	1.01	46.63	48.5	312.0	9.32	9.52	9.50	flat	N	N
49	UGC09542	10.32	9.31	16.64	1.65	79.70	72.7	214.3	9.56	9.56	9.56	flat	N	N
50	UGC09759	9.81	9.07	9.55	1.03	49.25	66.8	54.7	10.20	9.61	9.69	rise	N	N
51	UGC10205	10.88	9.60	19.95	2.21	94.92	51.7	118.6	9.56	9.82	9.81	flat	N	Y
52	UGC10710	10.72	9.88	29.51	2.63	121.69	69.6	329.5	9.61	9.50	9.50	flat	N	N

[a] The stellar mass assuming Kroupa IMF from the CALIFA survey (Sánchez et al. 2016).
[b] The molecular gas mass assuming CO-to-H_2 conversion factor of 4.4 $M_\odot$ pc^{-2} (K km s^{-1} pc^2)$^{-1}$ from the EDGE survey (Bolatto et al. 2017), including mass contribution from Helium.
[c] The radius where the surface brightness is 25 mag/arcsec^2 in the $B-$band, from the HyperLEDA catalog (Makarov et al. 2014).
[d] The physical beam size, calculated from the geometric mean of the major and minor axes of the EDGE beam.
[e] The luminosity distance computed from the CALIFA redshift for ionized gas lines assuming $H_0 = 70$ km s^{-1}, $\Omega_{\rm m} = 0.27$, and $\Omega_\Lambda = 0.73$.
[f] The inclination and position angle are taken from the following, ordered by priority: (1) the best fit of CO rotation curve (Levy et al. in preparation), whenever it is possible, (2) from the shape of the outer isophote, or (3) from the HyperLEDA catalog (Makarov et al. 2014).
[g] The bar assignments (`Yes` or `No`) are taken from the following, ordered by priority: (1) the photometric fit from Méndez-Abreu et al. (2017), or (2) the HyperLEDA catalog (Makarov et al. 2014).
[h] The assignment for interacting galaxies (`Yes` or `No`), taken from Barrera-Ballesteros et al. (2015).

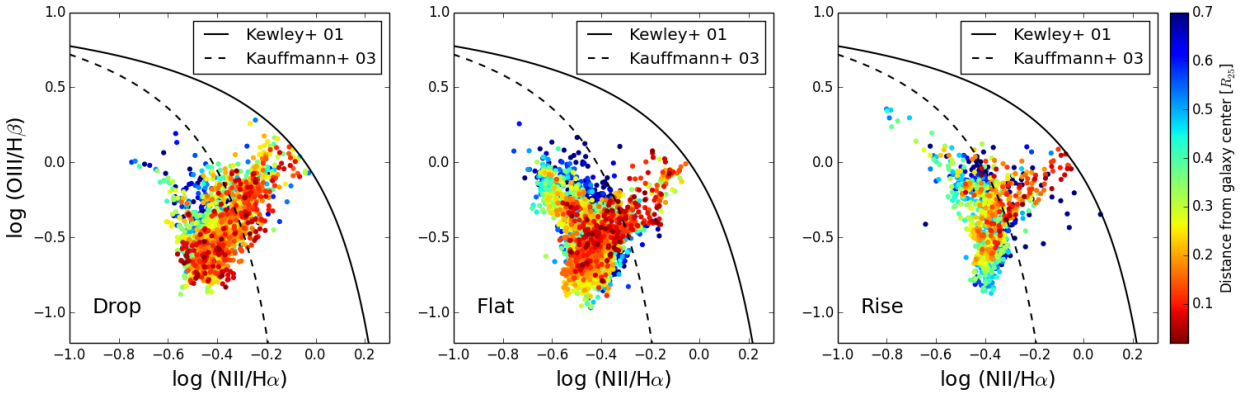

Figure 3.13: The plots of BPT diagram of galaxies that show fall, flat, and rise of $\tau_{\rm dep}$ at the centers, color coded by their distance from the galactic center, so that red is the center and blue is the outskirt. The red dots are placed on top of the other colors, i.e. there are blue dots at the same location with red dots but not shown in the figure. Two demarcation curves from Kewley & Dopita (2002) and Kauffmann et al. (2003) are shown as solid and dashed curves, respectively. Any data points above the solid lines have been blanked and are not shown in the figure.

3.7 Appendix B. The Locations of Central Regions in the BPT Diagram

Even though we already excluded pixels that show AGN and LINER emission, there may be a concern of whether the regions that have a drop of $\tau_{\rm center}$ are located in the composite region between AGN and star formation, i.e. the region between the demarcation curves of Kewley & Dopita (2002) and Kauffmann et al. (2003). In Figure 3.13, I show that this is not the case, where the percentages of the central pixels in the composite region are only 39% and 30% for the drop and flat $\tau_{\rm center}$ group, respectively. However, 78% of central pixels in the rise $\tau_{\rm center}$ group are located in the composite region, which means they may still be contaminated by AGN.

3.8 Appendix C. Balmer Decrement Method

In general, the intrinsic luminosity ($L_{\rm int}$) of an object is related to the observed luminosity ($L_{\rm obs}$) and extinction (in magnitude) at wavelength λ (A_λ) as $L_{\rm int} = L_{\rm obs} \times 10^{0.4A_\lambda}$. For a given extinction curve (k_λ; e.g., Cardelli et al. 1989; Calzetti et al. 2000), the extinction is related to color excess as

$$A_\lambda = k_\lambda \; E(B-V), \tag{3.2}$$

where $E(B-V) \equiv A_B - A_V = (B-V)_{\rm obs} - (B-V)_{\rm int}$. Color excess between H$\alpha$ and Hβ fluxes is

$$E(\mathrm{H}\beta - \mathrm{H}\alpha) = -2.5 \log \left[\frac{(\mathrm{H}\alpha/\mathrm{H}\beta)_{\rm int}}{(\mathrm{H}\alpha/\mathrm{H}\beta)_{\rm obs}} \right], \tag{3.3}$$

and related to $E(B-V)$ as

$$E(\mathrm{H}\beta - \mathrm{H}\alpha) = [k_{\mathrm{H}\beta} - k_{\mathrm{H}\alpha}]\ E(B-V). \tag{3.4}$$

Combining Equations 3.2, 3.3 and 3.4, we get

$$A_{\mathrm{H}\alpha} = \frac{2.5}{\frac{k_{\mathrm{H}\beta}}{k_{\mathrm{H}\alpha}} - 1} \log \left[\frac{(\mathrm{H}\alpha/\mathrm{H}\beta)_{\rm obs}}{2.86} \right], \tag{3.5}$$

where I use $(\mathrm{H}\alpha/\mathrm{H}\beta)_{\rm int} = 2.86$ for case B recombination at temperature of 10^4 K and electron density of 100 cm^{-3} (Osterbrock 1989). $A_{\mathrm{H}\alpha}$ is then applied to get the extinction free Hα luminosity as $L(\mathrm{H}\alpha)_{\rm int} = L(\mathrm{H}\alpha)_{\rm obs} \times 10^{0.4 A_{\mathrm{H}\alpha}}$.

3.9 Appendix D. The Radial Profiles of Depletion Time

The classification of $\tau_{\rm center}$ in §3.3.2 only takes into account the detected regions in both $\Sigma_{\rm mol}$ and $\Sigma_{\rm SFR}$. We now check the robustness of our results by including the upper and lower limits of $\tau_{\rm dep}$. For the upper limit, we replace $\Sigma_{\rm SFR}$ non-detection as zeros and $\Sigma_{\rm mol}$ non-detection as 2σ rms. Then, we calculate the molecular gas mass and SFR within an azimuthal ring (radial bin), and take their ratio as $\tau_{\rm dep}$. The same approach is done to calculate the lower limit of $\tau_{\rm dep}$, except we replace $\Sigma_{\rm SFR}$ non-detection as 2σ rms and $\Sigma_{\rm mol}$ non-detection as zero. This line is lower than some of the non-detected pixels (triangles) because pixels with zero value of $\Sigma_{\rm mol}$ or $\Sigma_{\rm SFR}$ has $\log(\tau_{\rm dep}) = \pm\infty$, and hence, these pixels cannot be plotted in Figure 3.14. These upper and lower limits mark the most optimistic and pessimistic values of $\tau_{\rm dep}$. However, the actual value of $\tau_{\rm dep}$ is within those limits. Therefore, we take the mean value between the upper and lower limits as the radial profile of $\tau_{\rm dep}$, which is shown as the blue line in Figure 3.14. This profile should be equivalent to a $\tau_{\rm dep}$ profile by replacing the non-detection with 1σ uncertainty. For comparison, the profiles of $\tau_{\rm dep}$ with the detection only are shown as the black lines in Figure 3.14.

As in §3.3.2, we define $\tau_{\rm center}$ as $\tau_{\rm dep}$ within 0.1 R_{25} and $\tau_{\rm disk}$ as $\tau_{\rm dep}$ between 0.1 and 0.7 R_{25}. Then, we compare the value of $\tau_{\rm center}$ and $\tau_{\rm disk}$ by using a threshold value of 0.26 dex. If $\log(\tau_{\rm center}/\tau_{\rm disk})$ is less than -0.26, then that galaxy is in the drop category, and vice versa. For $\log(\tau_{\rm center}/\tau_{\rm disk})$ in between -0.26 dex and 0.26 dex, we assign that galaxy in the flat category.

In Figure 3.15, we plot the values of $\log(\tau_{\rm center}/\tau_{\rm disk})$ that are obtained in §3.3.2 as the $x-$axis and by including non-detection as the $y-$axis. While there is a correlation between the two, it is not an one-to-one correlation. The discrepancy between the two methods is larger in the lower left, where $\tau_{\rm center} < \tau_{\rm disk}$. This is because galaxies in the drop category are

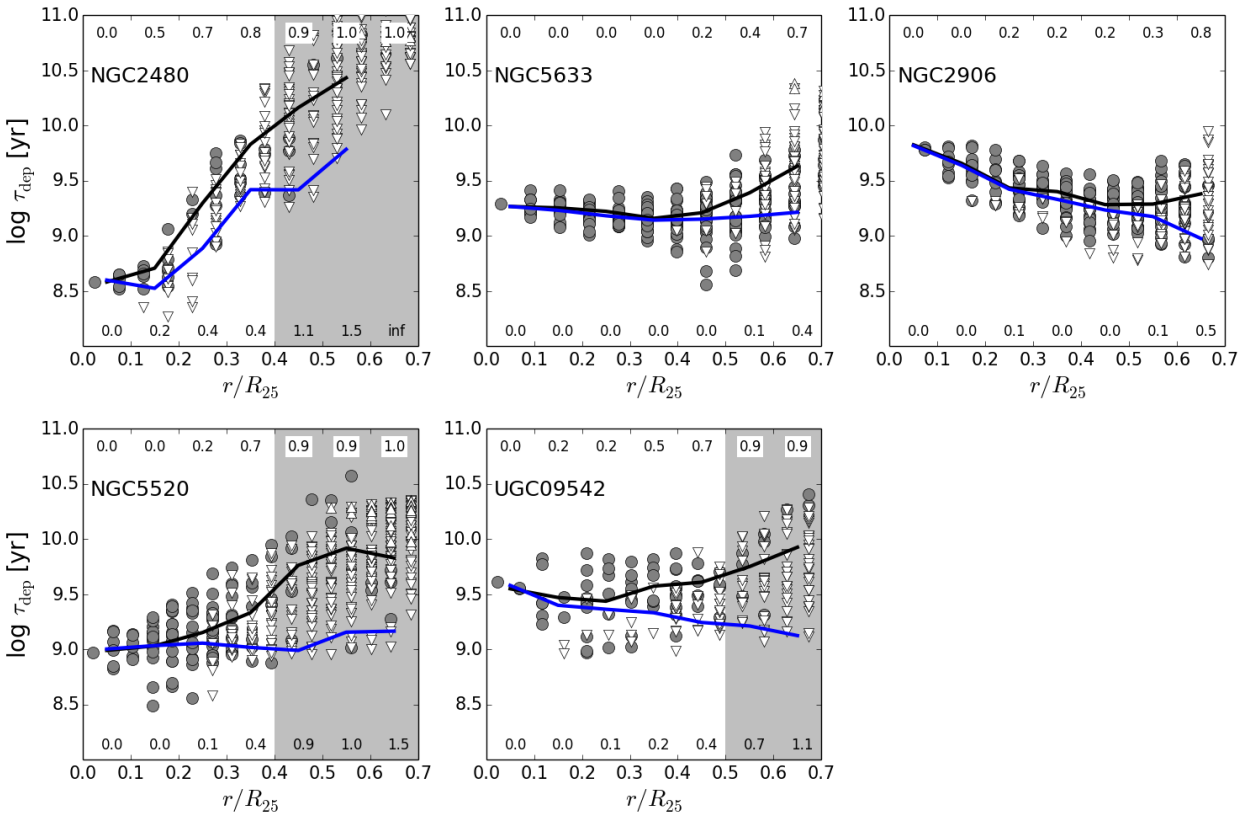

Figure 3.14: Examples of the azimuthally averaged profiles of $\tau_{\rm dep}$ for three groups: drop (left panel), flat (middle panel), and rising (right panel) $\tau_{\rm dep}$ in the center. Each panel in the *top row* is a galaxy that has the *same classification* in both the detection only and azimuthally averaged profiles. Each panel in the *bottom row* shows a galaxy that is classified as drop (left panel) and flat (middle panel) categories based on the detection only, but is classified as flat and rise, respectively, in the azimuthally averaged profile (see Table 3.9). The gray circles are the detection points and the triangles are upper and lower limits. The black lines are the radial profiles based on detection only, while the blue lines are the radial profiles after the inclusion of non-detection. The decimal numbers on top and bottom of each panels are the fraction of non-detection within radial bins and the difference between upper and lower blue line (in dex), respectively. The gray area indicates the radius where difference between the upper and lower limits of $\tau_{\rm dep}$ profiles is larger than 0.5 dex (i.e. where the effect of non-detections become important).

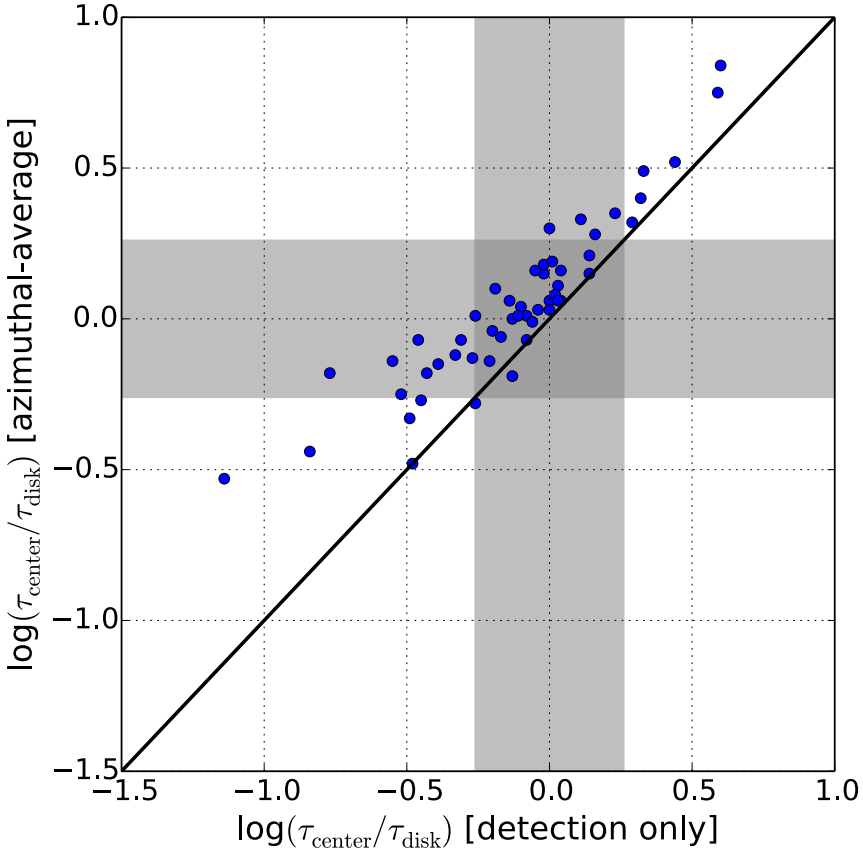

Figure 3.15: A comparison of $\log(\tau_{\rm center}/\tau_{\rm disk})$ between the detection only and after including non-detection (azimuthal-average) as $\sim 1\sigma$. The black line is one-to-one correlation. The gray bands mark the spaces of flat category in each method. The number of galaxies in each category is tabulated in Table 3.9.

more dominated by non-detections in the disk. This is also apparent in Figure 3.7, where the data points in the left panel are more concentrated toward the center than that in the middle panel.

A comparison of the number of galaxies in each group, obtained with the detection only and including the non-detection is presented in Table 3.9. After the inclusion of non-detection, the number of galaxies that are classified in the drop category is reduced from 14 to 5 (the rest of them becomes the members of flat category). This reduction is expected because of the combination of three effects: (1) the upper limit of $\tau_{\rm dep}$ tends to be smaller than the detected $\tau_{\rm dep}$, (2) the Hα measurement is more sensitive than the CO measurement, so that there are more upper limit pixels than lower limit pixels, and (3) non-detected pixels tend to be located in the disk where $\Sigma_{\rm mol}$ is smaller than that in the center. These effects also reduce the number of galaxies that previously classified into the flat category in §3.3.2,

Table 3.2: Comparison of categories between the method in §3.3.2 (detection only) and azimuthal-average profile by including non-detection (this section)

		Detection Only			
		Drop	Flat	Rise	Total
Azimuthal average	Drop	5	1	0	6
	Flat	9	27	0	36
	Rise	0	4	6	10
	Total	14	32	6	52

from 32 to 27 galaxies, while the number of galaxies in the rise category remains the same. If we refer to the number of galaxies that are classified in the same group for both method (i.e. the diagonal of Table 3.9) as "true-positive", then we get a true-positive rate of 73.1%.

These exercises show the sensitivity limit of our observations. Nevertheless, the variation of $\tau_{\rm dep}$ within the regions where CO is detected ($\Sigma_{\rm mol} \sim 10\ M_\odot\ {\rm pc}^{-2}$) is also important because these are the regions where the molecular gas dominates over the atomic gas, and supposedly denser regions where stars form (e.g. Giant Molecular Associations). Therefore, if this region forms stars more efficiently in the center than in the disk (or vice versa), then a physical mechanism must be in play to make this happens.

Acknowledgments

I thank the members of the EDGE–CALIFA collaboration: Alberto Bolatto, Tony Wong, Leo Blitz, Sebastian Sanchez, Stuart Vogel, Eve Ostriker, Adam Leroy, Dario Colombo, Rebecca Levy, and Yixian Cao. I also thank John Carpenter for his help in managing the schedule of CARMA observations, Christopher McKee and Christine Wilson for valuable inputs, and Garrett Keating and Shaye Storm for being my partners during CARMA observations. This work is supported by the National Science Foundation (NSF) under grants AST-1140063 and AST-1616924. I acknowledge the usage of the HyperLeda database (http://leda.univ-lyon1.fr). Support for the CARMA construction was derived from the states of California, Illinois, and Maryland, the James S. McDonnell Foundation, the Gordon and Betty Moore Foundation, the Kenneth T. and Eileen L. Norris Foundation, the University of Chicago, the Associates of the California Institute of Technology, and NSF. This research is based on observations collected at the Centro Astronomico Hispano Aleman (CAHA) at Calar Alto, operated jointly by the Max-Planck Institute for Astronomy (MPIA) and the Instituto de Astrofisica de Andalucia (CSIC).

Chapter 4

The Origin of Interstellar Turbulence in M33

I utilize the multi-wavelength data of M33 to study the origin of turbulent energy in the interstellar medium. First, I show that the (azimuthally-averaged) gas kinetic energy density is roughly constant ($\sim 3 \times 10^{45}$ erg pc^{-2}) from 3 kpc to 6 kpc of galactocentric radius, driven by the lack of variation in H I surface density and velocity dispersion. Inside 3 kpc, the kinetic energy density rises to $\sim 1 \times 10^{46}$ erg pc^{-2}, while in the outermost region ($\sim$ 7.5 kpc), the kinetic energy density declines to $\sim 5 \times 10^{44}$ erg pc^{-2} due to lack of H I detection.

Then, I separate the gas into the cold and warm neutral media (CNM and WNM, respectively) by using the thermal equilibrium in the Milky Way from Wolfire et al. (2003). The thermal energy is derived as the sum of the thermal energy of the gas in CNM and WNM. The turbulent energy is determined as the difference between the kinetic energy and the thermal energy. This turbulent energy dominates over the thermal energy inside 3 kpc radius, while both energy are comparable to each other outside 3 kpc radius of M33.

Finally, the energies injected by supernovae (SNe) and the magneto-rotational instability (MRI) are considered as the sources of turbulence. I find that the turbulence inside $r \sim 4$ kpc (equivalents to $r \sim 0.5\ R_{25}$) can be maintained by SNe energy, while the MRI has enough energy to maintain turbulence in the outer part of M33, where SNe energy is negligible. Furthermore, SNe energy can maintain turbulence within the individual molecular clouds with $\sim$ 10% of coupling efficiency. I conclude that the sum of SNe and MRI energy has enough energy to maintain turbulence at all radii in M33.

4.1 Introduction

The interstellar medium (ISM) is known to be turbulent, from kpc scale of galaxies to sub-pc scale of protoplanetary disk (e.g., Elmegreen & Scalo 2004; McKee & Ostriker 2007; Hennebelle & Falgarone 2012). At kpc scale, observations found that the H I velocity dispersion ($\sigma_{\rm HI}$) in the galactic disk is $\sim$ 10 km s^{-1} (e.g., Dickey et al. 1990), larger than

the thermal broadening (~ 7 km s^{-1} for the warm neutral phase; Wolfire et al. 1995). This extra kinetic energy that stirs ISM is attributed to turbulence.

The first evidence of turbulent dissipation is reported by Larson (1981), who showed that the linewidth of gas (ΔV) is related to the size of molecular clouds (R) as $\Delta V \propto R^{1/3}$. This empirical relation is identical to the predicted dissipation energy of turbulence through cascades by Kolmogorov (1941). In later work, however, Solomon et al. (1987) revised this scaling relation to the power of half, instead of a third, and hence, the linewidth–size relation is probably just a reflection of the virial equilibrium state (e.g., Heyer et al. 2009; Utomo et al. 2015).

Over many decades, the origin of turbulent energy and how turbulence is maintained over the Hubble time remain as questions. In this chapter, I attempt to answer that question by measuring the turbulent energy in M33 and compare it with various sources of turbulent energy (Mac Low & Klessen 2004): magneto-rotational instability (MRI), rotational instability, stellar feedback, and accretion. For each of them, I recollect the formula from the literature to measure their energy densities and compare them to the turbulent energy.

M33 is an ideal place to study the interstellar turbulence for two reasons. First, the existence of high quality multi-wavelength data (from UV to radio) enables us to compare the turbulent energy with the energy generated from the stellar feedback and MRI. Second, the high resolution data (~ 48 pc of resolution) allow us to study the turbulence down to the scale of molecular clouds. This cloud scale study is complementary to the kpc scales study of Tamburro et al. (2009) and Stilp et al. (2013), and makes an advance by probing directly to the scale of molecular clouds. In addition, I also provide a more detailed analysis by separating the thermal and turbulent component from the kinetic energy of the gas, and consider the variation of turbulent dissipation time as functions of number density and velocity dispersion of the gas.

This chapter is organized as follows. In Section 4.1, 4.6, and 4.7, I review the energy sources that may be able to maintain interstellar turbulence. In Section 4.2, I describe the archival data that I use. In Section 4.3, I measure the turbulent energy in both azimuthally average and cloud-by-cloud basis with an emphasis to explain their energy sources. Lastly, I discuss our findings in Section 4.4. I summarize the findings in Section 4.5. Throughout this paper, I adopt a distance of 859 kpc, an inclination of 56°, and a position angle of 22°.5 for M33 (Gratier et al. 2010).

4.1.1 Magneto-rotational Instability

Sellwood & Balbus (1999) proposed that the turbulence in the outer disk of spirals is driven by the differential rotation of galaxy under the existence of weak magnetic fields. Their conclusion is based on the fact that the velocity dispersion in the outer disk of spirals is approximately constant at ~ 6 km s^{-1} (Dickey et al. 1990), even though stellar winds and supernovae are negligible in that region. They applied the magneto-rotational instability (MRI), that was first applied to proto-stellars disk by Balbus & Hawley (1991), into galaxy scales, and confirmed that a magnetic field strength of 3μG is sufficient for MRI to generate

a velocity dispersion of 6 km s^{-1}. This magnetic field strength is about a factor of 2 smaller than what was measured in the Milky Way (Heiles & Troland 2005).

The energy per unit area produced by MRI is (see Appendix 4.6)

$$\Sigma_{\rm MRI} \approx 1.1 \times 10^{44} \text{ erg pc}^{-2}\ \epsilon_{\rm MRI}\ h_{\rm HI}^2\ B^2\ S\ \sigma_{\rm HI}^{-1}, \tag{4.1}$$

where $0 \leq \epsilon_{\rm MRI} \leq 1$ is the coupling efficiency of MRI energy (i.e. the fraction of MRI energy that deposits to turbulence), $h_{\rm HI}$ is the scale-height of H I gas in units of 100 pc, B is the magnetic field strength in units of 6μG, $S \equiv |d\Omega/d\ln R|$ is the shear rate in the unit of (220 Myr)$^{-1}$, and $\sigma_{\rm HI}$ is the velocity dispersion of H I gas in units of 10 km s^{-1}.

In the absence of Maxwell stress tensor (no MRI), the Newton stress tensor $T_{R\phi} = <\rho u_{GR} u_{G\phi}>$ can provide the energy input for turbulence from the positive correlation between the radial and azimuthal gravitational velocities (u_{GR} and $u_{G\phi}$, respectively; Lynden-Bell & Kalnajs 1972). By adopting the energy input rate from the gravitational instability as $\dot{\Sigma}_{\rm GI} \approx 1.23 \times 10^{-8}$ erg s^{-1} cm^{-2} (Wada et al. 2002; Mac Low & Klessen 2004), the energy surface density of the gravitational instability is

$$\Sigma_{\rm GI} = \epsilon_{\rm GI}\ \dot{\Sigma}_{\rm GI}\ \tau_D \approx 3.6 \times 10^{43} \text{ erg pc}^{-2}\ \epsilon_{\rm GI}, \tag{4.2}$$

where $0 \leq \epsilon_{\rm GI} \leq 1$ is the coupling efficiency of the gravitational instability and $\tau_D \approx 9.8$ Myrs is the dissipation time of turbulence. The calculation above assumes $h_{\rm HI} = 100$ pc, $\Sigma_{\rm gas} = 10\ M_\odot$ pc^{-2}, and $S = (220 \text{ Myr})^{-1}$. Since this energy is about an order-of-magnitude smaller than $\Sigma_{\rm MRI}$, it is not to be considered any further as a source of turbulent energy.

4.1.2 Feedback from Star Formation

Star formation can provide feedback through proto-stellar outflow, stellar wind, and supernovae (SNe). This feedback inject energy and momentum to the surrounding ISM. However, SNe energy is orders-of-magnitude higher than the energy from proto-stellar outflow and stellar wind (Mac Low & Klessen 2004). Therefore, the stellar feedback other than SNe are neglected.

We estimate the energy per unit area that needs to be injected by SNe to maintain turbulence in the ISM (i.e. the steady state energy surface density) as $\Sigma_{\rm SNE} = \eta\ \epsilon_{\rm SN}\ E_{\rm SN}\ \tau_D$ (Mac Low & Klessen 2004), where η is the rate of supernovae per unit area, $E_{\rm SN}$ is the energy of a single SN, $\epsilon_{\rm SN}$ is the fraction of $E_{\rm SN}$ that goes into turbulence, and τ_D is the dissipation time, defined as the crossing time across the turbulent driving scale. In Section 4.7, η, $E_{\rm SN}$, and τ_D were estimated to derive the SNe energy density as

$$\Sigma_{\rm SNE} \approx 3.9 \times 10^{45} \text{ erg pc}^{-2}\ \epsilon_{SN}\ \left(\frac{\Sigma_{\rm SFR}}{M_\odot \text{ Gyr}^{-1} \text{ pc}^{-2}} \right), \tag{4.3}$$

where $\Sigma_{\rm SFR}$ is the star formation rate surface density. In Equation 4.3, I assume τ_D is constant (9.8 Myr). The effect of non-constant τ_D is considered in Section 4.4.2. Note that Equation 4.3 is an estimate for the energy of individual supernova. Many SNe explode in clusters, making superbubbles, so that the energy injection from those SNe would be different (Bruhweiler et al. 1980).

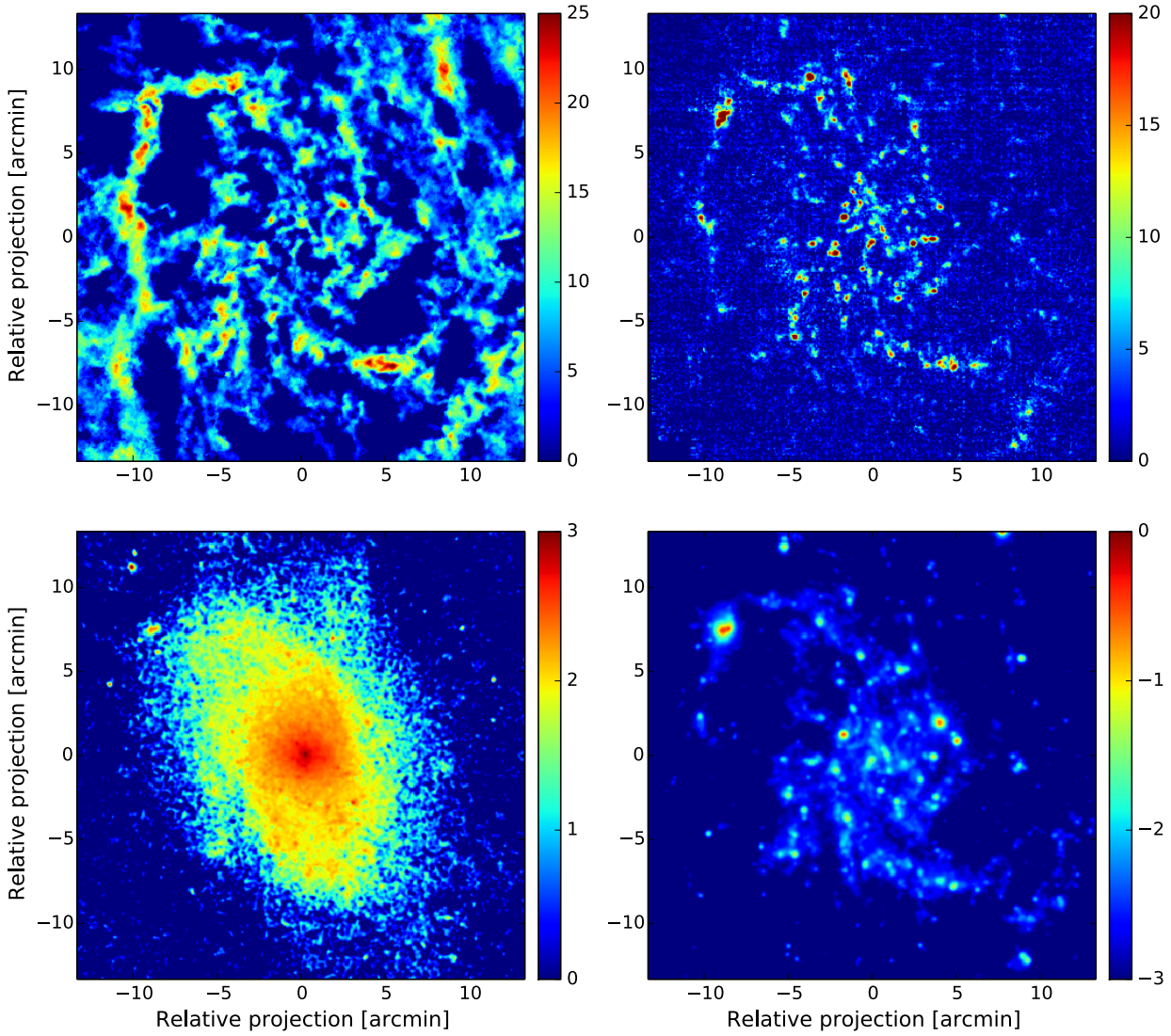

Figure 4.1: The map of the atomic gas surface density, color coded in $M_\odot$ pc^{-2} (top left), the molecular gas surface density in $M_\odot$ pc^{-2} (top right), the stellar surface density in log($M_\odot$ pc^{-2}) (bottom left), and the SFR surface density in log[$M_\odot$ yr^{-1} kpc^{-2}] (bottom right) at the same field-of-view.

4.2 Archival Data

4.2.1 Atomic Gas

Surface density: The H I data is retrieved from the VLA archival data (B, C, and D arrays) as part of the projects AT206 and AT286 in 1997, 1998, and 2001 (Thilker, personal

communication). Data calibration and imaging have been done using `CASA` software package by Gratier et al. (2010). The final data product has a spatial resolution of 12″ and a velocity resolution of 1.28 km s^{-1}. The H I integrated intensity ($I_{\rm HI}$) is converted to H I mass surface density ($\Sigma_{\rm atom}$), assuming H I is optically thin throughout the line-of-sight, using (Leroy et al. 2008)

$$\Sigma_{\rm atom}(M_\odot\ {\rm pc}^{-2}) = 0.020\ \cos(i)\ I_{\rm HI}({\rm K\ km\ s}^{-1}), \tag{4.4}$$

where i is the inclination of M33 and it includes a factor of 1.36 to reflect the presence of helium. The map and radial profile of $\Sigma_{\rm atom}$ are shown in Figure 4.1 and 4.2, respectively. Note that not all H I emission is optically thin. In M33, Braun (2012) suggested that the H I mass is higher by a factor of 1.36 due to the existence optically thick emission.

Kinematics: The centroid velocity and the velocity dispersion ($\sigma_{\rm HI}$) maps are derived by applying Gaussian fits to the spectra within a spectral window. The window is defined as the contiguous positive intensity around the first-moment velocity from Gratier et al. (2010). The aim of the window is to exclude spurious noise that affect $\sigma_{\rm HI}$. From this centroid velocity, the rotation curve and shear rate are also derived (see Appendix 4.8).

Turbulent Energy Density: The atomic gas kinetic energy per unit area is calculated as

$$E_k = \frac{3}{2}\ \Sigma_{\rm HI}\ \sigma^2_{\rm HI}. \tag{4.5}$$

In Section 4.3, thermal energy is subtracted from the kinetic energy to derive the turbulent energy of the gas.

Diffuse Gas Scale Height: I assume that $\sigma_{\rm gas}$ is isothermal in the vertical (z) direction, i.e. $\sigma_{\rm gas}$ is independent of z. In hydrostatic equilibrium, the H I gas scale height ($h_{\rm gas}$) is set by $\sigma_{\rm gas}$ and the total surface density of the disk ($\Sigma_{\rm tot}$) as (e.g., van der Kruit & Searle 1981)

$$h_{\rm gas} = \frac{\sigma^2_{\rm gas}}{2\pi G \Sigma_{\rm tot}}, \tag{4.6}$$

where $\Sigma_{\rm tot} = \Sigma_* + \Sigma_{\rm atom} + \Sigma_{\rm mol}$, i.e. the sum of the stellar, atomic, and molecular gas surface density. The H I scale-height derived from Equation (4.6) is shown in Figure 4.2, where $h_{\rm gas}$ varies from $\sim$ 10 pc in the center to $\sim$ 100 pc in the outer disk. Note that in Equation (4.6), I assume h_* is constant and $h_{\rm gas} \ll h_*$. Otherwise, the weight from stellar gravity is reduced by a factor of $\sim 1 - (2/3)(h_{\rm gas}/h_*)^2$ (Ostriker et al. 2010). Therefore, Equation (4.6) gives a lower limit for $h_{\rm gas}$ in the bulge where $h_* > h_{\rm gas}$, because not all stars in the bulge contribute to the gravitational pressure in the midplane.

4.2.2 Molecular Gas Surface Density

As part of the M33 CO Large Program, the CO(2–1) line has been observed over the whole disk down to a noise level of 20 mK per channel (Gratier et al. 2010; Druard et al. 2014). The data have a spatial resolution of 12″ and a spectral resolution of 2.6 km s^{-1}. The On-The-Fly mapping technique was used with the HERA multibeam dual-polarization receiver on the IRAM 30-meter telescope in Pico Veleta, Spain.

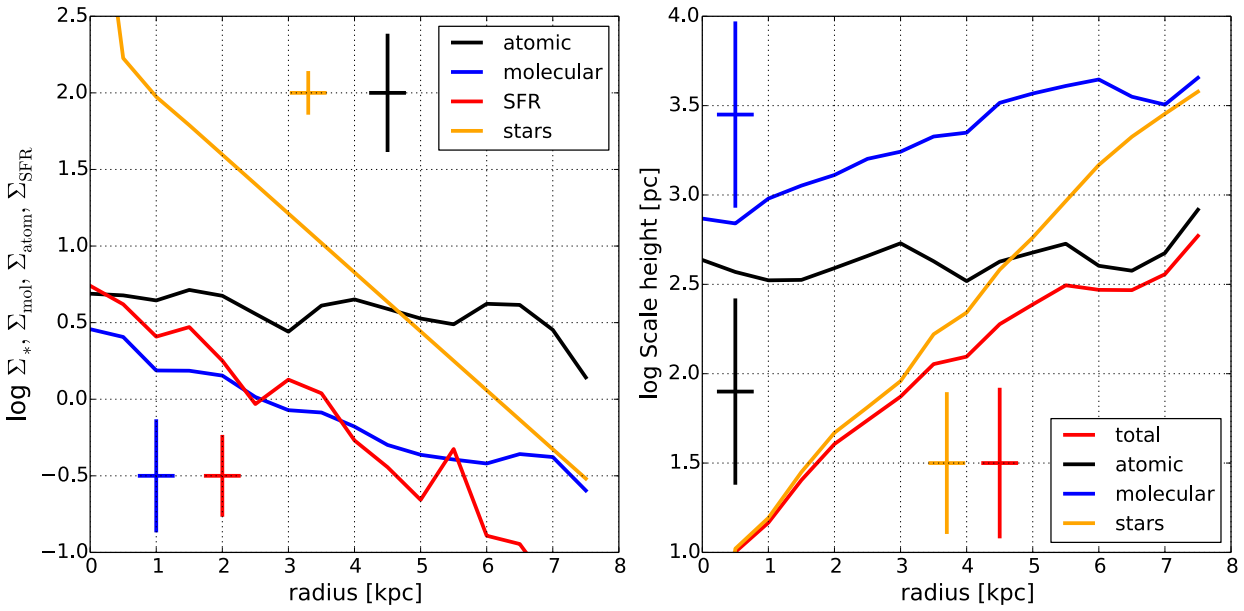

Figure 4.2: Left: The radial profiles of Σ_{atom}, Σ_{mol}, and Σ_{SFR} by taking their average values in radial bins with bin width of 0.5 kpc. The gas is atomic dominated throughout the galaxy. Three spikes in Σ_{SFR} at radius $\sim$ 3.5 kpc, $\sim$ 3.5 kpc, and $\sim$ 5.5 kpc are due to NGC595, NGC604 (the two largest H II region in the Local Group), and IC133, respectively. The typical uncertainties are marked as crosses. Right: The H I gas scale height if the gravity comes from atomic gas only (a black line), molecular gas only (a blue line), and stars only (an orange line). The H I gas scale height for total mass (stars+atomic+molecular) is shown as a red line. The typical uncertainties are marked as crosses.

The CO surface brightness is converted to the molecular gas surface density (Σ_{mol}) using a Galactic CO(1–0)-to-H_2 conversion factor of $\alpha_{CO} = 4.3\ M_\odot$ (K km s^{-1} pc^2)$^{-1}$ (e.g., Bolatto et al. 2013), including a mass contribution from Helium. I also adopt a line ratio CO(2–1)/CO(1–0) of 0.7 (e.g., Leroy et al. 2008). A correction for galaxy inclination has also been applied. The map and radial profile of Σ_{mol} are shown in Figure 4.1 and 4.2, respectively. The CO velocity dispersion is calculated using the 2nd-moment method (the intensity-weighted square of the velocity). Channels with CO intensity less than 0.1 K (typical noise in the data cube) are blanked, and only channels within 15.6 km s^{-1} from the mean velocity are included. The molecular gas turbulent energy is calculated using a formula analogous to Equation (4.5).

4.2.3 Stellar Mass Surface Density

The stellar mass surface density (Σ_*) is derived from the K-band image of 2MASS Large Galaxy Atlas (Jarrett et al. 2003) using a mass-to-light ratio (M/L) of 0.5 $M_\odot$ $L^{-1}_{\odot,K}$. The original image (1″ pixel size and 3″ resolution) is resampled and convolved to match the H I map with 4″ pixel size and 12″ resolution using the `MIRIAD` package (Sault et al. 1995). The major uncertainty is the M/L, which shows a factor of 2 variation in the K-band (Bell & de Jong 2001). A correction for galaxy inclination has also been applied.

The radial profile of Σ_* is well fitted by de Vaucouleurs profile for the inner 1 kpc and the exponential profile between 1 and 2 kpc. The stellar profile beyond 2 kpc is undetected. Therefore, the exponential fit is used to extend the stellar profile beyond 2 kpc radius. The map and radial profile of Σ_* is shown in Figure 4.1 and 4.2, respectively.

4.2.4 Star Formation Rate Surface Density

The far ultraviolet (FUV) map from *GALEX* is retrieved at effective wavelength of 1516 Å (Gil de Paz et al. 2007) as a tracer of obscured star formation energy, and the mid infrared map (MIR) from *Spitzer* MIPS 24μm (Dale et al. 2009) as a tracer of unobscured star formation energy that is reradiated by the dust. I correct the FUV map for Galactic extinction of $E(B-V) = 0.0418$ (Schlegel et al. 1998), and adopt a correction of $A_{\rm FUV} = 7.9E(B-V)$ (Gil de Paz et al. 2007) for extinction at FUV. The original resolutions of FUV and MIR maps are 4″.5 and 6″, respectively. Therefore, I convolve and regrid the FUV and MIR maps to match the H I map using the `MIRIAD` package (Sault et al. 1995).

The FUV and MIR surface brighness ($I_{\rm FUV}$ and $I_{\rm MIR}$) are converted to the star formation surface density ($\Sigma_{\rm SFR}$) using a prescription by Leroy et al. (2008):

$$\Sigma_{\rm SFR} = (8.1 \times 10^{-2}\ I_{\rm FUV}\ +\ 3.2 \times 10^{-2}\ I_{\rm MIR})\ \cos(i), \tag{4.7}$$

where $\Sigma_{\rm SFR}$ is in units of $M_\odot$ pc^{-2}, and both $I_{\rm FUV}$ and $I_{\rm MIR}$ are in units of MJy str^{-1}. Equation (4.7) assumes a Kroupa (2001) Initial Mass Function (IMF), which is a factor of 1.59 lower than a Salpeter (1955) IMF. The map and radial profile of $\Sigma_{\rm SFR}$ are shown in Figure 4.1 and 4.2, respectively.

4.3 Results

4.3.1 Separating Thermal and Turbulent Energy

The total kinetic energy of the gas consists of thermal plus turbulent energy. In order to calculate the thermal energy density ($e_{\rm th} = nk_{\rm B}T$), I need to know the volume density (n) and temperature (T) of the gas. For this study, it is necessary to consider the two-phases of ISM: cold and warm neutral media (CNM and WNM; Field 1965) because their density and temperature can vary by two orders-of-magnitude. These two-phases can co-exist stably at small range of pressure around $P/k_{\rm B} \sim 3,000$ K cm^{-3} in the Solar neighborhood (Wolfire

et al. 1995). The mass fraction of H I in each of these media affects the resulting thermal energy.

Calculating the physical state of the gas (n and T) requires calculating the thermal and chemical equilibrium in the gas, and it is beyond the scope of this dissertation. Therefore, I adopt the result by Wolfire et al. (2003), where they calculated n and T for CNM and WNM as a function of galactocentric radius in the Milky Way (MW). Hereby, I assume that M33 is a miniature version of MW, e.g. n and T for CNM and WNM at 0.5 R_{25} in the MW is the same as that at 0.5 R_{25} in M33, where I adopt $R_{25} = 16$ kpc in MW (Bigiel & Blitz 2012) and $R_{25} = 7.7$ kpc in M33 (Gratier et al. 2010).

The gas thermal energy is determined through the following steps. First, I calculate the volume density of each pixel as $n = \Sigma_{\rm HI}\ (2h)^{-1}$, where h is the scale-height of the H I gas (Figure 4.2). Then, I compare n with the minimum and maximum values of $n_{\rm CNM}$ and $n_{\rm WNM}$ as tabulated in Wolfire et al. (2003). In these comparisons, there are three conditions that are satisfied by our M33 data. (1) If $n > n_{\rm min}$(CNM), then most of the H I mass is in CNM. All H I mass is in CNM only when $n > n_{\rm max}$(CNM). However, for simplicity, we assume that all the gas is in CNM when $n > n_{\rm min}$(CNM). (2) If $n < n_{\rm max}$(WNM), then most of the volume is in WNM. For simplicity, we assume all the H I mass is in WNM. (3) If $n_{\rm min}$(CNM) $\leq n \leq n_{\rm max}$(WNM), then I assume that both phases exist and distribute the gas mass to be half CNM and half WNM (Heiles & Troland 2003). For most of the H I gas, the number density lies in between $n_{\rm WNM}$ and $n_{\rm CNM}$. Finally, I sum the thermal energy from the CNM and WNM as the gas thermal energy. The thermal energy is subtracted from the kinetic energy to get the turbulent energy.

The result is given in Figure 4.3. On the left panel, I show that the fraction of CNM (the gray points above the dashed blue line) decreases as a function of radius. However, both phases are still exist at the outermost radius where H I is detected. On the right panel of Figure 4.3, we see that the turbulent energy dominates over the thermal energy inside 3 kpc, while in the outer part, turbulent and thermal energy are comparable to each other. This result highlights the importance of thermal motion in the outer part of the galaxy. Whether the photoelectric heating from the dust and the UV stellar radiation have enough energy to maintain the thermal energy is beyond the scope of this dissertation. Nevertheless, the turbulent energy still exists at all radii, which means the driving mechanism (e.g. stellar feedback or MRI) is needed.

4.3.2 The Origin of Turbulent Energy

In the left panel of Figure 4.4, the radial profiles of turbulent energy per unit area is compared to the possible sources of turbulent energy (SNe and MRI) assuming 100% coupling efficiency (i.e. all SNe and MRI energy go to turbulence). There are four key points of our findings.

- The turbulent energy (black line) declines by about 0.5 dex from the center to ~ 3 kpc radius, then almost flat between ~ 3 and 6 kpc, and finally declines abruptly beyond

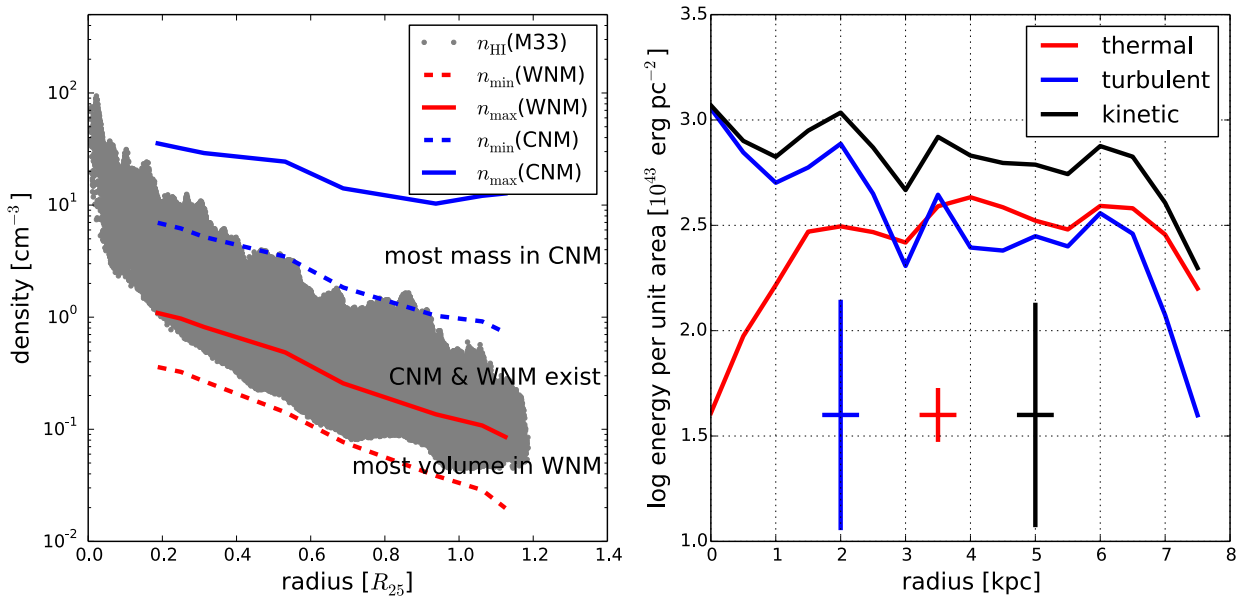

Figure 4.3: Left: The number density of H I for each detected pixels in M33 (gray points). The blue and red lines are the predicted number density of CNM and WNM, respectively (Wolfire et al. 2003). No data for CNM and WNM inside $0.2R_{25}$ and outside $1.1R_{25}$, therefore, I extrapolate the red and blue lines using the Univariate Spline method in `Scipy`. While the inner region of M33 is dominated by CNM, both phases exist in the outer part, consistent with that in the Milky Way (Heiles & Troland 2003). Right: The radial profile of kinetic energy (blue line), turbulent energy (black line), and thermal energy (red line) in M33. The uncertainties are marked as crosses. The turbulent energy dominates over thermal energy inside ~ 3 kpc, while both energy are comparable to each other in the outer part of M33.

6 kpc (due to lack of HI and larger annular area in the outer radius). This is due to the fact that both $\Sigma_{\rm atom}$ and $\sigma_{\rm HI}$ are almost constant at all radii but thermal energy is much smaller than the kinetic energy near the center.

- The SNe energy (red line) dominates over the MRI energy (blue line) inside ~ 4 kpc of galactocentric radius, and vice versa.
- *Individually*, the SNe energy is able to maintain turbulence inside of ~ 4 kpc radius, while MRI has enough energy to maintain turbulence outside ~ 4 kpc radius.
- The *sum* of SNe and MRI energy (dashed line) is able to maintain turbulence at all radii.

The SNe energy is higher than the turbulent energy in the inner part, while the MRI energy is higher than the turbulent energy in the outer part of M33, Therefore, the coupling

efficiency is less than 100%. If we assume that the SNe energy is the only source of turbulence inside $\sim$ 4 kpc, then the SNe coupling efficiency increases from $\epsilon_{SN} \sim 50\%$ at the center to 100% at $\sim$ 4 kpc. It is unknown why the coupling efficiency is smaller at the center (or equivalently at larger SFR surface density, see §4.4.2). However, this trend disappears when the variation of dissipation time is considered in §4.2. Furthermore, if we assume that the MRI energy is the only source of turbulence between $\sim$ 4 and 7 kpc, then the coupling efficiency is roughly constant at close to $\epsilon_{\rm MRI} \sim 100\%$. The total coupling efficiency (i.e. the sum of SNe and MRI energies divided by the turbulent energy) is given in §4.9. Note that there are many uncertainties (beyond the error propagation) in calculating the coupling efficiency. For example, if the magnetic field varied with radius, then the coupling efficiency of the MRI would have to vary, and if the field had a different value than we assumed, then the average value of the coefficient would differ from what we estimated above.

4.3.3 Turbulence in Molecular Clouds

Since star formation occurs in molecular clouds, I investigate whether the stellar feedback *alone* can maintain the turbulence in molecular clouds. To do so, individual molecular clouds in M33 are identified through the following procedures. I utilize the `CPROPS` package of Rosolowsky & Leroy (2006) to identify contiguous regions in the CO data cube. These regions must have at least one pixel with SNR ≥ 5 and bounded by pixels with SNR of 2 as their edges. The purpose of this process is to separate signal from noise. As the output, I have a masked cube with binary values: zeros for noise and ones for signals. I collapse this masked cube along the velocity axis. Then, each contiguous region in this 2-dimensional map is labeled as an individual molecular cloud. I blank pixels that only cover less than 3 channels because they are not sufficient for the calculation of velocity dispersion. Clouds with total number of pixels less than 15 (equivalents to an effective radius of 9.1 pc) are removed because smaller clouds are susceptible to noise. At the end, 124 molecular clouds in M33 are cataloged. This is fewer than 148 clouds that were cataloged by Engargiola et al. (2003) because our selection is more conservative and their catalog may also consist of many smaller clouds.

The kinetic and SNe energies within a molecular cloud are calculated by adding the respective energy from each pixel within the boundary of the molecular clouds. However, the measured SNe energy within the molecular cloud is probably an overestimate because the stars will move away from the clouds in the millions of years it takes for them to evolve to the end of their lives and the ionizing radiation from the stars pushes the gas away from the stars (McKee et al. 1984). The result is shown in the right panel of Figure 4.4. The molecular turbulent energy per cloud is correlated with the supernovae energy per cloud, with $\sim$ 10% of mean coupling efficiency. Therefore, supernovae energy has enough energy to maintain turbulence in molecular clouds.

As a comparison, I also tried to loose the constraint for clouds detection by reducing the peak SNR = 2 and keep the edge SNR as is. In addition, there is no decomposition for the contiguous regions. In other words, we are likely to identify Giant Molecular Associations

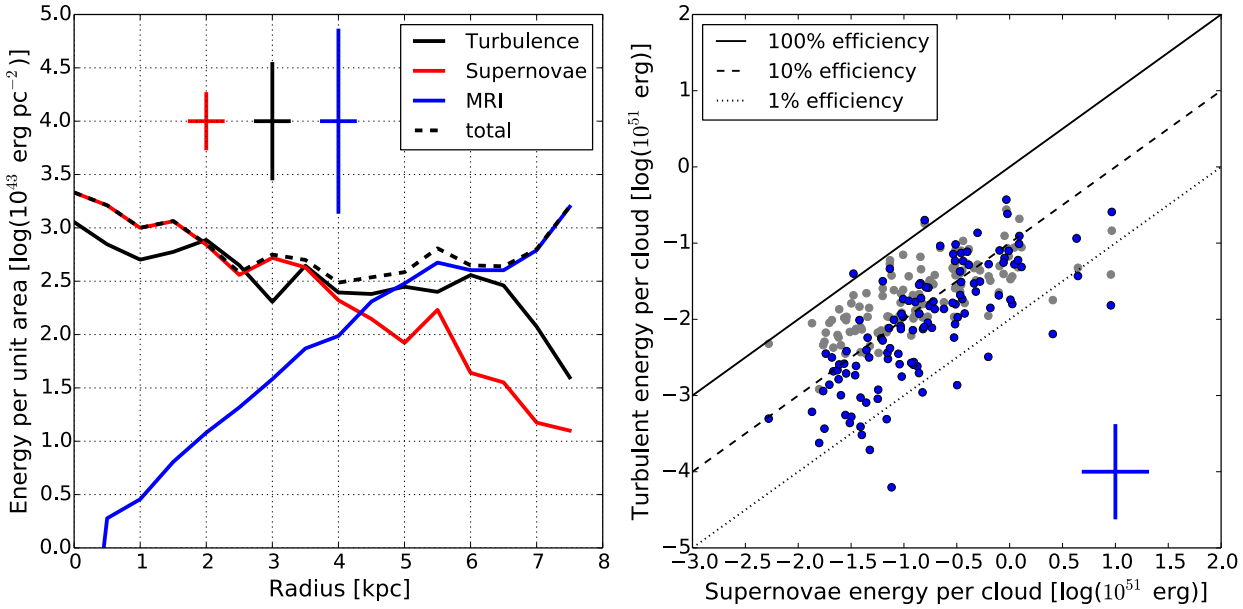

Figure 4.4: Left: Azimuthally-averaged values of turbulence energy (black line), SNe energy (red line), MRI energy (blue line), and total energy (SNe plus MRI energy; dashed black line) as a function of radius. The typical uncertainties are shown as cross symbols. This figure shows that the sum of SNe and MRI energy have enough energy to maintain turbulence at all radii. Right: a comparison between the turbulent energy and SNe energy in Giant Molecular Clouds (blue dots) and Giant Molecular Associations (gray dots). The typical uncertainty is marked as a cross. The solid, dashed, and dotted black lines mark the SNe coupling efficiency of 100%, 10%, and 1%, respectively. This figure shows that SNe energy ables to maintain turbulence in molecular clouds.

(GMAs) rather than GMCs. The aim is to include a more diffuse CO emission with low star formation rate, so that we can check whether the SNe energy can still maintain turbulence per GMA. As in GMC, the SNe energy per GMA is derived by adding SNe energy from all pixels within the boundary of GMA. I find that the turbulent energy per GMA is higher than that in each GMC, which is expected because the GMA covers larger area than GMC, but the SNe energy is relatively constant because star formation is more concentrated to the CO peak regions (gray points in the right panel of Figure 4.4). As a consequence, the mean coupling efficiency of SNe energy in GMAs is higher ($\epsilon_{\rm SN} \sim 20\%$). The fact that it is less than 100% means the SNe energy can still maintain turbulence, even after the inclusion of more diffuse CO emission.

4.4 Discussion

4.4.1 Comparisons with Previous Works

Here, I show that the stellar feedback has enough energy to maintain turbulence inside ~ 4 kpc radius in M33, while MRI energy matches turbulent energy outside ~ 4 kpc. These findings are in agreement with the previous study by Tamburro et al. (2009) in a sample of nearby galaxies selected from the THINGS survey (Walter et al. 2008). They also found that *both* SNe and MRI have enough energy to maintain turbulence at all radii.

However, there are at least two differences. First, their measured H I velocity dispersion increases towards the center and could reach a value of 25 km s^{-1}, while I measure ~ 10 km s^{-1} in the center of M33. This higher velocity dispersion could be a beam smearing effect because their physical resolution is ~ 500 pc at 10 Mpc distance. The resolution of M33 is one order-of-magnitude better (~ 50 pc), and hence, the result in this chapter confirms the conclusion that SNe and MRI drive turbulence is still true at smaller physical scale. Second, their measurement covered at least twice R_{25}. Unlike in M33, that MRI energy dominates over SNe energy at $\sim 0.5\ R_{25}$, Tamburro et al. (2009) found this occurred at R_{25}. This might be due to their choice of a constant dissipation time of 9.8 Myrs, rather than letting vary as functions of H I scale-height and velocity dispersion. In other words, they only have $h_{\rm HI}$ in Equation (1), instead of $h^2_{\rm HI}$. Since $h_{\rm HI}$ rises as a function of radius, our $\Sigma_{\rm MRI}$ profile is steeper than that in Tamburro et al. (2009), and hence, becomes comparable to $\Sigma_{\rm SNE}$ at smaller radius.s

Based on their study in dwarf galaxies, Stilp et al. (2013) found that SFR ables to maintain turbulence in regions where $\Sigma_{\rm SFR} \gtrsim 1\ M_\odot$ Gyr^{-1} pc^{-2}, which is equivalent to $\Sigma_{\rm ESN} \gtrsim 4 \times 10^{45}$ erg pc^{-2} for $\epsilon_{\rm SN} = 1$ (Equation 4.3). This threshold occurs at $r \sim 3$ kpc in M33, inside of which the SNe energy is larger than the turbulent energy (Figure 4.4). Therefore, the result in M33 confirms their finding. Stilp et al. (2013) also argued that MRI can not be the source of turbulent energy because the velocity dispersion of H I in the dwarf galaxies is similar to the the outer disk of spirals, but the rotation curve of dwarf galaxies is usually a solid body rotation, and hence, lack of shear. Even though not as massive as the Milky Way or M31, M33 is not as small as typical dwarfs either. Its rotation curve is almost flat at ~ 8 kpc (the outermost radius where it can be measured in this dissertation), and hence, still have significant shear rate (Figure 4.6).

4.4.2 Coupling Efficiency and Dissipation Time

Despite many uncertainties involved in the calculations, we see that the coupling efficiency of SNe, defined as the amount of SNe energy that is converted to turbulent energy ($\epsilon_{\rm SN} = E_{\rm turb}/E_{\rm SN}$), varies as a function of radius (the left panel of Figure 4.4). Near the center, $\epsilon_{\rm SN} \sim 50\%$ and increases outward until it reaches 100% at $r \sim 4$ kpc, beyond which the SNe energy cannot be the sole driver of turbulence because $\epsilon_{\rm SN} > 1$. Since $\Sigma_{\rm SFR}$ decreases as a function of radius, this means $\epsilon_{\rm SN}$ anti-correlates with $\Sigma_{\rm SFR}$. This anti-correlation has also

been observed in the sample of spirals and dwarfs (Tamburro et al. 2009; Stilp et al. 2013).

A possible reason of the $\epsilon_{\rm SN}$ variation is the leakage of SNe energy through SNe bubbles that drive gas outflow from the galaxy midplane. The H I gas mass surface density is known to have little variation, while $\Sigma_{\rm SFR}$ declines as a function of radius. This suggests that SNe bubbles tend to be overlapping with each other in the galaxy center, which increases the likelihood of energy leakage from the galaxy. This SNe leakage energy transfers its energy to the ionized medium out of the midplane, instead to the H I gas near the midplane which we measured here. In this view, the H I gas only captures a fraction of SNe energy, and hence, leads to a smaller $\epsilon_{\rm SN}$ in the center.

However, there is a caveat. So far, I assumed that the dissipation time is constant ($\tau_D = 4.27$ Myrs for SNe energy, see Section 4.7). Both Tamburro et al. (2009) and Stilp et al. (2013) also assumed a constant τ_D. In a more realistic scenario, τ_D is a time-scale of which the turbulent speed (interpreted as the turbulent velocity dispersion, $\sigma_{\rm turb}$, of the gas) propagates through its driving scale (interpreted as the cooling radius R_C of SNe). Since $\tau_D \propto R_C\ \sigma_{\rm turb}^{-1}$ and $R_C \propto n_H^{-0.42}$ (Section 4.7 and in Martizzi et al. 2015), τ_D increases as a function of radius. On the other hand, $\Sigma_{\rm SFR}$ decreases as a function of radius. This means the gradient of SNe energy density ($\Sigma_{\rm ESN} \propto \Sigma_{\rm SFR}\ \tau_D$) is flatter than what is shown in Figure 4.4, which in turn would affect the inferred value of coupling efficiency.

On the left panel of Figure 4.5, the radial profile of SNe energy density (with varying τ_D as functions of n_H and $\sigma_{\rm HI}$) is compared to the turbulent and MRI energy. The SNe energy density is higher than the turbulent energy density inside 5 kpc (rather than 3 kpc as in Figure 4.4). This is due to a longer τ_D by a factor of ~ 3 at 5 kpc radius compared to the adopted constant τ_D value of 4.27 Myr. Even in this picture, MRI is still needed and dominates over SNe energy outside 4 kpc. Therefore, it does not change the conclusion that *both* SNe and MRI energy are needed to maintain turbulence at all radii.

On the right panel of Figure 4.5, the coupling efficiencies, defined as $\epsilon = E_{\rm turb}/(E_{\rm SN} + E_{\rm MRI})$, are shown as a function of radius. The red color represents the coupling efficiency at a constant τ_D, while the blue color represents the coupling efficiency by varying τ_D as functions of n_H and $\sigma_{\rm HI}$. A constant τ_D gives $\epsilon > 1$ at $r \sim 2-3$ kpc, which is unphysical, while the variation of τ_D gives $\epsilon < 1$, except at the center. The central region is highly uncertain because the density and temperature of CNM and WNM is extrapolated from Wolfire et al. (2003, see Figure 4.3). In addition, I do not take into account the spheroidal distribution of stars in the center when the gas scale-height was calculated (Equation 4.6), i.e. all stars are assumed to lie on the midplane. The radial profile of stellar mass surface density inside 1 kpc (Figure 4.2) is not exponential, which points to the existence of bulge. A spheroidal stellar distribution in bulge will reduce the midplane pressure, which leads to a higher scale-height, a longer τ_D, and hence, a smaller ϵ. If the center is excluded, then the coupling efficiency has a mean value of 0.44 with a standard deviation of 0.22, and no clear trend with radius. This evidence suggests that both stellar feedback and MRI have enough energy to maintain turbulence at all radii.

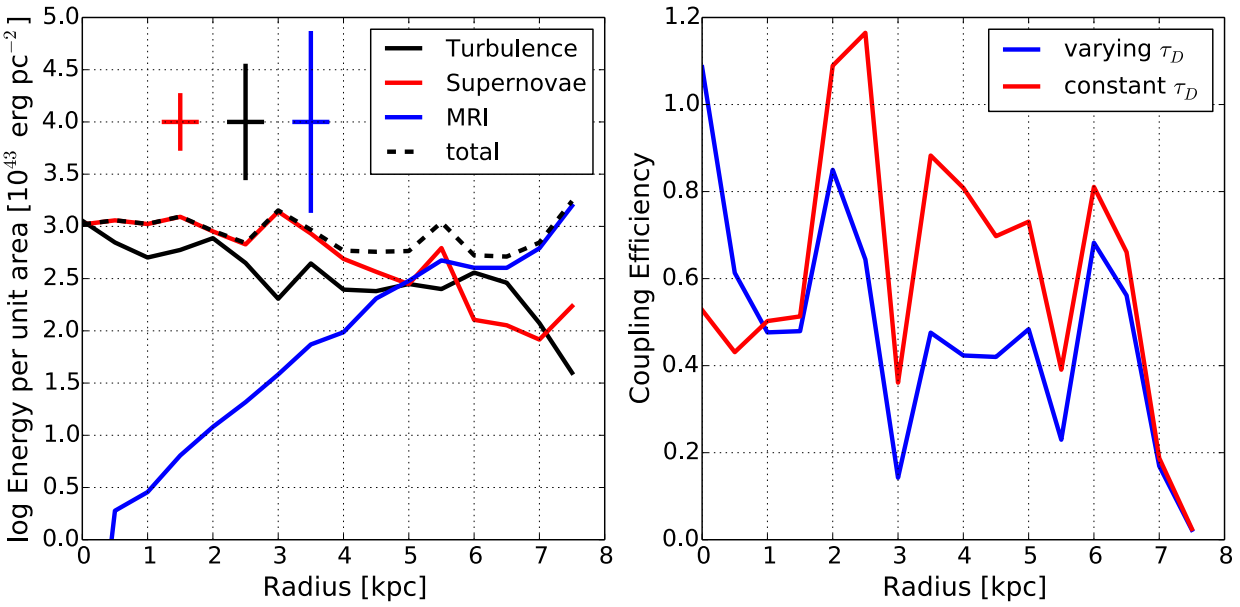

Figure 4.5: Left: Similar to the left panel of Figure 4.4, except that I calculate the dissipation time as functions of the number density and velocity dispersion of H I. The slope of SNe energy is shallower than that in Figure 4.4 because the dissipation time is longer in outer radius. however, the main conclusion in Figure 4.4 (both SNe and MRI energy are needed to maintain turbulence) does not change. Right: the coupling efficiency at a constant τ_D (red color) and the variation of τ_D (blue color) as a function of radius. Except in galaxy center, the coupling efficiency for varying τ_D is smaller than that at a constant τ_D.

4.4.3 The CO-to-H_2 Conversion Factor

Here, I consider the effect of the CO-to-H_2 conversion factor ($\alpha_{\rm CO}$) that varies as a function of metallicity and total mass surface density ($\Sigma_{\rm tot}$). A higher conversion factor than the Galactic value ($\alpha_{\rm CO} = 4.3\ M_\odot\ [{\rm K\ km\ s^{-1} pc^2}]^{-1}$, used in Sections 4.2 and 4.3) means the actual $\Sigma_{\rm mol}$ and the molecular gas kinetic energy are underestimated. However, a change of conversion factor due to surface density is unlikely because the azimuthally-averaged $\Sigma_{\rm tot}$ is less than 100 $M_\odot$ pc^{-2} at almost all radii (Figure 4.2), except at the center where $\Sigma_{\rm tot}$ is overestimated due to the bulge spheroidal component (Bolatto et al. 2013, and references therein). Therefore, in this sub-section, only the metallicity-dependent $\alpha_{\rm CO}$ is considered.

Gas in the lower metallicity environment has lower dust-to-gas ratio, and hence, requires higher column density to shield the gas to be molecular. Thus, a higher conversion factor is adopted. Bolatto et al. (2013) gives a prescription to estimate this correction of the conversion factor as

$$\alpha_{\rm CO} = 2.9\ \exp\left(\frac{0.4}{Z'\ \Sigma^{100}_{\rm GMC}}\right)\ M_\odot\ ({\rm K\ km\ s^{-1} pc^2})^{-1}, \tag{4.8}$$

en where Z' is the gas-phase metallicity relative to the Solar value of 12+log(O/H)= 8.7 (Allende Prieto et al. 2001), and $\Sigma_{\rm GMC}^{100}$ is the surface density of GMCs in the units of 100 $M_\odot$ pc^{-2}. What is the gas-phase metallicity in M33? Recent measurement by Toribio San Cipriano et al. (2016), based on the electron temperature, found 12+log(O/H)= $8.52 - 0.36(R/R_{25})$. This means the conversion factor varies from 1.2 times higher than the Galactic $\alpha_{\rm CO}$ in the center of M33 to 2.7 times higher than the Galactic $\alpha_{\rm CO}$ at $R_{25} \approx 7.7$ kpc. Those values of conversion factor is in agreement with what were found by Leroy et al. (2011), where they used dust emission as a tracer for H_2 surface density. When this metallicity dependent $\alpha_{\rm CO}$ is applied, it only has a marginal effect to the kinetic energy of molecular clouds. The mean coupling efficiency of SNe energy to be transferred to the kinetic energy of molecular clouds only rises from 5.5% for a Galactic $\alpha_{\rm CO}$ (Figure 4.4) to 8.4% for the metallicity dependent $\alpha_{\rm CO}$. Therefore, SNe energy is still sufficient to maintain turbulence in the molecular clouds.

4.4.4 Tidal interaction

M33 and M31 are known to be interacting (e.g., Putman et al. 2009; Lockman et al. 2012). Does their tidal interaction generate enough energy to fuel turbulence? The rate of energy injected by accretion can be estimated as the kinetic energy of the accreted materials (Klessen & Hennebelle 2010), i.e. $\dot{E}_{\rm acc} = 0.5\ \dot{M}_{\rm acc}\ V_{\rm acc}^2$, where $\dot{M}_{\rm acc}$ and $V_{\rm acc}$ are the accreted mass rate and velocity. For a galaxy with $R \sim 10$ kpc and turbulent dissipation time $\tau_D \sim 9.8$ Myrs, the energy surface density due to accretion is $\Sigma_{\rm acc} \approx 1 \times 10^{46}$ erg pc^{-2} $\epsilon_{\rm acc}$, where I have used the values of $\dot{M}_{\rm acc} = 3\ M_\odot$ yr^{-1} and $V_{\rm acc} = 100$ km s^{-1} as reported by Zheng et al. (2017). This energy density is a factor of ~ 3 higher than the turbulent energy density at the outer radius. Therefore, tidal interaction is a possible source of turbulent energy in the outer part of M33. However, I remain skeptical on how this energy can generate turbulence in the inner part of M33, where the mass inflow rate is much smaller than the mass accretion rate and the turbulent energy becomes comparable to the accretion energy. Also, if the accreting gas has a temperature much less than 1×10^6 K, then the interaction of the fast gas with the disk gas will result in a radiative shock, and most of the energy will be radiated away, resulting in $\epsilon_{\rm acc} \ll 1$.

4.5 Summary

M33 is an ideal place to study the interstellar turbulence given the wealth of archival, high-resolution, multi-wavelength data. Here, I investigate the origin of turbulence in the diffuse H I gas and in the molecular clouds. The two-phase model of ISM in the Milky Way (Wolfire et al. 2003) is adopted to calculate the fraction of H I gas in the WNM and CNM phases. Then, the thermal energy is estimated as the sum of WNM and CNM thermal energies. The turbulent energy is taken from the kinetic energy of H I gas, subtracted by its thermal energy. Inside ~ 3 kpc radius, turbulent energy dominates over thermal energy,

where most of the gas is in CNM phase. Outwards $\sim$ 3 kpc, both turbulent and thermal energies are comparable to each other.

By comparing turbulent energy against supernovae and MRI energies in radial bins, I show that the supernovae energy has enough energy to maintain turbulence inside $\sim$ 4 kpc, while the MRI energy is comparable to turbulent energy in the outer part of M33 where star formation becomes negligible. The sum of supernovae and MRI energies can maintain turbulence at all radii with coupling efficiency of $\sim$ 50%. Furthermore, by identifying individual molecular clouds in M33, I am able to measure their molecular kinetic energy. This energy is only $\sim$ 10% of the supernovae energy integrated within the area of molecular clouds. Therefore, the turbulent energy in molecular clouds can be originated from stellar feedback. This conclusion is unaffected by the change in the CO-to-H_2 conversion factor due to metallicity.

4.6 Appendix A. The Energy Injected by Magneto-rotational Instability

The energy per unit area of MRI is $\Sigma_{\rm MRI} = \epsilon_{\rm MRI}\ \dot{\Sigma}_{\rm MRI}\ \tau_D$, where $0 \leq \epsilon_{\rm MRI} \leq 1$ is the coupling efficiency of MRI (i.e. the fraction of MRI energy that goes to turbulence), $\dot{\Sigma}_{\rm MRI} = 3.7 \times 10^{-8}$ ergs^{-1} cm^{-2} $h_{\rm HI}\ B^2\ S$ is the energy injection rate of MRI (described below), and $\tau_D \approx 9.8$ Myrs $h_{\rm HI}\ \sigma_{\rm HI}^{-1}$ is the dissipation time of turbulence (Mac Low & Klessen 2004). Here, the units of H I scale-height ($h_{\rm HI}$), the magnetic field (B), the shear rate (S; defined in Equation 4.20), and the H I velocity dispersion ($\sigma_{\rm HI}$) are 100 pc, 6μG, (220 Myrs)$^{-1}$, and 10 km s^{-1}, respectively. Combining it altogether, I get Equation (4.1).

The MRI energy density ($e_{\rm MRI}$) comes from the positive correlation between the radial and azimuthal components of the magnetic field (represented as the Maxwell stress tensor $T_{R\Phi}$) that transfers the energy from shear to turbulence at a rate of $\dot{e}_{\rm MRI} = T_{R\Phi}S$ (Sellwood & Balbus 1999). The value of $T_{R\Phi}$ is 0.6 times the mean magnetic energy density $B^2(8\pi)^{-1}$ is adopted (Hawley et al. 1995). Then, $\dot{e}_{\rm MRI}$ is multiplied by the H I scale-height to get the injection rate of the MRI energy surface density, i.e. $\dot{\Sigma}_{\rm MRI} = \dot{e}_{\rm MRI}\ h_{\rm HI}$.

4.7 Appendix B. The Energy Injected by Supernovae

Supernovae Rates per Unit Area. Following Tamburro et al. (2009), the rate of supernovae explosions is given by the average number of newly formed stars (SFR/$\bar{m}_*$) multiplied by the fraction of the newly formed stars that become supernovae ($f_{\rm SN}$). Here, $\bar{m}_*$ is the average mass of a stellar population. If I assume IMF as $\phi(m) \propto m^{-\alpha}$, where $\alpha = 1.3$ for $0.1 < M/M_\odot < 0.5$ and $\alpha = 2.3$ for $0.5 < M/M_\odot < 120$ (similar to Kroupa IMF, Calzetti

et al. 2007), then $\bar{m}_*$ and $f_{\rm SN}$ are given by

$$\bar{m}_* = \frac{\int_{0.1M_\odot}^{120M_\odot} m\ \phi(m)\ dm}{\int_{0.1M_\odot}^{120M_\odot} \phi(m)\ dm}, \tag{4.9}$$

and

$$f_{\rm SN} = \frac{\int_{8M_\odot}^{120M_\odot} \phi(m)\ dm}{\int_{0.1M_\odot}^{120M_\odot} \phi(m)\ dm}. \tag{4.10}$$

In Equations (4.9) and (4.10) only stars with $8 < M/M_\odot < 120$ are assumed to end as SNe. Therefore, for core collapse (Type II) SNe,

$$\eta = \frac{f_{\rm SN}}{\bar{m}_*}\ \Sigma_{\rm SFR} \approx 1.3 \times 10^{-5}\ {\rm yr}^{-1}\ {\rm kpc}^{-2} \left(\frac{\Sigma_{\rm SFR}}{M_\odot\ {\rm Gyr}^{-1}\ {\rm pc}^{-2}}\right). \tag{4.11}$$

Note that Mannucci et al. (2005) found that the rate of Type Ia SNe is few times lower than Type II for Sb-c type galaxy, therefore, can approximately be neglected.

Dissipation Time Scale. Since the energy dissipation occurs at cooling radius (R_C), the driving scale for inhomogeneous medium can be estimated as (Martizzi et al. 2015)

$$R_C \approx 6.3\ {\rm pc}\ \left(\frac{n_H}{100\ {\rm cm}^{-3}}\right)^{-0.42} \approx 43.6\ {\rm pc}, \tag{4.12}$$

for $n_H = 1\ {\rm cm}^{-3}$. This gives a dissipation time as (Mac Low & Klessen 2004)

$$\tau_D \approx 9.8\ {\rm Myr}\ \left(\frac{R_C}{100\ {\rm pc}}\right)\ \left(\frac{\sigma}{10\ {\rm km/s}}\right)^{-1} \approx 4.27\ {\rm Myr}. \tag{4.13}$$

Energy Injected by Single Supernovae. To calculate the momentum injected by a SN ($P_{\rm SN}$), the fitting formula from Martizzi et al. (2015) for inhomogeneous ISM is adopted,

$$\frac{P_{\rm SN}}{M_*} = 1110\ {\rm km\ s}^{-1}\ \left(\frac{Z}{Z_\odot}\right)^{-0.114}\ \left(\frac{n_H}{100\ {\rm cm}^{-3}},\right)^{-0.190} \tag{4.14}$$

where $M_* = 100\ M_\odot$. For $Z = Z_\odot$ and $n_H = 1\ {\rm cm}^{-3}$, the momentum injected by a SN is $p_* \approx 5.3 \times 10^{43}\ {\rm g\ cm\ s}^{-1}$. This momentum sweeps out and injects energy to ISM at R_C. The mass of this ISM is about

$$M_{\rm ISM} = \frac{4\pi}{3}\ R_C^3\ \rho_{\rm ISM} \approx 2 \times 10^{37}\ {\rm grams}, \tag{4.15}$$

for $\rho_{\rm ISM} = 2 \times 10^{-24}\ {\rm g\ cm}^{-3}$. Therefore the energy injected by a SN into ISM is

$$E_{\rm SN} = \frac{p_*^2}{2M_{\rm ISM}} \approx 6.9 \times 10^{49}\ {\rm erg}, \tag{4.16}$$

which is 14 times lower than the common assumption of 10^{51} erg.

Total Energy Injected by Supernovae. Combining Equations (4.11), (4.13), and (4.16), I get

$$\Sigma_{\rm SNE} = \eta\ \epsilon_{SN}\ E_{\rm SN}\ \tau_D \approx \Sigma_{\rm SNE,0}\ \epsilon_{SN}\ \left(\frac{\Sigma_{\rm SFR}}{M_\odot\ {\rm Gyr}^{-1}\ {\rm pc}^{-2}}\right), \tag{4.17}$$

where $\Sigma_{\rm SNE,0} \approx 3.9 \times 10^{45}$ erg pc^{-2} and $0 \leq \epsilon_{SN} \leq 1$.

4.8 Appendix C. Rotation Curve and Shear Rate

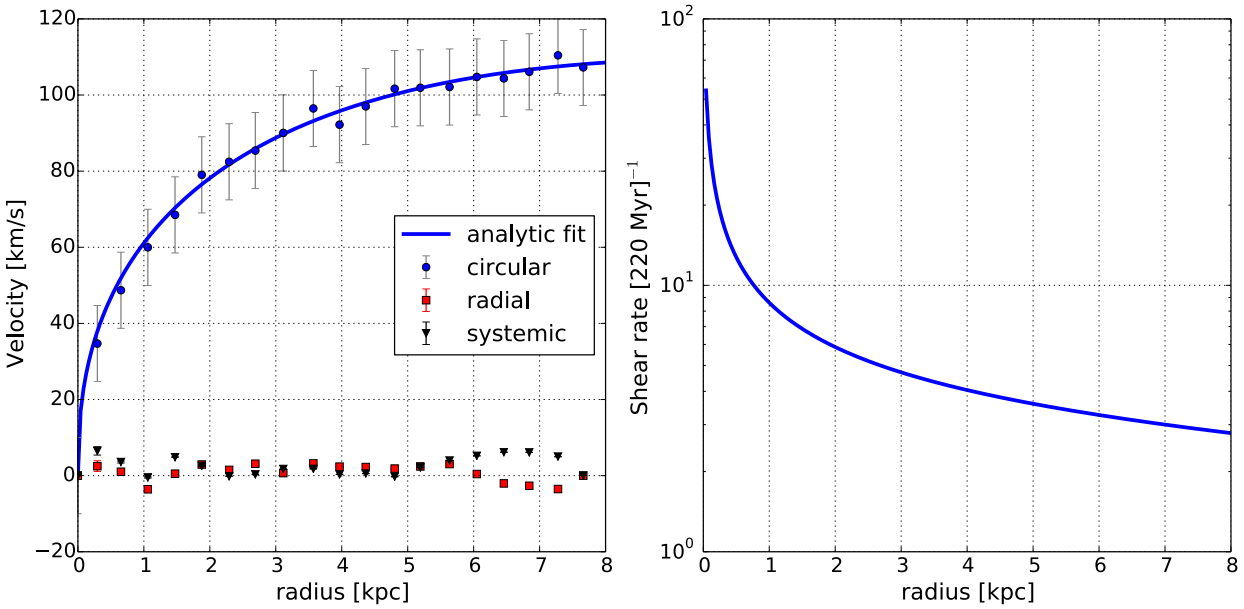

Figure 4.6: Left: The rotation curve (blue dots), radial velocity (red squares), and systemic velocity (black triangles) of M33 as a function of radius. The uncertainties are in the order of 10 km s^{-1} for the rotation curve, and 11% for both radial and systemic velocities. The blue curve is the analytical fit to the blue dots using Equation (4.19). Right: the shear rate as a function of radius, calculated using Equation (4.20).

The rotation curve from the first-moment map of atomic gas is derived using the algorithm from Bolatto et al. (2002). The line-of-sight velocities ($V_{\rm los}$) of each rings are fitted for the systemic ($V_{\rm sys}$), circular ($V_{\rm c}$), and radial ($V_{\rm rad}$) velocities, i.e.

$$V_{\rm los} = V_{\rm sys}\ +\ [V_{\rm c}\ \cos(\theta) + V_{\rm rad}\ \sin(\theta)]\ \cos(i), \tag{4.18}$$

where θ is the angle from the kinematic major axis (the receding part). In doing so, a constant value of position angle and inclination are used, i.e. no warp and no isophotal

twist. Then, the rotation curve is fitted using an analytical function (the blue curve in the left panel of Figure 4.6) that takes into account the rising part as power law and the flat part as exponential:

$$V_c(R) = a \left(\frac{R}{R_0} \right)^b \exp\left(-\frac{R}{R_0} \right), \tag{4.19}$$

where $a \approx 239.17 \pm 5.41$ km s^{-1}, $b \approx 0.41 \pm 0.04$, and $R_0 \approx 24.33 \pm 6.48$ kpc are the best fit parameters, where the uncertainties are taken from the square-root of the diagonal of covariance matrix. Therefore, the shear (S) due to differential rotation is

$$S = \frac{d\Omega}{d\ln R} = V_c \left(\frac{b-1}{R} - \frac{1}{R_0} \right), \tag{4.20}$$

which is shown in the right panel of Figure 4.6 and tabulated in Table 4.4.

4.9 Appendix D. Tables

Table 4.1: The radial profile of surface densities, H I velocity dispersion, and H I scale-height

Galactocentric radius kpc	Surface densities Atomic $M_\odot$ pc^{-2}	Molecular $M_\odot$ pc^{-2}	Stellar $M_\odot$ pc^{-2}	SFR $M_\odot$ pc^{-2}	H I Velocity dispersion km s^{-1}	H I Scale height pc
0.25 ± 0.25	4.88 ± 0.37	2.87 ± 0.27	7583.04 ± 0.13	5.50 ± 0.19	6.30 ± 2.64	0.28 ± 0.39
0.75 ± 0.25	4.76 ± 0.34	2.55 ± 0.28	168.44 ± 0.13	4.17 ± 0.20	6.01 ± 1.93	10.05 ± 0.31
1.25 ± 0.25	4.41 ± 0.36	1.54 ± 0.30	94.25 ± 0.13	2.56 ± 0.20	5.04 ± 1.75	14.67 ± 0.33
1.75 ± 0.25	5.17 ± 0.36	1.53 ± 0.31	61.51 ± 0.13	2.96 ± 0.24	5.76 ± 2.10	25.38 ± 0.34
2.25 ± 0.25	4.73 ± 0.37	1.43 ± 0.33	39.50 ± 0.13	1.78 ± 0.23	5.77 ± 2.53	40.41 ± 0.40
2.75 ± 0.25	3.61 ± 0.39	1.03 ± 0.35	25.37 ± 0.13	0.93 ± 0.21	5.08 ± 2.45	54.87 ± 0.43
3.25 ± 0.25	2.76 ± 0.41	0.85 ± 0.35	16.29 ± 0.13	1.34 ± 0.28	4.67 ± 2.29	74.43 ± 0.44
3.75 ± 0.25	4.08 ± 0.37	0.82 ± 0.36	10.47 ± 0.13	1.09 ± 0.28	5.82 ± 2.41	113.16 ± 0.38
4.25 ± 0.25	4.48 ± 0.36	0.66 ± 0.36	6.72 ± 0.13	0.54 ± 0.24	5.37 ± 1.89	124.58 ± 0.34
4.75 ± 0.25	3.89 ± 0.36	0.50 ± 0.38	4.32 ± 0.13	0.36 ± 0.25	5.83 ± 2.27	189.27 ± 0.38
5.25 ± 0.25	3.37 ± 0.38	0.43 ± 0.39	2.77 ± 0.13	0.22 ± 0.26	5.36 ± 2.21	243.94 ± 0.41
5.75 ± 0.25	3.08 ± 0.39	0.40 ± 0.39	1.78 ± 0.13	0.47 ± 0.35	5.33 ± 2.26	312.37 ± 0.44
6.25 ± 0.25	4.20 ± 0.36	0.38 ± 0.39	1.14 ± 0.13	0.13 ± 0.28	5.79 ± 2.24	294.54 ± 0.43
6.75 ± 0.25	4.13 ± 0.35	0.44 ± 0.40	0.73 ± 0.13	0.11 ± 0.29	5.57 ± 2.31	293.45 ± 0.45
7.25 ± 0.25	2.84 ± 0.39	0.42 ± 0.42	0.47 ± 0.13	0.06 ± 0.28	4.34 ± 1.88	360.16 ± 0.48
7.75 ± 0.25	1.39 ± 0.43	0.25 ± 0.43	0.30 ± 0.13	0.07 ± 0.31	2.62 ± 1.62	590.30 ± 0.62

Table 4.2: The radial profile of energy per unit area

Radius[a]	Kinetic[b]	Thermal[b]	Turbulent[b]	MRI[b]	SNe[b,c]	SNe[b]	Efficiency[b,c]	Efficiency[b]
0.25 ± 0.25	3.07 ± 3.14	1.61 ± 1.31	3.05 ± 3.14	-2.39 ± 2.13	3.33 ± 2.97	3.02 ± 2.86	0.53 ± 0.69	1.09 ± 1.53
0.75 ± 0.25	2.90 ± 2.90	1.97 ± 1.51	2.85 ± 2.90	0.28 ± 0.44	3.21 ± 2.87	3.06 ± 2.87	0.43 ± 0.53	0.61 ± 0.81
1.25 ± 0.25	2.82 ± 2.86	2.22 ± 1.68	2.70 ± 2.86	0.46 ± 0.64	3.00 ± 2.67	3.02 ± 2.85	0.50 ± 0.75	0.48 ± 0.75
1.75 ± 0.25	2.95 ± 2.99	2.47 ± 1.90	2.77 ± 2.99	0.81 ± 1.01	3.06 ± 2.80	3.09 ± 2.96	0.51 ± 0.89	0.48 ± 0.87
2.25 ± 0.25	3.03 ± 3.12	2.50 ± 1.92	2.89 ± 3.12	1.08 ± 1.36	2.84 ± 2.57	2.95 ± 2.84	1.09 ± 1.96	0.85 ± 1.60
2.75 ± 0.25	2.87 ± 2.99	2.47 ± 1.88	2.65 ± 2.99	1.32 ± 1.63	2.56 ± 2.25	2.83 ± 2.72	1.16 ± 2.61	0.64 ± 1.49
3.25 ± 0.25	2.67 ± 2.80	2.42 ± 1.82	2.31 ± 2.80	1.58 ± 1.90	2.72 ± 2.53	3.14 ± 3.10	0.36 ± 1.15	0.14 ± 0.46
3.75 ± 0.25	2.92 ± 2.99	2.59 ± 1.99	2.65 ± 2.99	1.87 ± 2.13	2.63 ± 2.44	2.93 ± 2.86	0.88 ± 2.04	0.48 ± 1.13
4.25 ± 0.25	2.83 ± 2.87	2.63 ± 2.03	2.39 ± 2.87	1.99 ± 2.20	2.32 ± 2.06	2.69 ± 2.56	0.81 ± 2.48	0.42 ± 1.30
4.75 ± 0.25	2.80 ± 2.85	2.59 ± 1.98	2.38 ± 2.86	2.31 ± 2.57	2.15 ± 1.91	2.57 ± 2.46	0.70 ± 2.23	0.42 ± 1.31
5.25 ± 0.25	2.79 ± 2.87	2.52 ± 1.92	2.45 ± 2.87	2.48 ± 2.77	1.92 ± 1.69	2.45 ± 2.35	0.73 ± 2.24	0.48 ± 1.39
5.75 ± 0.25	2.74 ± 2.84	2.48 ± 1.87	2.40 ± 2.84	2.67 ± 2.99	2.23 ± 2.13	2.79 ± 2.78	0.39 ± 1.23	0.23 ± 0.68
6.25 ± 0.25	2.88 ± 2.93	2.59 ± 1.97	2.56 ± 2.94	2.60 ± 2.91	1.64 ± 1.45	2.11 ± 2.02	0.81 ± 2.44	0.68 ± 1.95
6.75 ± 0.25	2.83 ± 2.89	2.58 ± 1.95	2.46 ± 2.89	2.60 ± 2.94	1.55 ± 1.38	2.05 ± 1.99	0.66 ± 2.22	0.56 ± 1.79
7.25 ± 0.25	2.61 ± 2.70	2.46 ± 1.81	2.07 ± 2.71	2.79 ± 3.15	1.17 ± 0.99	1.92 ± 1.85	0.19 ± 0.91	0.17 ± 0.80
7.75 ± 0.25	2.30 ± 2.50	2.20 ± 1.51	1.60 ± 2.50	3.20 ± 3.69	1.10 ± 0.95	2.24 ± 2.25	0.02 ± 0.21	0.02 ± 0.19

[a] The unit is kpc.
[b] The units are $\log(10^{43}$ erg pc$^{-2})$.
[c] For a constant dissipation time of 9.8 Myr.

Table 4.3: The properties of molecular clouds in M33.

No.	Distance[a] kpc	Size[b] pc	Mass[c] $10^5 M_\odot$	Velocity Dispersion[d] km s^{-1}	Turbulent Energy log(10^{51} erg pc^{-2})	SNe energy log(10^{51} erg pc^{-2})
1	0.20 ± 0.05	89.66 ± 16.66	2.49 ± 0.08	2.57 ± 0.91	-1.22 ± -2.43	0.08 ± -7.91
2	0.22 ± 0.02	47.00 ± 16.66	0.63 ± 0.04	2.82 ± 1.10	-1.77 ± -2.67	-0.72 ± -8.47
3	0.24 ± 0.05	42.04 ± 16.66	1.08 ± 0.03	3.89 ± 1.31	-1.28 ± -2.82	-0.20 ± -8.57
4	0.39 ± 0.11	99.03 ± 16.66	2.25 ± 0.07	2.81 ± 1.68	-1.10 ± -2.58	-0.01 ± -7.82
5	0.55 ± 0.03	79.76 ± 16.66	2.03 ± 0.13	3.14 ± 0.91	-1.13 ± -2.66	-0.46 ± -8.01
6	0.55 ± 0.12	87.17 ± 16.66	1.94 ± 0.09	2.65 ± 1.13	-1.29 ± -2.75	-0.39 ± -7.93
7	0.69 ± 0.03	54.00 ± 16.66	0.90 ± 0.03	3.76 ± 1.33	-1.34 ± -2.64	-1.13 ± -8.35
8	0.75 ± 0.04	59.45 ± 16.66	1.12 ± 0.05	2.61 ± 0.51	-1.59 ± -3.17	-0.77 ± -8.26
9	0.76 ± 0.05	63.05 ± 16.66	2.64 ± 0.21	3.61 ± 0.55	-0.94 ± -2.87	0.63 ± -8.21
10	0.76 ± 0.03	49.74 ± 16.66	0.86 ± 0.04	2.71 ± 0.43	-1.68 ± -3.20	-0.47 ± -8.42
11	0.80 ± 0.03	37.60 ± 16.66	0.34 ± 0.03	2.21 ± 0.52	-2.25 ± -3.53	-1.22 ± -8.66
12	0.82 ± 0.05	64.44 ± 16.66	2.01 ± 0.15	3.69 ± 0.76	-1.04 ± -2.72	-0.66 ± -8.19
13	0.82 ± 0.10	74.01 ± 16.66	1.07 ± 0.08	2.00 ± 0.74	-1.73 ± -2.92	-0.45 ± -8.07
14	0.89 ± 0.09	79.20 ± 16.66	2.09 ± 0.09	2.87 ± 0.45	-1.26 ± -2.95	-0.06 ± -8.01
15	0.90 ± 0.05	63.05 ± 16.66	1.38 ± 0.06	2.48 ± 0.26	-1.58 ± -3.35	-0.79 ± -8.21
16	0.94 ± 0.03	43.07 ± 16.66	0.52 ± 0.03	2.58 ± 0.71	-1.92 ± -3.05	-0.43 ± -8.54
17	0.95 ± 0.04	47.93 ± 16.66	0.35 ± 0.02	1.64 ± 0.34	-2.59 ± -3.28	-1.04 ± -8.45
18	1.09 ± 0.03	39.88 ± 16.66	0.77 ± 0.03	3.48 ± 0.33	-1.55 ± -3.24	-0.86 ± -8.61
19	1.12 ± 0.06	60.92 ± 16.66	0.69 ± 0.03	2.10 ± 0.73	-2.01 ± -5.19	-1.09 ± -8.24
20	1.13 ± 0.04	49.74 ± 16.66	0.39 ± 0.02	1.55 ± 0.32	-2.60 ± -5.48	-0.91 ± -8.42
21	1.19 ± 0.06	79.20 ± 16.66	1.27 ± 0.05	3.49 ± 9.34	-0.86 ± -2.86	-0.30 ± -8.01
22	1.19 ± 0.03	48.84 ± 16.66	0.75 ± 0.02	2.36 ± 0.42	-1.86 ± -3.43	-0.62 ± -8.43
23	1.20 ± 0.08	57.17 ± 16.66	1.70 ± 0.06	3.78 ± 0.92	-1.10 ± -2.64	-0.10 ± -8.30
24	1.24 ± 0.11	87.67 ± 16.66	3.15 ± 0.16	3.06 ± 0.67	-1.01 ± -2.62	0.09 ± -7.93
25	1.25 ± 0.05	75.20 ± 16.66	0.88 ± 0.05	1.97 ± 0.43	-2.06 ± -5.27	-0.52 ± -8.06
26	1.27 ± 0.05	57.17 ± 16.66	1.28 ± 0.08	2.74 ± 0.32	-1.51 ± -3.15	-0.46 ± -8.30
27	1.38 ± 0.02	37.60 ± 16.66	0.20 ± 0.01	1.04 ± 0.50	-3.52 ± -5.60	-1.40 ± -8.66
28	1.40 ± 0.05	54.00 ± 16.66	0.36 ± 0.01	... $\pm$ ...	... $\pm$ ...	-1.24 ± -8.35
29	1.47 ± 0.04	45.08 ± 16.66	0.54 ± 0.03	2.68 ± 0.44	-1.93 ± -3.32	-0.85 ± -8.50
30	1.48 ± 0.09	76.94 ± 16.66	1.15 ± 0.05	2.05 ± 0.65	-1.78 ± -5.05	-0.54 ± -8.04
31	1.49 ± 0.06	51.48 ± 16.66	1.01 ± 0.05	2.58 ± 0.33	-1.69 ± -3.15	-0.10 ± -8.39
32	1.56 ± 0.06	60.92 ± 16.66	0.83 ± 0.04	2.31 ± 0.72	-1.83 ± -2.99	-0.76 ± -8.24
33	1.67 ± 0.06	59.45 ± 16.66	1.35 ± 0.11	2.71 ± 0.40	-1.50 ± -3.20	-0.28 ± -8.26
34	1.68 ± 0.05	80.31 ± 16.66	1.47 ± 0.08	2.39 ± 0.89	-1.53 ± -2.70	-0.34 ± -8.00
35	1.69 ± 0.04	42.04 ± 16.66	0.41 ± 0.04	2.17 ± 0.76	-2.12 ± -3.52	-1.14 ± -8.57
36	1.74 ± 0.05	65.12 ± 16.66	0.83 ± 0.05	2.15 ± 0.53	-1.97 ± -5.19	-1.01 ± -8.18
37	1.74 ± 0.05	38.75 ± 16.66	0.19 ± 0.02	1.43 ± 0.26	-3.31 ± -5.61	-1.16 ± -8.64
38	1.75 ± 0.06	75.78 ± 16.66	1.10 ± 0.05	2.07 ± 0.63	-1.80 ± -3.07	0.02 ± -8.05
39	1.75 ± 0.05	58.70 ± 16.66	1.24 ± 0.05	2.94 ± 0.70	-1.43 ± -2.88	0.65 ± -8.28
40	1.78 ± 0.16	139.42 ± 16.66	3.70 ± 0.12	2.09 ± 0.75	-1.31 ± -2.78	0.11 ± -7.52
41	1.78 ± 0.03	37.60 ± 16.66	0.20 ± 0.01	1.44 ± 0.56	-2.92 ± -5.57	-1.24 ± -8.66
42	1.78 ± 0.11	122.19 ± 16.66	3.07 ± 0.15	2.37 ± 0.75	-1.28 ± -2.75	0.04 ± -7.64
43	1.80 ± 0.03	44.09 ± 16.66	0.49 ± 0.02	2.41 ± 0.58	-2.01 ± -3.25	-1.42 ± -8.52

Continued on Next Page

No.	Distance[a] kpc	Size[b] pc	Mass[c] $10^5 M_\odot$	Velocity Dispersion[d] km s^{-1}	Turbulent Energy log(10^{51} erg pc^{-2})	SNe energy log(10^{51} erg pc^{-2})
44	1.82 ± 0.05	70.96 ± 16.66	0.95 ± 0.05	2.28 ± 0.63	-1.87 ± -3.04	-0.71 ± -8.11
45	1.82 ± 0.04	50.62 ± 16.66	0.33 ± 0.02	1.30 ± 0.00	-4.20 ± -2.70	-1.12 ± -8.40
46	1.85 ± 0.06	74.01 ± 16.66	0.88 ± 0.02	1.89 ± 0.47	-2.10 ± -5.25	-0.81 ± -8.07
47	1.87 ± 0.05	67.78 ± 16.66	0.78 ± 0.03	2.88 ± 1.11	-1.76 ± -5.17	-0.95 ± -8.15
48	1.89 ± 0.04	38.75 ± 16.66	0.20 ± 0.01	1.12 ± 0.43	-3.41 ± -5.57	-1.41 ± -8.64
49	1.89 ± 0.03	37.60 ± 16.66	0.15 ± 0.01	1.30 ± 0.00	-3.71 ± -5.76	-1.32 ± -8.66
50	1.90 ± 0.07	57.17 ± 16.66	0.82 ± 0.05	2.04 ± 0.44	-1.97 ± -5.12	-0.49 ± -8.30
51	1.98 ± 0.02	42.04 ± 16.66	0.31 ± 0.03	1.88 ± 0.82	-2.45 ± -3.20	-1.05 ± -8.57
52	1.99 ± 0.02	37.60 ± 16.66	0.30 ± 0.02	2.24 ± 0.78	-2.42 ± -2.95	-1.54 ± -8.66
53	2.02 ± 0.06	52.33 ± 16.66	0.52 ± 0.03	1.92 ± 0.63	-2.19 ± -5.25	0.41 ± -8.37
54	2.04 ± 0.02	40.97 ± 16.66	0.79 ± 0.02	5.32 ± 1.73	-1.14 ± -2.50	-0.53 ± -8.59
55	2.07 ± 0.06	55.61 ± 16.66	0.46 ± 0.02	1.72 ± 0.56	-2.50 ± -3.34	-1.33 ± -8.32
56	2.07 ± 0.06	53.17 ± 16.66	0.39 ± 0.02	1.74 ± 0.41	-2.56 ± -5.50	-0.91 ± -8.36
57	2.17 ± 0.03	60.92 ± 16.66	1.56 ± 0.06	2.98 ± 0.29	-1.37 ± -3.31	-0.47 ± -8.24
58	2.18 ± 0.07	74.61 ± 16.66	1.08 ± 0.07	2.85 ± 0.74	-1.73 ± -2.67	-1.01 ± -8.07
59	2.20 ± 0.04	68.43 ± 16.66	2.38 ± 0.08	5.19 ± 2.63	-0.62 ± -1.98	-0.02 ± -8.14
60	2.21 ± 0.08	94.46 ± 16.66	2.64 ± 0.05	3.23 ± 1.59	-1.02 ± -2.16	-0.51 ± -7.86
61	2.24 ± 0.03	38.75 ± 16.66	0.15 ± 0.01	1.70 ± 0.37	-3.03 ± -5.79	-1.41 ± -8.64
62	2.30 ± 0.04	57.17 ± 16.66	0.61 ± 0.03	2.03 ± 0.82	-2.13 ± -3.16	-1.03 ± -8.30
63	2.31 ± 0.04	38.75 ± 16.66	0.24 ± 0.02	1.88 ± 0.51	-2.61 ± -5.56	-1.45 ± -8.64
64	2.33 ± 0.05	69.07 ± 16.66	1.75 ± 0.04	3.23 ± 0.51	-1.23 ± -2.82	-0.52 ± -8.13
65	2.34 ± 0.05	56.40 ± 16.66	1.35 ± 0.07	2.30 ± 0.33	-1.64 ± -3.12	-0.32 ± -8.31
66	2.36 ± 0.05	43.07 ± 16.66	0.62 ± 0.02	2.17 ± 0.34	-2.05 ± -3.56	-0.77 ± -8.54
67	2.40 ± 0.11	131.59 ± 16.66	5.70 ± 0.21	3.23 ± 8.27	-0.43 ± -2.42	-0.03 ± -7.57
68	2.43 ± 0.02	36.40 ± 16.66	0.15 ± 0.01	1.39 ± 0.24	-3.26 ± -5.79	-1.55 ± -8.69
69	2.44 ± 0.03	46.05 ± 16.66	0.74 ± 0.03	3.69 ± 0.55	-1.50 ± -2.74	-1.20 ± -8.49
70	2.51 ± 0.04	75.78 ± 16.66	3.70 ± 0.14	4.04 ± 0.66	-0.70 ± -2.66	-0.80 ± -8.05
71	2.53 ± 0.08	98.13 ± 16.66	2.50 ± 0.11	2.49 ± 0.90	-1.23 ± -2.65	-0.44 ± -7.83
72	2.65 ± 0.03	47.00 ± 16.66	0.58 ± 0.02	2.61 ± 0.17	-1.93 ± -3.34	-1.02 ± -8.47
73	2.66 ± 0.04	46.05 ± 16.66	0.35 ± 0.02	1.72 ± 0.71	-2.59 ± -5.43	-1.61 ± -8.49
74	2.77 ± 0.04	49.74 ± 16.66	0.32 ± 0.02	1.54 ± 0.34	-2.71 ± -5.58	-1.55 ± -8.42
75	2.86 ± 0.12	110.82 ± 16.66	3.16 ± 0.13	2.42 ± 0.96	-1.20 ± -2.65	-0.05 ± -7.72
76	2.91 ± 0.05	57.17 ± 16.66	0.72 ± 0.04	1.92 ± 0.42	-2.09 ± -5.24	-1.03 ± -8.30
77	3.00 ± 0.02	37.60 ± 16.66	0.19 ± 0.02	1.43 ± 0.31	-3.00 ± -5.69	-1.60 ± -8.66
78	3.09 ± 0.08	91.13 ± 16.66	2.87 ± 0.26	3.21 ± 1.65	-0.91 ± -2.32	0.09 ± -7.89
79	3.09 ± 0.05	58.70 ± 16.66	0.49 ± 0.02	1.59 ± 0.43	-2.44 ± -5.44	-1.16 ± -8.28
80	3.24 ± 0.04	67.78 ± 16.66	0.62 ± 0.03	1.80 ± 0.64	-2.40 ± -5.31	-1.35 ± -8.15
81	3.26 ± 0.04	47.00 ± 16.66	0.24 ± 0.02	1.41 ± 0.24	-3.04 ± -5.67	-1.25 ± -8.47
82	3.27 ± 0.03	38.75 ± 16.66	0.20 ± 0.02	1.58 ± 0.36	-2.94 ± -5.67	-1.76 ± -8.64
83	3.31 ± 0.05	58.70 ± 16.66	0.65 ± 0.03	1.93 ± 0.50	-2.13 ± -3.39	-0.82 ± -8.28
84	3.33 ± 0.06	83.54 ± 16.66	1.42 ± 0.04	2.00 ± 0.51	-1.74 ± -3.00	0.01 ± -7.97
85	3.44 ± 0.05	52.33 ± 16.66	0.50 ± 0.03	1.96 ± 0.53	-2.24 ± -2.98	-0.53 ± -8.37
86	3.46 ± 0.03	47.00 ± 16.66	1.11 ± 0.04	4.57 ± 0.97	-1.11 ± -2.52	-0.40 ± -8.47
87	3.51 ± 0.05	65.12 ± 16.66	3.53 ± 0.19	4.80 ± 1.29	-0.59 ± -2.31	0.97 ± -8.18
88	3.63 ± 0.04	48.84 ± 16.66	0.51 ± 0.02	1.92 ± 0.47	-2.38 ± -4.98	-1.13 ± -8.43
89	3.70 ± 0.04	55.61 ± 16.66	0.58 ± 0.03	1.76 ± 0.39	-2.24 ± -5.44	-1.34 ± -8.32

Continued on Next Page

No.	Distance[a] kpc	Size[b] pc	Mass[c] $10^5 M_\odot$	Velocity Dispersion[d] km s^{-1}	Turbulent Energy log(10^{51} erg pc^{-2})	SNe energy log(10^{51} erg pc^{-2})
90	3.72 ± 0.06	50.62 ± 16.66	0.37 ± 0.03	1.65 ± 0.37	-2.58 ± -5.48	-1.57 ± -8.40
91	3.72 ± 0.03	67.13 ± 16.66	1.03 ± 0.05	2.21 ± 0.49	-1.80 ± -3.12	-0.51 ± -8.16
92	3.74 ± 0.09	56.40 ± 16.66	0.45 ± 0.03	1.57 ± 0.52	-2.62 ± -5.41	-0.87 ± -8.31
93	3.75 ± 0.05	78.64 ± 16.66	1.25 ± 0.07	2.13 ± 0.65	-1.72 ± -3.00	-0.84 ± -8.02
94	3.79 ± 0.04	42.04 ± 16.66	0.27 ± 0.02	2.15 ± 0.62	-2.50 ± -5.47	-1.68 ± -8.57
95	3.79 ± 0.06	71.58 ± 16.66	1.00 ± 0.05	2.06 ± 0.72	-1.85 ± -3.13	-0.18 ± -8.10
96	3.86 ± 0.03	37.60 ± 16.66	0.14 ± 0.01	1.42 ± 0.28	-3.43 ± -5.73	-1.75 ± -8.66
97	3.91 ± 0.04	47.00 ± 16.66	0.26 ± 0.02	1.71 ± 0.38	-2.86 ± -5.56	-1.71 ± -8.47
98	3.95 ± 0.10	118.89 ± 16.66	0.96 ± 0.03	1.24 ± 0.25	-2.96 ± -4.96	-0.82 ± -7.66
99	3.96 ± 0.03	39.88 ± 16.66	0.07 ± 0.00	... $\pm$ ...	... $\pm$ ...	-1.83 ± -8.61
100	3.98 ± 0.05	47.00 ± 16.66	0.33 ± 0.02	1.63 ± 0.49	-2.75 ± -5.44	-1.02 ± -8.47
101	4.01 ± 0.03	36.40 ± 16.66	0.20 ± 0.01	1.91 ± 0.49	-2.68 ± -3.61	-1.67 ± -8.69
102	4.18 ± 0.06	53.17 ± 16.66	0.43 ± 0.03	2.04 ± 0.90	-2.28 ± -5.32	-1.20 ± -8.36
103	4.21 ± 0.03	36.40 ± 16.66	0.07 ± 0.00	... $\pm$ ...	... $\pm$ ...	-1.39 ± -8.69
104	4.23 ± 0.03	36.40 ± 16.66	0.79 ± 0.03	4.08 ± 0.33	-1.40 ± -2.90	-1.48 ± -8.69
105	4.24 ± 0.03	38.75 ± 16.66	0.28 ± 0.01	2.09 ± 0.62	-2.45 ± -5.37	-1.74 ± -8.64
106	4.24 ± 0.04	44.09 ± 16.66	0.29 ± 0.01	1.29 ± 0.01	-3.28 ± -5.37	-1.50 ± -8.52
107	4.25 ± 0.03	50.62 ± 16.66	0.57 ± 0.02	2.66 ± 1.27	-1.77 ± -2.65	-0.89 ± -8.40
108	4.36 ± 0.12	93.52 ± 16.66	1.50 ± 0.06	2.46 ± 0.91	-1.53 ± -2.86	-0.84 ± -7.87
109	4.37 ± 0.06	53.17 ± 16.66	0.36 ± 0.02	1.89 ± 0.65	-2.49 ± -5.48	-0.20 ± -8.36
110	4.39 ± 0.03	36.40 ± 16.66	0.20 ± 0.01	1.64 ± 0.34	-2.79 ± -5.62	-1.62 ± -8.69
111	4.45 ± 0.03	46.05 ± 16.66	0.34 ± 0.02	1.79 ± 0.33	-2.52 ± -5.57	-1.15 ± -8.49
112	4.46 ± 0.04	36.40 ± 16.66	0.17 ± 0.01	1.30 ± 0.00	-3.21 ± -5.76	-1.87 ± -8.69
113	4.49 ± 0.03	48.84 ± 16.66	0.31 ± 0.02	1.50 ± 0.30	-2.73 ± -5.59	-1.46 ± -8.43
114	4.57 ± 0.02	42.04 ± 16.66	0.15 ± 0.01	1.28 ± 0.01	-3.62 ± -5.78	-1.80 ± -8.57
115	4.60 ± 0.06	45.08 ± 16.66	0.22 ± 0.01	1.16 ± 0.37	-3.36 ± -5.62	-1.51 ± -8.50
116	4.81 ± 0.05	64.44 ± 16.66	0.44 ± 0.01	1.59 ± 0.49	-2.86 ± -5.31	-0.50 ± -8.19
117	4.86 ± 0.04	38.75 ± 16.66	0.21 ± 0.02	1.30 ± 0.01	-3.09 ± -5.73	-1.36 ± -8.64
118	5.55 ± 0.05	62.35 ± 16.66	0.64 ± 0.03	2.01 ± 0.60	-2.14 ± -5.26	-0.92 ± -8.22
119	5.65 ± 0.05	60.92 ± 16.66	0.79 ± 0.05	2.50 ± 0.81	-1.82 ± -5.07	0.96 ± -8.24
120	5.77 ± 0.05	46.05 ± 16.66	0.25 ± 0.03	1.93 ± 0.70	-2.67 ± -5.00	-1.63 ± -8.49
121	6.06 ± 0.05	85.12 ± 16.66	0.97 ± 0.06	1.81 ± 0.64	-2.11 ± -3.12	-0.74 ± -7.95
122	6.38 ± 0.03	37.60 ± 16.66	0.17 ± 0.02	1.30 ± 0.00	-3.30 ± -5.70	-2.28 ± -8.66
123	6.61 ± 0.05	43.07 ± 16.66	0.30 ± 0.01	1.76 ± 0.34	-2.57 ± -5.53	-0.93 ± -8.54
124	6.65 ± 0.05	52.33 ± 16.66	0.38 ± 0.03	1.56 ± 0.34	-2.71 ± -5.37	-0.86 ± -8.37

[a] Distance is measured from the nucleus of M33.
[b] Size is defined as (area/π)$^{0.5}$. The uncertainty is the physical size of one pixel.
[c] The uncertainty is calculated using bootstrap resampling with 1,000 iterations.
[d] The mean velocity dispersion within a cloud. The uncertainty is standard deviation of velocity dispersion within a cloud.

Table 4.4: The rotation curve of M33

Radius kpc	Circular velocity km s^{-1}	Radial velocity km s^{-1}	Systemic velocity km s^{-1}
0.3	34.7 ± 0.9	2.5 ± 1.4	6.5 ± 1.1
0.7	48.7 ± 0.3	1.0 ± 0.4	3.6 ± 0.3
1.1	60.0 ± 0.2	-3.6 ± 0.2	-0.5 ± 0.2
1.5	68.5 ± 0.2	0.5 ± 0.2	4.8 ± 0.1
1.9	79.0 ± 0.1	2.9 ± 0.1	2.6 ± 0.1
2.3	82.5 ± 0.1	1.5 ± 0.1	-0.2 ± 0.1
2.7	85.4 ± 0.1	3.1 ± 0.1	0.3 ± 0.1
3.1	90.0 ± 0.1	0.7 ± 0.1	1.7 ± 0.1
3.6	96.5 ± 0.1	3.2 ± 0.1	1.8 ± 0.1
4.0	92.2 ± 0.1	2.4 ± 0.1	0.3 ± 0.1
4.4	97.0 ± 0.1	2.3 ± 0.1	0.6 ± 0.1
4.8	101.7 ± 0.1	1.9 ± 0.1	-0.3 ± 0.1
5.2	101.9 ± 0.1	2.4 ± 0.1	2.1 ± 0.1
5.6	102.1 ± 0.1	3.0 ± 0.1	4.0 ± 0.1
6.0	104.8 ± 0.1	0.4 ± 0.1	5.2 ± 0.1
6.5	104.4 ± 0.1	-2.0 ± 0.1	6.2 ± 0.0
6.8	106.1 ± 0.1	-2.7 ± 0.1	6.1 ± 0.1
7.3	110.4 ± 0.1	-3.5 ± 0.1	5.0 ± 0.1
7.7	107.3 ± 0.5	0.0 ± 0.0	0.0 ± 0.0
8.1	111.6 ± 0.9	0.0 ± 0.0	0.0 ± 0.0

Acknowledgments

This research has been made available through the collaboration with Leo Blitz and Edith Falgarone, and funded by part from the France-Berkeley Fund (FBF). I thank Karl Schuster and Jonathan Braine to provide the CO map from IRAM, and Pierre Gratier for the HI map from VLA. I also thank Chris McKee, Eve Ostriker, Mikhail Belyaev, and Davide Martizzi for valuable discussions. I appreciate the hospitality of Ecole Normale Superieure and Observatoire de Paris during my visit to Paris. Throughout this project, I were supported by the National Science Foundation (NSF) under Grant No. AST-1140063. The IRAM telescope is supported by INSU/CNRS (France), MPG (Germany) and IGN (Spain).

Chapter 5

Concluding Remarks

The interplay between molecular gas and star formation on kilo-parsec scales is expected, because stars form in molecular gas and stars give feedback to their natal clouds. Their connection is also important in galaxy evolution because the build-up of stellar mass in a galaxy depends on the amount of molecular gas as a fuel of star formation and the rate to convert molecular gas into stars per unit gas mass, i.e. its efficiency. This dissertation aims to illuminate those processes, motivated by the following three open questions. (1) Are the properties of molecular clouds in the early-type galaxies similar or different than those in the well-studied spirals and dwarfs? (2) Is the central part of galaxies forming stars at a different efficiency than that in the disk? (3) Does stellar feedback (in the form of supernovae energy) have enough energy to maintain turbulence in atomic gas and molecular clouds? In this chapter, I highlight some major findings from the previous chapters to address those questions.

5.1 The Molecular Clouds in NGC4526

NGC4536 is a lenticular, early-type galaxy. This galaxy is part of the Atlas-3D sample, therefore, has been observed at high resolution ($\approx$ 20 pc scale) CO($2-1$) line using the CARMA array (Davis et al. 2013b). I make use of these data to identify 103 resolved individual Giant Molecular Clouds (GMCs) using the CPROPS program (Rosolowsky & Leroy 2006). As a population, GMCs in NGC4526 are in gravitational equilibrium with a mean virial parameter $\alpha \approx 0.99$ and a standard deviation of ≈ 0.14. This result is intriguing because this early-type galaxy lacks star formation, therefore, a higher virial parameter is expected. The cloud mass distribution has an exponent of -2.39 with a truncated mass of $4 \times 10^6 M_\odot$, steeper than the GMC mass distribution in the inner Milky Way, but comparable to those in nearby galaxies. This steep exponent means the total molecular mass in GMCs is dominated by the contribution of low mass clouds.

There are some differences between the properties of GMCs in NGC4526 and in the Milky Way:

- GMCs in NGC4526 are more luminous and more turbulent than the equal-size GMCs in the Milky Way disk by a factor of ~ 5 and ~ 3, respectively. The surface density of GMCs in NGC4526 is ~ 7 times higher than those in the Milky Way disk. These differences may be due to higher interstellar radiation field and cloud extinction in NGC4526.

- GMCs in NGC4526 are less turbulent than GMCs in the Galactic center. This may be caused by different equilibrium state of GMCs. Galactic center clouds are pressure-bound, while clouds in NGC4526 are gravitationally bound.

- There is no size-linewidth correlation in NGC4526, in contrast to what is expected from the Larson's relation in the Milky Way. This implies that the surface density of GMCs is not constant, but follows the relation $\sigma_v R^{-0.5} \propto \Sigma^{0.5}$, as expected from the gravitational equilibrium.

With the on-going project of WISDOM survey to observe CO in the early-type galaxies at high resolution using ALMA (Onishi et al. 2017; Davis et al. 2017, Liu et al. in prep.), more samples will become available to test whether those findings are representative for early-type galaxies.

5.2 The Molecular Depletion Time in Galactic Centers

The molecular gas depletion time in the disk of nearby galaxies is approximately constant (~ 2 Gyr). The fact that it is much longer than the free-fall time (~ 1 Myr) means that there must be support to counteract gravity (thought to be in the form of turbulent motions). It is also less than the age of the Universe (13.8 Gyr), which means molecular gas needs to be replenished (through atomic-to-molecular conversion, stellar ejecta, etc.) to sustain an on-going star formation in nearby galaxies. The combination of EDGE and CALIFA surveys opens an opportunity to find the variation of molecular depletion time within a galaxy, but also covers a significant sample of galaxies.

I found that the central part of a galaxy (defined as the region within 0.1 R_{25} from the center) can have shorter ($\sim 25\%$ of the sample), longer, or similar depletion time compared to that in the disks. The central drop of depletion time is caused by a higher central star formation rate, rather than a smaller amount of central molecular gas. Furthermore, the central drop of depletion time is coincident with a higher stellar surface density. This suggests that the central drop of depletion time is driven by a high gravitational potential, dominated by the stars, which is expected by the self-regulated model of star formation (Ostriker et al. 2010; Ostriker & Shetty 2011). A high feedback rate (in the form of shorter depletion time) is required to balance high pressure in a central region where the vertical gravity from stars and gas is very strong. This result places the galactic centers in the intermediate regime between the galactic disks and starburst galaxies.

5.3 The Origin of Interstellar Turbulence in M33

As one of the closest galaxies, M33 has been studied for many decades. The wealth of high resolution, multi-wavelength data from UV to radio, offers an opportunity to study the interstellar turbulence in M33 down to the scale of molecular clouds. An important question related to turbulence is "what is the energy source needed to maintain turbulence?" In this dissertation, I attempt to answer that question by considering energy sources from supernovae and magneto-rotational instability (MRI).

I derive the H I kinetic energy by measuring the velocity dispersion and H I surface density. Then, the thermal energy is subtracted from the kinetic energy. The radial profile of turbulent energy in M33 is approximately constant, even though the star formation rate declines as a function of radius. I found that supernovae have enough energy to maintain turbulence in the inner part of M33 ($r \lesssim 4$ kpc) and in the molecular clouds, while MRI has enough energy to maintain turbulence in the outer part of M33, where star formation is negligible. The mean coupling efficiency of supernovae energy to generate turbulence in H I gas is $\sim 50\%$, while in the molecular clouds, the coupling efficiency is $\sim 10\%$. I conclude that the sum of supernovae and MRI has enough energy to maintain turbulence at all radii in M33.

5.4 The Road Ahead

The study of molecular clouds will be done in greater detail in the upcoming decade. A large scale proposal to observe $\sim 100,000$ molecular clouds in nearby galaxies has been proposed using ALMA (E. Schinerer, A. Leroy, E. Rosolowsky, & D. Kruijssen, personal communication), where I will become one of the team members. This will expand the study of molecular clouds from galaxy-to-galaxy basis, towards a large statistical sample to answer the following questions: (1) how are the properties of molecular clouds related to the local environment of galaxies?, (2) what is the star formation efficiency per molecular cloud?, and (3) what is their lifetime? In addition, the on-going observations of molecular gas in the early-type galaxies (led by M. Bureau & T. Davis) will give an insight of why the early-type galaxies lack of star formation.

On scales larger than the size of molecular clouds, the optical IFU and mm-interferometric surveys provide the best combination to study the interplay between stars and gas. Currently, the optical IFU survey is a big "industry" in the astronomical community. In this respect, the CARMA EDGE survey is the first to observe CO as a counterpart of the CALIFA IFU survey. However, the EDGE survey only covers $\sim 20\%$ of the CALIFA sample. The ALMA EDGE survey (led by A. Bolatto, T. Wong & L. Blitz) has been proposed to double the CARMA EDGE sample, especially targeting the under-represented galaxy population, such as the early-types and low mass galaxies. Therefore, a complete census of the relation between molecular gas and star formation as a function of metallicities, ISM pressure, and kinematics will be gathered. An expansion to include archival ultraviolet and infrared data

is currently underway (led by A. Leroy and K. Sandstrom) as an effort to make the largest database of ISM in $z \approx 0$ galaxies.

On scales smaller than the size of molecular clouds, turbulence plays an important role because it not only counteracts gravity, but also provides a heat source to the ISM. Even though the chemical pathways for the formation of H_2 and CO have been established, it may under-predict some molecular abundances by orders of magnitude (Falgarone et al. 2010). An alternative chemistry has been developed by taking into account the energy dissipation from turbulence to alter chemical reactions in the ISM (Godard et al. 2009, 2014). In this respect, a future observational test can be conducted to check whether CO abundance is higher than what is predicted by "traditional" chemical reactions in regions where the intermittency of turbulence cascades occurs.

Bibliography

Abazajian, K. N., Adelman-McCarthy, J. K., Agüeros, M. A., et al. 2009, ApJS, 182, 543
Alatalo, K., Davis, T. A., Bureau, M., et al. 2013, MNRAS, 432, 1796
Allende Prieto, C., Lambert, D. L., & Asplund, M. 2001, ApJ, 556, L63
Alloin, D., Collin-Souffrin, S., Joly, M., & Vigroux, L. 1979, A&A, 78, 200
Amblard, A., Riguccini, L., Temi, P., et al. 2014, ApJ, 783, 135
Anselmet, F., Antonia, R. A., & Danaila, L. 2001, Planet. Space Sci., 49, 1177
Asplund, M., Grevesse, N., Sauval, A. J., & Scott, P. 2009, ARA&A, 47, 481
Bacon, R., Copin, Y., Monnet, G., et al. 2001, MNRAS, 326, 23
Balbus, S. A., & Hawley, J. F. 1991, ApJ, 376, 214
Baldwin, J. A., Phillips, M. M., & Terlevich, R. 1981, PASP, 93, 5
Ballesteros-Paredes, J., & Mac Low, M.-M. 2002, ApJ, 570, 734
Barrera-Ballesteros, J. K., García-Lorenzo, B., Falcón-Barroso, J., et al. 2015, A&A, 582, A21
Bauermeister, A., Blitz, L., & Ma, C.-P. 2010, ApJ, 717, 323
Belfiore, F., Maiolino, R., Maraston, C., et al. 2016, MNRAS, 461, 3111
Bell, E. F., & de Jong, R. S. 2001, ApJ, 550, 212
Bertoldi, F., & McKee, C. F. 1992, ApJ, 395, 140
Bigiel, F., & Blitz, L. 2012, ApJ, 756, 183
Bigiel, F., Leroy, A., Walter, F., et al. 2008, AJ, 136, 2846
Bigiel, F., Leroy, A. K., Walter, F., et al. 2011, ApJ, 730, L13
Blanton, M. R., & Moustakas, J. 2009, ARA&A, 47, 159
Blitz, L. 1993, in Protostars and Planets III, ed. E. H. Levy & J. I. Lunine, 125
Blitz, L., Bazell, D., & Desert, F. X. 1990, ApJ, 352, L13
Blitz, L., Fukui, Y., Kawamura, A., et al. 2007, Protostars and Planets V, 81
Blitz, L., & Rosolowsky, E. 2004, ApJ, 612, L29
—. 2006, ApJ, 650, 933
Blitz, L., & Shu, F. H. 1980, ApJ, 238, 148
Blitz, L., & Spergel, D. N. 1991, ApJ, 379, 631
Blitz, L., & Stark, A. A. 1986, ApJ, 300, L89
Blitz, L., & Thaddeus, P. 1980, ApJ, 241, 676
Bock, D. C.-J., Bolatto, A. D., Hawkins, D. W., et al. 2006, in Society of Photo-Optical Instrumentation Engineers (SPIE) Conference Series, Vol. 6267, Society of Photo-Optical

Instrumentation Engineers (SPIE) Conference Series
Bohlin, R. C., Savage, B. D., & Drake, J. F. 1978, ApJ, 224, 132
Bolatto, A. D., Leroy, A. K., Rosolowsky, E., Walter, F., & Blitz, L. 2008, ApJ, 686, 948
Bolatto, A. D., Simon, J. D., Leroy, A., & Blitz, L. 2002, ApJ, 565, 238
Bolatto, A. D., Wolfire, M., & Leroy, A. K. 2013, ARA&A, 51, 207
Bolatto, A. D., Leroy, A. K., Jameson, K., et al. 2011, ApJ, 741, 12
Bolatto, A. D., Wong, T., Utomo, D., et al. 2017, ArXiv e-prints, arXiv:1704.02504
Bonnor, W. B. 1956, MNRAS, 116, 351
Brand, J., & Wouterloot, J. G. A. 1994, A&AS, 103
Braun, R. 2012, ApJ, 749, 87
Bruhweiler, F. C., Gull, T. R., Kafatos, M., & Sofia, S. 1980, ApJ, 238, L27
Brunt, C. M., Kerton, C. R., & Pomerleau, C. 2003, ApJS, 144, 47
Bundy, K., Bershady, M. A., Law, D. R., et al. 2015, ApJ, 798, 7
Calzetti, D. 2001, PASP, 113, 1449
Calzetti, D., Armus, L., Bohlin, R. C., et al. 2000, ApJ, 533, 682
Calzetti, D., Kennicutt, R. C., Engelbracht, C. W., et al. 2007, ApJ, 666, 870
Cappellari, M. 2002, MNRAS, 333, 400
Cappellari, M., Emsellem, E., Krajnović, D., et al. 2011, MNRAS, 413, 813
Cappellari, M., Scott, N., Alatalo, K., et al. 2013a, MNRAS, 432, 1709
Cappellari, M., McDermid, R. M., Alatalo, K., et al. 2013b, MNRAS, 432, 1862
Cardelli, J. A., Clayton, G. C., & Mathis, J. S. 1989, ApJ, 345, 245
Carruthers, G. R. 1970, ApJ, 161, L81
Catalán-Torrecilla, C., Gil de Paz, A., Castillo-Morales, A., et al. 2015, A&A, 584, A87
Chieze, J. P. 1987, A&A, 171, 225
Ciesla, L., Boquien, M., Boselli, A., et al. 2014, A&A, 565, A128
Colombo, D., Rosolowsky, E., Ginsburg, A., Duarte-Cabral, A., & Hughes, A. 2015, MNRAS, 454, 2067
Colombo, D., Hughes, A., Schinnerer, E., et al. 2014, ApJ, 784, 3
Combes, F., Young, L. M., & Bureau, M. 2007, MNRAS, 377, 1795
Conroy, C. 2013, ARA&A, 51, 393
Crocker, A., Krips, M., Bureau, M., et al. 2012, MNRAS, 421, 1298
Croom, S. M., Lawrence, J. S., Bland-Hawthorn, J., et al. 2012, MNRAS, 421, 872
Daddi, E., Elbaz, D., Walter, F., et al. 2010, ApJ, 714, L118
D'Agostino, R. B., & Stephens, M. A. 1986, Goodness-of-fit techniques
Dale, D. A., & Helou, G. 2002, ApJ, 576, 159
Dale, D. A., Cohen, S. A., Johnson, L. C., et al. 2009, ApJ, 703, 517
Dame, T. M., Elmegreen, B. G., Cohen, R. S., & Thaddeus, P. 1986, ApJ, 305, 892
Davis, T. A., Bayet, E., Crocker, A., Topal, S., & Bureau, M. 2013a, MNRAS, 433, 1659
Davis, T. A., Bureau, M., Cappellari, M., Sarzi, M., & Blitz, L. 2013b, Nature, 494, 328
Davis, T. A., Bureau, M., Onishi, K., et al. 2017, MNRAS, 468, 4675
Davis, T. A., Alatalo, K., Sarzi, M., et al. 2011, MNRAS, 417, 882
Davis, T. A., Alatalo, K., Bureau, M., et al. 2013c, MNRAS, 429, 534

de Vaucouleurs, G., de Vaucouleurs, A., Corwin, Jr., H. G., et al. 1991, Third Reference Catalogue of Bright Galaxies. Volume I: Explanations and references. Volume II: Data for galaxies between 0^h and 12^h. Volume III: Data for galaxies between 12^h and 24^h.
Dickey, J. M., Hanson, M. M., & Helou, G. 1990, ApJ, 352, 522
Domínguez, A., Siana, B., Henry, A. L., et al. 2013, ApJ, 763, 145
Draine, B. T., & Li, A. 2007, ApJ, 657, 810
Druard, C., Braine, J., Schuster, K. F., et al. 2014, A&A, 567, A118
Dubinski, J. 1998, ApJ, 502, 141
Ebert, R. 1955, ZAp, 37, 217
Elmegreen, B. G. 1989, ApJ, 338, 178
—. 1993, ApJ, 411, 170
Elmegreen, B. G. 1997, in Revista Mexicana de Astronomia y Astrofisica Conference Series, Vol. 6, Revista Mexicana de Astronomia y Astrofisica Conference Series, ed. J. Franco, R. Terlevich, & A. Serrano, 165
Elmegreen, B. G., & Lada, C. J. 1977, ApJ, 214, 725
Elmegreen, B. G., & Scalo, J. 2004, ARA&A, 42, 211
Engargiola, G., Plambeck, R. L., Rosolowsky, E., & Blitz, L. 2003, ApJS, 149, 343
Falcón-Barroso, J., Sánchez-Blázquez, P., Vazdekis, A., et al. 2011, A&A, 532, A95
Falgarone, E., Pety, J., & Hily-Blant, P. 2009, A&A, 507, 355
Falgarone, E., Godard, B., Cernicharo, J., et al. 2010, A&A, 521, L15
Field, G. B. 1965, ApJ, 142, 531
Field, G. B., Blackman, E. G., & Keto, E. R. 2011, MNRAS, 416, 710
Fleck, Jr., R. C., & Clark, F. O. 1981, ApJ, 245, 898
Förster Schreiber, N. M., Genzel, R., Bouché, N., et al. 2009, ApJ, 706, 1364
Fukui, Y., & Kawamura, A. 2010, ARA&A, 48, 547
Fukui, Y., Kawamura, A., Minamidani, T., et al. 2008, ApJS, 178, 56
García-Benito, R., Zibetti, S., Sánchez, S. F., et al. 2015, A&A, 576, A135
Garcia-Burillo, S., Guelin, M., Cernicharo, J., & Dahlem, M. 1992, A&A, 266, 21
Gautier, III, T. N. 1978, PhD thesis, Arizona Univ., Tucson.
Genzel, R., Tacconi, L. J., Gracia-Carpio, J., et al. 2010, MNRAS, 407, 2091
Genzel, R., Tacconi, L. J., Lutz, D., et al. 2015, ApJ, 800, 20
Gil de Paz, A., Boissier, S., Madore, B. F., et al. 2007, ApJS, 173, 185
Glover, S. C. O., & Clark, P. C. 2012, MNRAS, 426, 377
Godard, B., Falgarone, E., & Pineau Des Forêts, G. 2009, A&A, 495, 847
Godard, B., Falgarone, E., & Pineau des Forêts, G. 2014, A&A, 570, A27
Goldsmith, P. F., Heyer, M., Narayanan, G., et al. 2008, ApJ, 680, 428
Goodman, A. A., Benson, P. J., Fuller, G. A., & Myers, P. C. 1993, ApJ, 406, 528
Gould, R. J., & Harwit, M. 1963, ApJ, 137, 694
Gould, R. J., & Salpeter, E. E. 1963, ApJ, 138, 393
Gratier, P., Braine, J., Rodriguez-Fernandez, N. J., et al. 2010, A&A, 522, A3
—. 2012, A&A, 542, A108
Grenier, I. A., Casandjian, J.-M., & Terrier, R. 2005, Science, 307, 1292

Hawley, J. F., Gammie, C. F., & Balbus, S. A. 1995, ApJ, 440, 742
Heiles, C., & Troland, T. H. 2003, ApJ, 586, 1067
—. 2005, ApJ, 624, 773
Helfer, T. T., Thornley, M. D., Regan, M. W., et al. 2003, ApJS, 145, 259
Hennebelle, P., & Falgarone, E. 2012, A&A Rev., 20, 55
Heyer, M., & Dame, T. M. 2015, ARA&A, 53, 583
Heyer, M., Krawczyk, C., Duval, J., & Jackson, J. M. 2009, ApJ, 699, 1092
Heyer, M. H., & Brunt, C. M. 2004, ApJ, 615, L45
Heyer, M. H., Carpenter, J. M., & Snell, R. L. 2001, ApJ, 551, 852
Hily-Blant, P., Falgarone, E., & Pety, J. 2008, A&A, 481, 367
Hollenbach, D., & Salpeter, E. E. 1971, ApJ, 163, 155
Hubble, E. P. 1926, ApJ, 64
Hughes, A., Wong, T., Ott, J., et al. 2010, MNRAS, 406, 2065
Hughes, A., Meidt, S. E., Colombo, D., et al. 2013, ApJ, 779, 46
Imara, N., Bigiel, F., & Blitz, L. 2011, ApJ, 732, 79
Imara, N., & Blitz, L. 2011, ApJ, 732, 78
Jameson, K. E., Bolatto, A. D., Leroy, A. K., et al. 2016, ApJ, 825, 12
Jarrett, T. H., Chester, T., Cutri, R., Schneider, S. E., & Huchra, J. P. 2003, AJ, 125, 525
Jeans, J. H. 1902, Philosophical Transactions of the Royal Society of London Series A, 199, 1
Jogee, S., Scoville, N., & Kenney, J. D. P. 2005, ApJ, 630, 837
Kane, B. D., & Clemens, D. P. 1997, AJ, 113, 1799
Kauffmann, G., Heckman, T. M., Tremonti, C., et al. 2003, MNRAS, 346, 1055
Kegel, W. H. 1989, A&A, 225, 517
Kennicutt, R. C., & Evans, N. J. 2012, ARA&A, 50, 531
Kennicutt, Jr., R. C. 1998a, ARA&A, 36, 189
—. 1998b, ARA&A, 36, 189
Kennicutt, Jr., R. C., Armus, L., Bendo, G., et al. 2003, PASP, 115, 928
Keto, E., Ho, L. C., & Lo, K.-Y. 2005, ApJ, 635, 1062
Kewley, L. J., & Dopita, M. A. 2002, ApJS, 142, 35
Kim, C.-G., Kim, W.-T., & Ostriker, E. C. 2011, ApJ, 743, 25
Kim, C.-G., Ostriker, E. C., & Kim, W.-T. 2013, ApJ, 776, 1
Klessen, R. S., & Hennebelle, P. 2010, A&A, 520, A17
Koda, J., Scoville, N., Sawada, T., et al. 2009, ApJ, 700, L132
Kolmogorov, A. 1941, Akademiia Nauk SSSR Doklady, 30, 301
Krajnović, D., Alatalo, K., Blitz, L., et al. 2013, MNRAS, 432, 1768
Kroupa, P. 2001, MNRAS, 322, 231
Kruijssen, J. M. D., & Longmore, S. N. 2014, MNRAS, 439, 3239
Krumholz, M. R., Dekel, A., & McKee, C. F. 2012, ApJ, 745, 69
Krumholz, M. R., & Kruijssen, J. M. D. 2015, MNRAS, 453, 739
Krumholz, M. R., Leroy, A. K., & McKee, C. F. 2011, ApJ, 731, 25
Krumholz, M. R., & McKee, C. F. 2005, ApJ, 630, 250

Krumholz, M. R., McKee, C. F., & Tumlinson, J. 2009, ApJ, 693, 216
Larson, R. B. 1981, MNRAS, 194, 809
Leroy, A., Bolatto, A., Stanimirovic, S., et al. 2007, ApJ, 658, 1027
Leroy, A., Bolatto, A., Walter, F., & Blitz, L. 2006, ApJ, 643, 825
Leroy, A. K., Walter, F., Brinks, E., et al. 2008, AJ, 136, 2782
Leroy, A. K., Walter, F., Bigiel, F., et al. 2009, AJ, 137, 4670
Leroy, A. K., Bolatto, A., Gordon, K., et al. 2011, ApJ, 737, 12
Leroy, A. K., Bigiel, F., de Blok, W. J. G., et al. 2012, AJ, 144, 3
Leroy, A. K., Walter, F., Sandstrom, K., et al. 2013, AJ, 146, 19
Leroy, A. K., Bolatto, A. D., Ostriker, E. C., et al. 2014, ArXiv e-prints, arXiv:1411.2836
Leung, C. M. 1976, ApJ, 209, 75
Lilly, S. J., Carollo, C. M., Pipino, A., Renzini, A., & Peng, Y. 2013, ApJ, 772, 119
Lockman, F. J., Free, N. L., & Shields, J. C. 2012, AJ, 144, 52
Longmore, S. N., Bally, J., Testi, L., et al. 2013, MNRAS, 429, 987
Lucero, D. M., & Young, L. M. 2013, AJ, 145, 56
Lynden-Bell, D., & Kalnajs, A. J. 1972, MNRAS, 157, 1
Ma, C.-P., Greene, J. E., McConnell, N., et al. 2014, ApJ, 795, 158
Mac Low, M.-M., & Klessen, R. S. 2004, Reviews of Modern Physics, 76, 125
Madau, P., & Dickinson, M. 2014, ARA&A, 52, 415
Maíz Apellániz, J., & Úbeda, L. 2005, ApJ, 629, 873
Makarov, D., Prugniel, P., Terekhova, N., Courtois, H., & Vauglin, I. 2014, A&A, 570, A13
Mannucci, F., Della Valle, M., Panagia, N., et al. 2005, A&A, 433, 807
Marino, R. A., Rosales-Ortega, F. F., Sánchez, S. F., et al. 2013, A&A, 559, A114
Martins, L. P., González Delgado, R. M., Leitherer, C., Cerviño, M., & Hauschildt, P. 2005, MNRAS, 358, 49
Martizzi, D., Faucher-Giguère, C.-A., & Quataert, E. 2015, MNRAS, 450, 504
Mateo, M. L. 1998, ARA&A, 36, 435
Mathis, J. S., Mezger, P. G., & Panagia, N. 1983, A&A, 128, 212
McKee, C. F. 1989, ApJ, 345, 782
McKee, C. F., & Ostriker, E. C. 2007, ARA&A, 45, 565
McKee, C. F., & Ostriker, J. P. 1977, ApJ, 218, 148
McKee, C. F., van Buren, D., & Lazareff, B. 1984, ApJ, 278, L115
Meidt, S. E., Schinnerer, E., García-Burillo, S., et al. 2013, ApJ, 779, 45
Meidt, S. E., Hughes, A., Dobbs, C. L., et al. 2015, ApJ, 806, 72
Méndez-Abreu, J., Ruiz-Lara, T., Sánchez-Menguiano, L., et al. 2017, A&A, 598, A32
Miesch, M. S., & Bally, J. 1994, ApJ, 429, 645
Miyamoto, Y., Nakai, N., & Kuno, N. 2014, PASJ, 66, 36
Miyazaki, A., & Tsuboi, M. 2000, ApJ, 536, 357
Mizuno, N., Rubio, M., Mizuno, A., et al. 2001, PASJ, 53, L45
Mouschovias, T. C., & Paleologou, E. V. 1979, ApJ, 230, 204
Mouschovias, T. C., & Spitzer, Jr., L. 1976, ApJ, 210, 326
Murphy, E. J., Condon, J. J., Schinnerer, E., et al. 2011, ApJ, 737, 67

Myers, P. C., Dame, T. M., Thaddeus, P., et al. 1986, ApJ, 301, 398
Oka, T., Hasegawa, T., Hayashi, M., Handa, T., & Sakamoto, S. 1998, ApJ, 493, 730
Oka, T., Hasegawa, T., Sato, F., et al. 2001, ApJ, 562, 348
Onishi, K., Iguchi, S., Davis, T. A., et al. 2017, MNRAS, 468, 4663
Osterbrock, D. E. 1989, Astrophysics of gaseous nebulae and active galactic nuclei
Ostriker, E. C., McKee, C. F., & Leroy, A. K. 2010, ApJ, 721, 975
Ostriker, E. C., & Shetty, R. 2011, ApJ, 731, 41
Parker, E. N. 1958, ApJ, 128, 664
Pettini, M., & Pagel, B. E. J. 2004, MNRAS, 348, L59
Pety, J., Schinnerer, E., Leroy, A. K., et al. 2013, ApJ, 779, 43
Phillips, J. P. 1999, A&AS, 134, 241
Putman, M. E., Peek, J. E. G., Muratov, A., et al. 2009, ApJ, 703, 1486
Rahman, N., Bolatto, A. D., Wong, T., et al. 2011, ApJ, 730, 72
Rahman, N., Bolatto, A. D., Xue, R., et al. 2012, ApJ, 745, 183
Rathborne, J. M., Johnson, A. M., Jackson, J. M., Shah, R. Y., & Simon, R. 2009, ApJS, 182, 131
Roman-Duval, J., Federrath, C., Brunt, C., et al. 2011, ApJ, 740, 120
Roman-Duval, J., Jackson, J. M., Heyer, M., Rathborne, J., & Simon, R. 2010, ApJ, 723, 492
Rosolowsky, E. 2005, PASP, 117, 1403
—. 2007, ApJ, 654, 240
Rosolowsky, E., & Blitz, L. 2005, ApJ, 623, 826
Rosolowsky, E., Engargiola, G., Plambeck, R., & Blitz, L. 2003, ApJ, 599, 258
Rosolowsky, E., Keto, E., Matsushita, S., & Willner, S. P. 2007, ApJ, 661, 830
Rosolowsky, E., & Leroy, A. 2006, PASP, 118, 590
Rosolowsky, E. W., Pineda, J. E., Kauffmann, J., & Goodman, A. A. 2008, ApJ, 679, 1338
Sage, L. J., Welch, G. A., & Young, L. M. 2007, ApJ, 657, 232
Saintonge, A., Kauffmann, G., Kramer, C., et al. 2011a, MNRAS, 415, 32
Saintonge, A., Kauffmann, G., Wang, J., et al. 2011b, MNRAS, 415, 61
Saintonge, A., Catinella, B., Cortese, L., et al. 2016, MNRAS, 462, 1749
Salpeter, E. E. 1955, ApJ, 121, 161
Sánchez, S. F., Kennicutt, R. C., Gil de Paz, A., et al. 2012, A&A, 538, A8
Sánchez, S. F., Rosales-Ortega, F. F., Iglesias-Páramo, J., et al. 2014, A&A, 563, A49
Sánchez, S. F., Pérez, E., Sánchez-Blázquez, P., et al. 2016, Rev. Mexicana Astron. Astrofis., 52, 171
Sánchez-Blázquez, P., Peletier, R. F., Jiménez-Vicente, J., et al. 2006, MNRAS, 371, 703
Sánchez-Menguiano, L., Sánchez, S. F., Pérez, I., et al. 2016, A&A, 587, A70
Sandstrom, K. M., Leroy, A. K., Walter, F., et al. 2013, ApJ, 777, 5
Sault, R. J., Teuben, P. J., & Wright, M. C. H. 1995, in Astronomical Society of the Pacific Conference Series, Vol. 77, Astronomical Data Analysis Software and Systems IV, ed. R. A. Shaw, H. E. Payne, & J. J. E. Hayes, 433
Schawinski, K., Urry, C. M., Simmons, B. D., et al. 2014, MNRAS, 440, 889

Schinnerer, E., Meidt, S. E., Pety, J., et al. 2013, ApJ, 779, 42
Schlegel, D. J., Finkbeiner, D. P., & Davis, M. 1998, ApJ, 500, 525
Schmidt, M. 1959, ApJ, 129, 243
Schruba, A., Leroy, A. K., Walter, F., Sandstrom, K., & Rosolowsky, E. 2010, ApJ, 722, 1699
Schruba, A., Leroy, A. K., Walter, F., et al. 2011, AJ, 142, 37
—. 2012, AJ, 143, 138
Scoville, N. Z., & Hersh, K. 1979, ApJ, 229, 578
Scoville, N. Z., Yun, M. S., Sanders, D. B., Clemens, D. P., & Waller, W. H. 1987, ApJS, 63, 821
Sellwood, J. A., & Balbus, S. A. 1999, ApJ, 511, 660
Shetty, R., Beaumont, C. N., Burton, M. G., Kelly, B. C., & Klessen, R. S. 2012, MNRAS, 425, 720
Silk, J. 1997, ApJ, 481, 703
Singh, R., van de Ven, G., Jahnke, K., et al. 2013, A&A, 558, A43
Solomon, P. M., Rivolo, A. R., Barrett, J., & Yahil, A. 1987, ApJ, 319, 730
Spergel, D. N., & Blitz, L. 1992, Nature, 357, 665
Spitzer, L. 1978, Physical processes in the interstellar medium
Sreenivasan, K. R., & Antonia, R. A. 1997, Annual Review of Fluid Mechanics, 29, 435
Sternberg, A., & Dalgarno, A. 1995, ApJS, 99, 565
Stilp, A. M., Dalcanton, J. J., Skillman, E., et al. 2013, ApJ, 773, 88
Tamburro, D., Rix, H.-W., Leroy, A. K., et al. 2009, AJ, 137, 4424
Tonry, J. L., Dressler, A., Blakeslee, J. P., et al. 2001, ApJ, 546, 681
Toribio San Cipriano, L., García-Rojas, J., Esteban, C., Bresolin, F., & Peimbert, M. 2016, MNRAS, 458, 1866
Utomo, D., Blitz, L., Davis, T., et al. 2015, ApJ, 803, 16
Utomo, D., Kriek, M., Labbé, I., Conroy, C., & Fumagalli, M. 2014, ApJ, 783, L30
van den Bergh, S. 2000, The Galaxies of the Local Group (Cambridge)
van der Kruit, P. C., & Searle, L. 1981, A&A, 95, 105
van Dishoeck, E. F., & Black, J. H. 1988, ApJ, 334, 771
Vazdekis, A., Sánchez-Blázquez, P., Falcón-Barroso, J., et al. 2010, MNRAS, 404, 1639
Vázquez-Semadeni, E., Gómez, G. C., Jappsen, A. K., et al. 2007, ApJ, 657, 870
Visser, R., van Dishoeck, E. F., & Black, J. H. 2009, A&A, 503, 323
Vogel, S. N., Kulkarni, S. R., & Scoville, N. Z. 1988, Nature, 334, 402
von Weizsäcker, C. F. 1951, ApJ, 114, 165
Wada, K., Meurer, G., & Norman, C. A. 2002, ApJ, 577, 197
Walcher, C. J., Wisotzki, L., Bekeraité, S., et al. 2014, A&A, 569, A1
Walter, F., Brinks, E., de Blok, W. J. G., et al. 2008, AJ, 136, 2563
Wang, J., Feigelson, E. D., Townsley, L. K., et al. 2009, ApJ, 696, 47
Weisz, D. R., Johnson, B. D., Johnson, L. C., et al. 2012, ApJ, 744, 44
Williams, J. P., de Geus, E. J., & Blitz, L. 1994, ApJ, 428, 693
Williams, J. P., & McKee, C. F. 1997, ApJ, 476, 166

Wilson, C. D., & Walker, C. E. 1994, ApJ, 432, 148
Wilson, R. W., Jefferts, K. B., & Penzias, A. A. 1970, ApJ, 161, L43
Wolfire, M. G., Hollenbach, D., & McKee, C. F. 2010, ApJ, 716, 1191
Wolfire, M. G., Hollenbach, D., McKee, C. F., Tielens, A. G. G. M., & Bakes, E. L. O. 1995, ApJ, 443, 152
Wolfire, M. G., McKee, C. F., Hollenbach, D., & Tielens, A. G. G. M. 2003, ApJ, 587, 278
Wong, T., & Blitz, L. 2002, ApJ, 569, 157
Wong, T., Hughes, A., Ott, J., et al. 2011, ApJS, 197, 16
Wong, T., Xue, R., Bolatto, A. D., et al. 2013, ApJ, 777, L4
Wright, E. L., Eisenhardt, P. R. M., Mainzer, A. K., et al. 2010, AJ, 140, 1868
York, D. G., Adelman, J., Anderson, Jr., J. E., et al. 2000, AJ, 120, 1579
Young, L. M. 2002, AJ, 124, 788
Young, L. M., Bureau, M., & Cappellari, M. 2008, ApJ, 676, 317
Young, L. M., Bureau, M., Davis, T. A., et al. 2011, MNRAS, 414, 940
Yusef-Zadeh, F., & Morris, M. 1987, AJ, 94, 1178
Zheng, Y., Peek, J. E. G., Werk, J. K., & Putman, M. E. 2017, ApJ, 834, 179